Title

Thermal Characterization of Novel Electrodes and Modeling of Novel Characterization Methods for Electrochemical Energy Storage Systems

Author

Zhou, Yucheng

Publication Date

2025

Peer reviewed|Thesis/dissertation

University of California
Los Angeles

Thermal Characterization of Novel Electrodes and Modeling of Novel Characterization Methods for Electrochemical Energy Storage Systems

A dissertation submitted in partial satisfaction
of the requirements for the degree
Doctor of Philosophy in Mechanical Engineering

by

Yucheng Zhou

2025

Abstract of the Dissertation

Thermal Characterization of Novel Electrodes and Modeling of Novel Characterization Methods for Electrochemical Energy Storage Systems

by

Yucheng Zhou
Doctor of Philosophy in Mechanical Engineering
University of California, Los Angeles, 2025
Professor Laurent G. Pilon, Chair

This dissertation aims to investigate the thermal behavior of materials and electrodes made from novel synthesis and fabrication methods in lithium-ion batteries and electrochemical capacitors. This dissertation also aims to develop novel characterization techniques with rigorous design and validation. A combination of experimental measurements, numerical simulations, and theoretical analysis are presented.

First, this dissertation compares the thermodynamics behavior and the *operando* heat generation in lithium-ion battery electrodes made of $Ti_2Nb_2O_9$ microparticles or nanoparticles synthesized by solid-state or sol-gel methods. Electrochemical testing showed that electrodes made of $Ti_2Nb_2O_9$ nanoparticles exhibited larger specific capacity, smaller polarization, and better capacity retention at large currents. Potentiometric entropy measurements revealed that both types of electrodes showed similar thermodynamics behavior governed by lithium intercalation in solid solution. However, electrodes made of $Ti_2Nb_2O_9$ nanoparticles featured smaller overpotential and faster lithium ion transport. In fact, *operando* isothermal calorimetry during galvanostatic cycling revealed smaller instantaneous and time-averaged irreversible heat generation rates at electrodes made of $Ti_2Nb_2O_9$ nanoparticles, highlighting their smaller resistive losses and larger electrical conductivity.

Similarly, this dissertation compares NMC622 lithium-ion battery electrodes fabricated using a novel 3D printing process or the conventional 2D tape casting process. Potentio-

metric entropy measurements revealed that their thermodynamics behavior were identical and consisted of lithium deintercalation in solid solution. However, *operando* isothermal calorimetry indicated that the 3D printed electrodes featured larger specific capacity and better rate performance, attributed to their larger electrode/electrolyte interfacial surface area and electrical conductivity as well as their faster lithium ion transport. Therefore, the instantaneous heat generation rates were smaller in 3D printed electrodes, reducing the overall specific electrical energy and thermal energy dissipation per unit charge stored.

Furthermore, this dissertation proposes a novel and fast microcalorimetry electrothermal impedance spectroscopy (ETIS) method based on heat generation rate measurements at each electrode of a lithium-ion battery cell. This new method is capable of retrieving the open-circuit voltage, the entropic potential, and the partial entropy changes at each electrode from measurements at a single temperature. It also shortens the measurement duration to a few hours compared to several days using the galvanostatic intermittent titration technique (GITT). This novel microcalorimetry ETIS method was first validated with numerical simulations and then experimentally demonstrated on PNb_9O_{25} or $TiNb_2O_7$ battery cells.

Finally, this dissertation validates the step potential electrochemical spectroscopy (SPECS) method and refines the associated analysis capable of differentiating the contributions of electrical double layer formation and Faradaic reactions to the total charge storage in three-dimensional porous pseudocapacitive electrodes. The modified Poisson-Nernst-Planck model coupled with the Frumkin-Butler-Volmer theory were used to numerically reproduce experimental data obtained from the SPECS method accounting for interfacial, transport, and electrochemical phenomena. The fitting analysis of the SPECS method was modified for the Faradaic current. The new model can accurately predict the individual contributions of EDL formation and Faradaic reactions to the total current. Moreover, the contributions of EDL formation at the electrode surface or at the electrode/electrolyte interface within the porous electrode can be identified. Similarly, the Faradaic reactions due to surface-controlled or diffusion-controlled mechanisms can be distinguished.

The dissertation of Yucheng Zhou is approved.

Timothy S. Fisher

Yongjie Hu

Adrienne S. Lavine

Laurent G. Pilon, Committee Chair

University of California, Los Angeles

2025

This dissertation is dedicated to my family.

Table of Contents

List of Figures

List of Tables

Acknowledgments

First, I would like to thank my advisor, Prof. Laurent Pilon, for his mentorship during my six-year journey in the Morrin-Martinelli-Gier Memorial Heat Transfer Laboratory. From an undergraduate intern to a doctoral candidate, my growth both as a researcher and as a person has been accompanied by his guidance, support, and encouragement every step of the way. I would also like to thank Prof. Timothy Fisher, Prof. Yongjie Hu, and Prof. Adrienne Lavine for serving on my thesis committee, and for their positive influence on me through our interactions at UCLA.

Furthermore, I would like to acknowledge all my current and former lab members, Dr. Sun Woong Baek, Dr. Matevž Frajnkovič, Dr. Obaidallah Munteshari, Dr. Ampol Likitchatchawankun, Dr. Bing-Ang Mei, Dr. Tiphaine Galy, Dr. Eylul Simsek, Dr. Sara Vallejo-Castaño, Dr. Ali Dashti, Dr. Jack Hoeniges, Dr. Abhinav Bhanawat, Dr. Michal Marszewski, Dr. Galit Bar, Dr. Refet Ali Yalcin, Nicolas Leport, Ricardo Martinez, Thomas Lee, and Aimeric Laperruque. I would also like to thank all my collaborators, Prof. Thierry Brousse, Prof. Olivier Crosnier, Prof. Bruce Dunn, Prof. Ram Seshadri, Prof. Anton Van der Ven, Prof. Sarah Tolbert, Dr. Etienne Le Calvez, Dr. Yunkai Luo, Dr. Rebecca Vincent, Dr. Kira Wyckoff, Dr. Arava Zohar, Dr. Daniel Robertson, Ashlea Patterson, Makena White, Minseok Choi, as well as all my collaborators at the Lawrence Livermore National Laboratory. None of the work would have been possible without the contributions of these and many more outstanding individuals and teams.

Finally, I would like to thank my entire family for their unwavering support. To my parents, Houpan Zhou and Qiu Zhou, external circumstances may have stopped us from seeing each other for so long, but your love, trust, and understanding keep shining through each of our virtual interactions. Your enlightening perspectives on life constantly power me to overcome the next obstacle and strive for the next goal. To my grandparents, cousins, and many other family members, thank you for always standing behind me along this journey on the other side of the world. Thank you all for making this the experience that I will remember for the rest of my life.

Vita

2015-2019 B.S. Mechanical Engineering, University of California, Los Angeles, U.S.

2019-2020 M.S. Mechanical Engineering, University of California, Los Angeles, U.S.

2020-2025 Ph.D. Mechanical Engineering, University of California, Los Angeles, U.S.

Publications

O. Munteshari, **Y. Zhou**, B.-A. Mei, L. Pilon, 2019. Theoretical validation of the step potential electrochemical spectroscopy (SPECS) and multiple potential step chronoamperometry (MUSCA) methods for pseudocapacitive electrodes, Electrochimica Acta, vol. 321, p. 134648.

O. Munteshari, A. Borenstein, R. H. DeBlock, J. Lau, G. Whang, **Y. Zhou**, A. Likitchatchawankun, R. B. Kaner, B. Dunn, L. Pilon, 2020. *In operando* calorimetric measurements for activated carbon electrodes in ionic liquid electrolytes under large potential windows, ChemSusChem, vol. 13, no. 5, pp. 1013–1026.

S. W. Baek, M. B. Preefer, M. Saber, K. Zhai, M. Frajnkovič, **Y. Zhou**, B. S. Dunn, A. Van der Ven, R. Seshadri, L. Pilon, 2022. Potentiometric entropy and *operando* calorimetric measurements reveal fast charging mechanisms in PNb_9O_{25}, Journal of Power Sources, vol. 520, p. 230776.

R. C. Vincent, Y. Luo, J. L. Andrews, A. Zohar, **Y. Zhou**, Q. Yan, E. M. Mozur, M. B. Preefer, J. N. Weker, A. K. Cheetham, J. Luo, L. Pilon, B. C. Melot, B. Dunn, R. Seshadri, 2022. High-rate lithium cycling and structure evolution in Mo_4O_{11}, Chemistry of Materials, vol. 34, no. 9, pp. 4122–4133.

Y. Zhou, E. Le Calvez, S. W. Baek, M. Frajnkovič, C. Douard, E. Gautron, O. Crosnier, T. Brousse, L. Pilon, 2022. Effect of particle size on thermodynamics and lithium ion transport in electrodes made of $Ti_2Nb_2O_9$ microparticles or nanoparticles, Energy Storage Materials, vol. 52, pp. 371–385.

M. Frajnkovič, A. Likitchatchawankun, C. Douard, **Y. Zhou**, S. W. Baek, I. Catton, O. Crosnier, T. Brousse, L. Pilon, 2022. Calorimetry can detect the early onset of hydrolysis in hybrid supercapacitors with aqueous electrolytes, Journal of Power Sources, vol. 548, p. 232069.

S. W. Baek, K. E. Wyckoff, D. D. Robertson, M. Frajnkovič, **Y. Zhou**, S. H. Tolbert, R. Seshadri, L. Pilon, 2023. *Operando* calorimetry investigation of particle size effects on heat generation in Wadsley–Roth $(W_{0.2}V_{0.8})_3O_7$-based electrodes, ACS Applied Energy Materials, vol. 6, no. 3, pp. 1355–1367.

Y. Luo, E. Le Calvez, **Y. Zhou**, E. Gautron, E. Quarez, M. Preefer, O. Crosnier, J. N. Weker, L. Pilon, T. Brousse, B. Dunn, 2023. Structure and electrochemical properties of bronze phase materials containing two transition metals, Chemistry of Materials, vol. 35, no. 20, pp. 8675–8685.

Y. Zhou, Y. Luo, A. Patterson, S. W. Baek, M. Frajnkovič, R. Seshadri, B. S. Dunn, L. Pilon, 2023. Microcalorimetry electrothermal impedance spectroscopy (ETIS) informs entropy evolution at individual electrodes of PNb_9O_{25} or $TiNb_2O_7$ battery cells, Electrochimica Acta, vol. 468, p. 143072.

S. W. Baek, C. Z. Salamat, R. Elizalde-Segovia, P. Das, M. Frajnkovič, **Y. Zhou**, B. C. Thompson, S. R. Narayan, S. H. Tolbert, L. Pilon, 2024. Measuring heat dissipation and entropic potential in battery cathodes made with conjugated and conventional polymer binders using *operando* calorimetry, ACS Applied Polymer Materials, vol. 6, no. 9, pp. 4954–4963.

Y. Zhou, M. Frajnkovič, A. Likitchatchawankun, O. Munteshari, B.-A. Mei, L. Pilon, 2024. Three-dimensional step potential electrochemical spectroscopy (SPECS) simulations of porous pseudocapacitive electrodes, Electrochimica Acta, vol. 505, p. 144934.

Y. Zhou, A. Orhan, J. Ye, N. Leport, M. A. Worsley, L. Pilon, 2024. Superior electrochemical performance and reduced heat generation in 3D printed vs. 2D tape-casted NMC622 electrodes, Journal of Power Sources, vol. 629, p. 235861.

CHAPTER 1

Introduction

1.1 Electrochemical capacitors

Electrochemical capacitors (ECs) have attracted significant interest as a promising category of electrochemical energy storage systems thanks to their high power and energy density, high cycle efficiency, and long cycle life [2]. ECs can be classified as electrical double layer capacitors (EDLCs) or pseudocapacitors [2, 3]. Typically, EDLCs consist of carbon-based electrodes immersed in a liquid electrolyte, and store charge physically via electrical double layer (EDL) formation at the electrode/electrolyte interface [2, 3]. On the other hand, in addition to EDL formation, pseudocapacitors also store charges chemically via reduction/oxidation (redox) or faradaic reactions at the electrode surface [3, 4]. This can be accompanied by ion intercalation/deintercalation in/out of the bulk electrode. This section reviews the materials commonly used for different components of ECs.

1.1.1 Electrodes

Electrodes used in ECs should preferably feature (i) high specific surface area (around 1000 - 2000 m^2/g), (ii) high electrical conductivity, (iii) good wettability, and (iv) low cost [2]. EDLC electrodes are typically made of porous carbon such as activated carbon [5], ordered mesoporous carbon [6], and carbon nanotubes [7, 8]. Those carbon-based materials provide benefits such as high electrical conductivity, low cost, and well established production techniques.

Pseudocapacitive electrodes are typically made of transition metal oxides or conductive polymers that react with cations in the electrolyte such as Li^+, K^+, and H^+ [2, 9, 10]. For

transition metal oxides, the most common choices include Nb_2O_5, MnO_2, MoO_3, and $RuO_2 \cdot xH_2O$ [11–14]. For conductive polymers, the most common choices include polyaniline, polypyrrole, polythiphene and their derivatives [15]. However, both transition metal oxides and conductive polymers suffer from relatively low electrical conductivity [15, 16]. This can cause considerable potential drop across the electrodes, which in turn leads to lower capacitance. One general approach towards improving the performance of such electrodes is to use materials with high electrical conductivity (e.g., activated carbon) as the base, on which thin films of pseudocapacitive materials are deposited [17–20].

1.1.2 Electrolytes

Electrolytes typically consist of a salt (e.g., Na_2SO_4, $LiClO_4$) dissolved in a solvent (e.g., water, organic liquid). Electrolytes for ECs should preferably feature (i) large relative permittivity or dielectric constant, (ii) large ionic conductivity, (iii) wide potential windows, (iv) wide temperature ranges, (v) low cost, and (vi) low safety and environmental hazards [2]. For EDLCs, the electrolyte material should be resistant to chemical reactions with the electrode material. For pseudocapacitors, the electrolyte material should be capable of undergoing redox reactions along with cation intercalation into the electrode material [2].

Electrolytes can be classified into three categories namely (i) aqueous electrolytes, (ii) organic electrolytes, and (iii) ionic liquid electrolytes. Aqueous electrolytes offer large relative permittivity and ionic conductivity, but they also have limited potential windows and temperature ranges due to the low decomposition voltage and high freezing point of water [2, 10, 21, 22]. Alternatively, organic electrolytes feature non-aqueous solvents such as propylene carbonate (PC), ethylene carbonate (EC), dimethyl carbonate (DMC), and ethylmethyl carbonate (EMC). Organic electrolytes enable increased potential windows of over 2 V, but this is offset by their small relative permittivity and ionic conductivity, high cost, flammability and toxicity [2, 21, 22]. Finally, examples of ionic liquid electrolytes include $PYR_{14}TFSI$ and $PIP_{13}FSI$ [23]. They can be used as neat or as dissolved in organic solvents for increased ionic conductivity, but even then, the value is small compared to aqueous or

organic electrolytes [21, 22, 24, 25]. On the other hand, ionic liquid electrolytes remain electrochemically stable across potential windows of over 3 V, and they provide other advantages such as wide temperature ranges and low flammability [21, 22, 24].

1.2 Lithium-ion batteries

Batteries have attracted significant interest as a promising category of electrochemical energy storage systems thanks to their extremely high gravimetric and volumetric energy density, with widespread applications in portable consumer electronics and electric vehicles [26–30]. Batteries can be classified as primary batteries or secondary batteries [31–33]. Primary batteries can only be used once and cannot be recharged as they discharge based on irreversible chemical reactions [31]. By contrast, secondary batteries are rechargeable as they operate according to reversible redox reactions [31]. The main types of secondary batteries include (i) nickel-metal hydride batteries, (ii) lithium-ion batteries (LIBs), and (iii) sodium-ion batteries (SIBs) [34–38]. In particular, LIBs set the performance benchmarks in terms of their high energy density, high reversibility, and small loss of charge when not in use [39, 40]. This section reviews the materials commonly used for different components of LIBs.

1.2.1 Electrodes

Electrodes used in LIBs can be divided as cathodes or anodes. Cathodes correspond to electrodes where reduction reactions occur and electrons flow from the external circuit during the discharging process. Anodes correspond to electrodes where oxidation reactions occur and electrons flow into the external circuit during the discharging process.

Cathode materials should be (i) efficient oxidizing agents, (ii) stable when in contact with electrolytes, and (iii) capable of operating at high working voltages [31, 41, 42]. One of the earliest cathode materials for LIBs is titanium disulfide (TiS_2) [43], with its layered crystal structure facilitating intercalation/deintercalation of Li^+ ions. However, the operating voltage of TiS_2 is relatively low ($\approx$ 2 V vs. Li/Li^+) [43]. Since then, oxides with similar layered crystal structures but enable higher operating voltages ($\approx$ 4 V vs. Li/Li^+), such as

lithium cobalt oxide ($LiCoO_2$) [44] and lithium manganese nickel cobalt oxide (NMC) [45], have been discovered and have become the most common cathode materials for LIBs.

Anode materials should be (i) efficient reducing agents, (ii) stable when in contact with electrolytes, and (iii) available of large specific capacities [31,41,42]. One of the earliest anode materials for LIBs is graphite [46], with its large theoretical specific capacity of 372 mAh/g and low fabrication cost. However, graphite has a very low operating voltage ($\approx$ 0.2 V vs. Li/Li^+), making it susceptible to the formation of solid electrolyte interphase (SEI) layers, which leads to performance degradation over long-term cycling [46]. Furthermore, the specific capacity of graphite drops rapidly during fast cycling, making it unsuitable for fast charging LIBs. Since then, transition metal oxides such as lithium titanate ($Li_4Ti_5O_{12}$) [47, 48], niobium oxide (Nb_2O_5) [49, 50], and titanium niobium oxide ($TiNb_2O_7$) [51] have emerged as promising anode materials for LIBs. These materials not only enable higher operating voltages ($\approx$ 1.5 V vs. Li/Li^+), but also retain excellent specific capacities during fast cycling.

1.2.2 Electrolytes

Electrolytes enable ion transport between the cathode and the anode simultaneously with the electric current in the external circuit. Similar to the electrolytes for ECs, electrolytes for LIBs should give good ionic conductivity but should maintain electrical insulation to avoid internal short-circuiting. In addition, electrolytes should preferably feature (i) stability when in contact with the electrodes, (ii) wide potential windows, (iii) wide temperature ranges, (iv) low cost, and (v) low safety and environmental hazards.

For research purposes in a laboratory setting, including the experimental studies in this dissertation, organic electrolytes are the most common choices for LIBs. Organic electrolytes are made by dissolving salt, such as lithium hexafluorophosphate ($LiPF_6$), into organic solvents, such as propylene carbonate (PC), ethylene carbonate (EC), dimethyl carbonate (DMC), ethyl-methyl carbonate (EMC), or a mixture of these compounds. With a variety of salt and solvent combinations, organic electrolytes can cover a wide scope of potential windows and temperature ranges. However, organic electrolytes generally have high volatility

and flammability that could pose serious safety concerns [52].

1.3 Potentiometric entropy measurements

Potentiometric entropy measurements consist of determining the open-circuit voltage $U_{OCV}(x,T)$ and the entropic potential $[\partial U_{OCV}/\partial T](x,T)$ of a battery cell at a given temperature T and pressure as functions of lithium composition x, specific capacity C_m, or state of charge. Our previous study [53] has not only described the fundamental relationships between $U_{OCV}(x,T)$, $[\partial U_{OCV}/\partial T](x,T)$, and the material thermodynamic properties, but also developed an interpretation guide of their measurements for LIBs. In brief, the open-circuit voltage $U_{OCV}(x,T)$ of a battery cell with an intercalation compound (denoted by MA) working electrode and a metallic lithium (denoted by Li) counter electrode can be expressed as [53, 54],

$$U_{OCV}(x,T) = -\frac{1}{e}\left[\frac{\partial g_{MA}}{\partial x}(x,T) - \frac{\partial g_{Li}}{\partial x}(x,T)\right] \tag{1.1}$$

where e is the elementary charge, $g_{MA}(x,T)$ is the Gibbs free energy of $\mathrm{Li}_x\mathrm{MA}$ per unit of MA, and $g_{Li}(x,T)$ is the Gibbs free energy per unit of metallic lithium. Similarly, the entropic potential $[\partial U_{OCV}/\partial T](x,T)$ can be expressed as [53, 55],

$$\frac{\partial U_{OCV}}{\partial T}(x,T) = \frac{1}{e}\left[\frac{\partial s_{MA}}{\partial x}(x,T) - \frac{\partial s_{Li}}{\partial x}(x,T)\right] \tag{1.2}$$

where $s_{MA}(x,T)$ is the entropy of $\mathrm{Li}_x\mathrm{MA}$ per unit of MA and $s_{Li}(x,T)$ is the entropy per unit of metallic lithium. As such, $[\partial s_{MA}/\partial x](x,T)$ and $-[\partial s_{Li}/\partial x](x,T)$ can be regarded as the respective partial entropy changes at each electrode. Furthermore, the counter electrode consists of macroscopic metallic lithium with negligible surface energy effects [56]. Thus, $[\partial g_{Li}/\partial x](x,T)$ corresponds to the standard Gibbs free energy per unit of metallic lithium $g^{\circ}_{Li}(T)$, and $-[\partial s_{Li}/\partial x](x,T)$ is equal to the standard entropy per unit of metallic lithium $-s^{\circ}_{Li}(T)$ [53, 57]. Both $g^{\circ}_{Li}(T)$ and $-s^{\circ}_{Li}(T)$ are independent of x. Finally, the evolution of $U_{OCV}(x,T)$ and $[\partial U_{OCV}/\partial T](x,T)$ during lithiation can provide insight into the charging mechanisms of the battery cell such as lithium ion insertion in a homogeneous solid solution, two-phase coexistence, phase transition, and intralayer lithium ion ordering [53].

In addition, the apparent diffusion coefficient $D_{Li^+}(x,T)$ of lithium ions in the intercalation compound working electrode can be estimated from galvanostatic intermittent titration technique (GITT) measurements based on Fick's second law of diffusion using two different approaches [58]. On the one hand, for electrodes with uniform thickness, $D_{Li^+}(x,T)$ can be estimated from the net cell potential changes during GITT measurements according to [58],

$$D_{Li^+}(x,T) = \frac{4}{\pi\tau}\left(\frac{V_{MA}}{A_{MA}}\right)^2\left[\frac{\Delta U_{OCV}(x,T)}{\Delta V(x,T)}\right]^2. \tag{1.3}$$

Here, τ is the duration of the current pulse, A_{MA} and V_{MA} are respectively the surface area and volume of the working electrode, $\Delta V(x,T)$ is the cell potential change caused by the current pulse but excluding the initial IR drop, and $\Delta U_{OCV}(x,T)$ is the open-circuit voltage change caused by the current pulse.

On the other hand, for electrodes with varying thickness, e.g., those made from additive manufacturing techniques, $D_{Li^+}(x,T)$ can be estimated from the transient behavior of the cell potential during GITT measurements such that [58],

$$D_{Li^+}(x,T) = -\left(\frac{V_{MA}}{\pi A_{MA}}\right)^2\frac{\mathrm{dlog}[V(x,T,t)-U_{OCV}(x,T)]}{\mathrm{d}t}. \tag{1.4}$$

Here, $V(x,T,t)$ is the recorded cell potential during the relaxation period after a given current pulse, and $U_{OCV}(x,T)$ is the equilibrium open-circuit voltage retrieved at the end of that particular relaxation period.

Potentiometric entropy measurements consist of imposing a series of constant current pulses on the battery cell at constant temperature similar to GITT [1,59,60]. However, each current pulse is followed by a relaxation period during which a step-like temperature profile with four temperature plateaus is applied to the battery cell. Simultaneously, the corresponding potential evolution of the battery cell is recorded by a high accuracy potentiostat. As such, the open-circuit voltage $U_{OCV}(x,T)$ can be retrieved from the measured potential at the end of the relaxation period. Furthermore, the entropic potential $[\partial U_{OCV}/\partial T](x,T)$ can be calculated by taking the finite difference of the potential in response to each temperature step and averaging over the four instances. This method has been demonstrated to accurately measure the open-circuit voltage $U_{OCV}(x,T)$ and the entropic potential $[\partial U_{OCV}/\partial T](x,T)$ of

coin cells with metallic lithium counter electrodes and working electrodes made of intercalation compounds such as graphite [53], $LiCoO_2$ [53], $LiFePO_4$ [53], $TiNb_2O_7$ [59], PNb_9O_{25} [1], $Ti_2Nb_2O_9$ [60], $LiScMo_3O_8$ [61], and Mo_4O_{11} [62]. However, it requires long relaxation periods to ensure that the battery cell has reached thermodynamic equilibrium before collecting data for each lithium composition x at each temperature T. In fact, the total measurement time for one lithiation/delithiation cycle of a coin cell usually ranges between 200 and 400 hours [1,59,60]. Such durations are prohibitively long and faster alternative methods capable of providing meaningful information would be highly desirable.

1.4 *Operando* isothermal calorimetry

Heat generation arises from multiple physicochemical phenomena occurring inside electrochemical energy storage systems during operation [63]. Therefore, accurate estimations of heat generation are essential in designing effective thermal management strategies to prevent potential fire hazards such as thermal runaway [64]. Accordingly, various calorimetric techniques have been developed to measure the heat generation in batteries including accelerating rate calorimetry [64, 65], differential scanning calorimetry [66, 67], and isothermal calorimetry [63]. In particular, several isothermal calorimetric studies have reported heat generation rates in coin cells [63, 67], cylindrical cells [68], Swagelok cells [66], and prismatic cells [64] under galvanostatic cycling. However, they only detected the heat generation rate for the entire cell. To overcome this limitation, Munteshari et al. [69] developed and validated experimentally an *operando* isothermal calorimeter capable of measuring the instantaneous heat generation rates at each electrode. Subsequently, the device has been used to measure heat generation rates at each electrode of electric double layer capacitors [69–74], hybrid pseudocapacitors [75, 76], and LIBs [1, 59, 60]. The measurements revealed the thermal signatures associated with physical, chemical, and transport processes including resistive losses [1, 59, 60, 71–76], entropic changes [1, 60], ion adsorption/desorption [71–76], ion solvation/desolvation [1, 76], enthalpy of mixing [1, 59], electrolyte decomposition [73, 74, 76], overscreening effect [70, 74], and insulator to metal transition [1, 59].

1.4.1 Heat generation in batteries

The instantaneous total heat generation rate $\dot{Q}_T(x,T)$ (in W) in a battery cell can be divided into several contributions including (i) Joule heating $\dot{Q}_J(x,T)$, (ii) reversible entropic heat generation $\dot{Q}_{rev}(x,T)$, (iii) enthalpy or heat of mixing $\dot{Q}_{mix}(x,T)$, and (iv) heat generation due to side reactions $\dot{Q}_{sr}(x,T)$, i.e. [1, 59, 63, 77, 78],

$$\dot{Q}_T(x,T) = \dot{Q}_J(x,T) + \dot{Q}_{rev}(x,T) + \dot{Q}_{mix}(x,T) + \dot{Q}_{sr}(x,T). \tag{1.5}$$

The heat generation rate $\dot{Q}_i(x,T)$ is positive (or negative) when the associated phenomena are exothermic (or endothermic) and release (or absorb) heat.

The heat generation rate from Joule heating $\dot{Q}_J(x,T)$ due to irreversible resistive losses can be expressed as [1, 59, 63, 77, 78],

$$\dot{Q}_J(x,T) = I[V(x,T) - U^{avg}(x,T)] \approx I[V(x,T) - U_{OCV}(x,T)]. \tag{1.6}$$

Here, I is the imposed current, $V(x,T)$ is the cell potential, and $U^{avg}(x,T)$ is the open-circuit voltage evaluated at the volume-average concentration in the cell considering a single electrochemical reaction [79]. In other words, $U^{avg}(x,T)$ is the potential to which the cell would relax if the current was interrupted [77]. It is equivalent to the open-circuit voltage $U_{OCV}(x,T)$ obtained from potentiometric entropy measurements. The overpotential $[V(x,T) - U^{avg}(x,T)]$ is the potential drop across the cell due to internal resistance. Therefore, it increases with (i) increasing charge transfer resistance [80], (ii) decreasing ionic conductivity [80], and (iii) increasing cell degradation due to electrode deformation and/or electrolyte decomposition during cycling [81, 82].

The reversible heat generation rate $\dot{Q}_{rev}(x,T)$ due to entropic changes can be expressed as [63, 77, 78],

$$\dot{Q}_{rev}(x,T) = IT\frac{\partial U^{avg}(x,T)}{\partial T} \approx IT\frac{\partial U_{OCV}(x,T)}{\partial T}. \tag{1.7}$$

In addition, based on Equation (1.2), $\dot{Q}_{rev}(x,T)$ can be defined as the sum of the reversible heat generation rates at the intercalation compound working electrode $\dot{Q}_{rev,MA}(x,T)$ and at the lithium metal counter electrode $\dot{Q}_{rev,Li}(T)$ such that $\dot{Q}_{rev}(x,T) = \dot{Q}_{rev,MA}(x,T) +$

$\dot{Q}_{rev,Li}(T)$ with [1],

$$\dot{Q}_{rev,MA}(x,T) = \frac{IT}{e}\frac{\partial s_{MA}(x,T)}{\partial x} = \frac{IT}{e}s^{\circ}_{Li}(T) + IT\frac{\partial U^{avg}(x,T)}{\partial T}$$
$$\text{and} \quad \dot{Q}_{rev,Li}(T) = -\frac{IT}{e}s^{\circ}_{Li}(T). \tag{1.8}$$

However, the reversible heat generation rate is associated not only with entropic changes due to electrochemical reactions [63, 77, 78, 83] but also with other physicochemical phenomena including ion adsorption/desorption [70–75] and ion solvation/desolvation accompanied by ion-pairing [84–88]. Finally, at extremely small currents, the overpotential and ion concentration gradients in the cell are negligible, and the total heat generation rate is dominated by $\dot{Q}_{rev}(x,T)$ [89].

The heat generation rate from enthalpy of mixing $\dot{Q}_{mix}(x,T)$ due to ion concentration gradients can be expressed as [63, 77, 78],

$$\dot{Q}_{mix}(x,T) = \int_{V_\infty} \sum_i [\bar{h}_i(x,T) - \bar{h}_i^{avg}(x,T)]\frac{\partial c_i}{\partial t}\mathrm{d}V \tag{1.9}$$

where V_∞ is the volume of the cell, $\bar{h}_i(x,T)$ and $\bar{h}_i^{avg}(x,T)$ are respectively the local and the volume-averaged partial molar enthalpy of ion species i, and c_i is the local concentration of ion species i in the electrolyte or the electrode. The heat generation rate from enthalpy of mixing is caused by ion concentration gradients (i) across the electrolyte due to diffusion limitations, (ii) across the electrode due to non-uniform current distribution, (iii) within the pores of the electrode filled with electrolyte, and (iv) among intercalated lithium ions in the electrode due to electrochemical reactions. The latter is typically the dominant contribution [77, 79, 90]. Therefore, fast lithium ion transport in the electrode reduces the heat generation rate $\dot{Q}_{mix}(x,T)$.

Finally, the heat generation rate due to side reactions $\dot{Q}_{sr}(x,T)$ can be expressed as [63, 77, 78],

$$\dot{Q}_{sr}(x,T) = -\sum_i \Delta H_i \dot{r}_i(t) \tag{1.10}$$

where ΔH_i is the enthalpy of reaction for side reaction i occurring at reaction rate $\dot{r}_i(t)$. However, past studies on heat generation in a battery cell have generally neglected $\dot{Q}_{sr}(x,T)$ [63, 77, 78]. Indeed, side reactions usually arise from the ageing process of a battery cell,

which is relatively slow unless the cell is operating under extreme conditions [63, 78, 91]. Therefore, for the studies covered in this dissertation, $\dot{Q}_{sr}(x,T)$ was also neglected.

1.4.2 Energy balance

The net thermal energy Q_i (in J) attributed to the different contributions previously mentioned and released over a charging/discharging cycle can be expressed as [63],

$$Q_i = \oint_{cycle} \dot{Q}_i(x,T,t)\mathrm{d}t \quad \text{with } i = T,\ J,\ \text{or } mix. \tag{1.11}$$

Note that the reversible heat generation rate $\dot{Q}_{rev}(x,T,t)$ averaged over a cycle yields zero, i.e., $Q_{rev} = 0$. Moreover, the net electrical energy loss ΔE_e (in J) over a charging/discharging cycle corresponds to the area enclosed by the hysteresis of $V(x,T)$ vs. the charge transferred q such that [92],

$$\Delta E_e = \oint_{cycle} V(x,T)\mathrm{d}q = \oint_{cycle} V(x,T,t)I(t)\mathrm{d}t. \tag{1.12}$$

According to the first law of thermodynamics, the total thermal energy released during a cycle is equal to the net electrical energy loss such that [1, 59],

$$\Delta E_e = Q_T = Q_J + Q_{mix}. \tag{1.13}$$

1.5 Motivation of the present study

Electrochemical energy storage systems such as lithium-ion batteries [30, 93–97] and electrochemical capacitors [4, 49, 50, 98–100] have come to the fore as essential components in enabling the global transition towards electrification and renewable energy. Over the past decades, there have been significant efforts on discovering new cathode and anode materials with large capacity, good rate performance, and long cycle life. Furthermore, novel synthesis and fabrication techniques, in particular (i) downsizing of the material particles towards nanoscale [101–103] and (ii) additive manufacturing or three-dimensional printing of the samples [104–107], have been widely proposed as ways to achieve improvements in both energy and power densities. However, there has been little focus on the thermal attributes

of these state-of-the-art electrodes including their transport phenomena, thermodynamics properties, and heat generation. In fact, the physicochemical mechanisms behind superior electrochemical performance should theoretically lead to benefits in thermal performance as well. Proving this hypothesis with experimental measurements can further demonstrate the prospects of these electrodes for fast charging applications.

In addition, regarding the field of experimental measurements, the list of characterization techniques designed for evaluating the performance of electrochemical energy storage systems is constantly growing. However, for some of these cutting-edge techniques, there remains considerable scope for validation, clarification, refinement, and adaptation in order to improve or expand their suitability for a wide range of applications. Electrothermal impedance spectroscopy (ETIS) [108, 109] and step potential electrochemical spectroscopy (SPECS) [110–115] are two prime examples. The ETIS method, when integrated with *operando* isothermal calorimetry, is potentially capable of retrieving basic thermodynamic properties of a battery cell including the open-circuit voltage, the entropic potential, and the partial entropy changes at each electrode, all within a significantly shortened duration than existing techniques. The SPECS method, with a specialized data fitting analysis procedure, has not been rigorously validated in numerical simulations for three-dimensional mesoporous pseudocapacitive electrodes, which are more representative of the electrode samples used in actual experiments.

1.6 Objectives of the present study

The present study aims (i) to investigate the effect of particle size on thermodynamics and lithium ion transport in electrodes made of $Ti_2Nb_2O_9$ microparticles or nanoparticles, (ii) to demonstrate the superior electrochemical performance and reduced heat generation in 3D printed vs. 2D tape-casted NMC622 electrodes, (iii) to develop a novel ETIS measurement method to rapidly determine the open-circuit voltage U_{OCV}, the entropic potential $\partial U_{OCV}/\partial T$, and the partial entropy changes at each electrode of a battery cell, and (iv) to numerically adapt and validate the SPECS method for three-dimensional porous pseudoca-

pacitive electrodes.

1.7 Organization of the document

From the aspects of electrochemical performance, thermodynamics behavior, lithium ion transport, and heat generation, Chapter 2 investigates the effect of particle size by comparing electrodes made of $Ti_2Nb_2O_9$ microparticles or nanoparticles, and Chapter 3 demonstrates the advantages of novel 3D printed NMC622 electrodes over conventional 2D tape-casted NMC622 electrodes. Chapter 4 presents a novel microcalorimetry ETIS measurement method to rapidly determine the open-circuit voltage U_{OCV}, the entropic potential $\partial U_{OCV}/\partial T$, and the partial entropy changes at each electrode of a battery cell. Chapter 5 validates the SPECS method and refines the associated analysis for differentiating the contributions of electrical double layer formation and Faradaic reactions to the total charge storage in three-dimensional porous pseudocapacitive electrodes. Finally, Chapter 6 summarizes the findings of this PhD thesis and provides recommendations for future research.

CHAPTER 2

Effect of particle size on thermodynamics and lithium ion transport in electrodes made of $Ti_2Nb_2O_9$ microparticles or nanoparticles

This chapter aims to reveal the effect of the particle size on the electrochemical cycling performance, thermodynamics behavior, and lithium ion transport in $Ti_2Nb_2O_9$ electrodes. First, it presents a novel sol-gel method to synthesize mesoporous $Ti_2Nb_2O_9$ nanoparticles [116]. The structures and performance of electrodes made of $Ti_2Nb_2O_9$ nanoparticles were systematically compared with those made of $Ti_2Nb_2O_9$ microparticles synthesized by the traditional solid-state method [117]. Characterization techniques including *in situ* X-ray diffraction (XRD), cyclic voltammetry, and galvanostatic cycling were combined with state-of-the-art potentiometric entropy measurements and *operando* isothermal calorimetry. Overall, this chapter extends our general understanding of transition metal oxides as fast-charging LIB electrode materials by optimizing their particle size to achieve better performance and cycling stability and to reduce electrical losses and heat generation.

2.1 Materials and methods

2.1.1 Synthesis of $Ti_2Nb_2O_9$ powder

In this study, $Ti_2Nb_2O_9$ powder was synthesized by either a solid-state or a sol-gel process. In the solid-state synthesis method, powder of Nb_2O_5 (Alfa Aesar, 99.9%), TiO_2 (Alfa Aesar, $\geq$ 99%), and K_2CO_3 (ACS Reagent, $\geq$ 99.0%) was mixed with a molar ratio of 1:2:1.2. Here, 20% excess of K_2CO_3 was added owing to its volatility at high temperatures. This

mixture was ground in an agate mortar for 10 minutes to obtain a homogeneous powder. This powder was calcined at 1100 °C in a platinum crucible in air for 12 hours to produce $KTiNbO_5$ powder [118, 119].

In the sol-gel synthesis method, 1.351 mg of $NbCl_5$ (Sigma Aldrich, 99%) was dissolved in 30 mL of ethanol. Meanwhile, 1.703 mg of titanium isopropoxide (Alfa Aesar, 97%) and 0.370 mg of KCl (ACS Reagent, 99.0-100.5%) were dissolved in 200 mL of ethylene glycol. Then, citric acid (Alfa Aesar, $\geq$ 99%) was added to this second solution to achieve a molar ratio of 10:1 between citric acid and the total number of cations in both solutions (Nb, Ti, and K). After waiting for 1 hour to ensure complete dissolution of all species, the two solutions were mixed, then stirred and heated at 120 °C until a blackish gel was formed. This gel was dehydrated at 300 °C in air overnight so that the organic species completely evaporated. It was then calcined at 700 °C in air for 2 hours to produce $KTiNbO_5$ powder. Note that it was necessary to evacuate the chlorinated gases out of the handling room.

The final step, common to both synthesis methods, consisted of mixing and stirring 1 g of the $KTiNbO_5$ powder in 200 mL of 3 M aqueous HNO_3 for 3 days. The acid solution was changed daily to ensure the complete exchange of potassium cations with protons [118]. The resulting suspension containing $HTiNbO_5$ powder was then centrifuged and rinsed with DI water until waste water at neutral pH was obtained. Finally, the dried $HTiNbO_5$ powder was calcined at 400 °C in air for 2 hours to obtain $Ti_2Nb_2O_9$ powder synthesized by solid-state or sol-gel methods [117].

2.1.2 Electrode and device fabrication

A first set of self-supported electrodes were fabricated from a slurry prepared by mixing one of the $Ti_2Nb_2O_9$ powders previously synthesized by solid-state or sol-gel methods with conductive carbon (carbon black, Superior Graphite) and aqueous polytetrafluoroethylene (PTFE, Sigma Aldrich) in a small amount of ethanol with a mass ratio of 7.5:1.5:1. This slurry was homogenized with a pestle in a mortar and then cold-rolled until self-supported electrodes were obtained with mass loading between 4 and 5 mg/cm^2 and thickness between 60 and

75 μm [120]. These self-supported electrodes were used for *in situ* X-ray diffraction (XRD), cyclic voltammetry, galvanostatic cycling, and potentiometric entropy measurements. *In situ* XRD was performed on cells made according to the procedure first reported by Leriche et al. [121] and consisting of (i) a self-supported solid-state or sol-gel $Ti_2Nb_2O_9$ working electrode, (ii) a polished lithium metal (Sigma Aldrich, 99.9%) counter electrode, (iii) a 675 μm thick glass microfiber filter (Whatman, Grade GF/D) as the separator, impregnated with (iv) 1 M $LiPF_6$ in EC:DMC 1:1 w/w (Solvionic, battery grade) electrolyte. Similarly, cyclic voltammetry and galvanostatic cycling measurements were performed on Swagelok cells consisting of (i) a self-supported solid-state or sol-gel $Ti_2Nb_2O_9$ working electrode, (ii) a polished lithium metal (Sigma Aldrich, 99.9%) counter electrode, (iii) a 675 μm thick glass microfiber filter (Whatman, Grade GF/D) as the separator, impregnated with (iv) 1 M $LiPF_6$ in EC:DMC 1:1 w/w (Solvionic, battery grade) electrolyte. Finally, potentiometric entropy measurements at C-rate of C/10 were performed on coin cells consisting of (i) a self-supported solid-state or sol-gel $Ti_2Nb_2O_9$ working electrode, (ii) a polished lithium metal (Sigma Aldrich, 99.9%) counter electrode, (iii) a 260 μm thick glass microfiber filter (Whatman, Grade GF/C) as the separator, impregnated with (iv) 1 M $LiPF_6$ in EC:DMC 1:1 v/v (Sigma Aldrich, battery grade) electrolyte. Here, the *in situ* XRD cells, Swagelok cells, and coin cells were assembled in a glove box containing Ar gas with less than 0.1 ppm of O_2 and H_2O.

Another set of electrodes were fabricated on copper current collectors from a slurry prepared by dispersing one of the $Ti_2Nb_2O_9$ powders previously synthesized by solid-state or sol-gel methods and conductive carbon (carbon black, Superior Graphite) in N-methyl-2-pyrrolidone (NMP) solvent with a $Ti_2Nb_2O_9$:conductive carbon mass ratio of 5:1. After dispersion in the solvent, polyvinylidene fluoride (PVDF) dissolved in NMP (7 wt%) was added to achieve a $Ti_2Nb_2O_9$:PVDF mass ratio of 7.5:1. Next, the slurry was spread on a large copper substrate using a doctor blade and then dried in ambient air overnight. The obtained slurry-cast electrodes had a $Ti_2Nb_2O_9$:conductive carbon:PVDF mass ratio of 7.5:1.5:1, mass loading around 5.5 mg/cm^2, and thickness around 150 μm. On the one hand, these electrodes were used in *operando* isothermal calorimetry on two-electrode cells consist-

ing of (i) a slurry-cast solid-state or sol-gel $Ti_2Nb_2O_9$ working electrode and cut into 1 cm × 1 cm square shape, (ii) a polished lithium metal (Sigma Aldrich, 99.9%) counter electrode also cut into 1 cm × 1 cm square shape, (iii) two 50 μm thick polypropylene/polyethylene (Celgard, C380) sheets acting as separators and thermal insulators, impregnated with (iv) 1 M $LiPF_6$ in EC:DMC 1:1 v/v (Sigma Aldrich, battery grade) electrolyte. On the other hand, potentiometric entropy measurements at C-rates of 1.5C and 6C were performed on coin cells consisting of (i) a slurry-cast solid-state or sol-gel $Ti_2Nb_2O_9$ working electrode, (ii) a polished lithium metal (Sigma Aldrich, 99.9%) counter electrode, (iii) a 260 μm thick glass microfiber filter (Whatman, Grade GF/C) as the separator, impregnated with (iv) 1 M $LiPF_6$ in EC:DMC 1:1 v/v (Sigma Aldrich, battery grade) electrolyte. Here also, the calorimetric cells and coin cells were assembled in a glove box containing Ar gas with less than 0.1 ppm of O_2 and H_2O.

2.1.3 Structural characterization

Transmission electron microscopy (TEM) and *in situ* XRD were performed in order to characterize the structure and phases of $Ti_2Nb_2O_9$ powder synthesized by solid-state or sol-gel methods. TEM images were collected using a probe-corrected Themis Z G3 microscope (Thermo Fisher Scientific) equipped with a high-angle annular dark-field detector (Fischione). Here, the $Ti_2Nb_2O_9$ powder was dispersed in ethanol and then deposited on a copper grid. Both the XRD patterns of pristine $Ti_2Nb_2O_9$ powders and the *in situ* XRD patterns of $Ti_2Nb_2O_9$ electrodes were collected using a PANalytical X'Pert Pro diffractometer (Malvern Panalytical). An X'Celerator detector with Cu-$K_{\alpha1}$-$K_{\alpha2}$ (λ = 1.54060 $\mathring{A}$, 1.54439 $\mathring{A}$) radiation was used at acceleration voltage of 40 kV and current of 40 mA. During charging and discharging of the cell, a series of constant current pulses at 0.02 A/g of $Ti_2Nb_2O_9$ were imposed. Each current pulse lasted 20 minutes followed by a relaxation period of 30 minutes for pattern acquisition between $2\theta = 5^\circ$ and 40°.

2.1.4 Electrochemical characterization

Cyclic voltammetry measurements consisted of imposing a triangular waveform as the cell potential V and recording the cell current I with a high accuracy potentiostat (BioLogic, VMP3). The specific capacity $C_m(\nu)$ (in mAh/g) at scan rate ν was calculated according to [122],

$$C_m(\nu) = \frac{1}{m} \oint_{cycle} \frac{I}{2\nu} \mathrm{d}V \tag{2.1}$$

where m is the mass loading of $Ti_2Nb_2O_9$ at the working electrode.

Similarly, the cell potential V under galvanostatic cycling at constant current $\pm I$ was also recorded by a high accuracy potentiostat (BioLogic, VMP3). The IR drop ΔV can be identified as the sharp potential change observed when switching between charging and discharging or vice versa. Then, the internal resistance R_{GC} of the cell was calculated according to [70, 123–126],

$$R_{GC} = \frac{\Delta V}{2I}. \tag{2.2}$$

2.1.5 Potentiometric entropy measurements

The open-circuit voltage $U_{OCV}(C_m, T)$ and entropic potential $\partial U_{OCV}(C_m, T)/\partial T$ of the coin cells with working electrodes made of $Ti_2Nb_2O_9$ microparticles or nanoparticles synthesized by solid-state or sol-gel methods were measured as functions of specific capacity C_m using the potentiometric entropy measurement technique and the apparatus described in Refs. [1, 59]. The measurements consisted of imposing a series of constant current pulses at a C-rate of C/10 at 20 °C. Each current pulse lasted 30 minutes followed by a relaxation period of 270 minutes during which a step-like temperature profile was applied to the coin cell from 15 °C to 25 °C in 5 °C increments with a thermoelectric cold plate (TE technology, CP-121). The corresponding coin cell potential evolution was recorded by a high accuracy potentiostat (BioLogic, VSP-300). Before recording the open-circuit voltage $U_{OCV}(C_m, T)$ at a given specific capacity C_m and temperature T, we verified that the coin cell had reached thermodynamic equilibrium by ensuring that (i) the temperature difference between the cold plate and the surface of the coin cell was less than 0.1 °C and (ii) the time rate of change of

the open-circuit voltage $\partial U_{OCV}(C_m, T)/\partial t$ was less than 1 mV/h.

2.1.6 *Operando* isothermal calorimetry

Operando isothermal calorimetry was performed in the aforementioned two-electrode cells using the apparatus described in Ref. [69]. Here, galvanostatic cycling was imposed using a high accuracy potentiostat (BioLogic, SP-150). Simultaneously, the instantaneous heat generation rates $\dot{Q}_i(t)$ (in mW) at the working electrode made of $Ti_2Nb_2O_9$ microparticles or nanoparticles and at the lithium metal counter electrode were calculated from the instantaneous heat fluxes $q_i''(t)$ (in mW/cm^2) measured by a 1 cm $\times$ 1 cm thermoelectric heat flux sensor (greenTEG, gSKIN-XP) in thermal contact with the back of each electrode "i" according to [69],

$$\dot{Q}_i(t) = q_i''(t)A_i = \frac{\Delta V_i(t)}{S_i}A_i \quad \text{with } i = TNO \text{ or } Li. \tag{2.3}$$

Here, A_i (in cm^2) is the footprint area of the electrode and $\Delta V_i(t)$ (in μV) is the instantaneous voltage difference measured by the heat flux sensor with sensitivity S_i [in μV/(W/cm^2)]. Then, the instantaneous total heat generation rate in the entire calorimetric cell $\dot{Q}_T(t)$ can be expressed as the sum of those at each electrode such that,

$$\dot{Q}_T(t) = \dot{Q}_{TNO}(t) + \dot{Q}_{Li}(t). \tag{2.4}$$

In addition, the instantaneous heat generation rates $\dot{Q}_i(t)$ at each electrode can be divided into an irreversible $\dot{Q}_{irr,i}(t)$ and a reversible $\dot{Q}_{rev,i}(t)$ contribution such that,

$$\dot{Q}_i(t) = \dot{Q}_{irr,i}(t) + \dot{Q}_{rev,i}(t). \tag{2.5}$$

To minimize the white noise in the signal from the heat flux sensors, the instantaneous heat generation rates $\dot{Q}_i(t)$ measured at each electrode were averaged over the last three consecutive cycles at any given current I, i.e.,

$$\dot{Q}_i(t) = \frac{1}{3}\sum_{j=1}^{3} \dot{Q}_i[t + (j-1)t_{cd}]. \tag{2.6}$$

Finally, the time-averaged irreversible heat generation rates $\bar{\dot{Q}}_{irr,i}$ during a charging/discharging cycle can be calculated according to [1, 59],

$$\bar{\dot{Q}}_{irr,i} = \bar{\dot{Q}}_i = \frac{1}{t_{cd}} \oint_{cycle} \dot{Q}_i(t) \mathrm{d}t \quad \text{with } i = TNO \text{ or } Li. \tag{2.7}$$

Note that $\dot{Q}_{rev,i}(t)$ averaged over a cycle yields zero.

2.2 Results and discussion

2.2.1 Structural characterization

Figure 2.1(a) shows the crystallographic structure of $Ti_2Nb_2O_9$, demonstrating its tunnel structure which facilitates lithium ion intercalation. Figures 2.1(b) and 2.1(c) show the transmission electron microscopy (TEM) images of $Ti_2Nb_2O_9$ microparticles or nanoparticles synthesized by solid-state or sol-gel methods, respectively. Here, the solid-state synthesis method produced microparticles with size around 1 μm while the sol-gel synthesis method produced nanoparticles with size around 50 nm. Furthermore, mesopores formed during the dehydration synthesis step were marked by green circles, showing that the sol-gel method created more nanoporosity in the synthesized $Ti_2Nb_2O_9$ than the solid-state method. In fact, the specific surface area measured by low-temperature nitrogen adsorption porosimetry of $Ti_2Nb_2O_9$ microparticles or nanoparticles reached 1.4 and 24.6 m^2/g, respectively. The respective volumes of micropores and mesopores were 3.16×10^{-5} and 0.0092 cm^3/g in $Ti_2Nb_2O_9$ microparticles, or 0.008 and 0.095 cm^3/g in $Ti_2Nb_2O_9$ nanoparticles. In other words, both types of particles were dense and slightly porous. The pore size distributions were bimodal with an average pore width of $Ti_2Nb_2O_9$ microparticles and nanoparticles recorded as 17.5 and 4.7 nm, respectively (see Figure A.1 in Appendix A). According to the IUPAC classification [127], the $Ti_2Nb_2O_9$ microparticles contained primarily mesopores with pore width between 2 and 50 nm while the $Ti_2Nb_2O_9$ nanoparticles had nanopores with pore width < 2 nm. Initially for both types of particles, the mesopores were mainly created during the synthesis of the precursor $HTiNbO_5$ while the nanopores were generated mostly due to the final calcination step of $HTiNbO_5$ to obtain $Ti_2Nb_2O_9$.

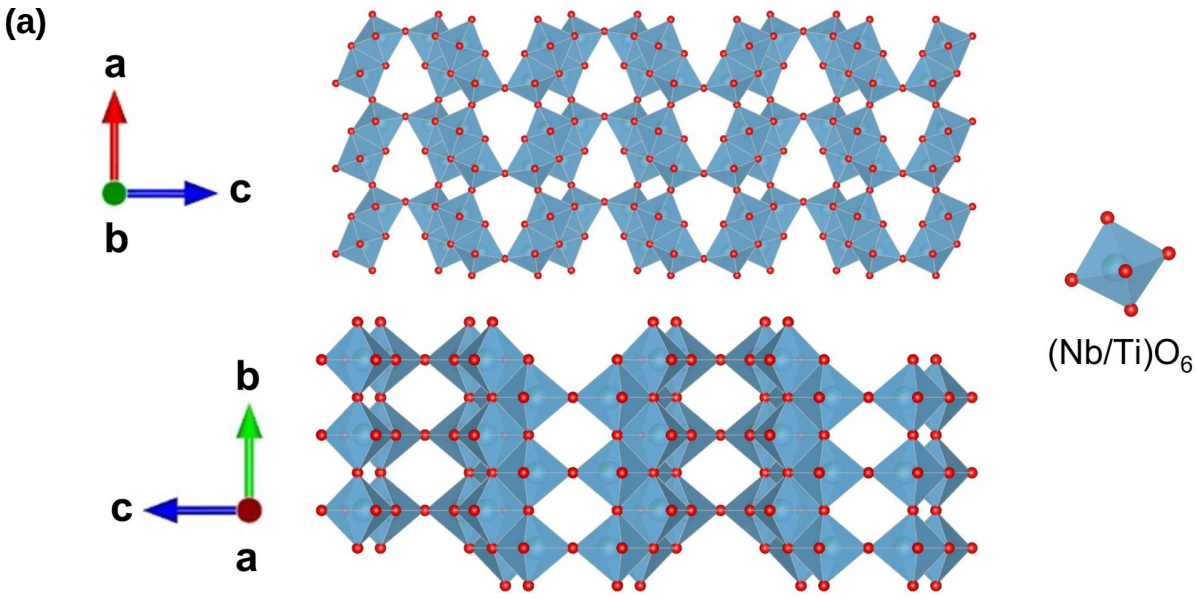

(b) $Ti_2Nb_2O_9$ microparticles synthesized by solid-state method

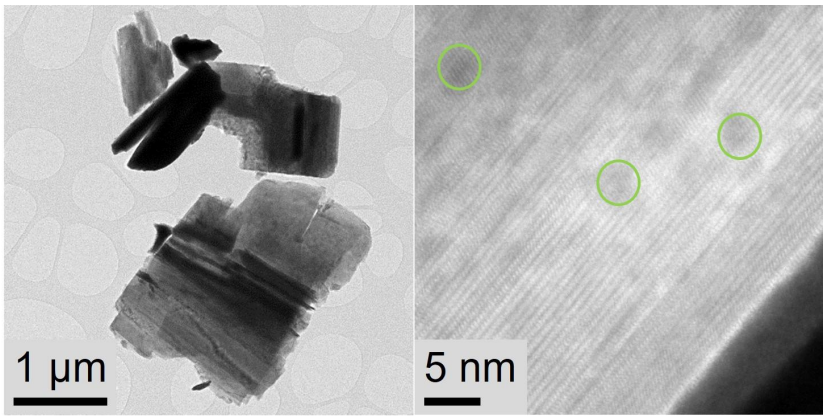

(c) $Ti_2Nb_2O_9$ nanoparticles synthesized by sol-gel method

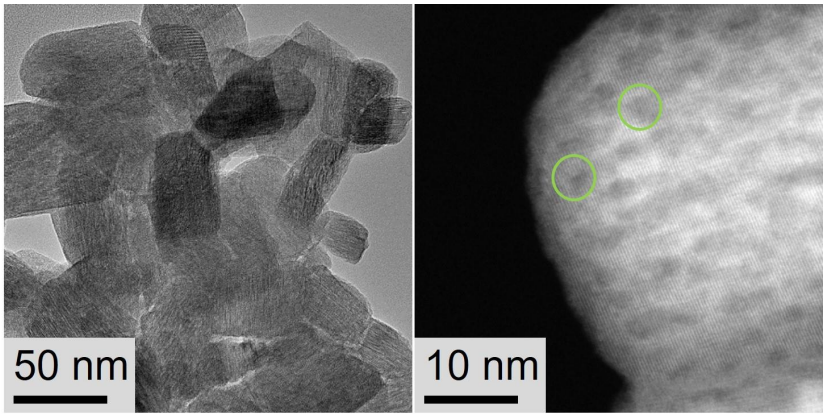

Figure 2.1: (a) Crystallographic structure of $Ti_2Nb_2O_9$. Transmission electron microscopy (TEM) images of $Ti_2Nb_2O_9$ (b) microparticles and (c) nanoparticles.

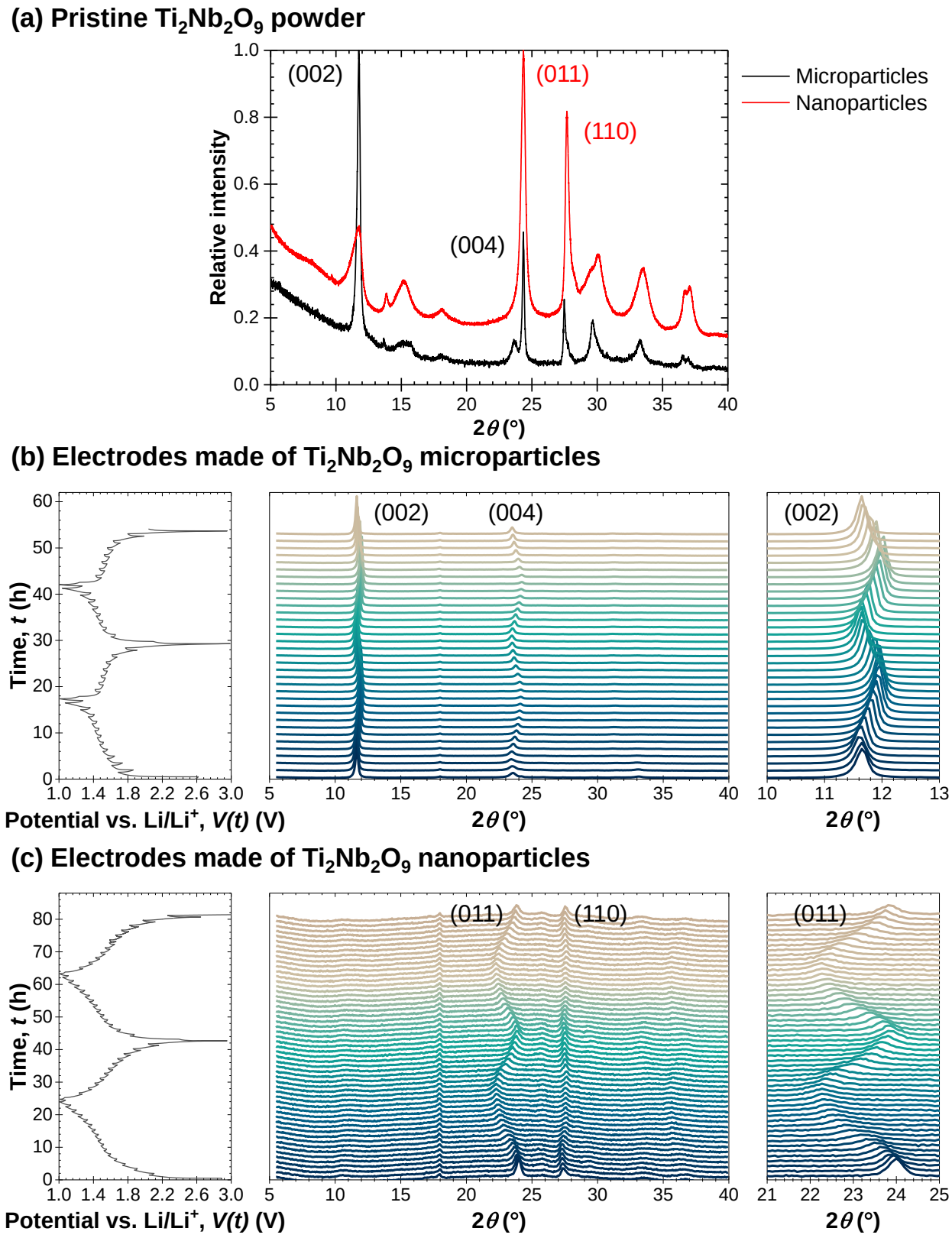

Figure 2.2: (a) XRD patterns of pristine $Ti_2Nb_2O_9$ powder. *In situ* XRD patterns of electrodes made of $Ti_2Nb_2O_9$ (b) microparticles or (c) nanoparticles.

First, Figure 2.2(a) shows the XRD patterns of pristine $Ti_2Nb_2O_9$ powders. Here, $Ti_2Nb_2O_9$ microparticles exhibited preferential orientation along the c-axis based on the high intensity of the (002) and (004) peaks. By contrast, $Ti_2Nb_2O_9$ nanoparticles did not develop preferential growth while the larger peak widths indicate their smaller crystallite size. Furthermore, Figure 2.2 shows the *in situ* XRD patterns of self-supported electrodes made of $Ti_2Nb_2O_9$ (b) microparticles or (c) nanoparticles. It indicates that not every expected diffraction peak was observed in the patterns for electrodes made of $Ti_2Nb_2O_9$ microparticles. This was due to (i) the aforementioned preferential orientation of the synthesized $Ti_2Nb_2O_9$ microparticles and (ii) the treatment during synthesis of the powder to form a self-supported paste. Nevertheless, the (002) peak around $2\theta = 12^\circ$ and the (004) peak around $2\theta = 24^\circ$ were clearly visible and could be attributed to $Ti_2Nb_2O_9$ [117, 118, 128]. Similarly, not every expected diffraction peak was observed for electrodes made of $Ti_2Nb_2O_9$ nanoparticles. This was due to the low crystallinity of the synthesized $Ti_2Nb_2O_9$ nanoparticles. Nonetheless, the (011) peak around $2\theta = 24^\circ$ and the (110) peak around $2\theta = 27^\circ$ were clearly visible and could be attributed to $Ti_2Nb_2O_9$ [117, 118, 128]. In addition, in both cases the peak around $2\theta = 18^\circ$ did not shift and could be attributed to PTFE in the binder [129]. It is interesting to note that every diffraction peak was maintained at constant intensity and featured small and continuous shifts during lithiation and delithiation which returned to their original position after each cycle. This suggests that the prevailing charging mechanism corresponded to reversible lithium ion insertion in a homogeneous solid solution of $Ti_2Nb_2O_9$ for electrode material synthesized by either method. In other words, the lithiation and delithiation processes caused only minor and reversible distortions to the crystallographic structure of $Ti_2Nb_2O_9$. Finally, the recent study by Drozhzhin et al. [130] reported, during the first lithiation half-cycle, an irreversible phase transformation between two orthorhombic phases within the same space group (Pnmm) along with changes in the unit cell parameters. We hypothesize that this discrepancy possibly appears due to (i) the different specifications of the diffractometers used in the two studies and (ii) differences in the synthesis methods. Indeed, Drozhzhin et al. [130] produced the intermediate compound NH_4TiNbO_5 and the residue NH_3 which potentially created a slight difference in the initial structure. Intercalation in a

solid solution was reported for subsequent half-cycles, as observed in the present study.

2.2.2 Electrochemical characterization

Figure 2.3 plots the cyclic voltammogram of the Swagelok cells with self-supported working electrodes made of $Ti_2Nb_2O_9$ (a) microparticles or (b) nanoparticles cycled between 1.0 and 3.0 V vs. Li/Li^+ at scan rates ν ranging between 0.1 and 50 mV/s. It also shows (c) the peak specific current $I_{m,peak}(\nu)$, and (d) the specific capacity $C_m(\nu)$ as functions of scan rate ν. The pair of cathodic and anodic peaks around 1.4/1.6 V vs. Li/Li^+, observed at $\nu = 0.1$ mV/s, could be attributed to both Ti^{4+}/Ti^{3+} and Nb^{5+}/Nb^{4+} redox reactions [117,131,132]. At any given scan rate ν, the polarization of the cell with $Ti_2Nb_2O_9$ nanoparticles was smaller than that with $Ti_2Nb_2O_9$ microparticles. This resulted in greater cycling reversibility for the cell with $Ti_2Nb_2O_9$ nanoparticles than that with $Ti_2Nb_2O_9$ microparticles. Moreover, the b-value associated with this pair of redox peaks was obtained by least squares fitting of the peak specific current $I_{m,peak}$ according to the power law $I_{m,peak} = a\nu^b$ [133]. Note that the b-value analysis is a qualitative technique widely used to assess the charging mechanisms in both battery and pseudocapacitive electrode materials ranging between the limiting cases of slow redox reactions limited by ion diffusion in a semi-infinite medium (b = 0.5) and fast redox reactions without ion transport limitation (b = 1). In fact, a series of studies [134, 135] validated the b-value analysis in hybrid pseudocapacitors using state-of-the-art numerical simulations and physicochemical models based on first principles. Between $\nu = 0.1$ and 2 mV/s, the b-value of the cell with $Ti_2Nb_2O_9$ microparticles or nanoparticles was 0.51 and 0.88, respectively. This suggests that redox reactions and lithium ion intercalation were faster and less diffusion-limited in the working electrode made of $Ti_2Nb_2O_9$ nanoparticles than that made of $Ti_2Nb_2O_9$ microparticles thanks to their larger surface area and smaller size. Finally, at any given scan rate ν, the specific capacity $C_m(\nu)$ of the cell with $Ti_2Nb_2O_9$ nanoparticles was larger than that with $Ti_2Nb_2O_9$ microparticles. In addition, the decrease in the specific capacity $C_m(\nu)$ with increasing scan rate ν was less significant for the cell with $Ti_2Nb_2O_9$ nanoparticles than that with $Ti_2Nb_2O_9$ microparticles.

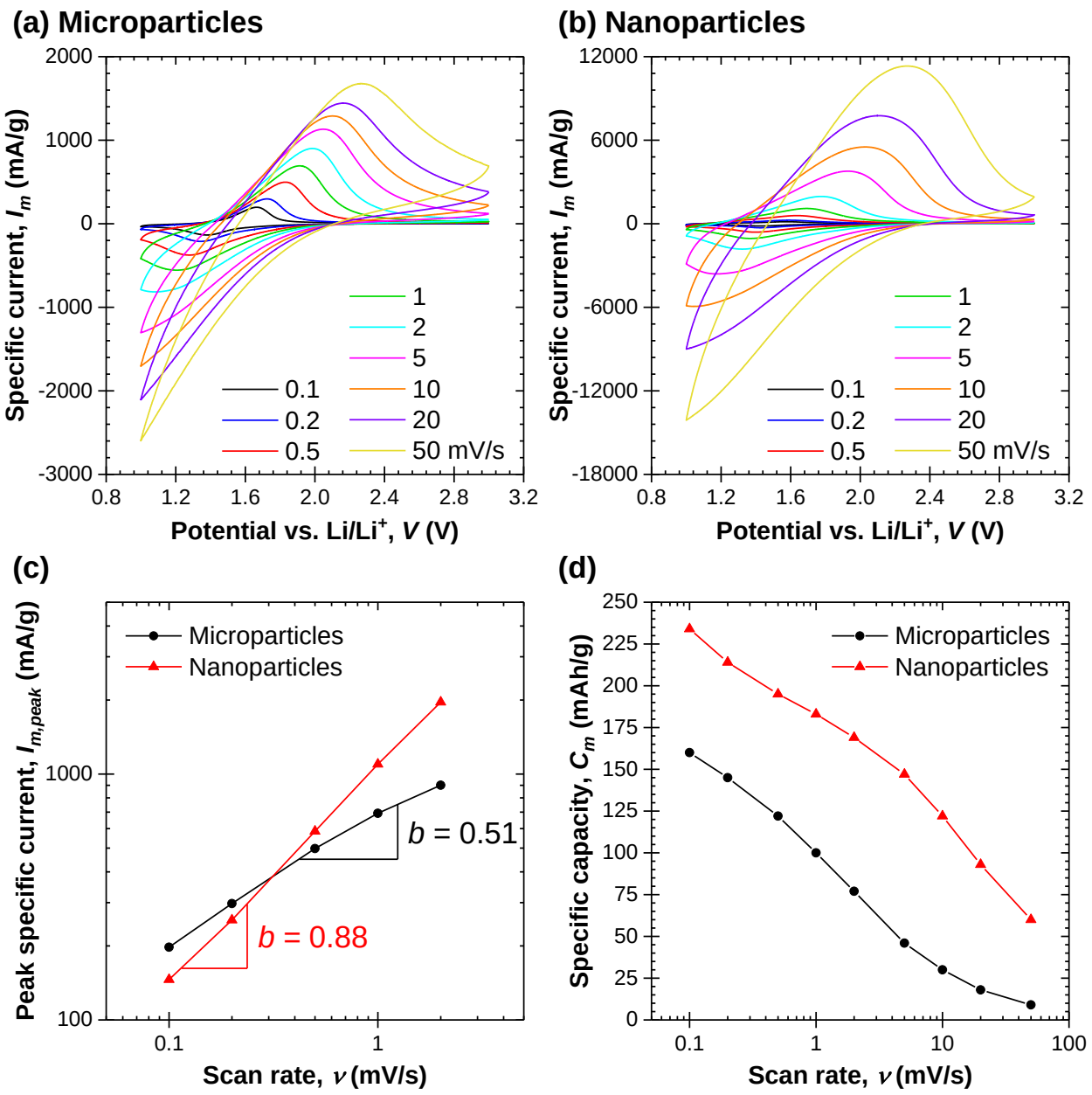

Figure 2.3: Cyclic voltammogram of Swagelok cells with working electrodes made of $Ti_2Nb_2O_9$ (a) microparticles or (b) nanoparticles cycled between 1.0 and 3.0 V vs. Li/Li$^+$ at scan rates ν ranging between 0.1 and 50 mV/s, along with (c) peak specific current $I_{m,peak}(\nu)$, and (d) specific capacity $C_m(\nu)$ as functions of scan rate ν.

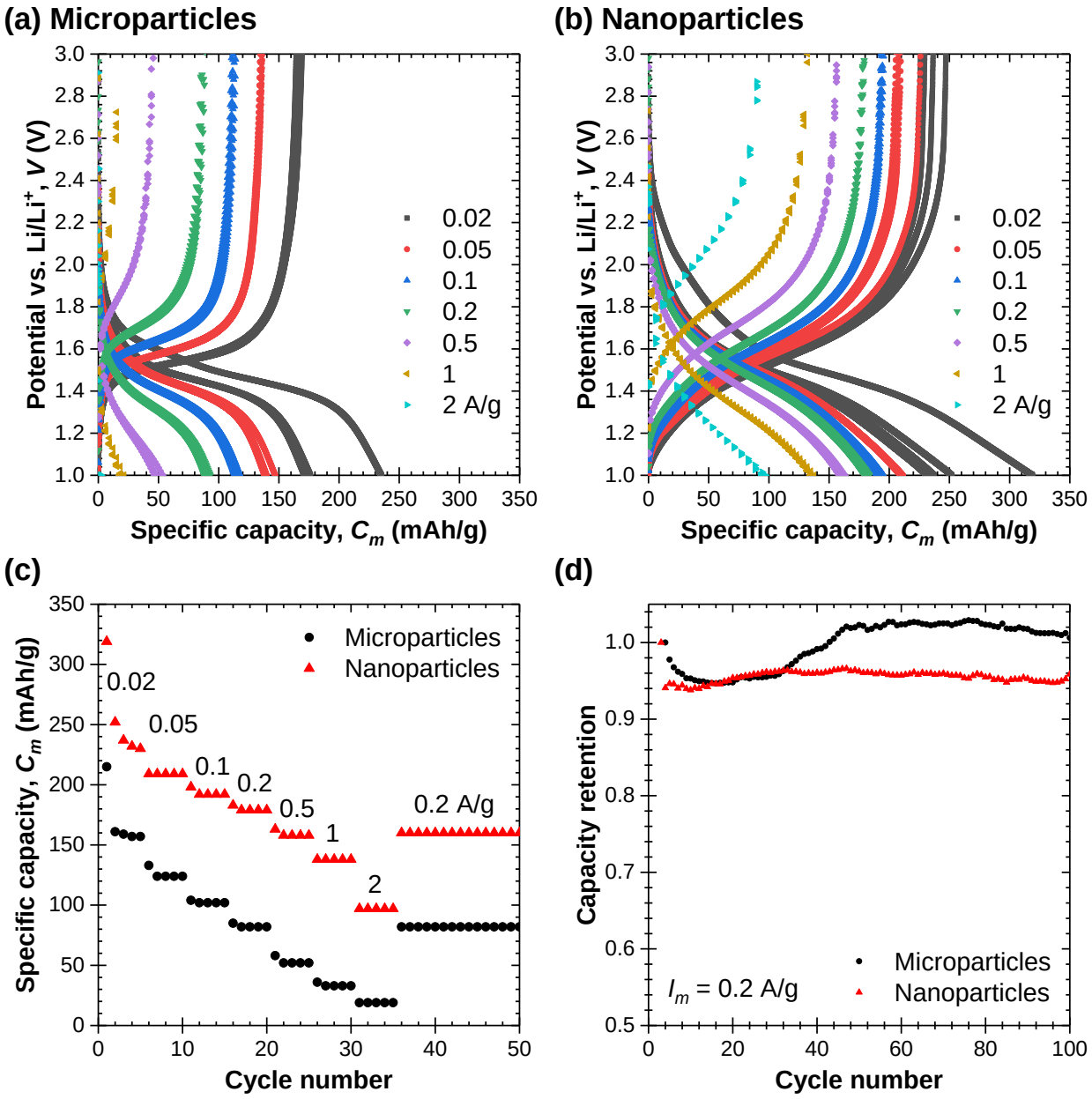

Figure 2.4: Potential profiles during galvanostatic cycling of Swagelok cells with working electrodes made of $Ti_2Nb_2O_9$ (a) microparticles or (b) nanoparticles cycled between 1.0 and 3.0 V vs. Li/Li^+ at specific current I_m ranging between 0.02 and 2 A/g of $Ti_2Nb_2O_9$, along with (c) the specific capacity $C_m(I_m)$ as a function of cycle number at different specific current I_m, and (d) the capacity retention ratio over 100 cycles with respect to $C_m(I_m)$ of the second cycle at $I_m = 0.2$ A/g of $Ti_2Nb_2O_9$ ($\sim$1C).

Figure 2.4 plots the potential profiles during galvanostatic cycling of the Swagelok cells with self-supported working electrodes made of $Ti_2Nb_2O_9$ (a) microparticles or (b) nanoparticles cycled between 1.0 and 3.0 V vs. Li/Li^+ at specific current I_m ranging between 0.02 and 2 A/g of $Ti_2Nb_2O_9$. It also shows (c) the specific capacity $C_m(I_m)$ as a function of cycle number at different specific current I_m, and (d) the capacity retention ratio over 100 cycles with respect to $C_m(I_m)$ of the second cycle at $I_m = 0.2$ A/g of $Ti_2Nb_2O_9$ ($\sim$1C). At any given specific current I_m, the specific capacity $C_m(I_m)$ of the cell with $Ti_2Nb_2O_9$ nanoparticles was larger than that with $Ti_2Nb_2O_9$ microparticles. For example, at 0.02 A/g of $Ti_2Nb_2O_9$ ($\sim$C/10), the cell with $Ti_2Nb_2O_9$ nanoparticles showed a reversible specific capacity of 230 mAh/g compared with 157 mAh/g for the cell with $Ti_2Nb_2O_9$ microparticles. The former achieved an improvement of 14% over the specific capacity previously reported in the literature [117,130]. Moreover, at large specific currents I_m, the capacity retention of the cell with $Ti_2Nb_2O_9$ nanoparticles was superior to that with $Ti_2Nb_2O_9$ microparticles. In fact, at 2 A/g of $Ti_2Nb_2O_9$ ($\sim$10C), the cell with $Ti_2Nb_2O_9$ nanoparticles still retained a specific capacity of 97 mAh/g compared with 19 mAh/g for the cell with $Ti_2Nb_2O_9$ microparticles. Finally, the long-term cycling degradation of both types of $Ti_2Nb_2O_9$ working electrodes was minimal. After 100 cycles at 0.2 A/g of $Ti_2Nb_2O_9$, the ratio of the specific capacity of the cell with $Ti_2Nb_2O_9$ microparticles or nanoparticles relative to the second cycle was 1.01 and 0.96, respectively. Note that in many battery electrode materials such as graphite and NMC, the first cycle features low coulombic efficiency and/or substantial irreversible loss in the specific capacity [136]. Accordingly, it is more appropriate to use the specific capacity of the second cycle as the reference when calculating the capacity retention [137–139].

2.2.3 Potentiometric entropy measurements

Figure 2.5 plots the open-circuit voltage $U_{OCV}(C_m, T)$ and entropic potential $\partial U_{OCV}(C_m, T)/\partial T$ of the coin cells with self-supported working electrodes made of $Ti_2Nb_2O_9$ microparticles or nanoparticles as functions of specific capacity C_m during lithiation and delithiation of the first two cycles at C-rate of C/10. Here, the $Ti_2Nb_2O_9$ active material mass loading of the cell with $Ti_2Nb_2O_9$ microparticles or nanoparticles was 4.7 and 4.3

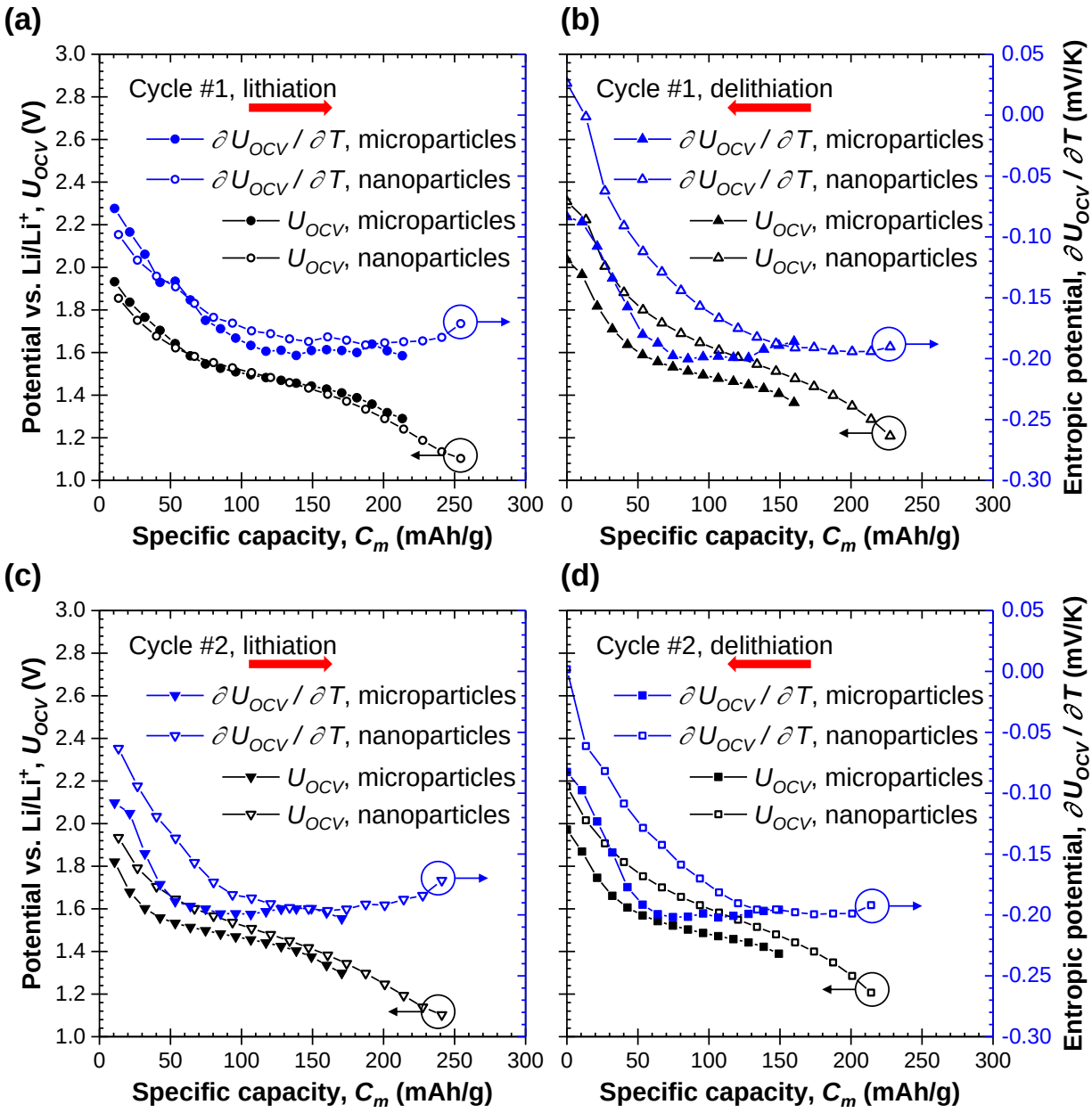

Figure 2.5: Open-circuit voltage $U_{OCV}(C_m, T)$ and entropic potential $\partial U_{OCV}(C_m, T)/\partial T$ of coin cells with working electrodes made of $Ti_2Nb_2O_9$ microparticles or nanoparticles as functions of specific capacity C_m during lithiation and delithiation of the first two cycles at C-rate of C/10.

mg/cm^2, respectively. First, within the same potential window of 1.0 to 3.0 V vs. Li/Li$^+$, the maximum specific capacity of the cell with $Ti_2Nb_2O_9$ nanoparticles was larger than that with $Ti_2Nb_2O_9$ microparticles during both lithiation or delithiation half-cycles. These results are consistent with those previously observed in galvanostatic cycling measurements (Figure 2.4). Second, $U_{OCV}(C_m, T)$ and $\partial U_{OCV}(C_m, T)/\partial T$ of both cells monotonously decreased with increasing lithium composition during the lithiation half-cycle. This behavior is characteristic of lithium ion insertion in a homogeneous solid solution [1, 59]. These observations are also consistent with those previously made from *in situ* XRD measurements (Figure 2.2).

Furthermore, $U_{OCV}(C_m, T)$ and $\partial U_{OCV}(C_m, T)/\partial T$ of both cells were the same during the first lithiation half-cycle. This suggests that for pristine $Ti_2Nb_2O_9$, the contrasting particle sizes resulting from distinct synthesis methods had no influence on the thermodynamics properties of the electrodes. However, $U_{OCV}(C_m, T)$ and $\partial U_{OCV}(C_m, T)/\partial T$ between the two cells showed minor discrepancies during the subsequent half-cycles which could be attributed to several factors. First, it could result from the hysteresis of $U_{OCV}(C_m, T)$ and $\partial U_{OCV}(C_m, T)/\partial T$ between lithiation and delithiation. Moreover, it could be caused by the specific capacity loss between the first lithiation and delithiation half-cycles. On the one hand, such initial specific capacity loss could arise when certain lithium ions lithiated into the pristine structure became trapped and therefore unable to be delithiated [140]. On the other hand, it could also emerge due to increasing kinetic barriers including (i) growing passivation layers on both working and counter electrodes which inhibit lithium ion transport and (ii) broken or cracked $Ti_2Nb_2O_9$ particles which reduce the number of available intercalation sites [141]. For example, cracking can affect the grain boundaries along which electronic and ionic transports occur [142, 143]. In fact, a more recent study [144] applied *operando* optical scattering microscopy to monitor the actual process of particle cracking in anode materials leading to nonfunctional particle fragments and degradation of performance caused by the loss of electrical connection to the rest of the electrode.

As previously proposed by Hudak et al. [141], Figure 2.6(a) plots the entropic potential $\partial U_{OCV}(C_m, T)/\partial T$ of the coin cells with working electrodes made of $Ti_2Nb_2O_9$ microparticles or nanoparticles as a function of open-circuit voltage $U_{OCV}(C_m, T)$ during lithiation

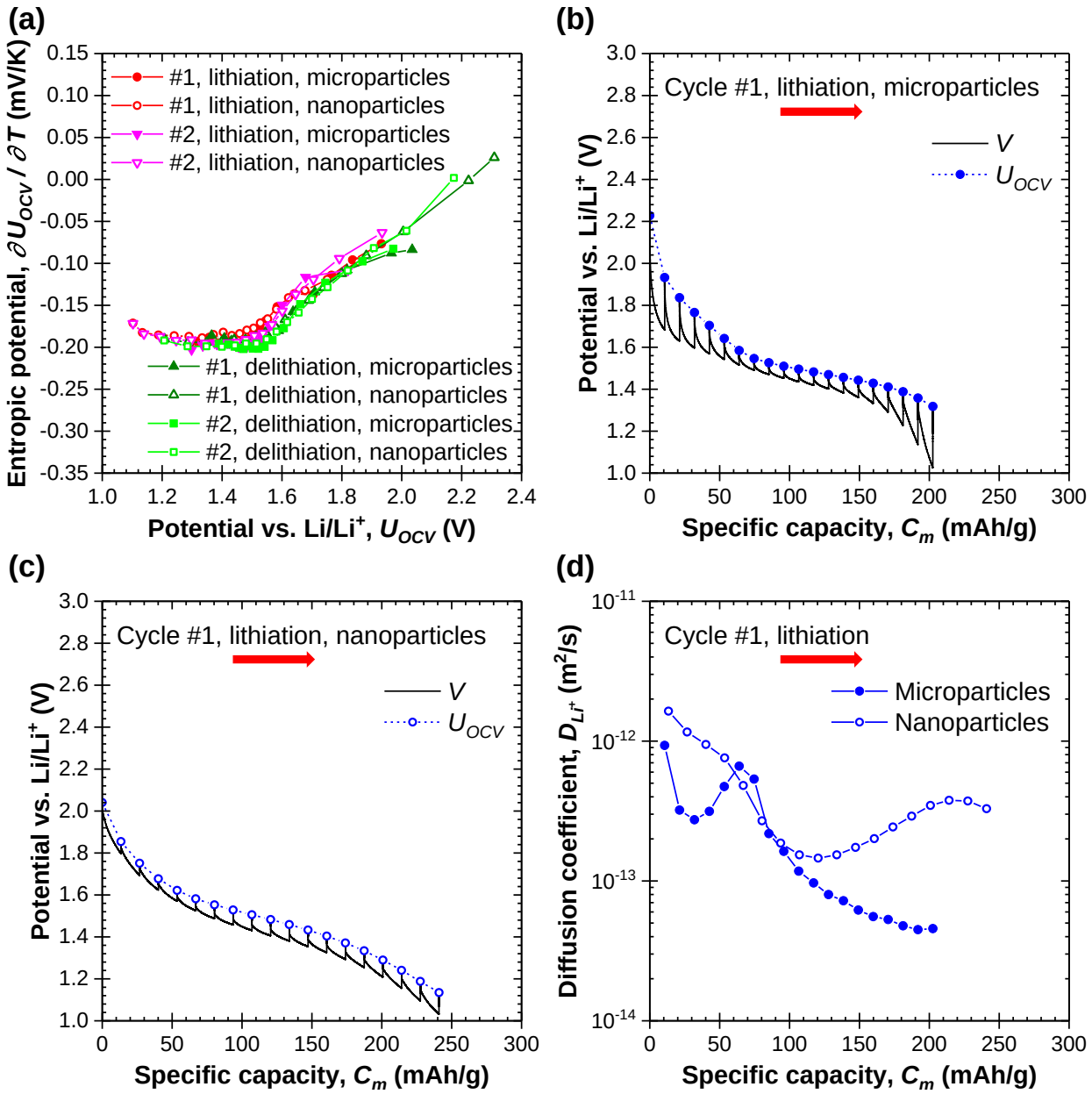

Figure 2.6: (a) Entropic potential $\partial U_{OCV}(C_m, T)/\partial T$ of coin cells with working electrodes made of $Ti_2Nb_2O_9$ microparticles or nanoparticles as a function of open-circuit voltage $U_{OCV}(C_m, T)$ during lithiation and delithiation of the first two cycles at C-rate of C/10. Cell potential $V(C_m, T)$ and open-circuit voltage $U_{OCV}(C_m, T)$ as functions of specific capacity C_m during the first lithiation half-cycle at C-rate of C/10 for coin cells with working electrodes made of $Ti_2Nb_2O_9$ (b) microparticles or (c) nanoparticles. (d) Apparent diffusion coefficient $D_{Li^+}(C_m, T)$ [Equation (1.3)] of lithium ions in the working electrodes made of $Ti_2Nb_2O_9$ microparticles or nanoparticles.

and delithiation of the first two cycles at C-rate of C/10. Here, the entropic potential profiles of both types of electrodes overlapped. This suggests that the thermodynamics behavior of $Ti_2Nb_2O_9$ powder synthesized by either method remained similar and stable, at least during the first two cycles. Therefore, the aforementioned minor discrepancies in $U_{OCV}(C_m, T)$ and $\partial U_{OCV}(C_m, T)/\partial T$ vs. C_m between the two cells could be attributed to the lithiation/delithiation hysteresis of $U_{OCV}(C_m, T)$ and $\partial U_{OCV}(C_m, T)/\partial T$ as well as the initial specific capacity loss from trapped lithium ions and/or increasing kinetic barriers.

Moreover, Figures 2.6(b) and 2.6(c) plot the cell potential $V(C_m, T)$ and open-circuit voltage $U_{OCV}(C_m, T)$ as functions of specific capacity C_m during the first lithiation half-cycle at C-rate of C/10 for the coin cells with working electrodes made of $Ti_2Nb_2O_9$ microparticles or nanoparticles, respectively. It is evident that, for a given state of charge, the overpotential $[V(C_m, T) - U_{OCV}(C_m, T)]$ of the cell with $Ti_2Nb_2O_9$ nanoparticles was smaller than that with $Ti_2Nb_2O_9$ microparticles. This indicates that the working electrode made of $Ti_2Nb_2O_9$ nanoparticles had larger electrical conductivity and/or faster lithium ion transport than that made of $Ti_2Nb_2O_9$ microparticles [80].

Finally, Figure 2.6(d) plots the apparent diffusion coefficient $D_{Li^+}(C_m, T)$ of lithium ions in the working electrodes made of $Ti_2Nb_2O_9$ microparticles or nanoparticles calculated according to Equation (1.3). It indicates that, for a given state of charge, $D_{Li^+}(C_m, T)$ of the working electrode made of $Ti_2Nb_2O_9$ nanoparticles was larger than that made of $Ti_2Nb_2O_9$ microparticles, particularly in the second part of the lithiation process. This result confirms the faster lithium ion transport in $Ti_2Nb_2O_9$ nanoparticles compared with microparticles, which manifested itself in the less polarized cyclic voltammograms, the larger b-value, and the larger specific capacity C_m at high C-rates (Figures 2.3 and 2.4).

2.2.4 *Operando* isothermal calorimetry

2.2.4.1 Cell potential

Figure A.2 in Appendix A plots the temporal evolution of the potential $V(t)$ of the calorimetric cells with slurry-cast working electrodes made of $Ti_2Nb_2O_9$ (a) microparticles or (b)

nanoparticles and lithium metal counter electrodes for six consecutive galvanostatic cycles with potential window between 1.0 and 3.0 V vs. Li/Li^+ for each current I ranging from 2 to 8 mA. It indicates that the cycle period t_{cd} of both cells decreased with increasing current I. In fact, larger currents I led not only to faster charging and discharging rates but also to smaller specific capacity C_m, as observed in Figure 2.4. Furthermore, the cycle period t_{cd} of the cell with $Ti_2Nb_2O_9$ nanoparticles was longer than that with $Ti_2Nb_2O_9$ microparticles and did not decrease as much with increasing current I. This reflects the larger specific capacity C_m and the better capacity retention of the cell with $Ti_2Nb_2O_9$ nanoparticles compared with the cell with $Ti_2Nb_2O_9$ microparticles.

2.2.4.2 Instantaneous heat generation rates

Figure 2.7 plots the instantaneous heat generation rates (a, b) $\dot{Q}_{TNO}(t)$ measured at the working electrodes made of $Ti_2Nb_2O_9$ microparticles or nanoparticles and (c, d) $\dot{Q}_{Li}(t)$ measured at the respective lithium metal counter electrodes as functions of dimensionless time t/t_{cd} averaged over the last three consecutive cycles for current I ranging from 2 to 8 mA. Note that the measurements of $\dot{Q}_{TNO}(t)$ and $\dot{Q}_{Li}(t)$ were repeatable cycle after cycle (see Figures A.3 and A.4 in Appendix A). First, the magnitudes of $\dot{Q}_{TNO}(t)$ and $\dot{Q}_{Li}(t)$ in both cells increased with increasing current I. Moreover, Figures 2.7(a) and 2.7(b) show that, for any given current I, $\dot{Q}_{TNO}(t)$ was significantly larger at the working electrode made of $Ti_2Nb_2O_9$ microparticles than at that made of $Ti_2Nb_2O_9$ nanoparticles. Furthermore, $\dot{Q}_{TNO}(t)$ in both cells increased with time during both lithiation or delithiation half-cycles. This could be attributed to the increase in the reversible heat generation rate $\dot{Q}_{rev,TNO}(x,T)$ [Equation (1.8)] caused by the monotonously decreasing entropic potential $\partial U_{OCV}(C_m,T)/\partial T$ with increasing lithium composition x, as observed in Figure 2.5. On the other hand, Figures 2.7(c) and 2.7(d) establish that, for any given current I, $\dot{Q}_{Li}(t)$ was similar in both cells and was positive and relatively constant during the lithiation half-cycle of the $Ti_2Nb_2O_9$ working electrode. This was associated with lithium ion stripping and exothermic solvation with ion pairing at the lithium metal counter electrode [1]. By contrast, $\dot{Q}_{Li}(t)$ increased towards the end of the delithiation half-cycle of the $Ti_2Nb_2O_9$ working electrode accompanied

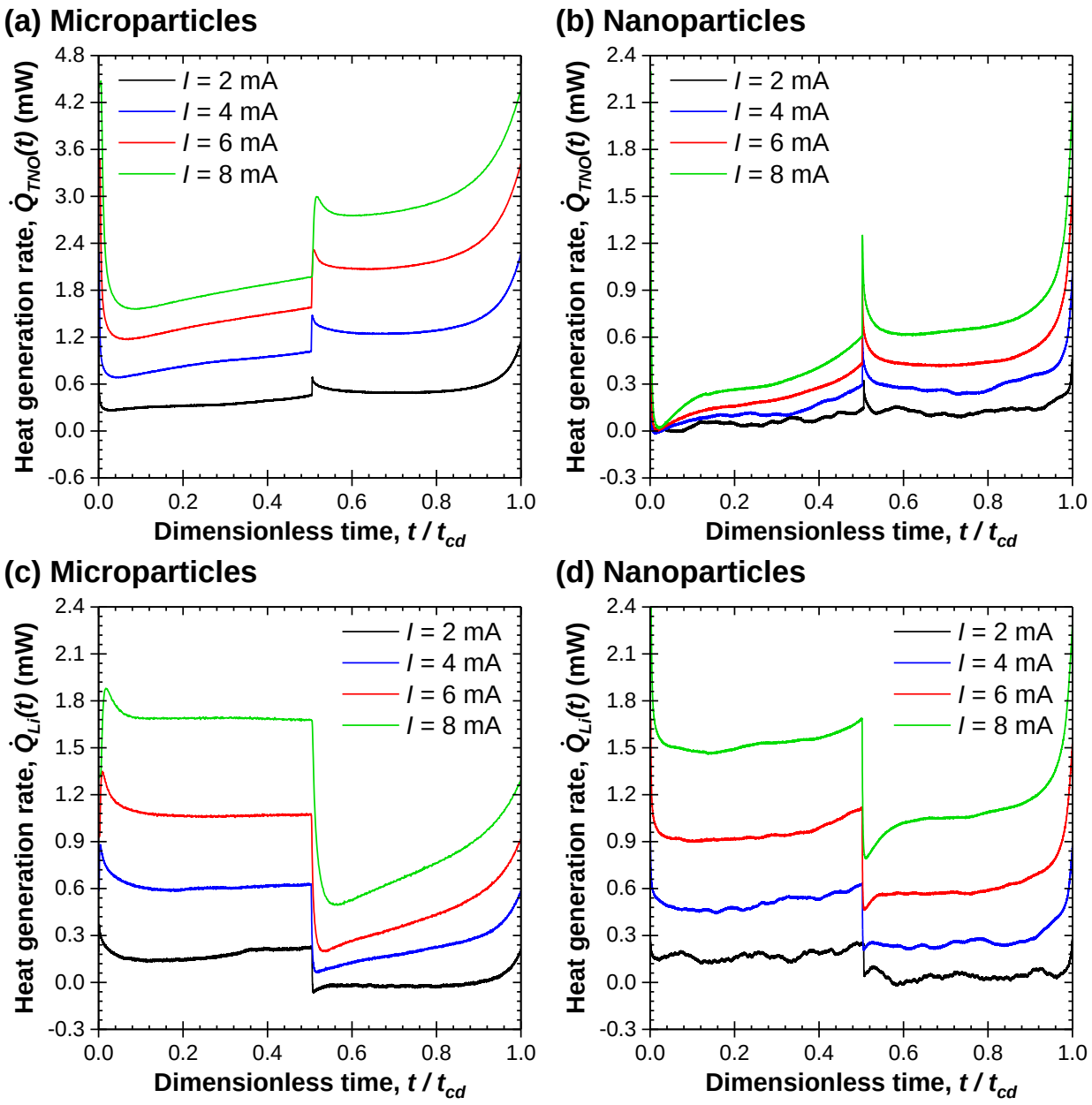

Figure 2.7: Instantaneous heat generation rates (a, b) $\dot{Q}_{TNO}(t)$ measured at the working electrodes made of $Ti_2Nb_2O_9$ microparticles or nanoparticles and (c, d) $\dot{Q}_{Li}(t)$ measured at the corresponding lithium metal counter electrodes as functions of dimensionless time t/t_{cd} averaged over the last three consecutive cycles for current I ranging from 2 to 8 mA.

simultaneously by plating of the lithium metal counter electrode. As such, the rise in $\dot{Q}_{Li}(t)$ could be attributed to the exothermic dendrite formation on the surface of the lithium metal counter electrode [145, 146]. These phenomena were also observed in cells with PNb_9O_{25} working electrodes and lithium metal counter electrodes in 1 M $LiPF_6$ in EC:DMC 1:1 v/v electrolyte [1].

In our previous studies with $TiNb_2O_7$ [59] and PNb_9O_{25} [1], the heat generation rate $\dot{Q}_J(x,T) + \dot{Q}_{rev}(x,T)$ calculated according to Equations (1.6) and (1.7) agreed well with the measurements of $\dot{Q}_T(x,T)$. However, in the present study, such a comparison was not possible. Indeed, during *operando* isothermal calorimetry, the cells were tested under galvanostatic cycling at high C-rates resulting in poor capacity retention. However, the values of $U_{OCV}(C_m,T)$ and $\partial U_{OCV}(C_m,T)/\partial T$ determined by potentiometric entropy measurements with current pulses at the same high C-rates spanned a wider range of specific capacity C_m thanks to the long relaxation periods imposed during the measurements (see Figures A.6 to A.9 in Appendix A). Therefore, the measured $U_{OCV}(C_m,T)$ and $\partial U_{OCV}(C_m,T)/\partial T$ did not represent the actual values of $U^{avg}(x,T)$ and $\partial U^{avg}(x,T)/\partial T$ of the cells during *operando* isothermal calorimetry.

2.2.4.3 Time-averaged heat generation rates

Figure 2.8(a) plots the time-averaged irreversible heat generation rates $\bar{\dot{Q}}_{irr,TNO}$ and $\bar{\dot{Q}}_{irr,Li}$ as functions of current I for calorimetric cells with working electrodes made of $Ti_2Nb_2O_9$ microparticles or nanoparticles. First, $\bar{\dot{Q}}_{irr,TNO}$ and $\bar{\dot{Q}}_{irr,Li}$ in both cells increased with increasing current I. In fact, least squares fitting revealed that $\bar{\dot{Q}}_{irr,Li}$ increased quadratically with respect to current I, i.e., $\bar{\dot{Q}}_{irr,Li} \propto I^2$. This suggests that Joule heating dominated the irreversible heat generation at the lithium metal counter electrode whose electrical resistivity was independent of current I. Furthermore, for any given current I, $\bar{\dot{Q}}_{irr,Li}$ was identical in both cells. Indeed, each lithium metal counter electrode was cut from the same piece into the same size and therefore should have approximately the same resistance.

By contrast, in both calorimetric cells $\bar{\dot{Q}}_{irr,TNO}$ increased linearly with respect to cur-

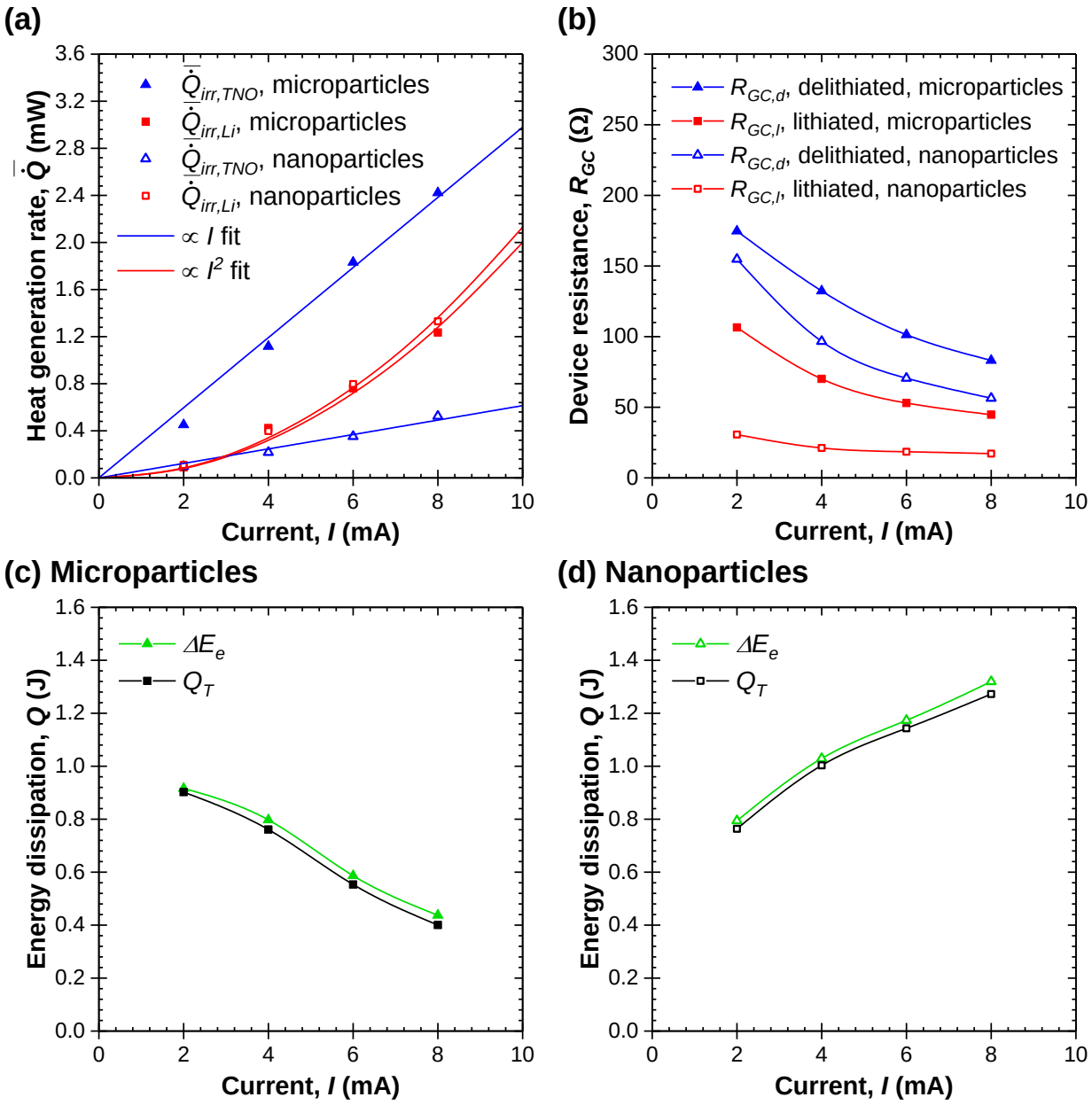

Figure 2.8: (a) Time-averaged irreversible heat generation rates $\bar{\dot{Q}}_{irr,TNO}$ and $\bar{\dot{Q}}_{irr,Li}$ as functions of current I for calorimetric cells with working electrodes made of $Ti_2Nb_2O_9$ microparticles or nanoparticles. (b) Resistances $R_{GC,d}$ and $R_{GC,l}$ [Equation (2.2)] of calorimetric cells with working electrodes made of $Ti_2Nb_2O_9$ microparticles or nanoparticles in delithiated or lithiated states during cycling at a given current I. Net electrical energy loss ΔE_e [Equation (1.12)] and total thermal energy dissipated Q_T [Equation (1.11)] over a charging/discharging cycle for calorimetric cells with working electrodes made of $Ti_2Nb_2O_9$ (c) microparticles or (d) nanoparticles.

rent I, i.e., $\bar{\dot{Q}}_{irr,TNO} \propto I$. However, $\bar{\dot{Q}}_{irr,TNO}$ was larger at the working electrode made of $Ti_2Nb_2O_9$ microparticles than at that made of $Ti_2Nb_2O_9$ nanoparticles. This could be due, in part, to the fact that the electrical resistivity of the working electrode made of $Ti_2Nb_2O_9$ microparticles was larger than that made of $Ti_2Nb_2O_9$ nanoparticles. In fact, Figure 2.8(b) plots the resistances $R_{GC,d}$ and $R_{GC,l}$ calculated from the IR drop [Equation (2.2)] in the calorimetric cells with working electrodes made of $Ti_2Nb_2O_9$ microparticles or nanoparticles at the end of the delithiation or lithiation steps during cycling at a given current I. First, the resistances $R_{GC,d}$ and $R_{GC,l}$ of the cell with $Ti_2Nb_2O_9$ microparticles were systematically larger than that with $Ti_2Nb_2O_9$ nanoparticles for any given current I. Moreover, the resistances $R_{GC,d}$ and $R_{GC,l}$ of both cells decreased with increasing current I. This could be attributed to the smaller range of lithium composition x reached at larger currents I. Finally, both cells had larger resistance in delithiated state than in lithiated state, i.e., $R_{GC,d} > R_{GC,l}$. To the best of our knowledge, the electrical resistivity of $Ti_2Nb_2O_9$ as a function of state of charge has not been reported to date. However, the closely-related $TiNb_2O_7$ is known to be an insulator in its unlithiated state and its resistivity decreases sharply upon lithiation up to $x = 0.5$ [59]. Thus, a similar behavior could be the origin of the changes in the electrical resistivity of the $Ti_2Nb_2O_9$-based electrodes.

2.2.4.4 Energy balance

Figure 2.8 plots the net electrical energy loss ΔE_e [Equation (1.12)] and the total thermal energy dissipated Q_T [Equation (1.11)] over a charging/discharging cycle for calorimetric cells with working electrodes made of $Ti_2Nb_2O_9$ (c) microparticles or (d) nanoparticles. For the cell with $Ti_2Nb_2O_9$ microparticles, the total thermal energy Q_T (in J) released over a cycle decreased with increasing current I. This was due to the decrease in the cycle period t_{cd} with increasing current I [Figure A.2(a) in Appendix A] which was more significant than the concurrent increase in the instantaneous total heat generation rate $\dot{Q}_T(t)$ (in W) [Figures 2.7(a) and 2.7(c)]. By contrast, Q_T increased with increasing current I for the cell with $Ti_2Nb_2O_9$ nanoparticles as the increase in $\dot{Q}_T(t)$ [Figures 2.7(b) and 2.7(d)] was more significant than the decrease in t_{cd} [Figure A.2(b)]. Finally, for both cells at any given current

I, the total dissipated thermal energy Q_T measured by *operando* isothermal calorimetry fell within 10% of the net electrical energy loss ΔE_e measured by the potentiostat. In other words, the net electrical energy loss was entirely dissipated in the form of heat. These results confirm the accuracy of our measurements.

2.3 Chapter summary

This chapter investigates the tunnel-structured $Ti_2Nb_2O_9$ with fast charging capabilities at potentials above 1.0 V vs. Li/Li^+ which reduces SEI and dendrite formation. A novel sol-gel method was proposed to synthesize $Ti_2Nb_2O_9$ nanoparticles for use in lithium-ion battery electrodes. These electrodes were compared with those made of $Ti_2Nb_2O_9$ microparticles synthesized by the traditional solid-state method using unique characterization techniques including potentiometric entropy measurements and *operando* isothermal calorimetry. Cyclic voltammetry and galvanostatic cycling demonstrated the superior specific capacity, greater cycling reversibility, and smaller capacity drop with increasing current for electrodes made of $Ti_2Nb_2O_9$ nanoparticles compared to those made of $Ti_2Nb_2O_9$ microparticles. Furthermore, *in situ* XRD measurements revealed only minor and reversible distortions to the crystallographic structure of $Ti_2Nb_2O_9$. In addition, potentiometric entropy measurements indicated that both types of electrodes underwent lithium ion intercalation/deintercalation in a homogeneous solid solution of $Ti_2Nb_2O_9$ during cycling. In fact, overlapping entropic potential profiles suggested that the particle size had no influence on the thermodynamics behavior of $Ti_2Nb_2O_9$. However, electrodes made of $Ti_2Nb_2O_9$ nanoparticles exhibited smaller overpotential than those made of $Ti_2Nb_2O_9$ microparticles, thanks to their smaller particle size and larger specific surface area which facilitate lithium ion transport. This, along with their larger electrical conductivity and thus smaller resistive losses, contributed to the smaller instantaneous and time-averaged irreversible heat generation rates at electrodes made of $Ti_2Nb_2O_9$ nanoparticles than those made of $Ti_2Nb_2O_9$ microparticles at any given C-rate, as determined by *operando* isothermal calorimetry.

CHAPTER 3

Superior electrochemical performance and reduced heat generation in 3D printed vs. 2D tape-casted NMC622 electrodes

This chapter aims to compare the thermodynamics behavior and the heat generation rates in 3D printed electrodes with those in conventional slurry-casted electrodes made with the same lithium manganese nickel cobalt oxide $LiNi_{0.6}Mn_{0.2}Co_{0.2}O_2$ (NMC622) slurry. This compound was chosen because it has been widely adopted as a cathode material in commercial batteries for not only its stability but also its large specific capacity and rate performance [147, 148]. This chapter provides insight into the energy losses and heat dissipation mechanisms in 3D printed electrodes, particularly during fast charging.

3.1 Background

3.1.1 Additive manufacturing techniques for electrode fabrication

3.1.1.1 3D printing of active material mixtures

In recent years, substantial attention has been paid to applications of novel additive manufacturing techniques such as 3D printing in the electrode fabrication process, with rapid progress in multiple areas for different anode, cathode, and pseudocapacitive materials [107]. The first approach consists of printing a mixture of active materials. For example, Fu et al. [104] produced inks for 3D printing of electrodes where the raw materials consisted of lithium iron phosphate (LFP) or lithium titanium oxide (LTO) mixed with graphene oxide

(GO). The corresponding ink viscoelasticity was optimized for extrusion-based fabrication. The resulting 3D printed electrodes exhibited promising specific capacity, rate performance, and cycling stability. In a similar study, Drews et al. [149] presented a silicon/graphite blend slurry designed for 3D printed electrodes of interdigitated microbatteries, which also recorded excellent cycling performance. Moreover, Zhao et al. [150] described a fabrication method of graphene-based composite aerogel microlattices built upon 3D printing. In fact, graphene/ZnV_2O_6@$Co_3V_2O_8$ and graphene/vanadium nitride (VN) electrodes prepared according to the porous microlattice structure achieved superior energy and power densities than other conventionally fabricated pseudocapacitive electrodes. Finally, Zhu et al. [151] proposed a direct ink writing procedure utilizing concentrated inks featuring low electrical resistivity, submillimeter particle size, and high mechanical stability. The process was used to produce a 1 mm-thick zinc electrode with sizeable areal and volumetric capacity without significant microstructural degradation during long-term cycling.

3.1.1.2 3D printing of precursor material mixtures

3D printing can also be performed using a mixture of precursor materials. For instance, Zhu et al. [105] created a mixture containing graphene oxide (GO) precursor to form graphene composite aerogel electrodes with a composite microlattice structure. These electrodes displayed excellent capacity even under high currents and power densities comparable to 10 times thinner slurry-casted electrodes. Similarly, Yao et al. [152] prepared a 3D printing ink by combining cellulose nanocrystals (CNC) and a silica microsphere suspension. The resulting multiscale porous carbon aerogel electrodes achieved capacitance of 149 F/g at 5 mV/s and 71 F/g at 200 mV/s when tested at -70 °C. These capacitance values were 6.5 times higher than slurry-casted electrodes. In contrast to these pseudocapacitive electrodes, Idrees et al. [153] proposed a novel porous carbon (PC)/silicon oxycarbide (SiOC) composite for 3D printing into anodes for zinc-ion batteries. Thanks to the interpenetrated SiOC network within the PC, the electrodes enjoyed not only improved transport properties but also uniform nucleation of zinc ions within the voids. As a result, the superior capacity of the electrodes was accompanied by significantly reduced dendrite formation, thus extend-

ing their cycle life. In the case of sodium-ion batteries, Brown et al. [154] demonstrated a 3D printing ink consisting of ammonium thiomolybdate mixed with graphene oxide (GO) nanosheets. This produced MoS_2-graphene aerogel electrodes with excellent specific capacity along with fast and highly reversible sodium ion transport. As such, when utilized as anodes for sodium-ion batteries these samples showed outstanding rate performance and cycling stability.

3.1.1.3 Deposition of active materials on 3D printed aerogels

Another 3D printing technique relies on depositing active materials on separately 3D printed and patterned aerogels to generate the desired electrodes for different types of supercapacitor or battery chemistries. Yao et al. [106, 155] demonstrated (i) cathodes made of 3D printed graphene aerogels with high mass loading of deposited MnO_2 and (ii) anodes made of 3D printed graphene aerogels with high density of surface functional groups. When paired together, the full supercapacitor device achieved excellent energy and power densities, where the primary charge storage mechanism came from redox reactions with fast kinetic processes. More recently, Lin et al. [156] manufactured 3D printed graphene aerogels with both sparsely separated exterior ligaments to create large open channels for mass transport and densely arranged interior ligaments to provide large ion-accessible active surface. Similar approaches have been used to produce (i) sulfur cathodes in lithium-sulfur batteries [157], (ii) lithium anodes in lithium-lithium iron phosphate (LFP) batteries [158], (iii) sodium anodes in sodium-ion batteries [159], and (iv) zinc anodes in zinc-ion batteries [160]. In general, the controlled deposition of active materials on intricately designed 3D printed hosts not only enabled high mass loading and excellent transport kinetics but also mitigated dendrite formation by virtue of the more uniform ion nucleation on the electrode/electrolyte interface.

3.1.1.4 3D printing of NMC materials

For the NMC group of materials akin to the NMC622 investigated in the present study, there have been previous attempts to utilize 3D printing. Martinez et al. [161] employed a vat

photopolymerization precursor procedure to synthesize NMC111 electrodes with complex shapes and submicron features which maintained adequate mechanical rigidity. Tao et al. [162] used a conformal heat-drying direct ink writing process to produce NMC811 electrodes with enhanced rate performance (144 mAh/g at 3C) and cycling stability (60% capacity recovered after 800 cycles at 1C). The rising number of experimental studies featuring 3D printed electrodes has also prompted several numerical modeling efforts [163–165]. These studies sought to quantitatively elucidate the reasons of performance enhancement obtained with additive manufacturing techniques in order to propose design rules and optimization strategies.

3.2 Materials and methods

3.2.1 Electrode and device fabrication

In this study, 3D printed NMC622 electrodes were prepared using an ink consisting of NMC622 powder (Targray), conductive carbon (Super C65 Carbon Black Conductive Additive, MSE Pro), and polyvinylidene fluoride (Solef 5140 PVDF, Solvay) with a mass ratio of 90:5:5. Here, both NMC622 and conductive carbon powders were ground with mortar and pestle before being added to a solution of 8 wt% PVDF in N-methyl-2-pyrrolidone (NMP) solvent. The final solvent content of the slurry was 29 wt%. The slurry was then filtered using a stainless steel 300 × 300 mesh with 0.0021-inch opening size before being printed on an aluminum foil current collector using a Hyrel 3D printer (Engine High Resolution). Specifically, 10 mm × 10 mm squares with zig-zag line patterns were printed with nozzle diameter of 0.2 mm, speed of 180 mm/min, and hatch spacing of 0.4 mm, resulting in electrodes with an active material mass loading around 5 mg/cm^2.

As a reference, 2D tape-casted NMC622 electrodes were prepared with the same procedure, except that additional NMP solvent was added to the slurry for a final solvent content of 58 wt% to facilitate uniform casting. Then, the slurry was casted using a tape caster with thickness of 150 μm to obtain electrodes with an active material mass loading also around 5

mg/cm^2. Finally, both 3D printed and 2D tape-casted NMC622 electrodes were dried in a vacuum oven at 80 °C overnight. The approximately uniform thickness of the 2D tape-casted electrodes was around 34 μm.

One set of each type of electrodes was cut using a 0.5-inch diameter hole punch to assemble CR2032 coin cells for potentiometric entropy measurements. Here, the coin cells consisted of (i) a 3D printed or a 2D tape-casted NMC622 working electrode, (ii) lithium metal (MTI, 99.9%) as the counter electrode (250 μm thickness, 16 mm diameter), (iii) a 25 μm thick PP-PE-PP trilayer microporous membrane (Celgard 2325) as the separator, and (iv) 1.2 M $LiPF_6$ in EC:EMC 3:7 w/w (Soulbrain MI) electrolyte. Note that two pieces of 500 μm thick stainless steel spacers and one wave spring were used in the cell assembly. The coin cells were assembled in a glove box containing Ar gas with less than 0.5 ppm of O_2 and H_2O.

Another set of each type of electrodes was cut into 1 cm $\times$ 1 cm square to be used in *operando* isothermal calorimetry. Here, the so-called calorimetric cells consisted of (i) a 3D printed or a 2D tape-casted NMC622 working electrode, (ii) a 1 cm $\times$ 1 cm polished lithium metal (Sigma Aldrich, 99.9%) piece 750 μm in thickness serving as the counter electrode, (iii) a 670 μm thick glass microfiber filter sheet (Whatman GF/D) acting as the separator and thermal insulator, and (iv) 1.2 M $LiPF_6$ in EC:EMC 3:7 w/w (Soulbrain MI) electrolyte. The calorimetric cells were also assembled in a glove box containing Ar gas with less than 0.5 ppm of O_2 and H_2O.

3.2.2 Potentiometric entropy measurements and *operando* isothermal calorimetry

Potentiometric entropy measurements and *operando* isothermal calorimetry followed the same procedures as those described in our previous studies [1, 59, 60, 166]. For potentiometric entropy measurements, a series of constant current pulses was imposed to the coin cell corresponding to a C-rate of C/10 at 20 °C. Each current pulse lasted 30 minutes followed by a relaxation period of 270 minutes. Towards the end of each relaxation period, a step-like

temperature profile was applied to the coin cell from 15 °C to 25 °C in 5 °C increments with a thermoelectric cold plate (TE technology, CP-121). The corresponding coin cell potential evolution was simultaneously recorded by a high accuracy potentiostat (BioLogic, VSP-300).

For *operando* isothermal calorimetry, galvanostatic cycling was imposed to the calorimetric cell using a high accuracy potentiostat (BioLogic, SP-150). The instantaneous heat generation rates at the working electrode made of 3D printed or 2D tape-casted NMC622 and at the lithium metal counter electrode were measured simultaneously using 1 cm × 1 cm thermoelectric heat flux sensors (greenTEG, gSKIN-XP) in thermal contact with the back of each electrode. Note that the calorimeter operated under isothermal conditions and the thermal mass of the electrodes were small so that the electrode temperature was uniform and constant over time despite heat generation.

3.3 Results and discussion

3.3.1 Electrode morphology

Figure 3.1 shows the scanning electron microscopy (SEM) images of (a, b, c) 3D printed or (d, e, f) 2D tape-casted NMC622 electrodes with the broad view, the top view, and the cross-sectional view, respectively. Every ribbon line of the 3D printed electrodes had an average width of 240 μm and an average height of 50 μm, while the 2D tape-casted electrodes had an approximately uniform thickness of 34 μm. Both types of electrodes were laid on an aluminum foil current collector around 15 μm in thickness. Here, we assume that the material in both types of electrodes had identical porosity and effective density. In addition, the cross-sectional geometry of the 3D printed electrodes is modeled as a parabola with a width of 240 μm and a height of 50 μm, while the 2D tape-casted electrodes have a rectangular cross-section with a height of 34 μm equal to the electrode thickness. Finally, the length perpendicular to the cross-section is also the same between both types of electrodes. Overall, calculated according to these geometries, the 3D printed electrodes had nearly 15% larger exterior surface area exposed to the electrolyte per unit volume of the bulk electrode

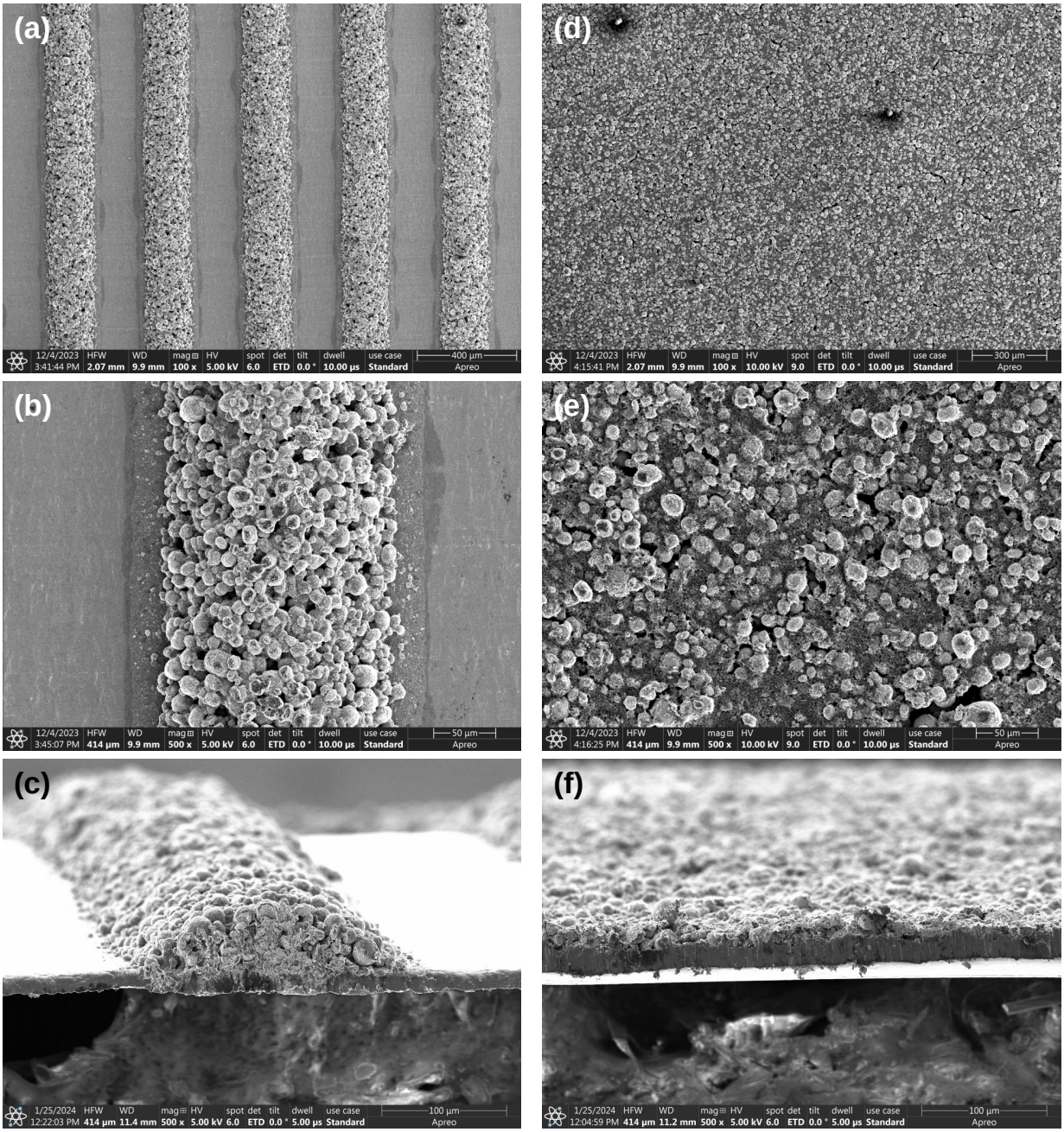

Figure 3.1: Scanning electron microscopy (SEM) images of (a, b, c) 3D printed or (d, e, f) 2D tape-casted NMC622 electrodes with the broad view, the top view, and the cross-sectional view, respectively.

than the 2D tape-casted electrodes. It was also observed that the NMC622 particles in the 3D printed electrodes were more concentrated in the outer than in the inner region of the ribbon lines, as established from the varying textures in Figure 3.1(c). By contrast, for the 2D tape-casted electrodes shown in Figure 3.1(f), the NMC622 particles were more homogeneously distributed. As a result, the 3D printed electrodes featured reduced diffusion length required to reach the NMC622 particles, which could improve the utilization rate of the NMC622 active materials, particularly under faster cycling conditions.

3.3.2 Potentiometric entropy measurements

Figure 3.2 plots the cell potential $V(x,T)$, open-circuit voltage $U_{OCV}(x,T)$, and entropic potential $\partial U_{OCV}(x,T)/\partial T$ of the coin cells with working electrodes made of (a, c) 3D printed or (b, d) 2D tape-casted NMC622 as functions of lithium composition x during (a, b) delithiation and (c, d) lithiation at C-rate of C/10. Here, the NMC622 mass loading of the 3D printed and 2D tape-casted NMC622 electrodes was 4.7 and 5.4 mg/cm^2, respectively. First, within the same potential window from 2.5 to 4.2 V vs. Li/Li$^+$, the range of lithium composition x was almost identical between the two cells, i.e., $0 < x < 0.6$. This corresponds to a specific capacity of 166 mAh/g consistent with that reported in other studies [147, 148].

Furthermore, the similar evolutions of $U_{OCV}(x,T)$ and $\partial U_{OCV}(x,T)/\partial T$ for both cells indicate the same charge storage mechanisms during both delithiation and lithiation. In Region I ($0 < x < 0.2$), $U_{OCV}(x,T)$ increased monotonously and $\partial U_{OCV}(x,T)/\partial T$ mostly decreased corresponding to lithium deintercalation in a homogeneous solid solution [53]. A similar behavior was observed in Region III ($0.4 < x < 0.6$), where the increasing $U_{OCV}(x,T)$ and the decreasing $\partial U_{OCV}(x,T)/\partial T$ were again associated with lithium ion deinsertion in a homogeneous solid solution [53]. Finally, in the intermediate Region II ($0.2 < x < 0.4$), $U_{OCV}(x,T)$ increased with a reduced slope while $\partial U_{OCV}(x,T)/\partial T$ increased rapidly. Interestingly, Region II coincided with the so-called transition from a hexagonal (H1) phase (Region I) to another hexagonal (H2) phase (Region III) through a monoclinic (M) phase, as described in Ref. [148]. In contrast to a typical transformation between two fundamentally

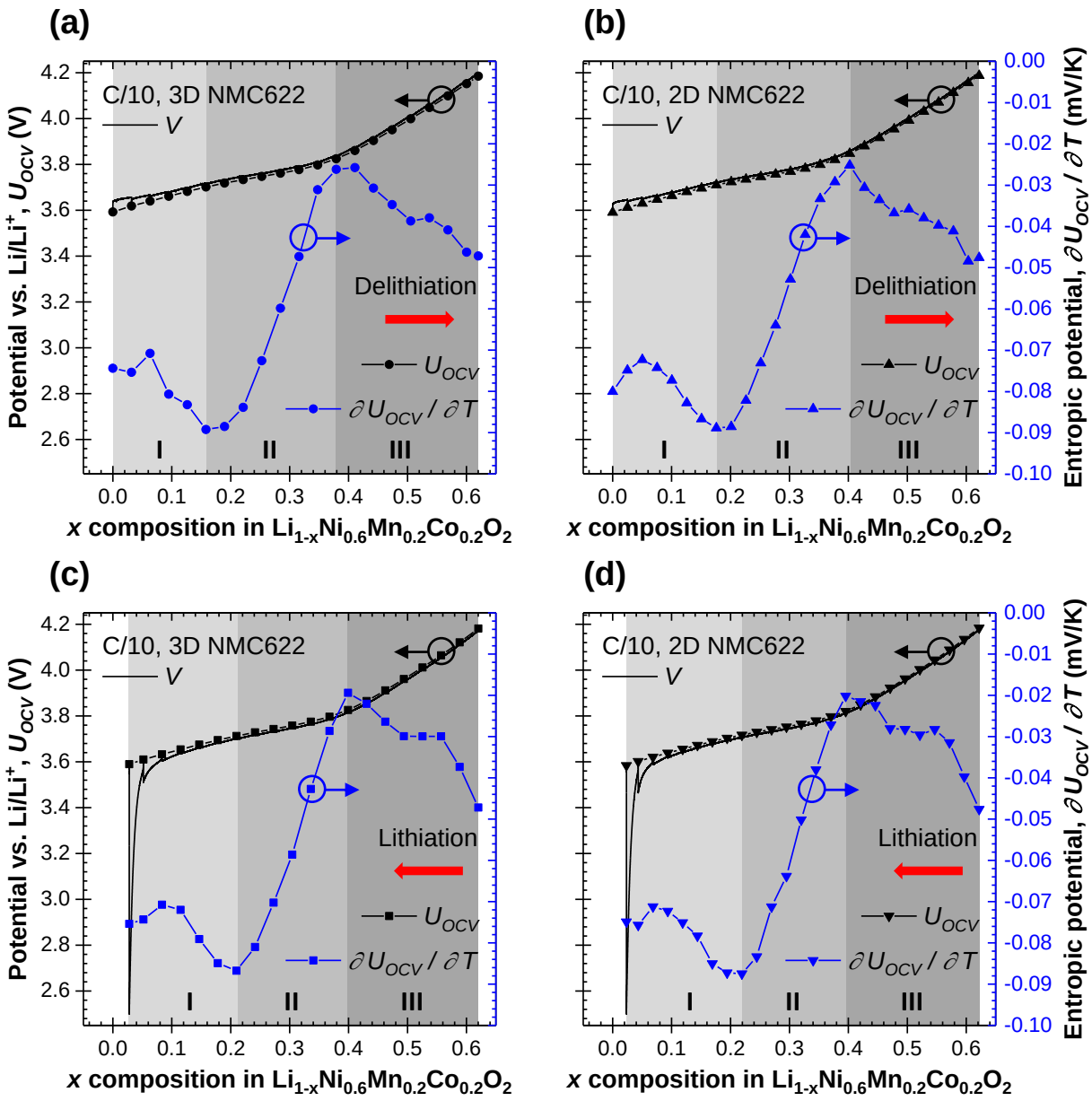

Figure 3.2: Cell potential $V(x,T)$, open-circuit voltage $U_{OCV}(x,T)$, and entropic potential $\partial U_{OCV}(x,T)/\partial T$ of coin cells with working electrodes made of 3D printed or 2D tape-casted NMC622 as functions of lithium composition x during delithiation and lithiation at C-rate of C/10.

distinct phases, here the transition only caused a minor increase in the c lattice parameter of NMC622 during delithiation. This resulted in a slight gliding between adjunct transition metal-oxygen layers and a slight repulsion of neighboring oxygen layers [148]. Nevertheless, this structural distortion likely shifted the configurational entropy which in turn resulted in an increase in $\partial U_{OCV}(x,T)/\partial T$ [53].

Figure 3.3 plots the entropic potential $\partial U_{OCV}(x,T)/\partial T$ of the coin cells as a function of open-circuit voltage $U_{OCV}(x,T)$ during (a) delithiation and (b) lithiation at C-rate of C/10 for working electrodes made of (c) 3D printed or (d) 2D tape-casted NMC622. This so-called entropic potential profile, first proposed by Hudak et al. [141], enables a direct comparison between the thermodynamics behavior of different cells. In fact, this profile eliminates interferences from factors such as specific capacity differences, lithiation/delithiation hysteresis, and specific capacity loss from trapped lithium ions and/or increasing kinetic barriers over cycles. Here, Figures 3.3(a) and 3.3(b) indicate that the entropic potential profiles of both cells overlapped with negligible discrepancy during both delithiation and lithiation. In addition, Figures 3.3(c) and 3.3(d) establish that the entropic potential profiles of both types of NMC622 electrodes were highly reversible between delithiation and lithiation. Only minor hysteresis existed at potentials above 3.8 V previously identified as Region III and associated with lithium deintercalation within the H2 phase.

The GITT procedure as part of potentiometric entropy measurements can also inform transport phenomena within the cells. First, it is evident from Figure 3.2 that both cells exhibited very small overpotential $[V(x,T) - U_{OCV}(x,T)]$ and very small hysteresis in $U_{OCV}(x,T)$. Figure 3.4 plots the apparent diffusion coefficient $D_{Li^+}(x,T)$ of lithium ions in the working electrodes made of 3D printed or 2D tape-casted NMC622 during (a) delithiation and (b) lithiation calculated according to Equation (1.3). It indicates that the rate of lithium ion transport in both samples was relatively consistent throughout the entire range of lithium composition x. Overall, the 3D printed NMC622 electrodes showed slightly less overpotential and slightly enhanced apparent diffusion coefficient compared to the 2D tape-casted NMC622 electrodes. In order to observe the effects of the larger electrical conductivity and/or faster lithium ion transport in 3D printed vs. 2D tape-casted NMC622

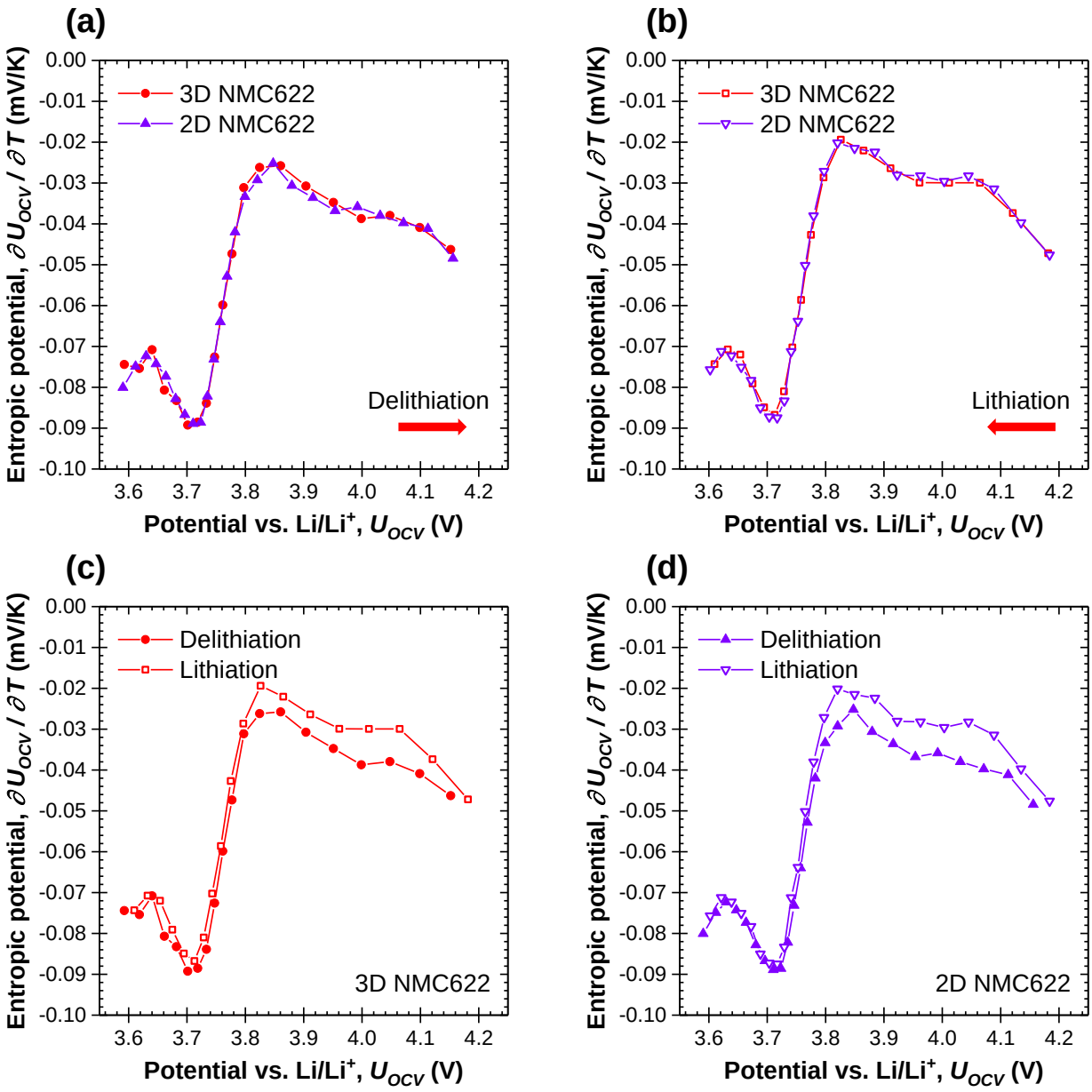

Figure 3.3: Entropic potential $\partial U_{OCV}(x,T)/\partial T$ of coin cells as a function of open-circuit voltage $U_{OCV}(x,T)$ during delithiation and lithiation at C-rate of C/10 for working electrodes made of 3D printed or 2D tape-casted NMC622.

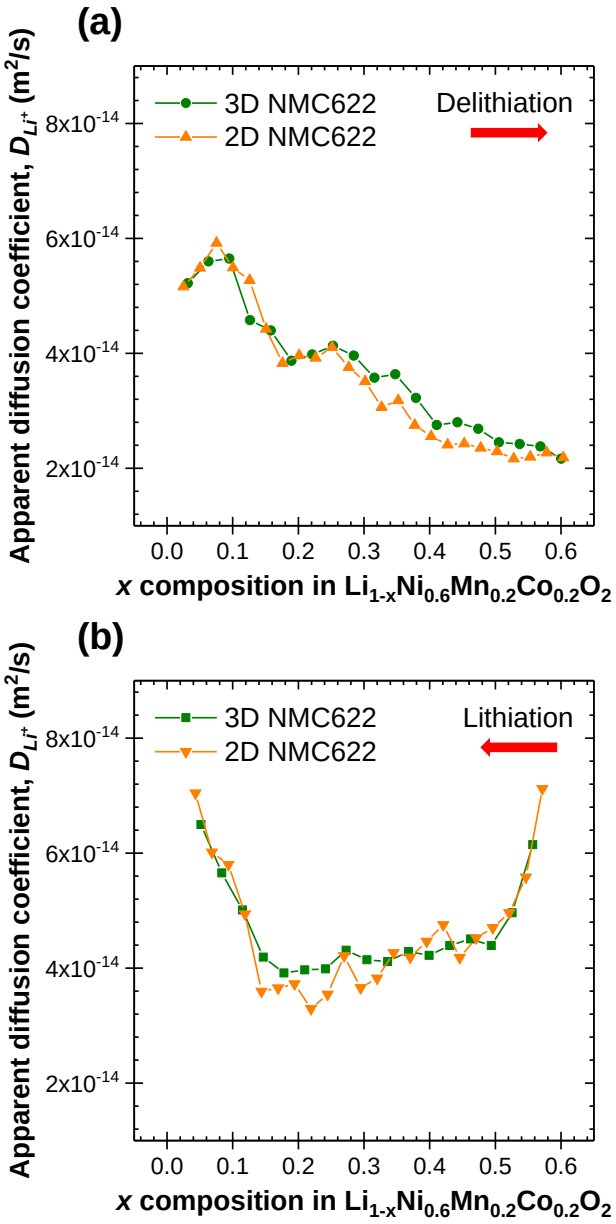

Figure 3.4: Apparent diffusion coefficient $D_{Li^+}(x,T)$ [Equation (1.3)] of lithium ions in the working electrodes made of 3D printed or 2D tape-casted NMC622 during (a) delithiation and (b) lithiation.

electrodes [80], the cells should to be tested under faster cycling conditions using *operando* isothermal calorimetry measurements.

3.3.3 *Operando* isothermal calorimetry

3.3.3.1 Cell potential

Figure 3.5 plots the temporal evolution of the potential $V(t)$ of the calorimetric cells with working electrodes made of (a) 3D printed or (b) 2D tape-casted NMC622 and lithium metal counter electrodes were subjected to galvanostatic cycling within the potential window from 1.7 to 5.0 V vs. Li/Li^+ at C-rates of 1C (around 0.8 mA/cm^2), 2C, and 3C. Although NMC622 is indeed a material with good rate performance compared to other cathode materials, an NMC622/lithium cell still typically shows visible capacity fade for C-rates exceeding 1C [167]. Therefore, the calorimetric cells were not tested at C-rates higher than 3C, as the specific capacity at higher C-rates would be too small to be relevant in practice. Note that this potential window was wider than that imposed in other measurements to account for the increased amount of overpotential observed in the calorimeter due to the thicker separator. Here, the NMC622 mass loading of the 3D printed and 2D tape-casted NMC622 electrodes was 4.3 and 5.0 mg/cm^2, respectively. Each colored region in Figure 3.5 corresponded to the five consecutive galvanostatic cycles at each of the C-rates considered. It shows that the potential $V(t)$ of both cells was nonlinear, asymmetric between charging and discharging, and repeatable at any given C-rate except for the first formation cycle. The duration of charging or discharging half-cycles were denoted respectively by t_c or t_d [Figure 3.5(c)]. Higher C-rates led not only to faster charging and discharging rates but also to smaller specific capacity. Moreover, the cycle period $t_{cd} = t_c + t_d$ and thus the specific capacity of the cell with the 3D printed NMC622 electrode was longer than that with the 2D tape-casted NMC622 electrode and did not decrease as much with increasing C-rate. Figure 3.5(d) compares the specific capacity of charging or discharging half-cycles, denoted respectively by $C_{m,c}$ or $C_{m,d}$, for the two cells at various C-rates. It reveals the superior rate performance of the 3D printed NMC622 electrode. Note that the absolute values of capacity shown in Figure 3.5(d) is rela-

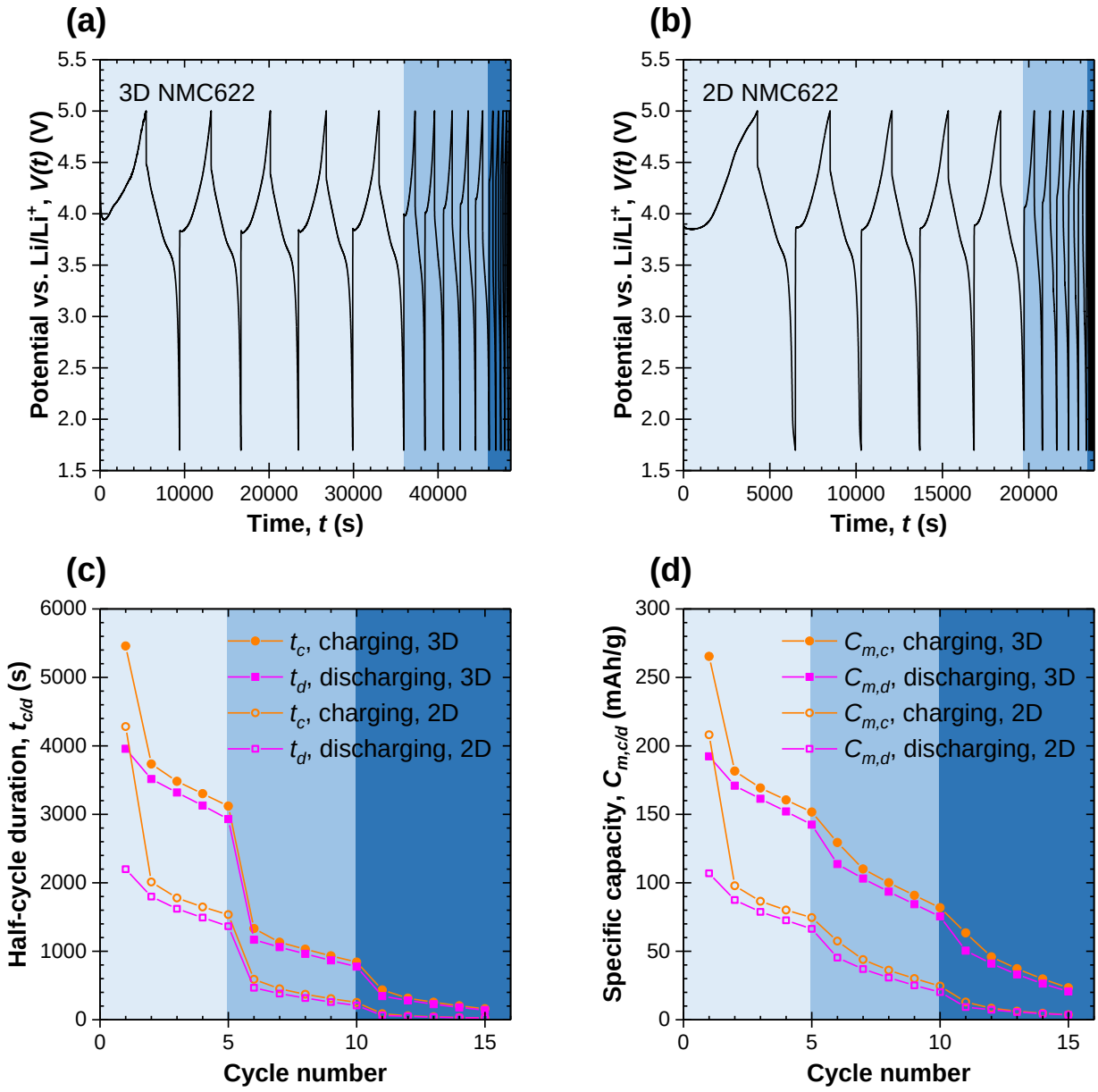

Figure 3.5: Temporal evolution of potential $V(t)$ of calorimetric cells with working electrodes made of (a) 3D printed or (b) 2D tape-casted NMC622 and lithium metal counter electrodes, for five consecutive galvanostatic cycles within the potential window from 1.7 to 5.0 V vs. Li/Li^+ at C-rates of 1C, 2C, and 3C. (c) Duration of charging t_c or discharging t_d half-cycles and (d) specific capacity $C_{m,c}$ of charging or $C_{m,d}$ of discharging half-cycles during *operando* isothermal calorimetry.

tively small since the thicker separator serving as thermal insulation between the electrodes in the calorimetric measurements increased the total cell resistance and reduced the specific capacity compared to most other cell configurations.

3.3.3.2 Instantaneous heat generation rates

Figure 3.6 plots the instantaneous heat generation rates (a, b) $\dot{Q}_{NMC}(t)$ measured at the working electrodes made of 3D printed or 2D tape-casted NMC622 and (c, d) $\dot{Q}_{Li}(t)$ measured at the respective lithium metal counter electrodes as functions of dimensionless time t/t_{cd} averaged over the last three consecutive cycles at C-rates of 1C, 2C, and 3C. Note that the measurements of $\dot{Q}_{NMC}(t)$ and $\dot{Q}_{Li}(t)$ were repeatable cycle after cycle. First, the magnitudes of $\dot{Q}_{NMC}(t)$ and $\dot{Q}_{Li}(t)$ in both cells followed similar temporal behavior and increased with increasing C-rate. More importantly, Figures 3.6(a) and 3.6(b) indicate that, at any given C-rate, $\dot{Q}_{NMC}(t)$ was larger by nearly a factor of 2 at the working electrode made of 2D tape-casted NMC622 than at that made of 3D printed NMC622 with similar mass loading. Furthermore, $\dot{Q}_{NMC}(t)$ in both cells not only decreased at the start of delithiation but also increased towards the end of lithiation. This could be attributed to the increasing electrical resistivity of NMC622 with lithiation [147, 148], resulting in increasing Joule heating.

Figures 3.6(c) and 3.6(d) establish that the heat generation rate $\dot{Q}_{Li}(t)$ of the lithium metal counter electrode was nearly the same in either cell at any given C-rate. In addition, $\dot{Q}_{Li}(t)$ remained relatively constant during delithiation of NMC622. This could be attributed to the constant electrical resistivity of lithium metal [1, 60, 166] and the continuous process involving endothermic desolvation of lithium ions prior to the exothermic plating of the lithium metal counter electrode. By contrast, $\dot{Q}_{Li}(t)$ increased towards the end of lithiation of NMC622. This was possibly due to the onset of exothermic ion pairing [1,60,166] in addition to the endothermic lithium ion stripping followed by exothermic lithium ion solvation at the lithium metal counter electrode. The transition between the endothermic desolvation and the exothermic solvation events explained the upturn in $\dot{Q}_{Li}(t)$ when switching from delithiation to lithiation of NMC622, and vice versa. Similar phenomena were also observed in our

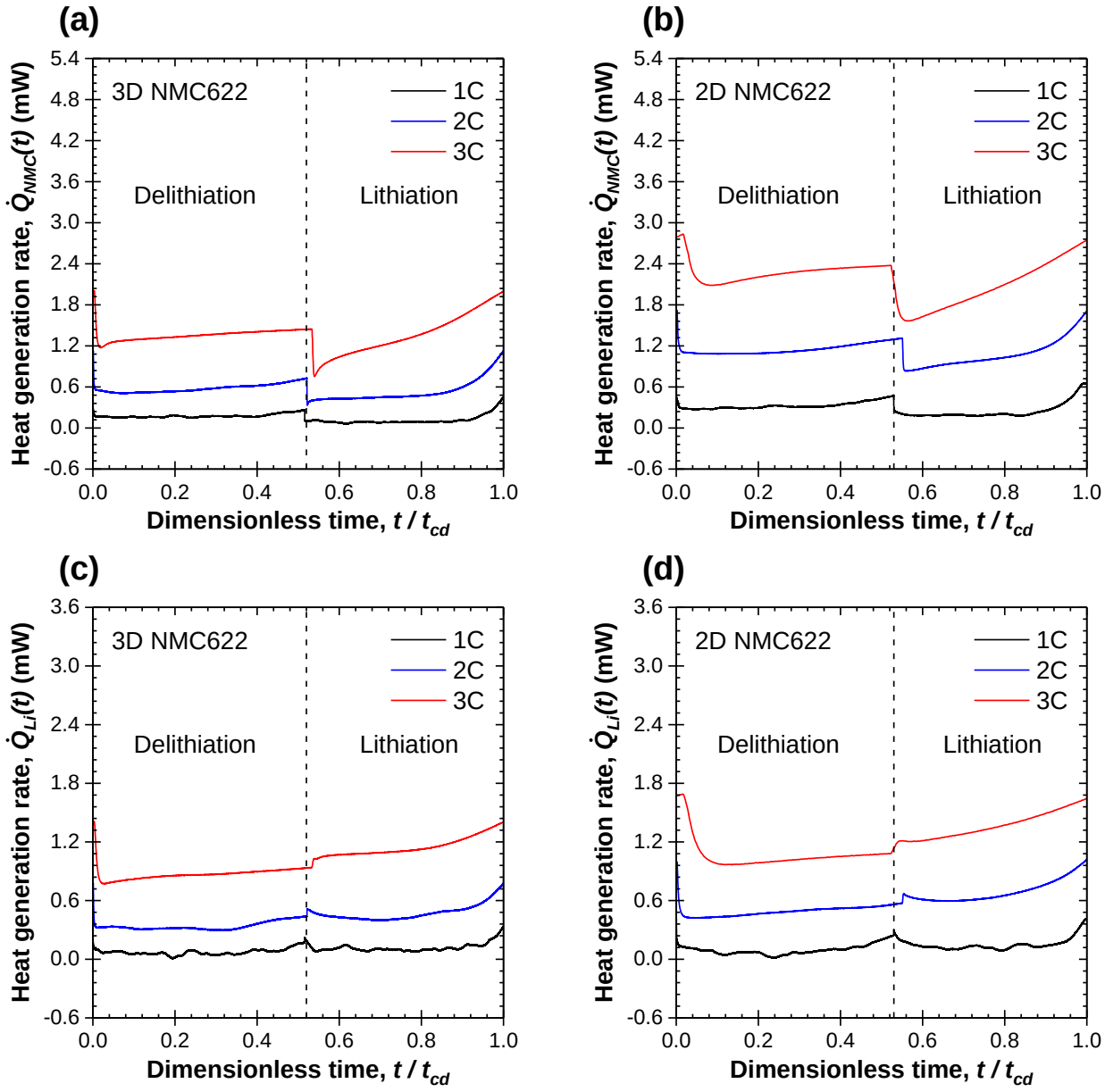

Figure 3.6: Instantaneous heat generation rates (a, b) $\dot{Q}_{NMC}(t)$ measured at the working electrodes made of 3D printed or 2D tape-casted NMC622 with similar mass loading and (c, d) $\dot{Q}_{Li}(t)$ measured at the respective lithium metal counter electrodes as functions of dimensionless time t/t_{cd} averaged over the last three consecutive cycles at C-rates of 1C, 2C, and 3C.

previous studies with PNb_9O_{25} [1], $Ti_2Nb_2O_9$ [60], or $(W_{0.2}V_{0.8})_3O_7$ [166] working electrodes and lithium metal counter electrodes.

3.3.3.3 Total heat generation rate of the cell

Figure 3.7 plots the measured total heat generation rate $\dot{Q}_T(x,T)$ in the calorimetric cells with working electrodes made of (a, b) 3D printed or (c, d) 2D tape-casted NMC622 and lithium metal counter electrodes as a function of lithium composition x during delithiation and lithiation at C-rate of 1C. Here, the measured cell potential $V(x,T)$ and open-circuit voltage $U_{OCV}(x,T)$ were also plotted. Figure 3.8 shows that the overpotential $[V(x,T) - U_{OCV}(x,T)]$ was smaller in the cell with 3D printed NMC622 than that with 2D tape-casted NMC622. This demonstrates that, under such faster cycling conditions, the cell with 3D printed NMC622 achieved smaller internal resistance, which can be associated with smaller electrode/electrolyte interfacial resistance due to faster interfacial kinetics, as well as smaller mass transfer resistance due to faster lithium ion transport. Figure 3.7 also shows the heat generation rates $\dot{Q}_J(x,T)$ and $\dot{Q}_J(x,T) + \dot{Q}_{rev}(x,T)$ predicted according to Equations (1.6) and (1.7). Note that the values of $U_{OCV}(x,T)$ and $\partial U_{OCV}(x,T)/\partial T$ previously determined by potentiometric entropy measurements (Figure 3.2) were used as the values of $U^{avg}(x,T)$ and $\partial U^{avg}(x,T)/\partial T$ in these equations. Here, the measured total heat generation rate $\dot{Q}_T(x,T)$ agreed relatively well with the calculated heat generation rate $\dot{Q}_J(x,T) + \dot{Q}_{rev}(x,T)$. The contribution from Joule heating $\dot{Q}_J(x,T)$ was generally larger in the cell with 2D tape-casted NMC622 than that with 3D printed NMC622. In addition, in both cells $\dot{Q}_J(x,T)$ surged towards the end of lithiation due to the growing difference between $V(x,T)$ and $U_{OCV}(x,T)$ (Figure 3.2). Moreover, the reversible entropic heat generation $\dot{Q}_{rev}(x,T)$ was endothermic during delithiation and exothermic during lithiation, since $\partial U_{OCV}(x,T)/\partial T$ always carried a negative value. Nevertheless, $\dot{Q}_{rev}(x,T)$ was found to be negligible compared to $\dot{Q}_J(x,T)$ which dominated heat generation. The difference between $\dot{Q}_T(x,T)$ and $\dot{Q}_J(x,T) + \dot{Q}_{rev}(x,T)$ originated from the irreversible exothermic enthalpy of mixing $\dot{Q}_{mix}(x,T)$ due to ion concentration gradients.

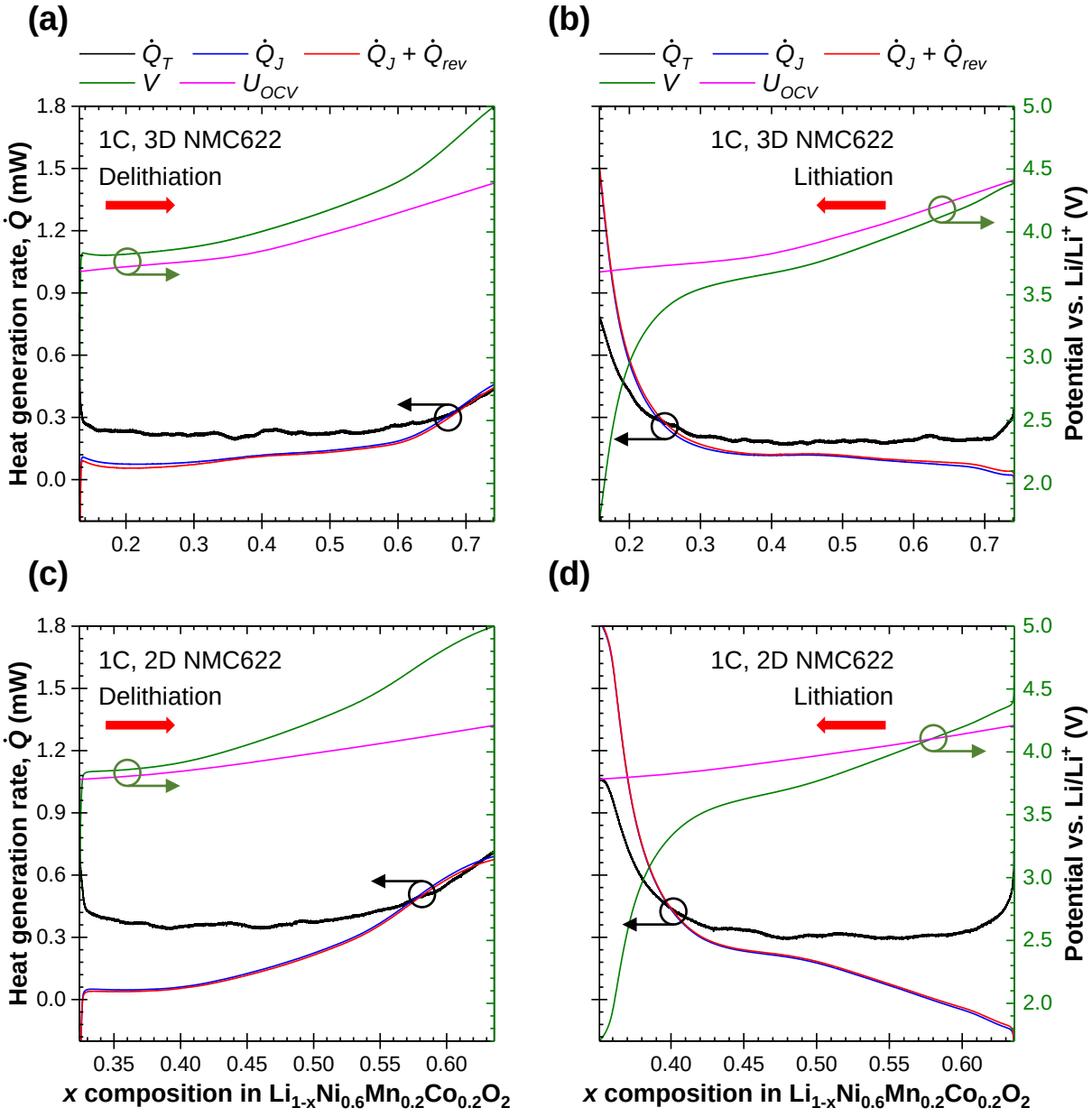

Figure 3.7: Measured total heat generation rate $\dot{Q}_T(x,T)$, along with heat generation rates $\dot{Q}_J(x,T)$ and $\dot{Q}_J(x,T) + \dot{Q}_{rev}(x,T)$ calculated according to Equations (1.6) and (1.7), as well as measured cell potential $V(x,T)$ and open-circuit voltage $U_{OCV}(x,T)$ as functions of lithium composition x during delithiation and lithiation at C-rate of 1C in calorimetric cells with working electrodes made of 3D printed or 2D tape-casted NMC622 and lithium metal counter electrodes.

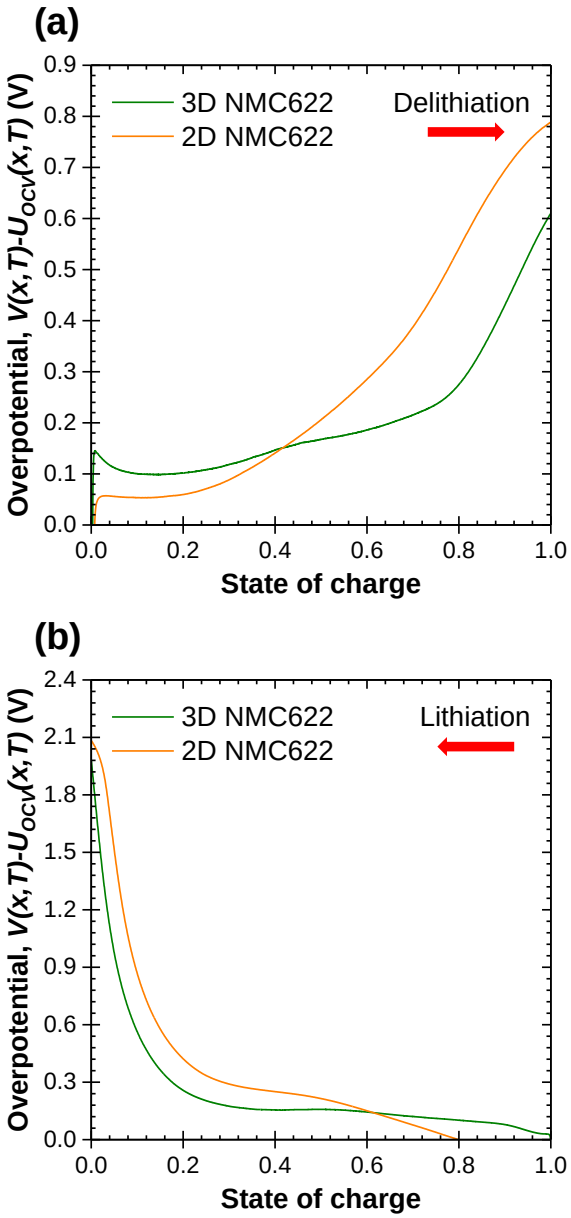

Figure 3.8: Overpotential calculated according to $[V(x,T) - U_{OCV}(x,T)]$ as functions of state of charge during delithiation and lithiation at C-rate of 1C in calorimetric cells with working electrodes made of 3D printed or 2D tape-casted NMC622 and lithium metal counter electrodes.

3.3.3.4 Time-averaged heat generation rates

Figure 3.9(a) plots the time-averaged irreversible heat generation rates $\bar{\dot{Q}}_{irr,NMC}$ and $\bar{\dot{Q}}_{irr,Li}$ as functions of current I for calorimetric cells with working electrodes made of 3D printed or 2D tape-casted NMC622. First, $\bar{\dot{Q}}_{irr,NMC}$ and $\bar{\dot{Q}}_{irr,Li}$ in both cells increased with increasing current I. Specifically, least squares fitting revealed that both $\bar{\dot{Q}}_{irr,NMC}$ and $\bar{\dot{Q}}_{irr,Li}$ increased quadratically with respect to current I, i.e., $\bar{\dot{Q}}_{irr,NMC} \propto I^2$ and $\bar{\dot{Q}}_{irr,Li} \propto I^2$. This suggests that in both cells Joule heating dominated the irreversible heat generation at both electrodes. Furthermore, for any given current I, $\bar{\dot{Q}}_{irr,Li}$ was similar in both cells as observed in Figures 3.6(c) and 3.6(d). Indeed, each lithium metal counter electrode was cut from the same piece into the same size and therefore should have approximately the same resistance. By contrast, for any given current I, $\bar{\dot{Q}}_{irr,NMC}$ was larger at the working electrode made of 2D tape-casted NMC622 than at that made of 3D printed NMC622 with similar mass loading. This could be due to the fact that the electrical resistivity was larger and the lithium ion transport was slower in 2D tape-casted NMC622 than in 3D printed NMC622.

In fact, Figure 3.9(b) plots the half-cell resistances estimated as $R_{ave,NMC} = \bar{\dot{Q}}_{irr,NMC}/I^2$ and $R_{ave,Li} = \bar{\dot{Q}}_{irr,Li}/I^2$ at constant C-rate. While the resistance $R_{ave,Li}$ of the lithium metal counter electrode was nearly the same between the two cells, the resistance $R_{ave,NMC}$ was larger for the half-cell with 2D tape-casted than that with 3D printed NMC622 working electrode. In addition, Figure 3.9(c) plots the cell resistance R_{GC} calculated from the IR drop [Equation (2.2)] in the calorimetric cells with working electrodes made of 3D printed or 2D tape-casted NMC622 at the end of the lithiation or delithiation steps during cycling at constant current I. Here also, the resistance R_{GC} of the cell with 2D tape-casted NMC622 was systematically larger than that with 3D printed NMC622. Both sets of independently obtained results were consistent, as the sum of half-cell resistances $R_{ave,NMC}$ and $R_{ave,Li}$ [Figure 3.9(b)] was within the range of cell resistances $R_{GC,l}$ and $R_{GC,d}$ in lithiated or delithiated state [Figure 3.9(c)].

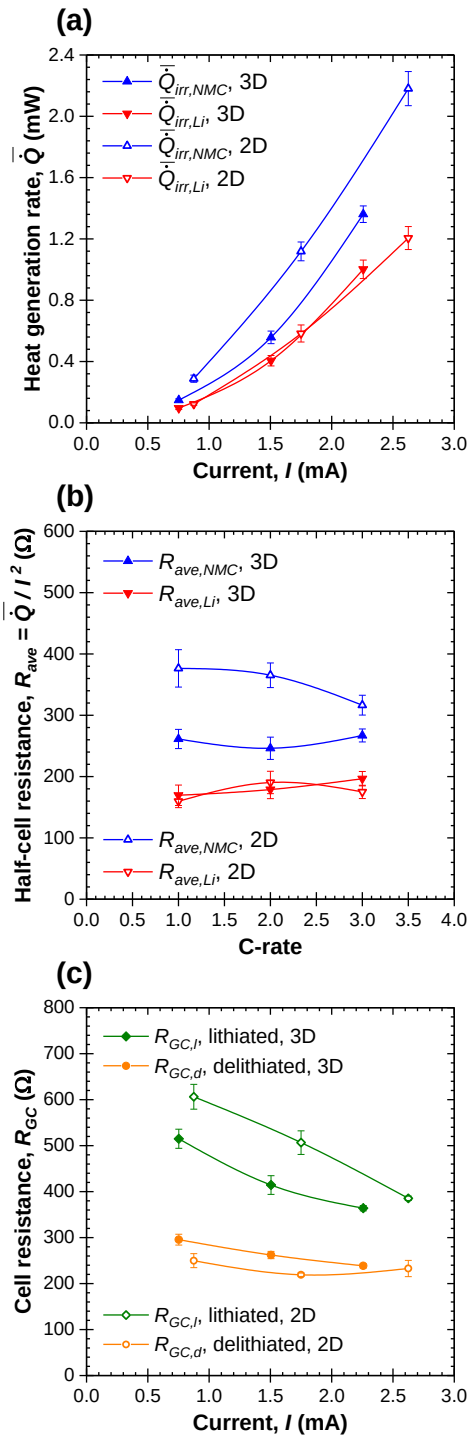

Figure 3.9: (a) Time-averaged irreversible heat generation rates $\bar{\dot{Q}}_{irr,NMC}$ and $\bar{\dot{Q}}_{irr,Li}$ as functions of current I. (b) Half-cell resistances $R_{ave,NMC}$ and $R_{ave,Li}$ and (c) cell resistances $R_{GC,l}$ and $R_{GC,d}$ in lithiated or delithiated state [Equation (2.2)] for calorimetric cells with working electrodes made of 3D printed or 2D tape-casted NMC622 under constant current cycling.

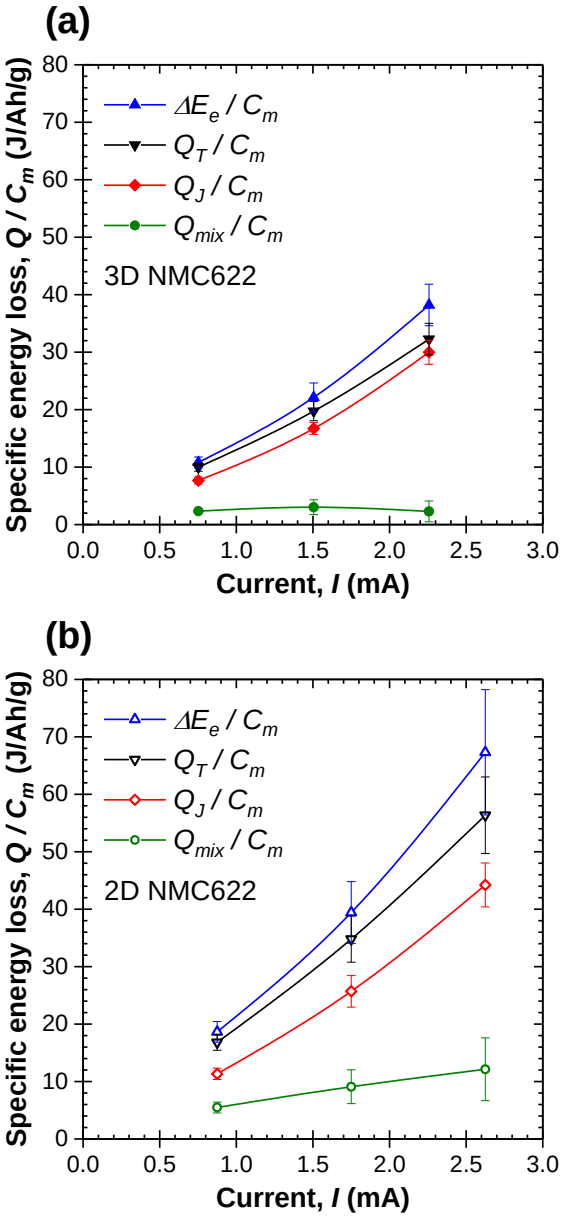

Figure 3.10: Specific net electrical energy loss $\Delta E_e/C_m$ [Equation (1.12)] and specific total thermal energy dissipated Q_T/C_m [Equation (1.11)] per unit charge stored, as well as predicted contributions from Joule heating Q_J/C_m and enthalpy of mixing Q_{mix}/C_m, averaged over the last three consecutive charging/discharging cycles for calorimetric cells with working electrodes made of (a) 3D printed or (b) 2D tape-casted NMC622 and lithium metal counter electrodes.

3.3.3.5 Energy balance

Figure 3.10 plots the specific net electrical energy loss $\Delta E_e/C_m$ [Equation (1.12)] and the specific total thermal energy dissipated Q_T/C_m [Equation (1.11)] per unit charge stored, as well as the predicted contributions from Joule heating Q_J/C_m and enthalpy of mixing Q_{mix}/C_m, averaged over the last three consecutive charging/discharging cycles for calorimetric cells with working electrodes made of (a) 3D printed or (b) 2D tape-casted NMC622 and lithium metal counter electrodes. Note that each term was divided by the specific capacity C_m of the cell to correct for any difference in mass loading. Here, for both cells at any given current I, the specific total dissipated thermal energy Q_T/C_m measured by *operando* isothermal calorimetry fell within experimental uncertainty of the specific net electrical energy loss $\Delta E_e/C_m$ measured by the potentiostat. In other words, the net electrical energy loss was entirely dissipated in the form of heat. These results confirm the accuracy of our measurements. As expected, the contributions of each energy dissipation mechanism increased with increasing C-rate in both cells. However, the cell with the 3D printed NMC622 electrode displayed 33% less thermal energy dissipation per unit charge stored than that with the 2D tape-casted NMC622 electrode. These results demonstrate that the novel 3D printing technology produced NMC622 electrodes with improved ionic transport and enhanced electronic transport resulting in superior specific capacity and significantly reduced heat generation. These features make 3D printed electrodes particularly attractive for fast charging applications, requiring less stringent thermal management to prevent thermal runaway, thus enhancing safety during operation.

3.4 Chapter summary

This chapter compares the thermodynamics behavior, ion transport, and energy dissipation in NMC622 electrodes made by a novel 3D printing technology with those made by the conventional 2D tape casting procedure. Potentiometric entropy measurements indicated that both types of electrodes had similar thermodynamics behavior. They both underwent lithium deintercalation in a homogeneous solid solution of NMC622 followed by a transi-

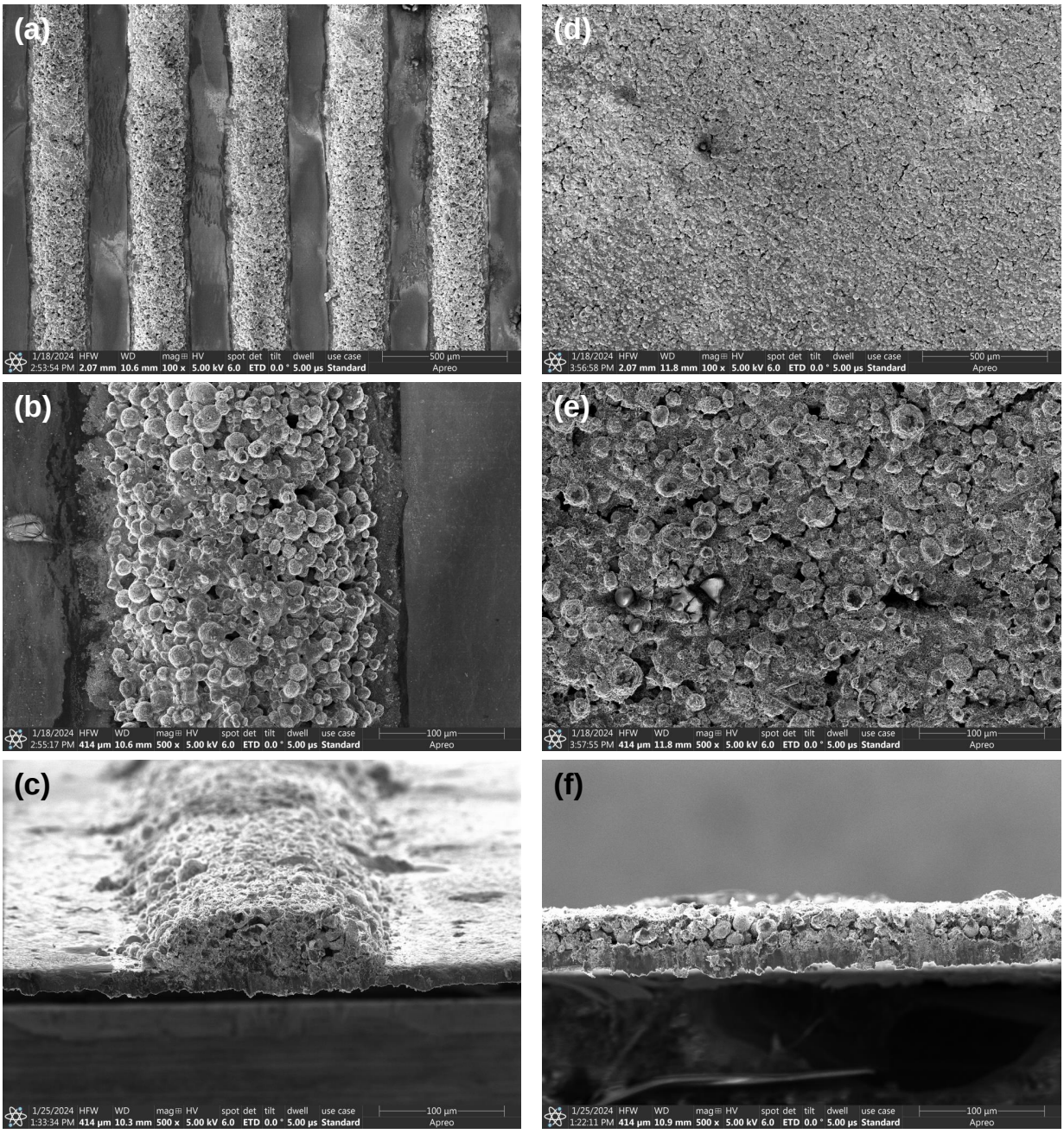

Figure 3.11: Scanning electron microscopy (SEM) images of (a, b, c) 3D printed or (d, e, f) 2D tape-casted NMC622 electrodes with the broad view, the top view, and the cross-sectional view, respectively, as recovered after being cycled during *operando* isothermal calorimetry. These images did not show visible signs of issues including structural deformation, blocking of diffusion pathways, and parasitic reactions such as the formation of cathode-electrolyte interphase (CEI), lithium plating, or oxygen evolution reactions.

tion from a hexagonal (H1) phase to another hexagonal (H2) phase through a monoclinic (M) phase, as identified in other studies. *Operando* isothermal calorimetry revealed that, at high C-rates, the 3D printed electrodes exhibited larger specific capacity and better rate performance than the 2D tape-casted electrodes. This could be attributed to the larger electrode/electrolyte interfacial surface area and electrical conductivity, and to the faster lithium ion transport in the 3D printed electrodes. These attributes also contributed to the smaller instantaneous heat generation rates and the reduced overall specific electrical energy and thermal energy dissipation per unit charge stored at the 3D printed electrodes than at the 2D tape-casted electrodes when tested under the same conditions. The superior electrochemical performance and the reduced heat generation of 3D printed NMC622 electrodes highlights the prospects of employing additive manufacturing techniques to create electrodes for fast charging batteries.

CHAPTER 4

Microcalorimetry electrothermal impedance spectroscopy (ETIS) informs entropy evolution at individual electrodes of PNb_9O_{25} or $TiNb_2O_7$ battery cells

This chapter presents a novel microcalorimetry electrothermal impedance spectroscopy (ETIS) measurement method to rapidly determine the open-circuit voltage U_{OCV}, the entropic potential $\partial U_{OCV}/\partial T$, and the partial entropy changes at each electrode of a battery cell. This new method uses an *operando* isothermal calorimeter capable of measuring the instantaneous heat generation rates at individual electrodes with small mass loadings. After validating the method using numerical simulations, it was demonstrated experimentally with PNb_9O_{25} or $TiNb_2O_7$ battery cells assembled in the calorimeter.

4.1 Background

4.1.1 Fast Fourier transform (FFT)

Fast Fourier transform (FFT) is an algorithm computing the discrete Fourier transform of a sequence and converting it from time domain to frequency domain [168]. It is an effective tool to reveal any periodically oscillating feature within a signal which may not be obvious from its temporal evolution. For example, let us consider a signal which can be represented by the function $f(t)$ over time t such that,

$$f(t) = A_0 + A_A\cos\left(2\pi f_A t + \phi_A\right) + A_B\cos\left(2\pi f_B t + \phi_B\right) + \cdots \tag{4.1}$$

By applying FFT to $f(t)$, the amplitudes (A_A, A_B, $\cdots$), frequencies (f_A, f_B, $\cdots$), and phase angles (ϕ_A, ϕ_B, $\cdots$) of every sinusoidal term can be identified. Note that the phase angle given by FFT has a range between -π and π.

4.1.2 Electrothermal impedance spectroscopy (ETIS)

Previously, multiple characterization techniques have been developed to enable the simultaneous analysis of both electrochemical and thermal behavior of electrical energy storage systems. For example, Hess et al. [169] designed an in situ simultaneous thermal analysis (STA) cell for electric double layer capacitors. This technique monitors the change in heat flow, mass loss, resistance, and capacitance within electric double layer capacitors during operation. It was employed to investigate the impact of operating voltage and temperature on the cycling degradation of electric double-layer capacitors and on the associated thermal processes occurring within the devices [169–171]. Similarly for LIBs, Schmidt et al. [109] first proposed ETIS as an alternative to the time-consuming potentiometric entropy measurements based on GITT. The ETIS method consists of imposing on a battery cell a current $I(t)$ with a very small constant offset I_0 and a sinusoidal oscillation with amplitude I_1 at frequency f_1, i.e.,

$$I(t) = I_0 + I_1 \sin(2\pi f_1 t)\,. \tag{4.2}$$

Note that I_0 is small enough to be negligible compared to I_1, i.e., $|I_0| \ll |I_1|$. Under such conditions, the irreversible Joule heating $\dot{Q}_J(t)$ can be expressed as [109],

$$\dot{Q}_J(t) = I(t)^2 R \approx -\frac{{I_1}^2 R}{2}\cos(4\pi f_1 t) + \frac{{I_1}^2 R}{2} \tag{4.3}$$

where R is the internal resistance of the battery cell. Similarly, the reversible entropic heat generation rate $\dot{Q}_{rev}(t)$ can be written as [109],

$$\dot{Q}_{rev}(t) = I(t) T_m \frac{\partial U_{OCV}}{\partial T}(x,T) \approx I_1 T_m \frac{\partial U_{OCV}}{\partial T}(x,T)\sin(2\pi f_1 t) \tag{4.4}$$

where T_m is the measured cell temperature averaged over the sinusoidal period.

The measured instantaneous temperature response $T_{cell}(t)$ of the battery cell can be

expressed as [109],

$$T_{cell}(t) = T_{amb} + \Delta T_J(t) + \Delta T_{rev}(t) \tag{4.5}$$

where T_{amb} is the ambient temperature (assumed to be constant) while $\Delta T_J(t)$ and $\Delta T_{rev}(t)$ are the cell temperature changes due to irreversible Joule heating and reversible entropic heat generation, respectively. The thermal impedance $Z_{th}(f)$ (in K/W) of a battery cell at frequency f can be defined as,

$$Z_{th}(f) = \frac{T_{cell}(f) - T_{amb}(f)}{\dot{Q}_T(f)} = \frac{\Delta T_J(f) + \Delta T_{rev}(f)}{\dot{Q}_J(f) + \dot{Q}_{rev}(f)}. \tag{4.6}$$

Note that in the frequency domain, $T_{amb}(f) = 0$ unless $f = 0$. As such, the cell temperature changes $\Delta T_J(t)$ and $\Delta T_{rev}(t)$ were related to the heat generation rates $\dot{Q}_J(t)$ and $\dot{Q}_{rev}(t)$ through the thermal impedance $Z_{th}(f)$ of the battery cell such that [109],

$$\Delta T_J(t) = -\frac{{I_1}^2 R}{2} \left|Z_{th}(2f_1)\right| \cos\left[4\pi f_1 t + \phi_{Z_{th}}(2f_1)\right] + \frac{{I_1}^2 R}{2} \left|Z_{th}(2f_1)\right|, \text{ and} \tag{4.7}$$

$$\Delta T_{rev}(t) = I_1 T_m \frac{\partial U_{OCV}}{\partial T}(x, T) \left|Z_{th}(f_1)\right| \sin\left[2\pi f_1 t + \phi_{Z_{th}}(f_1)\right] \tag{4.8}$$

where the thermal impedance $Z_{th}(f)$ can be defined as a frequency-dependent complex function with magnitude $|Z_{th}(f)|$ and phase difference $\phi_{Z_{th}}(f)$ at frequency f. Here, the sinusoidal oscillations within $\Delta T_J(t)$ and $\Delta T_{rev}(t)$ have distinct frequencies $2f_1$ and f_1, respectively. Thus, they can be distinguished in the frequency domain by applying FFT to the measured $T_{cell}(t)$. In fact, Schmidt et al. [109] expressed the amplitude $A_T(2f_1)$ associated with the temperature oscillation at frequency $2f_1$ as,

$$A_T(2f_1) = \frac{{I_1}^2 R}{2} \left|Z_{th}(2f_1)\right| \tag{4.9}$$

and $A_T(f_1)$ at frequency f_1 as,

$$A_T(f_1) = I_1 T_m \frac{\partial U_{OCV}}{\partial T}(x, T) \left|Z_{th}(f_1)\right|. \tag{4.10}$$

As a result, the internal resistance R can be retrieved from the FFT output $A_T(2f_1)$ as,

$$R = \frac{2}{{I_1}^2 \left|Z_{th}(2f_1)\right|} A_T(2f_1). \tag{4.11}$$

Similarly, the entropic potential $[\partial U_{OCV}/\partial T](x,T)$ can be obtained from the FFT output $A_T(f_1)$ as,

$$\frac{\partial U_{OCV}}{\partial T}(x,T) = \frac{1}{I_1 T_m \left|Z_{th}(f_1)\right|} A_T(f_1). \tag{4.12}$$

To obtain the thermal impedance magnitudes $|Z_{th}(2f_1)|$ and $|Z_{th}(f_1)|$, the following procedure was suggested [109]. First, the entropic potential of the battery cell at a given state of charge (SOC) is predetermined by potentiometric entropy measurements based on GITT at four different temperatures. Then, the battery cell is set to this SOC and excited with a sinusoidal current at frequency $2f_1$. As the entropic potential at this SOC is known, the reversible entropic heat generation rate $\dot{Q}_{rev}(t)$ can be calculated using Equation (4.4). Simultaneously, the instantaneous temperature response $T_{cell}(t)$ of the battery cell is measured. Subsequently, both the measured $T_{cell}(t)$ and the calculated $\dot{Q}_{rev}(t)$ are analyzed by FFT. This identifies the amplitudes of the sinusoidal oscillations at frequency $2f_1$ within $T_{cell}(t)$ and $\dot{Q}_{rev}(t)$. Finally, the thermal impedance magnitude $|Z_{th}(2f_1)|$ arises as the ratio of these two amplitudes, i.e., $|Z_{th}(2f_1)| = |T_{cell}(2f_1)| \,/\, \left|\dot{Q}_{rev}(2f_1)\right|$. The same procedure is repeated at frequency f_1 to obtain the thermal impedance magnitude $|Z_{th}(f_1)|$, i.e., $|Z_{th}(f_1)| = |T_{cell}(f_1)| \,/\, \left|\dot{Q}_{rev}(f_1)\right|$.

Overall, this method was successfully demonstrated on commercial cylindrical and pouch cells with capacities around 1 Ah [109]. The retrieved entropic potential $[\partial U_{OCV}/\partial T](x,T)$ agreed with that determined by potentiometric entropy measurements based on GITT, and the measurement duration was shortened from several days to a few hours [109]. Nevertheless, in practice this method becomes unnecessarily complicated because of the requirement to measure the temperature. First, accurate values of the thermal impedance magnitudes $|Z_{th}(2f_1)|$ and $|Z_{th}(f_1)|$ must be obtained. The thermal impedance serves as the only available relationship from the measured temperature response $T_{cell}(t)$ back to the heat generation rates $\dot{Q}_J(t)$ and $\dot{Q}_{rev}(t)$ in the battery cell which are not directly measured. However, several studies have illustrated that the thermal impedance can vary substantially with minor changes in ambient temperature [108] and ambient relative humidity [172]. Thus, consistent conditions must be maintained for the duration of the experiment. For example, throughout their experiment, Schmidt et al. [109] placed the battery cell and mounted the

temperature sensor in the same positions. Furthermore, the entire setup was housed in an incubator to ensure constant ambient temperature and ambient relative humidity. Moreover, the imposed sinusoidal current needs to have large amplitude (on the order of amperes) and low frequency (on the order of millihertz) to create temperature oscillations on the order of a few degrees Celsius which are detectable by conventional temperature sensors [109]. These criteria are challenging for battery cells with large thermal conductivity and/or large specific heat capacity, as a larger heat generation rate is required to induce sufficiently large temperature oscillations [108].

To address these drawbacks, Hu et al. [173, 174] attempted to eliminate the step of retrieving the heat generation rate from the measured temperature response. Instead, they directly measured the total heat generation rate $\dot{Q}_T(t)$ using an isothermal calorimeter at temperature T_m [173, 174]. The imposed current $I(t)$ was given by Equation (4.2) and $\dot{Q}_T(t)$ was expressed as the sum of $\dot{Q}_J(t)$ and $\dot{Q}_{rev}(t)$ given by Equations (4.3) and (4.4), respectively. Therefore, after applying FFT to the measured $\dot{Q}_T(t)$, they expressed the amplitude $A_Q(2f_1)$ associated with the heat generation rate oscillation at frequency $2f_1$ as,

$$A_Q(2f_1) = \frac{{I_1}^2 R}{2} \tag{4.13}$$

and $A_Q(f_1)$ at frequency f_1 as,

$$A_Q(f_1) = I_1 T_m \frac{\partial U_{OCV}}{\partial T}(x, T). \tag{4.14}$$

Then, the internal resistance R and the entropic potential $[\partial U_{OCV}/\partial T](x, T)$ can be retrieved from the FFT output $A_Q(2f_1)$ and $A_Q(f_1)$ as,

$$R = \frac{2}{{I_1}^2} A_Q(2f_1) \tag{4.15}$$

$$\frac{\partial U_{OCV}}{\partial T}(x, T) = \frac{1}{I_1 T_m} A_Q(f_1). \tag{4.16}$$

This modified ETIS method was successfully demonstrated on a commercial LMO-NMC/graphite pouch cell with a capacity of 25.9 Ah [173, 174]. The isothermal calorimeter measured the heat generation rate and retrieved the entropic potential of the entire pouch cell. It simplified the experimental procedure and improved the accuracy of the retrieved

entropic potential and internal resistance [173, 174]. However, the isothermal calorimeter had a maximum measurement error of 0.67 W and a response time of at least a few seconds [173, 174]. Thus, its most appropriate application is for commercial pouch cells with mass loadings on the order of grams. However, in the discovery of novel LIB materials in a laboratory setting, one typically synthesizes electrodes with mass loadings on the order of a few mg/cm^2 tested in coin cells with heat generation rates on the order of microwatts [1, 59, 60]. For coin cells, an isothermal calorimeter with considerably better sensitivity and shorter response time is necessary to capture the instantaneous heat generation rate typically featuring rapid fluctuations of relatively small magnitudes [69]. In addition, measuring the heat generation rates at each electrode could be used to investigate their individual partial entropy changes. This could provide insight into the thermodynamics behavior of both the anode and the cathode and contribute in selecting the pair of electrodes for full cells.

This study aims to develop a novel microcalorimetry ETIS measurement method to quickly determine the open-circuit voltage U_{OCV} and the entropic potential $\partial U_{OCV}/\partial T$ of battery cells with electrode mass loadings on the order of milligrams and fabricated in a laboratory setting. This new method uses an *operando* isothermal calorimeter designed to measure the instantaneous heat generation rates on the order of microwatts at individual electrodes, making it the first method capable of investigating the partial entropy changes at each electrode during cycling.

4.2 Analysis

4.2.1 Imposed current

Figure 4.1 shows the schematic of the new procedure developed to determine the open-circuit voltage $U_{OCV}(x, T)$ and the entropic potential $[\partial U_{OCV}/\partial T](x, T)$ of an LIB cell from microcalorimetry ETIS measurements. The apparatus consists of the *operando* isothermal calorimeter described in Ref. [69] and reproduced in Figure 4.2 for the sake of complete-

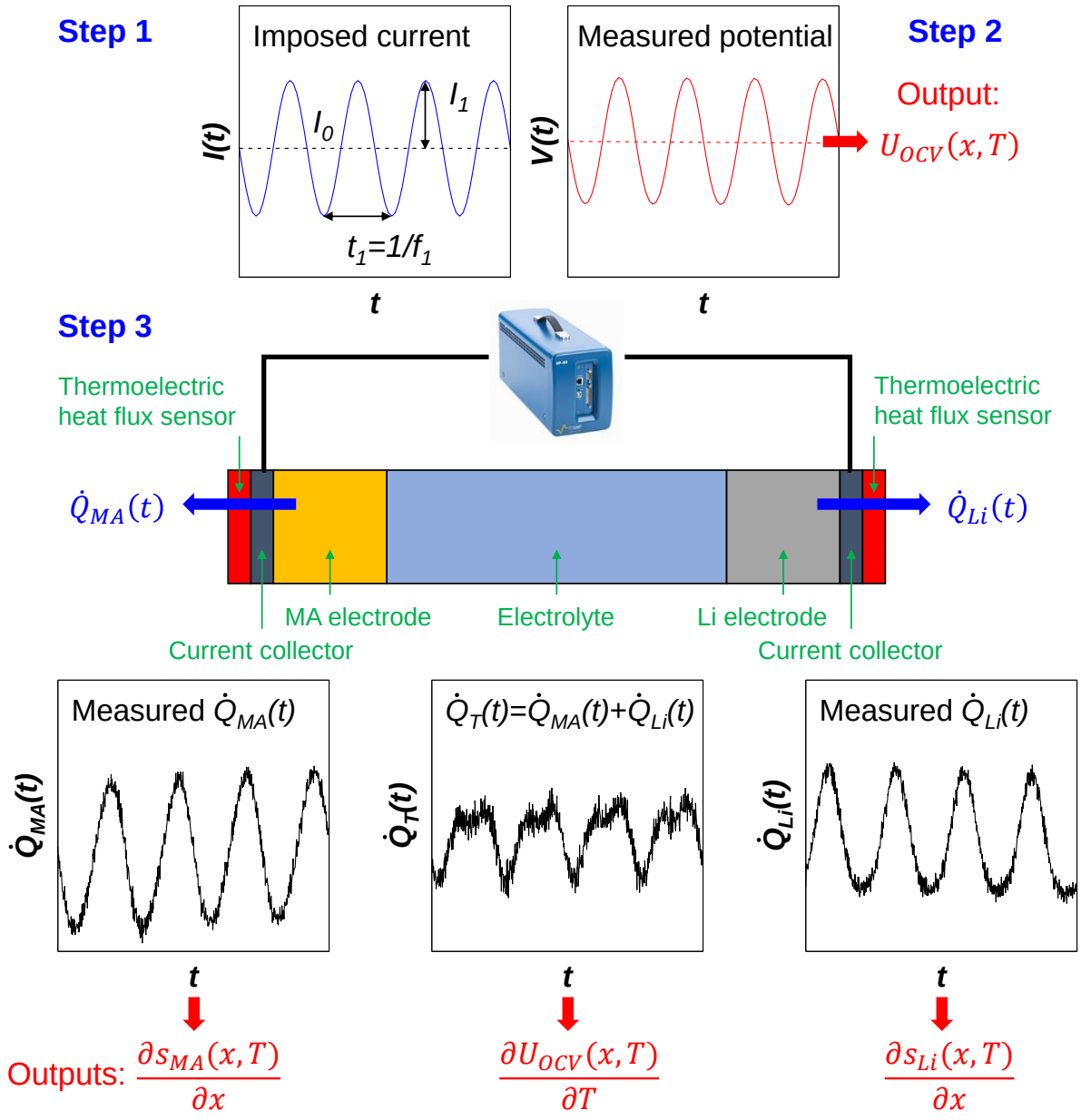

Figure 4.1: Schematic of the procedure and experimental apparatus developed to determine the open-circuit voltage $U_{OCV}(x,T)$ and the entropic potential $[\partial U_{OCV}/\partial T](x,T)$ of an LIB cell from the novel microcalorimetry ETIS measurements.

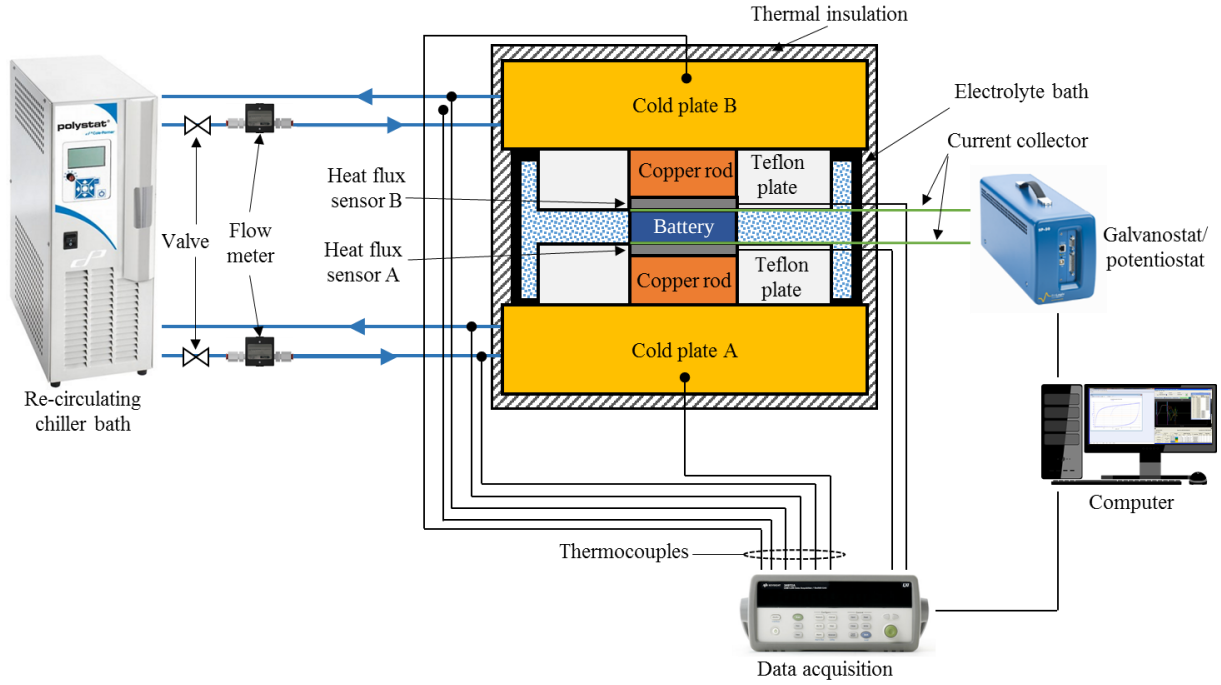

Figure 4.2: Schematic of the *operando* isothermal calorimeter used in microcalorimetry ETIS measurements.

ness. Battery cells consisting of two bare electrodes cast on current collectors and two thick separators impregnated with electrolyte are assembled in the calorimeter and cycled using a high accuracy potentiostat. Instantaneous heat generation rates at individual electrodes are measured by thermoelectric heat flux sensors in thermal contact with the back of each electrode.

To complement previous studies [109,173,174], here we describe how to retrieve the open-circuit voltage from the measured cell potential and the entropic potential as well as the partial entropy changes at each electrode from the measured instantaneous heat generation rates. The technique starts by imposing a current $I(t)$ consisting of a constant offset I_0 and a sinusoidal function oscillating with amplitude I_1 at frequency f_1, i.e.,

$$I(t) = I_0 - I_1 \sin(2\pi f_1 t) = I_0 + I_1 \cos\left(2\pi f_1 t + \frac{\pi}{2}\right). \tag{4.17}$$

As discussed in detail by Schmidt et al. [109], the choice of I_0, I_1, and f_1 is a compromise among several different considerations. Here, I_0 is negative which slowly but continuously discharges the battery cell. Note also that I_0 should be negligible compared to I_1, i.e., $|I_0| \ll |I_1|$. However, a large magnitude of I_0 results in faster discharging and thus quicker measurements. Similarly, I_1 should be large enough to ensure an adequate signal-to-noise ratio in the measured oscillating heat generation rates. However, a small I_1 is preferable as (i) it maximizes the proportion of reversible entropic heat generation $\dot{Q}_{rev}(t)$ compared to Joule heating $\dot{Q}_J(t)$ and (ii) it minimizes the sinusoidal variation in the lithium composition x over a period. In fact, every data point of the open-circuit voltage $U_{OCV}(x,T)$ and the entropic potential $[\partial U_{OCV}/\partial T](x,T)$ retrieved by microcalorimetry ETIS measurements is actually the time-average over a sinusoidal period of an oscillating variable function of x. Therefore, this uncertainty can be alleviated by reducing the variation in x, which in turn improves the resolution of the retrieved $U_{OCV}(x,T)$ and $[\partial U_{OCV}/\partial T](x,T)$. In addition, f_1 should be sufficiently large to acquire enough data points. Here also, a large frequency f_1 shortens the period of every sinusoid, reduces the variation in x, and improves the resolution of the retrieved results. However, every period needs to last at least a few seconds to provide sufficient time for the periodically alternating redox reactions to occur within the battery

cell. Finally, the phase angle of $I(t)$ is chosen as $\pi/2$ such that (i) $I(t) \approx 0$ at $t = 0$ to avoid a sudden load on the potentiostat at the start of the measurements and (ii) $I(t)$ is negative during the first half-period to avoid overcharging the battery cell when it already begins in fully charged (delithiated) state.

The elapsed time t (in s) can be converted into the lithium composition x in Li_xMA such that,

$$x(t) = -\frac{x_{theo}\Delta q(t)}{3600 m C_{m,theo}} = -\frac{x_{theo}\int_0^t I(t')\mathrm{d}t'}{3600 m C_{m,theo}}. \tag{4.18}$$

Here, $\Delta q(t)$ (in mC) is the amount of charge transferred to the battery cell between times 0 and t, $I(t)$ (in mA) is the imposed current given by Equation (4.17), m (in g) is the mass loading of active material MA, and $C_{m,theo}$ (in mAh/g) is the theoretical specific capacity of the intercalation compound corresponding to the theoretical lithium composition x_{theo}. For example, in the case of a PNb_9O_{25} working electrode, $C_{m,theo} = 190$ mAh/g assuming $x_{theo} = 9$ [1], while for a $TiNb_2O_7$ working electrode, $C_{m,theo} = 388$ mAh/g assuming $x_{theo} = 5$ [59].

4.2.2 Potential response and open-circuit voltage

Under the imposed current $I(t)$ of Equation (4.17) and assuming $|I_0| \ll |I_1|$, the measured potential response $V(t)$ can be expressed as,

$$V(t) = U_{OCV}(x,T) + I_1\,|Z(f_1)|\cos\left[2\pi f_1 t + \frac{\pi}{2} + \phi_Z(f_1)\right]. \tag{4.19}$$

Here, $Z(f_1)$ (in Ω) is the electrochemical impedance of the battery cell at frequency f_1. Note that $Z(f_1)$ is a complex number such that $Z(f_1) = Z_{re}(f_1) + iZ_{im}(f_1)$. Alternatively, $Z(f_1)$ can be described by its magnitude $|Z(f_1)|$ and phase difference $\phi_Z(f_1)$, i.e., $Z(f_1) = |Z(f_1)|\exp[i\phi_Z(f_1)]$ [126, 175]. Accordingly, the open-circuit voltage $U_{OCV}(x_i,T)$ at lithium composition x_i can be calculated by averaging the measured cell potential $V(t)$ over a period such that,

$$U_{OCV}(x_i,T) = \frac{1}{t_1}\int_{(i-1)t_1}^{it_1} V(t')\mathrm{d}t' \tag{4.20}$$

where $t_1 = 1/f_1$ is the period of $I(t)$ and time t falls within this period from $(i-1)t_1$ to it_1. In other words, $U_{OCV}(x,T)$ is considered equal to $U_{OCV}(x_i,T)$ for any lithium composition

x between x_{i-1} and x_i such that,

$$x_i = -\frac{x_{theo}\int_0^{it_1} I(t')\mathrm{d}t'}{3600mC_{m,theo}}. \tag{4.21}$$

4.2.3 Heat generation rates

The total instantaneous heat generation rate $\dot{Q}_T(t)$ in a battery cell can be divided into several contributions including (i) Joule heating $\dot{Q}_J(t)$, (ii) reversible entropic heat generation $\dot{Q}_{rev}(t)$, (iii) enthalpy of mixing $\dot{Q}_{mix}(t)$, and (iv) heat generation due to side reactions $\dot{Q}_{sr}(t)$, i.e. [1, 59, 60, 63, 77, 78],

$$\dot{Q}_T(t) = \dot{Q}_J(t) + \dot{Q}_{rev}(t) + \dot{Q}_{mix}(t) + \dot{Q}_{sr}(t). \tag{4.22}$$

The heat generation rate $\dot{Q}_J(t)$ associated with irreversible resistive losses can be expressed as [1, 59, 60, 63, 77, 78],

$$\dot{Q}_J(t) = I(t)\left[V(t) - U_{OCV}(x,T)\right]. \tag{4.23}$$

Substituting $I(t)$ given by Equation (4.17) (assuming $|I_0| \ll |I_1|$) and $V(t)$ given by Equation (4.19) into Equation (4.23) yields,

$$\dot{Q}_J(t) = \frac{{I_1}^2}{2}|Z(f_1)|\cos\left[4\pi f_1 t + \pi + \phi_Z(f_1)\right] + \frac{{I_1}^2}{2}|Z(f_1)|\cos\left[\phi_Z(f_1)\right]. \tag{4.24}$$

Similarly, the reversible heat generation rate $\dot{Q}_{rev}(t)$ due to entropic changes can be expressed as [63, 77, 78],

$$\dot{Q}_{rev}(t) = I(t)T\frac{\partial U_{OCV}}{\partial T}(x,T). \tag{4.25}$$

Here, T is the temperature of the battery cell imposed to be constant during *operando* isothermal calorimetry. Although $[\partial U_{OCV}/\partial T](x,T)$ is a real number, for the convenience of FFT analysis we describe it by its magnitude $|[\partial U_{OCV}/\partial T](x,T)|$ and phase difference ϕ_{rev}. Then, substituting $I(t)$ given by Equation (4.17) into Equation (4.25) and assuming $|I_0| \ll |I_1|$ yields,

$$\dot{Q}_{rev}(t) = I_1 T\left|\frac{\partial U_{OCV}}{\partial T}(x,T)\right|\cos\left(2\pi f_1 t + \frac{\pi}{2} + \phi_{rev}\right). \tag{4.26}$$

Mathematically during discharging (lithiation) with negative $I(t)$, if $\phi_{rev} \approx 0$ then $[\partial U_{OCV}/\partial T](x,T)$ is positive and $\dot{Q}_{rev}(t)$ is endothermic, or if $\phi_{rev} \approx \pi$ then $[\partial U_{OCV}/\partial T](x,T)$ is negative and $\dot{Q}_{rev}(t)$ is exothermic.

Furthermore, $\dot{Q}_{rev}(t)$ can be defined as the sum of the reversible heat generation rates at the intercalation compound working electrode $\dot{Q}_{rev,MA}(t)$ and at the metallic lithium counter electrode $\dot{Q}_{rev,Li}(t)$ such that $\dot{Q}_{rev}(t) = \dot{Q}_{rev,MA}(t) + \dot{Q}_{rev,Li}(t)$ [1, 60]. Then, $\dot{Q}_{rev,MA}(t)$ can be expressed as,

$$\dot{Q}_{rev,MA}(t) = \frac{I(t)T}{e}\frac{\partial s_{MA}}{\partial x}(x,T) = \frac{I_1 T}{e}\left|\frac{\partial s_{MA}}{\partial x}(x,T)\right|\cos\left(2\pi f_1 t + \frac{\pi}{2} + \phi_{rev,MA}\right). \quad (4.27)$$

Here also, the partial entropy change at the intercalation compound working electrode $[\partial s_{MA}/\partial x](x,T)$ is a real number that can be described by its magnitude $|[\partial s_{MA}/\partial x](x,T)|$ and its phase difference $\phi_{rev,MA}$. Similarly, $\dot{Q}_{rev,Li}(t)$ can be written as,

$$\dot{Q}_{rev,Li}(t) = -\frac{I(t)T}{e}\frac{\partial s_{Li}}{\partial x}(x,T) = \frac{I_1 T}{e}\left|\frac{\partial s_{Li}}{\partial x}(x,T)\right|\cos\left(2\pi f_1 t + \frac{3\pi}{2} + \phi_{rev,Li}\right). \quad (4.28)$$

Finally, $\dot{Q}_{mix}(t)$ is the heat generation rate associated with the enthalpy of mixing caused by ion concentration gradients. Here, $\dot{Q}_{mix}(t)$ is related to the local values of the partial molar enthalpy and the concentration gradient of each ion species in the battery cell [63, 77, 78]. These parameters are difficult to know for any given location within the cell at any given time. Therefore, an exact relationship between $\dot{Q}_{mix}(t)$ and $I(t)$ cannot be established. Nevertheless, $\dot{Q}_{mix}(t)$ is typically negligible at low C-rates [77], as assumed in the present FFT analysis. Furthermore, the heat generation rate due to side reactions $\dot{Q}_{sr}(t)$ is generally neglected unless the battery cell is operating under extreme conditions [63, 77, 78, 91].

4.2.4 Entropic potential and partial entropy changes

Substituting Equations (4.24) and (4.26) into Equation (4.22) yields,

$$\dot{Q}_T(t) = A_{tot}(0) + A_{tot}(f_1)\cos\left[2\pi f_1 t + \phi_{tot}(f_1)\right] + A_{tot}(2f_1)\cos\left[4\pi f_1 t + \phi_{tot}(2f_1)\right] \quad (4.29)$$

where the terms $A_{tot}(0)$, $A_{tot}(f_1)$, and $A_{tot}(2f_1)$ are given by,

$$A_{tot}(0) = \frac{{I_1}^2}{2} |Z(f_1)| \cos\left[\phi_Z(f_1)\right], \tag{4.30}$$

$$A_{tot}(f_1) = I_1 T \left| \frac{\partial U_{OCV}}{\partial T}(x,T) \right|, \text{ and} \tag{4.31}$$

$$A_{tot}(2f_1) = \frac{{I_1}^2}{2} |Z(f_1)|. \tag{4.32}$$

Applying FFT to the measured $\dot{Q}_T(t)$ during a given period from $(i-1)t_1$ to it_1 yields the amplitude $A_{tot}(f_1)$ of the sinusoidal oscillation at frequency f_1 given by Equation (4.31) and the corresponding phase angle $\phi_{tot}(f_1)$ expressed as,

$$\phi_{tot}(f_1) = \frac{\pi}{2} + \phi_{rev}. \tag{4.33}$$

Thus, the entropic potential $[\partial U_{OCV}/\partial T](x_i, T)$ at discrete lithium composition x_i can be written as,

$$\frac{\partial U_{OCV}}{\partial T}(x_i,T) = \left| \frac{\partial U_{OCV}}{\partial T}(x,T) \right| \cos\left(\phi_{rev}\right) = \frac{A_{tot}(f_1)}{I_1 T} \cos\left[\phi_{tot}(f_1) - \frac{\pi}{2}\right]. \tag{4.34}$$

Similarly, FFT can also be applied to the instantaneous heat generation rates $\dot{Q}_{MA}(t)$ measured at the intercalation compound working electrode and $\dot{Q}_{Li}(t)$ measured at the metallic lithium counter electrode, both during the same period from $(i-1)t_1$ to it_1. Applying FFT to $\dot{Q}_{MA}(t)$ given by Equation (4.27) yields the amplitude $A_{MA}(f_1)$ of the sinusoidal oscillation at frequency f_1 expressed as,

$$A_{MA}(f_1) = \frac{I_1 T}{e} \left| \frac{\partial s_{MA}}{\partial x}(x,T) \right| \tag{4.35}$$

while the phase angle $\phi_{MA}(f_1)$ is given by,

$$\phi_{MA}(f_1) = \frac{\pi}{2} + \phi_{rev,MA}. \tag{4.36}$$

Then, the partial entropy change at the intercalation compound working electrode $[\partial s_{MA}/\partial x](x_i, T)$ at discrete lithium composition x_i can be written as,

$$\frac{\partial s_{MA}}{\partial x}(x_i,T) = \frac{A_{MA}(f_1) e}{I_1 T} \cos\left[\phi_{MA}(f_1) - \frac{\pi}{2}\right]. \tag{4.37}$$

Likewise, applying FFT to $\dot{Q}_{Li}(t)$ given by Equation (4.28) yields the amplitude $A_{Li}(f_1)$ of the sinusoidal oscillation at frequency f_1 expressed as,

$$A_{Li}(f_1) = \frac{I_1 T}{e} \left| \frac{\partial s_{Li}}{\partial x}(x, T) \right| \tag{4.38}$$

while the phase angle $\phi_{Li}(f_1)$ is given by,

$$\phi_{Li}(f_1) = \frac{3\pi}{2} + \phi_{rev,Li}. \tag{4.39}$$

Thus, the partial entropy change at the metallic lithium counter electrode $-[\partial s_{Li}/\partial x](x_i, T)$ at discrete lithium composition x_i can be written as,

$$-\frac{\partial s_{Li}}{\partial x}(x_i, T) = -s^{\circ}_{Li}(T) = \frac{A_{Li}(f_1)e}{I_1 T} \cos\left[\phi_{Li}(f_1) - \frac{\pi}{2}\right]. \tag{4.40}$$

4.3 Materials and methods

4.3.1 Synthesis of PNb_9O_{25} powder

To synthesize the PNb_9O_{25} powder, 0.9 mmol of Nb_2O_5 (Sigma Aldrich, 99.99%) and 0.2 mmol of $NH_4H_2PO_4$ (Sigma Aldrich, 98%) powders were mixed. This mixture was ground with a pestle in an agate mortar for 10 minutes to obtain a homogeneous powder. This powder was transferred into an alumina crucible and placed in a tube furnace with Ar flow at room temperature for 2 hours to get rid of air. The furnace was first heated to 350 °C at 1 °C/minute of ramp rate where it was maintained for 8 hours with Ar flow. Then, the Ar flow was stopped and the furnace was heated to 1000 °C at 5 °C/minute of ramp rate where it was maintained for 24 hours. Finally, this sample was naturally cooled down to room temperature to obtain PNb_9O_{25} powder.

4.3.2 Synthesis of $TiNb_2O_7$ powder

To synthesize the $TiNb_2O_7$ powder, TiO_2 (Sigma Aldrich, 99%) and Nb_2O_5 (Materion, 99.95%) powders were mixed in stoichiometric ratio. This mixture was ground with a pestle in an agate mortar for 30 minutes to obtain a homogeneous powder. Then, 300 mg of this

powder was pressed into a pellet. The latter was placed on a bed of sacrificial powder of the same material in an alumina crucible, which was nestled into a larger alumina crucible filled with 7 g of activated charcoal. This stack was heated in a microwave oven at 1125 W for 8 to 9 minutes. Finally, the insulation was removed and the $TiNb_2O_7$ pellet was left to cool to room temperature.

4.3.3 Electrode fabrication

To fabricate the PNb_9O_{25} or $TiNb_2O_7$ electrodes, the previously synthesized PNb_9O_{25} powder or $TiNb_2O_7$ pellet was mixed with SuperP (TIMCAL) and ground with a pestle in an agate mortar for 10 minutes. To prepare the PNb_9O_{25} or $TiNb_2O_7$ slurry, polyvinylidene fluoride (PVDF) was first dissolved in N-Methyl-2-pyrrolidone (NMP). The PNb_9O_{25}/SuperP or $TiNb_2O_7$/SuperP mixture was then added to the PVDF/NMP solution. The resulting slurry had a PNb_9O_{25} or $TiNb_2O_7$:SuperP:PVDF mass ratio of 7.5:1.5:1. Finally, the slurry was cast on a large copper foil using a doctor blade adjusted to the desired gap. The electrodes were first dried on a 40 °C hot plate overnight and then dried in a 110 °C vacuum oven for 6 hours. The thickness of the PNb_9O_{25} electrodes was around 40 μm and their PNb_9O_{25} mass loading was around 2 mg/cm^2. For the $TiNb_2O_7$ electrodes, the thickness was around 20 μm and the $TiNb_2O_7$ mass loading was around 1 mg/cm^2. Note that X-ray diffraction spectra, cyclic voltammetry, and galvanostatic cycling measurements of similar cells with PNb_9O_{25} or $TiNb_2O_7$ electrodes made using the same material synthesis and electrode fabrication methods can be found in our previous studies [1, 59].

4.3.4 *Operando* isothermal calorimeter

Microcalorimetry ETIS measurements were performed in an *operando* isothermal calorimeter described in Ref. [69]. Here, the two-electrode calorimetric battery cells consisted of (i) a PNb_9O_{25} or $TiNb_2O_7$ working electrode previously fabricated and cut into 1 cm × 1 cm square shape, (ii) a polished metallic lithium (Sigma Aldrich, 99.9%) counter electrode also cut into 1 cm × 1 cm square shape, (iii) two 260 μm thick glass microfiber filters (Whatman,

Grade GF/C) acting as both separators and thermal insulators, impregnated with (iv) 1 M $LiPF_6$ in EC:DMC 1:1 v/v (Sigma Aldrich, battery grade) electrolyte. Note that the two-electrode calorimetric battery cells were assembled in a glove box containing Ar gas with less than 0.1 ppm of O_2 and H_2O.

During microcalorimetry ETIS measurements, the current was imposed and the potential was measured using a high accuracy potentiostat (BioLogic, SP-150). Simultaneously, the instantaneous heat generation rates $\dot{Q}_i(t)$ (in mW) at the PNb_9O_{25} or $TiNb_2O_7$ working electrode and at the metallic lithium counter electrode were calculated from the instantaneous heat fluxes $q''_i(t)$ (in mW/cm^2) measured by a 1 cm $\times$ 1 cm thermoelectric heat flux sensor (greenTEG, gSKIN-XP) in thermal contact with the back of each electrode "i" according to [69],

$$\dot{Q}_i(t) = q''_i(t)A_i = \frac{\Delta V_i(t)}{S_i}A_i \quad \text{with } i = MA \text{ or } Li. \tag{4.41}$$

Here, A_i (in cm^2) is the footprint area of the electrode and $\Delta V_i(t)$ (in μV) is the instantaneous voltage difference measured by the heat flux sensor with sensitivity S_i [in μV/(W/cm^2)]. Then, the total instantaneous heat generation rate in the battery cell $\dot{Q}_T(t)$ can be expressed as the sum of those at each electrode, i.e.,

$$\dot{Q}_T(t) = \dot{Q}_{MA}(t) + \dot{Q}_{Li}(t). \tag{4.42}$$

4.4 Results and discussion

4.4.1 Numerical simulations of microcalorimetry ETIS

To evaluate the data analysis procedure previously described, numerical simulations of the novel microcalorimetry ETIS method were performed. The open-circuit voltage $U_{OCV}(x,T)$ and the entropic potential $[\partial U_{OCV}/\partial T](x,T)$ of a PNb_9O_{25} battery cell as functions of lithium composition x previously obtained experimentally from GITT measurements [1] were used as input parameters. In addition, the following parameters were imposed: (i) the ambient temperature was T = 293.15 K, (ii) the electrochemical impedance of the battery cell was defined as $|Z(f_1)|$ = 100 Ω and $\phi_Z(f_1)$ = -π/6, and (iii) the data acquisition period was Δt =

0.1 s. The offset (I_0 = -0.05, -0.1, or -0.2 mA), amplitude (I_1 = 0.5, 1, or 2 mA), and frequency (f_1 = 25, 50, or 100 mHz) of the imposed current $I(t)$ calculated according to Equation (4.17) were realistic values typical of experimental measurements. Based on the imposed current $I(t)$, the corresponding lithium composition x at time t was calculated according to Equation (4.18). If x fell between any two nearest compositions x_1 and x_2 available from the GITT dataset, then the value of $U_{OCV}(x,T)$ was interpolated linearly between $U_{OCV}(x_1,T)$ and $U_{OCV}(x_2,T)$. Then, the potential response $V(t)$ was calculated according to Equation (4.19). Likewise, the value of $[\partial U_{OCV}/\partial T](x,T)$ was also interpolated between $[\partial U_{OCV}/\partial T](x_1,T)$ and $[\partial U_{OCV}/\partial T](x_2,T)$ given by GITT. Then, the irreversible $\dot{Q}_J(t)$ and reversible $\dot{Q}_{rev}(t)$ heat generation rates were calculated according to Equations (4.23) and (4.25), respectively. The sum gave the total instantaneous heat generation rate $\dot{Q}_T(t)$ such that $\dot{Q}_T(t) = \dot{Q}_J(t) + \dot{Q}_{rev}(t)$. Note that, in the present microcalorimetry ETIS method, the battery cell is assumed to be operating at low C-rates, such that the heat generation rates $\dot{Q}_{mix}(t)$ associated with the enthalpy of mixing and $\dot{Q}_{sr}(t)$ due to side reactions both become negligible. Moreover, to reproduce actual experimental measurements, white noise was added to the calculated $\dot{Q}_T(t)$ with signal-to-noise ratio equal to ∞, 10, or 5. By applying FFT to the calculated heat generation rate $\dot{Q}_T(t)$ with white noise, $[\partial U_{OCV}/\partial T](x,T)$ was determined according to Equation (4.34).

Figure 4.3 plots the entropic potential $[\partial U_{OCV}/\partial T](x,T)$ of a PNb_9O_{25} battery cell retrieved from numerical simulations of microcalorimetry ETIS after applying FFT to the calculated $\dot{Q}_T(t)$ with white noise for different values of (a) current offset I_0, (b) current amplitude I_1, (c) current frequency f_1, and (d) signal-to-noise ratio (SNR). The baseline case corresponds to T = 293.15 K, I_0 = -0.1 mA, I_1 = 1 mA, f_1 = 50 mHz, and SNR = ∞. Figure 4.3 also compares the retrieved entropic potential $[\partial U_{OCV}/\partial T](x,T)$ with the input parameters previously obtained experimentally with GITT at 20 °C [1]. Here, it is interesting to note that the choice of I_0 had a strong impact on the retrieved $[\partial U_{OCV}/\partial T](x,T)$ while the influence of I_1 and f_1 was less visible. In fact, the deviation of the retrieved $[\partial U_{OCV}/\partial T](x,T)$ relative to that obtained from GITT was reduced by minimizing I_0. Nevertheless, in every case the $[\partial U_{OCV}/\partial T](x,T)$ retrieved from simulations accurately reflected the evolution of

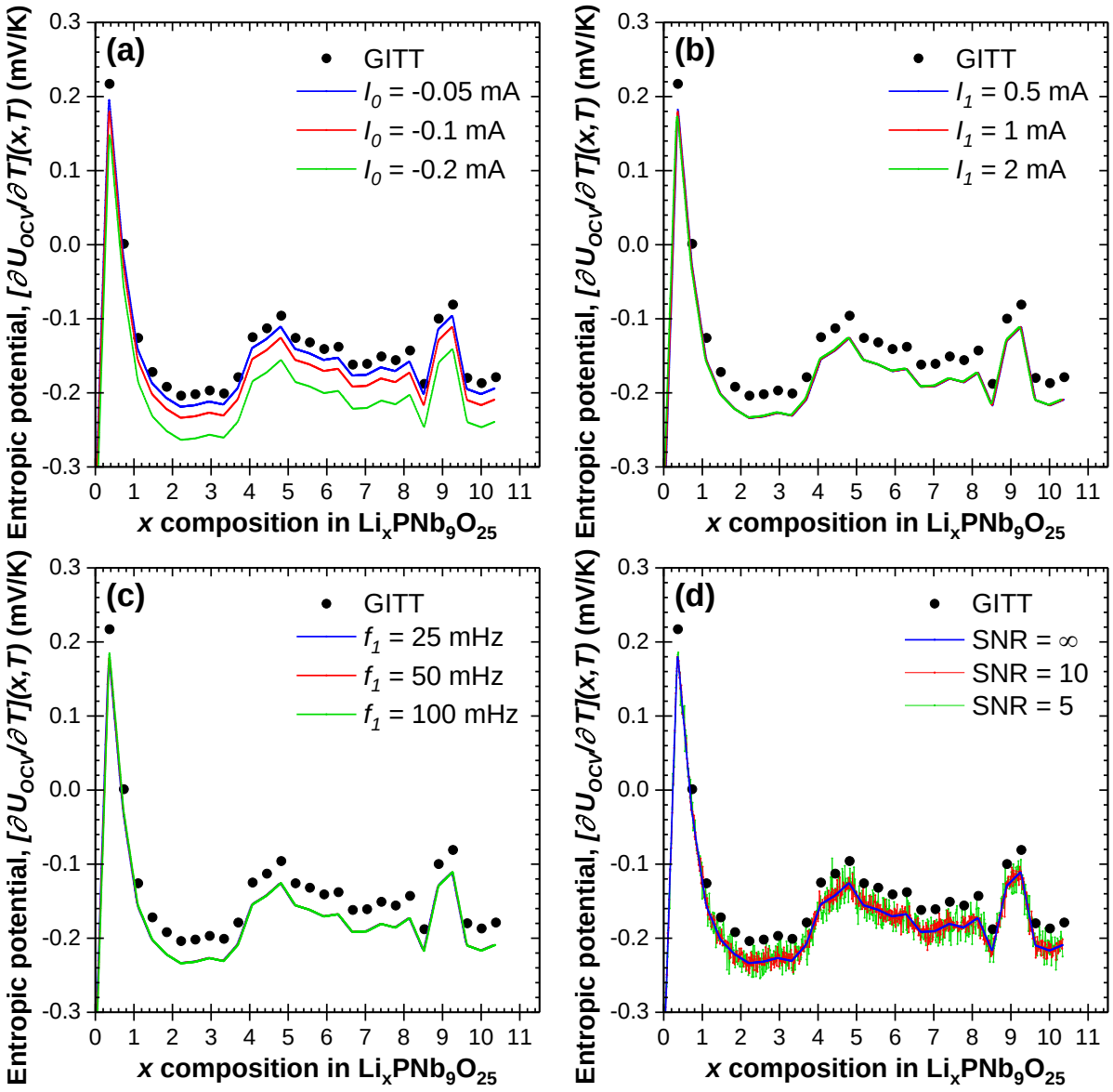

Figure 4.3: Entropic potential $[\partial U_{OCV}/\partial T](x,T)$ of a PNb_9O_{25} battery cell retrieved from numerical simulations of microcalorimetry ETIS for different values of (a) current offset I_0, (b) current amplitude I_1, (c) current frequency f_1, and (d) signal-to-noise ratio (SNR), with comparison to the $[\partial U_{OCV}/\partial T](x,T)$ obtained experimentally from GITT [1] and used as input. Unless otherwise noted, T = 293.15 K, I_0 = -0.1 mA, I_1 = 1 mA, f_1 = 50 mHz, and SNR = ∞.

$[\partial U_{OCV}/\partial T](x,T)$ imposed and obtained experimentally from GITT. Finally, Figure 4.3(d) illustrates that even with a signal-to-noise ratio of 10 the evolution of $[\partial U_{OCV}/\partial T](x,T)$ can be successfully retrieved.

Furthermore, the profile of $[\partial U_{OCV}/\partial T](x,T)$ with respect to x is generally more informative than its magnitude. In fact, the former was sufficient in creating the interpretation guide of different charging mechanisms from our previous study [53]. Therefore, the retrieved entropic potential $[\partial U_{OCV}/\partial T](x,T)$ can be normalized according to,

$$\left[\frac{\partial U_{OCV}}{\partial T}\right]^{*}(x,T) = \frac{[\partial U_{OCV}/\partial T](x,T) - [\partial U_{OCV}/\partial T]_{min}(x,T)}{[\partial U_{OCV}/\partial T]_{max}(x,T) - [\partial U_{OCV}/\partial T]_{min}(x,T)} \tag{4.43}$$

where $[\partial U_{OCV}/\partial T]_{max}(x,T)$ and $[\partial U_{OCV}/\partial T]_{min}(x,T)$ are respectively the maximum and minimum values of the entropic potential over the entire window of lithium composition. Figure 4.4 plots the normalized entropic potential $[\partial U_{OCV}/\partial T]^{*}(x,T)$ for the same cases as those presented in Figure 4.3. First, in every case the relative difference between the normalized entropic potential $[\partial U_{OCV}/\partial T]^{*}(x,T)$ retrieved from simulations and that obtained experimentally from GITT (Figure 4.4) was smaller than the difference between their original values (Figure 4.3). This illustrates the fact that normalization can alleviate the impact of the arbitrary choice of I_0 while accurately retrieving the features of $[\partial U_{OCV}/\partial T]^{*}(x,T)$ necessary for its interpretation. In addition, the results can be further improved by minimizing I_1 and maximizing f_1. These observations can inform the experimental implementation of the present microcalorimetry ETIS method.

4.4.2 Microcalorimetry ETIS measurements on a battery cell

4.4.2.1 Imposed current and potential response

To validate experimentally the novel microcalorimetry ETIS method, measurements using *operando* isothermal calorimetry were performed on battery cells at temperature $T = 293.15$ K. Here, the full cell was assembled in the *operando* isothermal calorimeter previously described with a PNb_9O_{25} or $TiNb_2O_7$ working electrode and a metallic lithium counter electrode immersed in 1 M $LiPF_6$ in EC:DMC 1:1 v/v electrolyte. The experimentally imposed

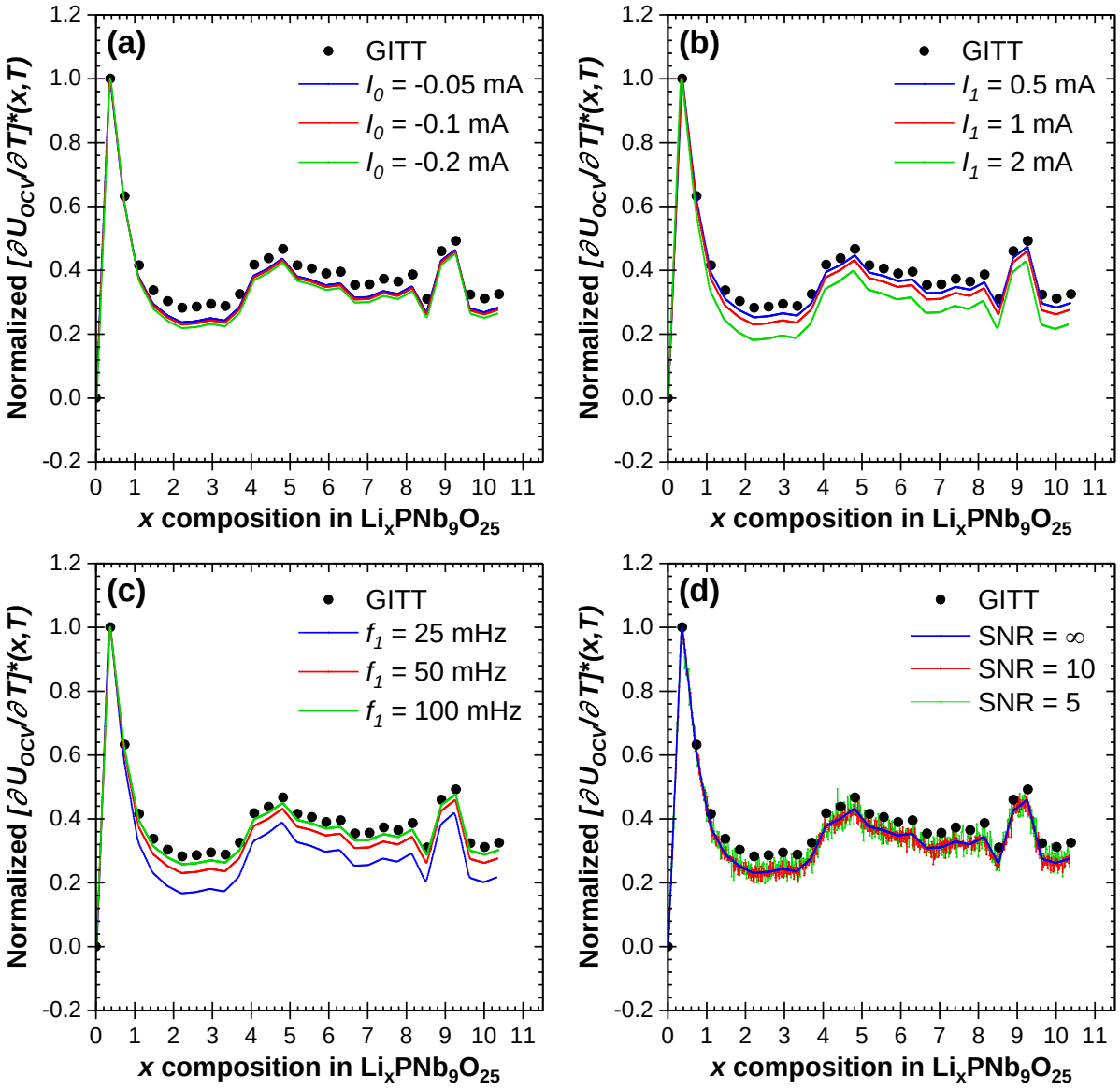

Figure 4.4: Normalized entropic potential $[\partial U_{OCV}/\partial T]^*(x,T)$ of the results shown in Figure 4.3 for a PNb_9O_{25} battery cell retrieved from numerical simulations of microcalorimetry ETIS for different values of (a) current offset I_0, (b) current amplitude I_1, (c) current frequency f_1, and (d) signal-to-noise ratio (SNR), with comparison to the normalized entropic potential $[\partial U_{OCV}/\partial T]^*(x,T)$ obtained experimentally from GITT [1] and used as input.

current $I(t)$ during discharging (lithiation) featured offset I_0 = -0.1 mA, amplitude I_1 = 1 mA, frequency f_1 = 50 mHz, and period t_1 = 20 s. Note that these settings were chosen as a compromise between (i) superior accuracy of results calling for small I_0, small I_1, and large f_1, and (ii) the constraints of actual experimental conditions favoring large I_0 for shorter measurement duration, large I_1 for adequate heat generation rate signal, and small f_1 to give redox reactions sufficient time to proceed.

Figure 4.5 plots the measured potential $V(t)$ and the retrieved open-circuit voltage $U_{OCV}(x,T)$ determined using Equation (4.20) as the average of $V(t)$ over every period. As predicted by Equation (4.19), the sinusoidal oscillation of $V(t)$ was at the same frequency f_1 as $I(t)$. The overall duration for this discharging half-cycle was 5 hours for the PNb_9O_{25} battery cell and 3 hours for the $TiNb_2O_7$ battery cell, compared to 150 hours and 90 hours, respectively, for potentiometric entropy measurements based on GITT [1].

4.4.2.2 Heat generation rates

Figure 4.6 plots the instantaneous heat generation rates (a) $\dot{Q}_{PNO}(t)$ measured at the PNb_9O_{25} working electrode or (b) $\dot{Q}_{TNO}(t)$ measured at the $TiNb_2O_7$ working electrode, as well as $\dot{Q}_{Li}(t)$ measured at the corresponding metallic lithium counter electrode, and (c) $\dot{Q}_T(t) = \dot{Q}_{PNO}(t) + \dot{Q}_{Li}(t)$ or (d) $\dot{Q}_T(t) = \dot{Q}_{TNO}(t) + \dot{Q}_{Li}(t)$ measured in the entire battery cell over four consecutive periods. Interestingly, $\dot{Q}_{PNO}(t)$, $\dot{Q}_{TNO}(t)$, and $\dot{Q}_{Li}(t)$ were all sinusoidal functions with the same frequency f_1 as $I(t)$ and $V(t)$. As a result, $\dot{Q}_T(t)$ was periodic with complex patterns and period $t_1 = 1/f_1$ = 20 s. Moreover, $\dot{Q}_{PNO}(t)$ or $\dot{Q}_{TNO}(t)$ was endothermic (< 0) for negative current $I(t)$ and exothermic (> 0) for positive $I(t)$, whereas $\dot{Q}_{Li}(t)$ was exothermic for negative $I(t)$ and endothermic for positive $I(t)$. In fact, according to Equations (4.27) and (4.28), such behavior indicates that the partial entropy changes were positive at the PNb_9O_{25} or $TiNb_2O_7$ working electrodes and negative at the corresponding metallic lithium counter electrodes. These results were consistent with the observations made in our previous study [1]. Finally, even though state-of-the-art potentiostat and heat flux sensors were used, Figure 4.6 illustrates that with I_1 = 1 mA and f_1 = 50

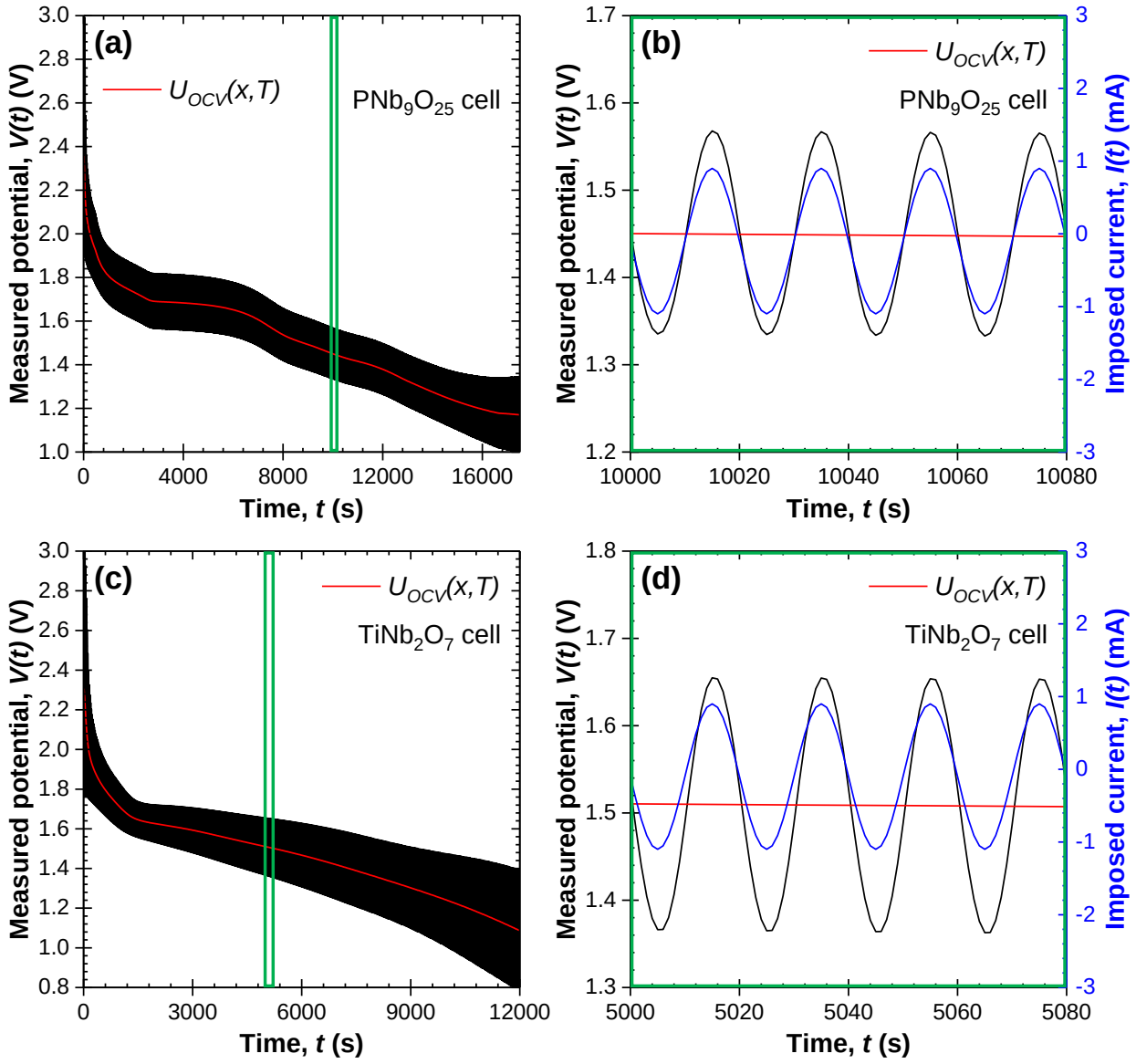

Figure 4.5: Measured potential $V(t)$ during discharging and retrieved open-circuit voltage $U_{OCV}(x,T)$ determined using Equation (4.20) as the average of $V(t)$ over every period during microcalorimetry ETIS measurements on a (a, b) PNb_9O_{25} or (c, d) $TiNb_2O_7$ battery cell. The imposed current $I(t)$ was given by Equation (4.17) with I_0 = -0.1 mA, I_1 = 1 mA, and f_1 = 50 mHz. Note that Figures 4.5(b) and 4.5(d) are enlargements of arbitrary time windows shown in green in Figures 4.5(a) and 4.5(c), respectively.

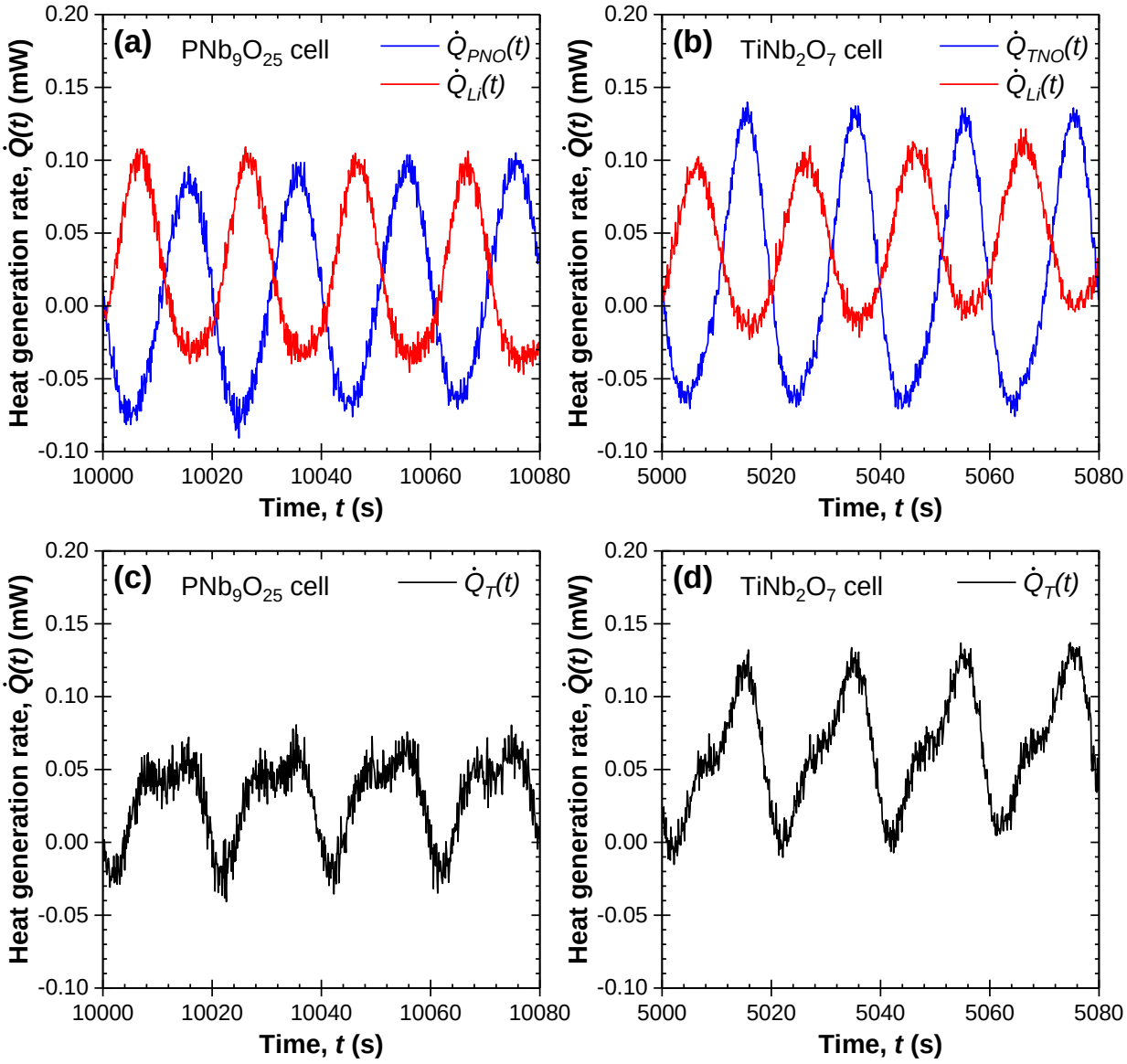

Figure 4.6: (a, b) Instantaneous heat generation rates (a) $\dot{Q}_{PNO}(t)$ measured at the PNb_9O_{25} working electrode or (b) $\dot{Q}_{TNO}(t)$ measured at the $TiNb_2O_7$ working electrode and $\dot{Q}_{Li}(t)$ measured at the corresponding metallic lithium counter electrode over four consecutive periods. (c, d) Total instantaneous heat generation rate (c) $\dot{Q}_T(t) = \dot{Q}_{PNO}(t) + \dot{Q}_{Li}(t)$ or (d) $\dot{Q}_T(t) = \dot{Q}_{TNO}(t) + \dot{Q}_{Li}(t)$ measured in the entire (c) PNb_9O_{25} or (d) $TiNb_2O_7$ battery cell.

mHz, the signal-to-noise ratio in the measured heat generation rates was already around 10. Based on the numerical simulation results shown in Figure 4.3(d), a signal-to-noise ratio of at least 10 was necessary to successfully retrieve the evolution of $[\partial U_{OCV}/\partial T](x,T)$. Further decreasing I_1 and/or increasing f_1 would decrease the magnitude of the heat generation rates and, consequently, the signal-to-noise ratio would fall below 10 which would compromise the precision of the retrieved $[\partial U_{OCV}/\partial T](x,T)$.

4.4.2.3 Open-circuit voltage and entropic potential

After applying FFT to the total heat generation rate $\dot{Q}_T(t)$ in each battery cell, the entropic potential $[\partial U_{OCV}/\partial T](x,T)$ was determined according to Equation (4.34). The entropic potential was then normalized to compute $[\partial U_{OCV}/\partial T]^*(x,T)$ according to Equation (4.43). Figure 4.7 compares the open-circuit voltage $U_{OCV}(x,T)$ and the normalized entropic potential $[\partial U_{OCV}/\partial T]^*(x,T)$ of the investigated (a, b) PNb_9O_{25} or (c, d) $TiNb_2O_7$ battery cell determined by GITT [1] and by microcalorimetry ETIS measurements. Here, $U_{OCV}(x,T)$ and $[\partial U_{OCV}/\partial T]^*(x,T)$ determined by both methods were in very good agreement for both battery cells. In fact, while GITT only offered a limited number of data points, hundreds of data points were acquired from microcalorimetry ETIS which created continuous curves for $U_{OCV}(x,T)$ and $[\partial U_{OCV}/\partial T]^*(x,T)$. This is particularly noticeable for the PNb_9O_{25} cell for $0 < x < 0.5$ and for the $TiNb_2O_7$ cell for $3.2 < x < 4.3$, when sharp changes in $[\partial U_{OCV}/\partial T]^*(x,T)$ occurred but were not captured by the GITT method. In addition, combining the profiles of both $U_{OCV}(x,T)$ and $[\partial U_{OCV}/\partial T]^*(x,T)$ enables the identification of different regions with distinctive features [1].

For the PNb_9O_{25} battery cell, seven regions could be identified [53]. (i) Region I for $0 < x < 0.5$: U_{OCV} decreased sharply as a result of lithium intercalation in a homogeneous solid solution [1]. By contrast, $[\partial U_{OCV}/\partial T]^*$ featured a sharp peak and a maximum. This can be attributed to the fact that PNb_9O_{25} is an insulator in pristine phase but quickly becomes a semiconductor upon lithiation [176, 177]. As the electrical conductivity increases, so does the electronic entropy, which in turn led to an increase in $[\partial U_{OCV}/\partial T]^*$ [1]. Note

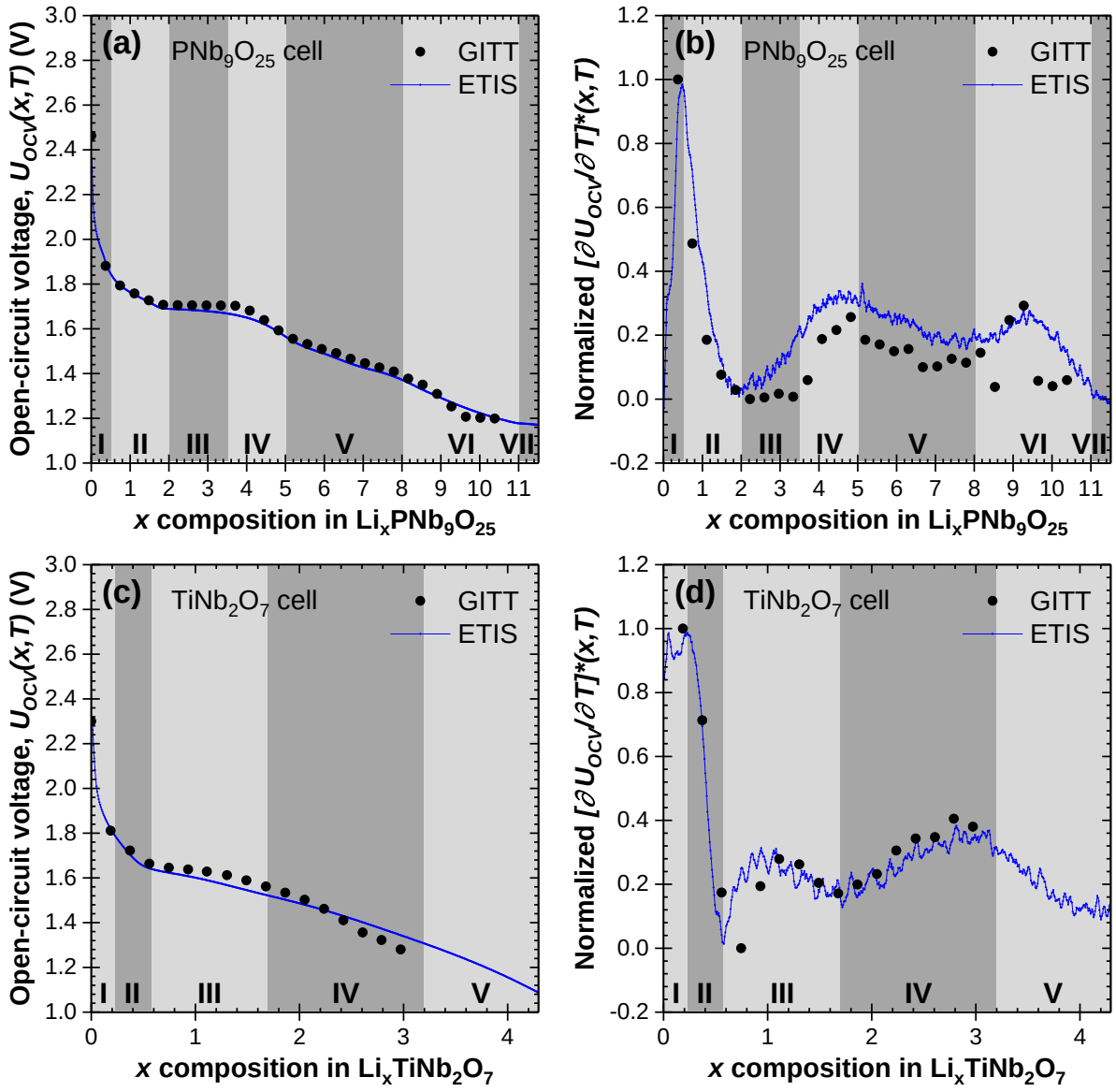

Figure 4.7: (a, c) Open-circuit voltage $U_{OCV}(x,T)$ and (b, d) normalized entropic potential $[\partial U_{OCV}/\partial T]^*(x,T)$ of a PNb_9O_{25} or $TiNb_2O_7$ battery cell determined by GITT [1] or microcalorimetry ETIS measurements. The different colored regions correspond to specific phenomena occurring in the battery cell.

that this was not captured by previous GITT measurements. (ii) Region II for $0.5 < x < 2$: both U_{OCV} and $[\partial U_{OCV}/\partial T]^*$ decreased indicating lithium intercalation in a homogeneous solid solution and the associated configurational entropy change [53]. (iii) Region III for $2 < x < 3.5$: U_{OCV} plateaued as a sign of phase transition accompanied by two-phase coexistence [53]. Curiously, $[\partial U_{OCV}/\partial T]^*$ retrieved from microcalorimetry ETIS increased as opposed to staying relatively constant in GITT measurements. Note that PNb_9O_{25} has also been reported to undergo a semiconductor-to-metal transition around this range of lithium composition [176, 177]. It is possible that microcalorimetry ETIS could not capture the plateau in $[\partial U_{OCV}/\partial T]^*$ associated with two-phase coexistence as effectively as GITT. In fact, phase transition is a kinetically slow process, which is captured by the long relaxation periods of GITT but not by microcalorimetry ETIS due to the constant switching between lithiation/delithiation half-periods arising from the sinusoidal current $I(t)$. (iv) Region IV for $3.5 < x < 5$: U_{OCV} decreased again suggesting lithium intercalation in a homogeneous solid solution [53]. Moreover, $[\partial U_{OCV}/\partial T]^*$ first increased then decreased resulting in a local maximum, during which the semiconductor-to-metal transition was completed [1]. (v) Region V for $5 < x < 8$: this region also featured lithium intercalation in a homogeneous solid solution as both U_{OCV} and $[\partial U_{OCV}/\partial T]^*$ decreased monotonously [53]. (vi) Region VI for $8 < x < 11$: the decrease in U_{OCV} was accompanied by a tilde-shaped fluctuation in $[\partial U_{OCV}/\partial T]^*$, which can be attributed to intralayer ion ordering [53]. It is interesting to note that the intralayer ion ordering spanned a wider range of lithium composition when measured by microcalorimetry ETIS than by GITT. Likewise, this difference possibly emerged as a result of the constant switching between lithiation/delithiation half-periods during microcalorimetry ETIS measurements, which might have prolonged the ion ordering process. (vii) Region VII for $11 < x < 11.5$: both U_{OCV} and $[\partial U_{OCV}/\partial T]^*$ featured a plateau indicative of phase transition accompanied by two-phase coexistence.

In the case of the $TiNb_2O_7$ battery cell, five regions could be identified [59]. (i) Region I for $0 < x < 0.2$: U_{OCV} featured a sharp drop indicating lithium intercalation in a homogeneous solid solution [53]. By contrast, $[\partial U_{OCV}/\partial T]^*$ rose to reach a maximum. This can also be attributed to the rapid electrical conductivity increase of $TiNb_2O_7$ upon lithi-

ation [59, 178]. (ii) Region II for $0.2 < x < 0.6$: both U_{OCV} and $[\partial U_{OCV}/\partial T]^*$ decreased due to lithium intercalation in a homogeneous solid solution [53]. The configurational entropy change contributed to the sharp decrease in $[\partial U_{OCV}/\partial T]^*$ [53]. (iii) Region III for $0.6 < x < 1.7$: U_{OCV} decreased slowly while $[\partial U_{OCV}/\partial T]^*$ featured a tilde-shaped fluctuation characteristic of intralayer ion ordering [53]. (iv) Region IV for $1.7 < x < 3.2$: U_{OCV} continued decreasing while $[\partial U_{OCV}/\partial T]^*$ first increased then decreased resulting in a local maximum. This behavior can be attributed to the continuous electrical conductivity increase of $TiNb_2O_7$ during lithiation [59,178]. Here also, the electronic entropy increased like the semiconductor-to-metal transition observed within region IV of the PNb_9O_{25} cell, thus leading to an analogous shape of the entropic potential. (v) Region V for $3.2 < x < 4.3$: both U_{OCV} and $[\partial U_{OCV}/\partial T]^*$ decreased monotonously corresponding to lithium intercalation in a homogeneous solid solution [53]. Note that this last region was observed only in the microcalorimetry ETIS method. In fact, our previous GITT measurements [1, 59] imposed a cell potential cutoff of 1 V to prevent the formation of solid electrolyte interphase (SEI) and dendrites in the battery cell under continuous discharging below 1 V [179, 180]. During microcalorimetry ETIS measurements though, the sinusoidal current $I(t)$ meant that whenever the cell potential went below 1 V, it only lasted a few seconds before the direction of current flow and ion diffusion was reversed again. This enabled the cell potential cutoff to be lower than 1 V without significantly damaging the battery cell. In particular, the potential of the $TiNb_2O_7$ cell was allowed to reach as low as 0.8 V during microcalorimetry ETIS measurements.

4.4.2.4 Partial entropy changes

FFT analysis was also applied to the heat generation rates $\dot{Q}_{PNO}(t)$ or $\dot{Q}_{TNO}(t)$ and $\dot{Q}_{Li}(t)$ measured at each electrode to determine the partial entropy changes at the PNb_9O_{25} or $TiNb_2O_7$ working electrodes and at the corresponding metallic lithium counter electrodes according to Equations (4.37) and (4.40). Here also, the partial entropy changes were nor-

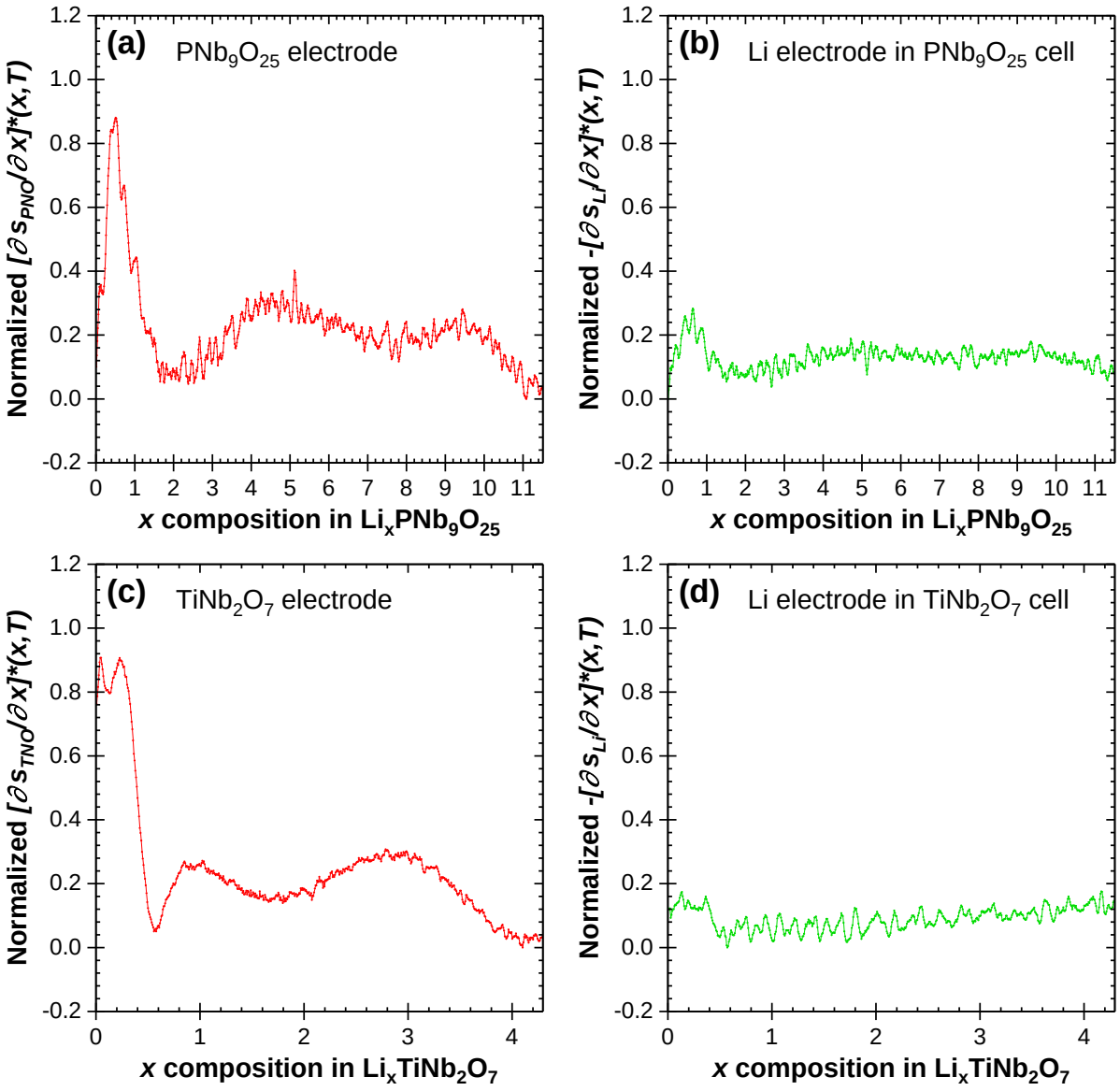

Figure 4.8: Normalized partial entropy changes (a) $[\partial s_{PNO}/\partial x]^*(x,T)$ at the PNb_9O_{25} working electrode or (c) $[\partial s_{TNO}/\partial x]^*(x,T)$ at the $TiNb_2O_7$ working electrode determined by microcalorimetry ETIS measurements. (b, d) Normalized partial entropy changes $-[\partial s_{Li}/\partial x]^*(x,T)$ at the corresponding metallic lithium counter electrode.

malized, i.e., at electrode "j" ($= PNO$, TNO, or Li) according to,

$$\left[\frac{\partial s_j}{\partial x}\right]^*(x,T) = \frac{(1/e)[\partial s_j/\partial x](x,T) - (1/e)[\partial s_j/\partial x]_{min}(x,T)}{[\partial U_{OCV}/\partial T]_{max}(x,T) - [\partial U_{OCV}/\partial T]_{min}(x,T)} \tag{4.44}$$

where $[\partial s_j/\partial x]_{min}(x,T)$ is the minimum value of the partial entropy change $[\partial s_j/\partial x](x,T)$ over the entire window of lithium composition. For comparison, Figure 4.8 plots the normalized partial entropy changes $[\partial s_j/\partial x]^*(x,T)$ at the PNb_9O_{25} or $TiNb_2O_7$ working electrodes and at the corresponding metallic lithium counter electrodes. Here, the normalized partial entropy changes $[\partial s_{PNO}/\partial x]^*(x,T)$ or $[\partial s_{TNO}/\partial x]^*(x,T)$ at the working electrodes essentially replicated qualitatively the features of the normalized entropic potential $[\partial U_{OCV}/\partial T]^*(x,T)$ for the full cell. By contrast, the normalized partial entropy changes $-[\partial s_{Li}/\partial x]^*(x,T)$ at the counter electrodes stayed relatively constant near 0 with varying state of charge. Such behavior was consistent with our previous theoretical derivation [53]. Specifically, the partial entropy change $-[\partial s_{Li}/\partial x](x,T)$ at the metallic lithium counter electrode should be equal to the standard entropy per unit of metallic lithium $-s^\circ_{Li}(T)$ and thus independent of x. Therefore, $-[\partial s_{Li}/\partial x]^*(x,T)$ should theoretically be equal to 0, as confirmed by Figure (4.8). This suggests that continuous lithium stripping and plating were the dominant processes occurring at the counter electrodes. Overall, these results demonstrate the capability of the novel microcalorimetry ETIS method to extract the partial entropy changes at each electrode, which has not been achieved by any other existing method.

4.5 Chapter summary

This chapter presented a novel and fast microcalorimetry ETIS measurement method using an *operando* isothermal calorimeter to determine the open-circuit voltage U_{OCV}, the entropic potential $\partial U_{OCV}/\partial T$, and the partial entropy changes at each electrode as functions of the state of charge of a battery cell, all within only a few hours. The apparatus was designed for bare electrodes (i.e., without casing) with material mass loadings on the order of milligrams and measured heat generation rates on the order of microwatts. The method consists of imposing a sinusoidal current and measuring the potential response as well as the heat generation rates at each electrode separately. The open-circuit voltage U_{OCV} of the cell

was acquired by time-averaging the measured potential response. Furthermore, FFT analysis of the measured total heat generation rate was used to retrieve the entropic potential $\partial U_{OCV}/\partial T$ of the entire cell without having to measure the cell potential at several different temperatures. The procedure was first validated numerically and then demonstrated experimentally with battery cells consisting of PNb_9O_{25} or $TiNb_2O_7$ working electrodes and metallic lithium counter electrodes. The open-circuit voltage and the normalized entropic potential retrieved from the novel microcalorimetry ETIS measurements agreed well with those previously determined by potentiometric entropy measurements based on GITT at three different temperatures [1, 59]. Finally, the partial entropy changes at each electrode were calculated from the individually measured heat generation rates. Compared to other state-of-the-art methods, this is the first method capable of retrieving the entropy evolution of LIB materials at each electrode.

CHAPTER 5

Three-dimensional step potential electrochemical spectroscopy (SPECS) simulations of porous pseudocapacitive electrodes

This chapter aims to numerically validate and, if necessary, modify the step potential electrochemical spectroscopy (SPECS) method for three-dimensional (3D) mesoporous pseudocapacitive electrodes. Numerical simulations were based on the modified Poisson-Nernst-Planck (MPNP) model coupled with the Frumkin-Butler-Volmer theory. In addition, the SPECS method was combined with the multiple potential step chronoamperometry (MUSCA) method to identify the contributions of EDL formation and Faradaic reactions to the total current density and to provide physical interpretation of the fitting parameters.

Nomenclature

A	Surface area (nm^2)
A_{BET}	Total electrode/electrolyte interfacial area (nm^2)
$A_{BET,1}$	Geometric surface area of the electrode/electrolyte interface (nm^2)
$A_{BET,2}$	Porous surface area of the electrode/electrolyte interface (nm^2)
A_{fp}	Footprint surface area (nm^2)
a_i	Effective ion diameter of species i (nm)
C_1	Geometric surface electrical double layer capacitance (μF cm^{-2})
C_2	Porous surface electrical double layer capacitance (μF cm^{-2})
C_{diff}	Differential capacitance (μF cm^{-2})
C_{int}	Integral capacitance (μF cm^{-2})
C_s^{St}	Stern layer capacitance (μF cm^{-2})
C_{EDL}	Total electrical double layer capacitance (μF cm^{-2})
$c_{1,P}$	Concentration of Li^+ ions in the electrode (mol L^{-1})
$c_{1,P,0}$	Initial concentration of Li^+ ions in the electrode (mol L^{-1})
$c_{1,P,max}$	Maximum concentration of Li^+ ions in the electrode (mol L^{-1})
c_i	Concentration of ion species i in the electrolyte (mol L^{-1})
c_∞	Ion concentration in the bulk electrolyte (mol L^{-1})
$D_{1,P}$	Diffusion coefficient of Li^+ ions in the electrode (m^2 s^{-1})
D_i	Diffusion coefficient of ion species i in the electrolyte (m^2 s^{-1})
e	Elementary charge, $e = 1.602 \times 10^{-19}$ C
F	Faraday constant, $F = eN_A = 9.648 \times 10^4$ C mol^{-1}
H	Stern layer thickness (nm)
j	Magnitude of current density (A m^{-2})
$j_{F,0}$	Exchange current density due to Faradaic reactions (A m^{-2})
k_0	Reaction rate constant ($m^{2.5}$ $mol^{-0.5}$ s^{-1})
k_B	Boltzmann constant, $k_B = 1.38 \times 10^{-23}$ m^2 kg s^{-2} K^{-1}
L	Electrolyte domain thickness (nm)

L_C	Current collector thickness (nm)
L_P	Electrode thickness (nm)
N	Number of layers of electrode spherical particles
N_A	Avogadro number, $N_A = 6.022 \times 10^{23}$ mol^{-1}
$\mathbf{N}_i$	Molar flux vector of ion species i (mol m^{-2} s^{-1})
N_s	Number of data points per potential step
$\mathbf{n}$	Normal vector of a surface
n_c	Cycle number
n_s	Total number of potential steps
p_s	Potential step number
ΔQ_F	Total amount of charge stored due to the Faradaic current (C)
R_1	Geometric surface electrical double layer resistance (Ω cm^2)
R_2	Porous surface electrical double layer resistance (Ω cm^2)
R_{ct}	Charge transfer resistance (Ω cm^2)
R_d	Diffusion resistance (Ω cm^2)
R_{EDL}	Total electrical double layer resistance (Ω cm^2)
R_u	Universal gas constant, $R_u = 8.314$ J mol^{-1} K^{-1}
r	Radius of electrode spherical particles (nm)
$\mathbf{r}$	Location in three-dimensional space (nm)
$\mathbf{r}_{cl}$	Location of the device centerline (nm)
$\mathbf{r}_{C/E}$	Location of the current collector/electrolyte interface (nm)
$\mathbf{r}_{E/E}$	Location of the electrode/electrolyte interface (nm)
$\mathbf{r}_H$	Location of the Stern/diffuse layer interface (nm)
T	Temperature (K)
t	Time (s)
t_{cd}	Charging/discharging cycle period (s)
t_e	Equilibration time (s)
t_t	Transition time (s)
t_ν	Time window in the MUSCA method (s)

Δt	Time step (data acquisition time) (s)
z_i	Valency of ion species i

Greek symbols

α	Transfer coefficient
δ	Objective function
ϵ_0	Vacuum permittivity, $\epsilon_0 = 8.854 \times 10^{-12}$ F m^{-1}
ϵ_r	Relative permittivity of the electrolyte
η	Overpotential (V)
Λ	Electrochemical Biot number
ν	Scan rate (V s^{-1})
ψ	Electric potential (V)
ψ_s	Potential vs. Ag/AgCl at the current collector/electrode interface (V)
$\psi_{s,min}$, $\psi_{s,max}$	Minimum and maximum of the potential window vs. Ag/AgCl (V)
$\Delta\psi_{eq}$	Equilibrium potential difference vs. Ag/AgCl (V)
$\Delta\psi_{eq,0}$	Initial equilibrium potential difference vs. Ag/AgCl (V)
$\Delta\psi_H$	Potential drop across the Stern layer (V)
$\Delta\psi_s$	Potential step (V)
σ_C	Electrical conductivity of the current collector (S m^{-1})
σ_P	Electrical conductivity of the electrode (S m^{-1})
τ	Time constant (s)
τ_d	Diffusion time constant (s)

Superscripts and subscripts

BET	Refers to the electrode/electrolyte interface
EDL	Refers to the electrical double layer component
$EDL1$	Refers to the geometric surface electrical double layer component
$EDL2$	Refers to the porous surface electrical double layer component
F	Refers to the Faradaic component
$F1$	Refers to the surface-controlled Faradaic component
$F2$	Refers to the diffusion-controlled Faradaic component

fp	Refers to the footprint surface
M	Refers to the MUSCA method
n	Refers to the normal component of a variable
r	Refers to the residual component
S	Refers to the SPECS method
T	Refers to the total component

5.1 Background

5.1.1 SPECS method

Chronoamperometry is a family of techniques where a step function is applied to the potential of the working electrode as the current response is recorded. The current response to each potential step is typically a decay as a function of time and can be analyzed to distinguish the various charge storage mechanisms of the working electrode [41]. The most common example is the double potential step chronoamperometry where the imposed potential consists of a single step up and step down in sequence [41]. Multiple variants of chronoamperometry have also been developed over time, such as the double potential step chronocoulometry. In this case, instead of the current response, the integral of the current versus time is recorded corresponding to the amount of charge passed. Here, the response in the charge passage can equally be analyzed to separate the contributions of EDL formation and Faradaic reactions to the total amount of charge storage [41]. One latest adaptation of chronoamperometry is the SPECS method. The SPECS method consists of imposing a series of small potential steps $\Delta\psi_s$ on a pseudocapacitor within a potential window from $\psi_{s,min}$ to $\psi_{s,max}$ and measuring the total footprint current density response $j_T(t)$ (in $\mathrm{A/m^2}$) at each potential step defined per unit footprint surface area A_{fp} of the current collector [110–112]. This method has been developed to identify the contributions of EDL formation and Faradaic reactions to the total current in pseudocapacitive electrodes [113–115]. Dupont and Donne [113–115] suggested that the total current density response to an imposed potential step in a porous pseudocapacitive electrode should be fitted to a function $j_T^S(t)$ expressed as the sum of an EDL current density $j_{EDL}^S(t)$, a Faradaic current density $j_F^S(t)$, and a residual current density $j_r^S(t)$, i.e.,

$$j_T^S(t) = j_{EDL}^S(t) + j_F^S(t) + j_r^S(t). \tag{5.1}$$

The EDL current density $j_{EDL}^S(t)$ was further divided into two contributions from EDL formation (i) at the so-called geometric surface defined as the interface of the electrode with the bulk electrolyte and (ii) at the interfacial surface of micropores and mesopores

within the porous electrode, represented by $j^S_{EDL1}(t)$ and $j^S_{EDL2}(t)$, respectively [113–115]. Here, $j^S_{EDL1}(t)$ and $j^S_{EDL2}(t)$ were modeled based on an equivalent circuit of a resistor and a capacitor in series so that [113–115],

$$j^S_{EDL}(t) = j^S_{EDL1}(t) + j^S_{EDL2}(t) = \frac{\Delta\psi_s}{R_1}\exp\left(-\frac{t}{R_1C_1}\right) + \frac{\Delta\psi_s}{R_2}\exp\left(-\frac{t}{R_2C_2}\right) \tag{5.2}$$

where R_1, C_1 and R_2, C_2 are the resistances and capacitances due to EDL formation at the geometric surface denoted by $A_{BET,1}$ and at the inner porous electrode/electrolyte interface denoted by $A_{BET,2}$ (see Figure 5.1 for illustration). Furthermore, the total EDL resistance R_{EDL} and the total EDL capacitance C_{EDL} were expressed as [113–115],

$$R_{EDL} = \frac{R_1R_2}{R_1+R_2} \quad \text{and} \quad C_{EDL} = C_1 + C_2. \tag{5.3}$$

On the other hand, the Faradaic current density $j^S_F(t)$ was modeled based on Fick's second law of diffusion in spherical coordinates as [113–115],

$$j^S_F(t) = \frac{6\Delta Q_F}{\tau_d A}\sum_{n=1}^{\infty}\exp\left(-\frac{n^2\pi^2 t}{\tau_d}\right). \tag{5.4}$$

Here, A is the surface area over which the current density is averaged (i.e., either the footprint surface area A_{fp} of the current collector or the total electrode/electrolyte interfacial area A_{BET}), while ΔQ_F and τ_d are the total amount of charge stored due to the Faradaic reactions and the diffusion time constant respectively expressed as [181, 182],

$$\Delta Q_F = \int_t^{t+\Delta t} j^S_F(t)A\mathrm{d}t = -\frac{FA_{BET}r\Delta c_{1,P}}{3} \quad \text{and} \quad \tau_d = \frac{r^2}{D_{1,P}} \tag{5.5}$$

where $F = eN_A = 9.648 \times 10^4$ C mol^{-1} is the Faraday constant, r is the average radius of redox-active spherical particles making up the electrode, $\Delta c_{1,P}$ is the net concentration change of cations in the electrode due to the potential step, and $D_{1,P}$ is the diffusion coefficient of cations in the redox-active materials. After a sufficiently long relaxation duration (i.e., $t \gg \tau_d$), the high order terms ($n > 1$) in Equation (5.4) are negligible leading to [182, 183],

$$j^S_F(t) = \frac{6\Delta Q_F}{\tau_d A}\exp\left(-\frac{\pi^2 t}{\tau_d}\right). \tag{5.6}$$

This model is representative of diffusion-controlled Faradaic reactions only.

Alternatively, Montella [182] proposed a model for $j_F^S(t)$ accounting for finite interfacial charge transfer kinetics given by,

$$j_F^S(t) = \frac{6\Delta Q_F}{\tau_d A} \sum_{n=1}^{\infty} \frac{\Lambda^2}{\Lambda^2 - \Lambda + b_n^2} \exp\left(-\frac{b_n^2 t}{\tau_d}\right). \tag{5.7}$$

Here, b_n is the n^{th} root of the following equation [182, 184],

$$b_n \cot b_n + \Lambda - 1 = 0 \tag{5.8}$$

where Λ is the electrochemical Biot number expressed as [182, 184],

$$\Lambda = -\frac{r j_{F,0}}{D_{1,P} R_u T} \frac{\partial \Delta\psi_{eq}}{\partial c_{1,P}} = \frac{R_d}{R_{ct}}. \tag{5.9}$$

Here, $j_{F,0}$ is the exchange current density, $R_u = 8.314$ J mol^{-1} K^{-1} is the universal gas constant, T is the temperature, $\Delta\psi_{eq}$ is the equilibrium potential difference (i.e., the potential difference between the electrode and the electrolyte across their interface at zero net reaction rate), $c_{1,P}$ is the concentration of cations in the electrode, R_d and R_{ct} are the diffusion and interfacial charge transfer resistances, respectively. Here also, after a sufficiently long relaxation duration (i.e., $t \gg \tau_d$), the high order terms ($n > 1$) in Equation (5.7) become negligible leading to [182, 183],

$$j_F^S(t) = \frac{6\Delta Q_F}{\tau_d A} \frac{\Lambda^2}{\Lambda^2 - \Lambda + b_1^2} \exp\left(-\frac{b_1^2 t}{\tau_d}\right) = P_1 \exp(-P_2 t) \tag{5.10}$$

where the fitting parameters P_1 and P_2 can be identified as,

$$P_1 = \frac{6\Delta Q_F}{\tau_d A} \frac{\Lambda^2}{\Lambda^2 - \Lambda + b_1^2} \quad \text{and} \quad P_2 = \frac{b_1^2}{\tau_d}. \tag{5.11}$$

The value of Λ characterizes the main limitation for the rate of Faradaic reactions. For diffusion-controlled processes, $R_d \gg R_{ct}$, $\Lambda \gg 1$, and $b_1 = \pi$, so that Equation (5.10) reduces to Equation (5.6) [182, 184]. By contrast, when processes are controlled by finite interfacial charge transfer kinetics, $R_d \ll R_{ct}$, $\Lambda \ll 1$, and $b_1 \backsimeq \sqrt{3\Lambda}$ [182, 184]. Finally, the residual current density $j_r^S(t)$ is a constant accounting for electrolyte decomposition reactions and/or parasitic reactions in the electrode material [113–115]. Note, however, that the above expressions for the different contributions to the total current density $j_T(t)$ have been previously validated theoretically for 1D homogeneous electrodes but not for 3D heterogeneous porous pseudocapacitive electrodes.

5.1.2 MUSCA method

The MUSCA method aims to explicitly quantify the contributions of different charge storage mechanisms to the total capacitance. It has proved effective in correcting for ohmic polarization effects and the drift of redox peaks with increasing scan rate typically observed in CV measurements [185, 186]. Similar to SPECS, MUSCA starts by imposing a series of small potential steps $\Delta\psi_s$ within a potential window from $\psi_{s,min}$ to $\psi_{s,max}$ and measuring the total current density response $j_T(t)$ to each potential step. Then, for a given scan rate ν, $j_T(t)$ is averaged over a certain time window t_ν defined from the beginning of the potential step $\Delta\psi_s$ to obtain the mean current density $j_T^A(\psi_s)$ at potential ψ_s as [185],

$$j_T^A(\psi_s) = \frac{1}{t_\nu}\int_0^{t_\nu} j_T(t)\mathrm{d}t \tag{5.12}$$

where superscript "A" refers to the mean current density from the MUSCA method, and t_ν is chosen according to [185],

$$t_\nu = \frac{\Delta\psi_s}{\nu}. \tag{5.13}$$

Finally, cyclic voltammograms with minimized ohmic polarization effects are reconstructed by plotting $j_T^A(\psi_s)$ vs. ψ_s [185].

5.1.3 Application of the SPECS and MUSCA methods

Both the SPECS and MUSCA methods have been employed in a wide range of applications. For example, Forghani et al. [187] used the SPECS method to identify the geometric and porous capacitances during the electrochemical characterization of symmetrical activated carbon electrochemical capacitors with organic electrolyte. The MUSCA method was used to quantify the performance over a range of scan rates, both for the entire device and for each individual electrode. Subsequently, the authors assembled prototype pouch cells using the same electrode and electrolyte materials and evaluated their electrochemical behavior [188]. Here, the temporal evolution of the fitting parameters retrieved from SPECS and the rate performance from MUSCA were combined to identify issues within the cell including leakage current, cell degradation, and electrolyte depletion.

In another study, the SPECS and MUSCA methods were used to optimize experimentally electrolytic amorphous carbon as electrode materials by distinguishing and quantifying the EDL and pseudocapacitive contributions at different scan rates [189]. A similar study applied the SPECS and MUSCA methods to demonstrate that the capacitive charge storage in glassy carbon electrodes was better with non-aqueous electrolytes than with aqueous electrolytes due to ion solvation [190]. In fact, the study compared the fitted total EDL resistance R_{EDL} and total EDL capacitance C_{EDL} between the same electrodes in different electrolytes. Based on those results, the authors reasoned that the solvation shells surrounding the adsorbing ions in aqueous electrolytes not only increased resistance but also inhibited denser packing of ions at the electrode surface, thus decreasing the capacitive charge storage.

Another study utilized both the SPECS and MUSCA methods in place of conventional CV measurements to validate experimentally the two methods and simultaneously investigate the charge storage mechanisms in four electrochemical capacitor systems [191]. The Swagelok cells consisted of activated carbon, RuO_2, MnO_2, or $Ni(OH)_2$ working electrodes and activated carbon counter electrodes in alkaline electrolytes. In addition, Forghani et al. [192] used CV, EIS, SPECS, and MUSCA methods to analyze the semiconducting properties of electrolytic MnO_2 deposited on titanium substrates as electrodes for electrochemical capacitors. Here, SPECS combined with EIS enabled the determination of electronic properties across the full potential window, identifying both n-type and p-type behavior in the electrolytic MnO_2 electrodes. Furthermore, in two separate studies the SPECS and MUSCA methods provided mechanistic insights into the microstructures of various porous carbon electrodes [193, 194]. Of particular value was their ability to reveal the capacitances associated with EDL formation at the geometric surface or at the porous surface in each unique porous structure.

Overall, the SPECS and MUSCA methods give an unmatched capability to distinguish and quantify the charge storage contributions from various mechanisms using relatively simple experimental procedures applicable to most electrochemical systems. These methods have been validated qualitatively using experimental data. This study aims to rigorously validate the SPECS method and the MUSCA method, using state-of-the-art physical mod-

eling and numerical simulations, to quantify the contributions, to the total current density, of EDL formation and Faradaic reactions occurring at the surface or within 3D pseudocapacitive electrodes.

5.2 Analysis

5.2.1 Schematic and assumptions

Figure 5.1(a) shows the schematic of the simulated 3D mesoporous pseudocapacitive electrode consisting of monodisperse spherical particles of radius r ordered in face-centered cubic (FCC) packing supported by a planar current collector in an electrolyte containing Li^+ ions in a three-electrode configuration with Ag/AgCl as the reference electrode. The example shown here had a number of particle layers $N = 3.5$. The current collector, electrode, and electrolyte domain thicknesses were denoted by L_C, L_P, and L, respectively. Figure 5.1(b) shows the geometric surface area $A_{BET,1}$ corresponding to the exterior electrode surface with direct access to the bulk electrolyte. Figure 5.1(c) shows the interior electrode/electrolyte interface also known as the porous surface area $A_{BET,2}$ [113–115].

To make the problem mathematically tractable, the following assumptions were made: (1) The electrolyte was binary and symmetric, i.e., it consisted of two ion species of opposite valency $\pm z$. (2) Cations and anions had the same effective diameter a and diffusion coefficient D in the electrolyte [195, 196]. (3) The Stern layer contained no free charge and its thickness H was approximated as the effective radius of the ions, so that $H = a/2$ [41, 197, 198]. (4) The transport properties of the electrode and electrolyte were taken as constant and independent of state-of-charge. (5) Bulk motion of the electrolyte was negligible. (6) Ion intercalation/deintercalation in/out of the electrode spherical particles was modeled as a diffusion process. (7) The temperature T was uniform in the simulated domain and constant over time. (8) Electrical contact resistance between the current collector and the electrode, and between the electrode spherical particles, was negligible. (9) Residual current density associated with electrolyte decomposition reactions and/or parasitic reactions in the electrode

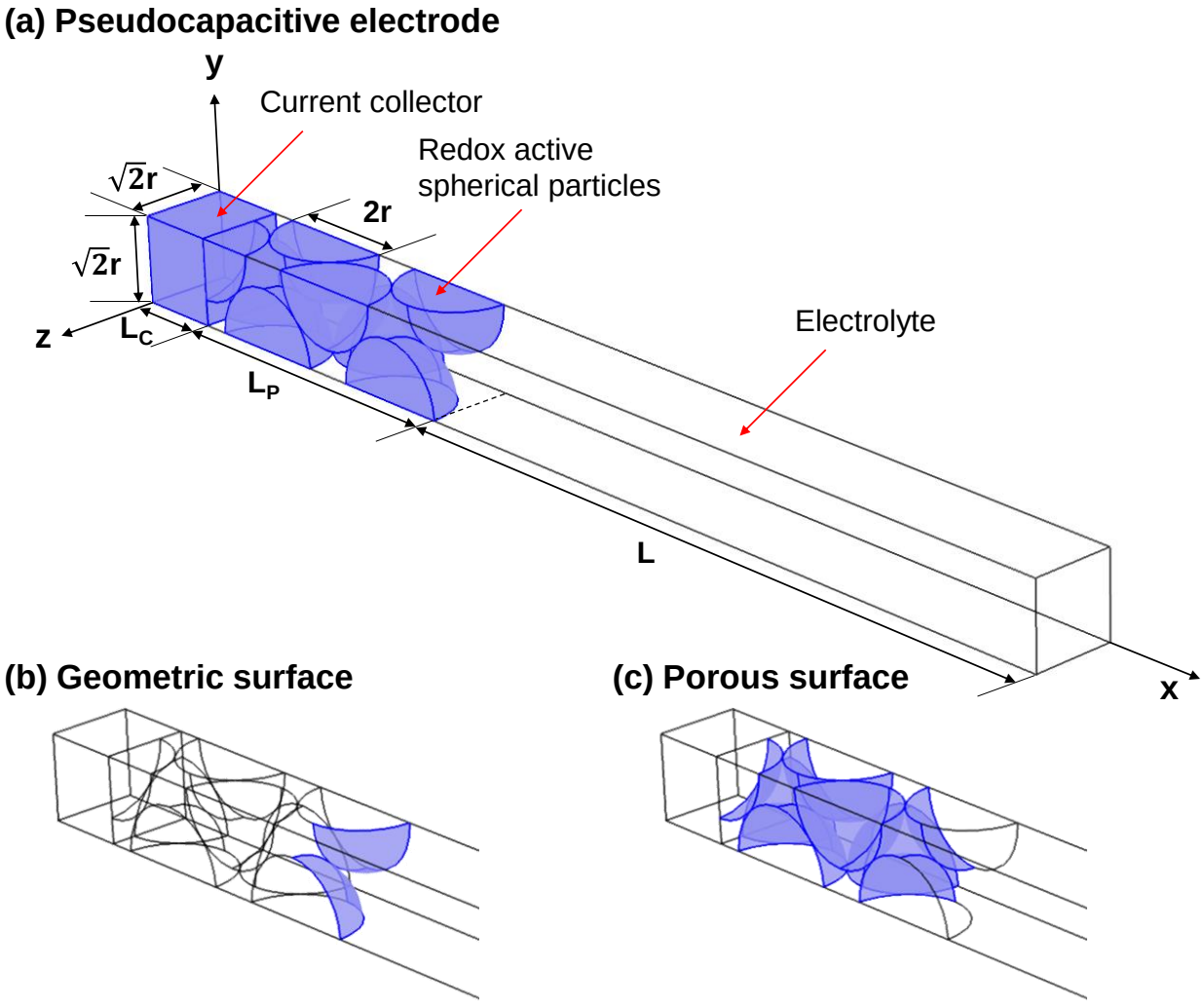

Figure 5.1: (a) Schematic, coordinate system, and dimensions of the simulated 3D mesoporous pseudocapacitive electrode consisting of monodisperse spherical particles of radius r ordered in face-centered cubic (FCC) packing supported by a planar current collector in an electrolyte containing Li^+ ions in a three-electrode configuration with Ag/AgCl as the reference electrode. (b) Geometric surface area $A_{BET,1}$ and (c) porous surface area $A_{BET,2}$ of the electrode/electrolyte interface.

material was ignored, i.e., $j_r^S(t) = 0$. (10) Current arising from EDL formation at the current collector/electrolyte interface was negligible compared to that at the electrode/electrolyte interface.

5.2.2 Governing equations

The modified Poisson-Nernst-Planck (MPNP) model coupled with the Frumkin-Butler-Volmer theory were used to numerically reproduce experimental data obtained from the SPECS method accounting for interfacial, transport, and electrochemical phenomena in the simulated domain [199]. The governing equations have been described in our previous studies [135, 175, 200] and are reproduced in Appendix B for the sake of completeness (see Section B.1). In brief, the spatiotemporal evolution of (i) the local electric potential $\psi(\mathbf{r}, t)$ in the current collector, the electrode, and the electrolyte, as well as (ii) the local concentrations $c_1(\mathbf{r}, t)$ of cations and $c_2(\mathbf{r}, t)$ of anions in the electrolyte were governed by the MPNP model [135, 175, 200]. The local concentration $c_{1,P}(\mathbf{r}, t)$ of Li^+ ions in the electrode was governed by the 3D transient mass diffusion equation [134, 201, 202].

5.2.3 Initial and boundary conditions

All initial and boundary conditions necessary to solve the 3D transient governing equations are described in detail in Appendix B (see Section B.2). The potential at the current collector surface $(0, y, z)$ was imposed as a multi-step function for SPECS simulations according to [186],

$$\psi_s(0, y, z, t) = \begin{cases} \psi_{s,min} + (p_s - 1)\Delta\psi_s & \text{for} \quad 1 \leq p_s \leq (n_s + 1)/2 \quad \text{(charging)} \\ \psi_{s,max} - \left(p_s - \dfrac{n_s + 1}{2}\right)\Delta\psi_s & \text{for} \quad (n_s + 1)/2 \leq p_s \leq n_s \quad \text{(discharging)} \end{cases} \tag{5.14}$$

where $\psi_{s,min}$ and $\psi_{s,max}$ are the minimum and maximum of the potential window, respectively. Here, p_s is the potential step number and n_s is the total number of potential steps $\Delta\psi_s$ to cover the entire potential window, i.e., $n_s = [2(\psi_{s,max} - \psi_{s,min})/\Delta\psi_s] + 1$, with each step lasting an equilibration time of t_e.

On the other hand, for simulating cyclic voltammograms, the potential at the current

collector surface $(0, y, z)$ was imposed as a triangular function of time t given by [203],

$$\psi_s(0,y,z,t) = \begin{cases} \psi_{s,min} + \nu[t - (n_c - 1)t_{cd}] & \text{for} \quad (n_c - 1)t_{cd} \leq t < (n_c - 1/2)t_{cd} \quad \text{(charging)} \\ \psi_{s,max} - \nu[t - (n_c - 1/2)t_{cd}] & \text{for} \quad (n_c - 1/2)t_{cd} \leq t < n_c t_{cd} \quad \text{(discharging)} \end{cases} \tag{5.15}$$

where n_c is the cycle number, t_{cd} is the cycle period, and ν is the scan rate, i.e., $\nu = 2(\psi_{s,max} - \psi_{s,min})/t_{cd}$.

5.2.4 Constitutive relationships

The present study used realistic material properties summarized in Table 5.1 and taken from the literature for the current collector, the porous pseudocapacitive electrode consisting of Nb_2O_5 nanoparticles [41, 204–206], and the electrolyte consisting of 1 M $LiClO_4$ salt in propylene carbonate (PC) solvent [207,208]. The thickness of the current collector was taken as $L_C = 10$ nm with electrical conductivity $\sigma_C = 5$ S m^{-1} corresponding to carbon-based materials [22]. The electrodes were made of spherical particles with radius $r = 3.75$ nm, while the number of particle layers N varied between 2.5 and 4.5 for different cases of the parametric study (3.5 for the baseline case), resulting in electrode thicknesses L_P ranging from 14.4 to 25.0 nm (19.7 nm for the baseline case). The capacitance of the electrodes quantitatively varied with both the radius of electrode spherical particles r and the number of particle layers N. Note that the purpose of this study is to validate the SPECS and MUSCA methods under numerically controlled conditions. Therefore, the dimensions selected were smaller than typical experiments in order to reduce the computational resources and time required to perform the numerous simulations. The electrode electrical conductivity was taken as $\sigma_P = 10^{-4}$ S m^{-1} [16] and the reaction rate constant k_0 varied between 10^{-10} and 10^{-8} m$^{2.5}$ mol$^{-0.5}$ s^{-1} for different cases of the parametric study (10^{-10} m$^{2.5}$ mol$^{-0.5}$ s^{-1} for the baseline case) [204, 209, 210]. For electrodes consisting of transition metal oxides, the equilibrium potential difference $\Delta\psi_{eq}$ is typically determined experimentally as a function of the state-of-charge (SOC) defined as $c_{1,P}/c_{1,P,max}$ by fitting experimental data for open-circuit potential [211–213]. In the absence of experimental data for Nb_2O_5, $\Delta\psi_{eq}$ was modeled as a linear function of SOC as measured for 100 μm thick MnO_2 dense films vs. Ag/AgCl

Table 5.1: Values or ranges of current collector, electrode, and electrolyte dimensions and properties used in the simulations reported in this study.

Variable	**Symbol**	**Value**	**Unit**
Effective ion diameter	a	0.67	nm
Initial ion concentration in the electrode	$c_{1,P,0}$	6.58	mol L^{-1}
Maximum ion concentration in the electrode	$c_{1,P,max}$	32.9	mol L^{-1}
Ion concentration in the bulk electrolyte	c_{∞}	1	mol L^{-1}
Ion diffusion coefficient in the electrolyte	D	2×10^{-11}	m^2 s^{-1}
Ion diffusion coefficient in the electrode	$D_{1,P}$	10^{-14} - 10^{-12}	m^2 s^{-1}
Reaction rate constant	k_0	10^{-10} - 10^{-8}	$m^{2.5}$ $mol^{-0.5}$ s^{-1}
Electrolyte domain thickness	L	100	nm
Current collector thickness	L_C	10	nm
Electrode thickness	L_P	14.4 - 25.0	nm
Number of layers of electrode spherical particles	N	2.5 - 4.5	
Radius of electrode spherical particles	r	3.75	nm
Temperature	T	293	K
Valency	z	1	
Transfer coefficient	α	0.5	
Relative permittivity of the electrolyte	ϵ_r	64.4	
Potential window vs. Ag/AgCl	$\psi_{s,min}$	0	V
	$\psi_{s,max}$	0.4	V
Electrical conductivity of the current collector	σ_C	5	S m^{-1}
Electrical conductivity of the electrode	σ_P	10^{-4}	S m^{-1}

reference electrode and expressed as [205],

$$\Delta\psi_{eq}(t) = 10.5[4 - c_{1,P}(t)/c_{1,P,max}] - 39.9. \tag{5.16}$$

Here, the maximum Li^+ ion concentration $c_{1,P,max} = 32.9$ mol L^{-1} corresponded to fully lithiated manganese dioxide $LiMnO_2$ [206], and the initial Li^+ ion concentration $c_{1,P,0} = 6.58$ mol L^{-1} was such that the initial equilibrium potential difference $\Delta\psi_{eq,0}$ was zero. The transfer coefficient α in the Frumkin-Butler-Volmer equation was assumed to be 0.5 to consider the ideal case of identical energy barriers for forward and backward reversible redox reactions [41]. The diffusion coefficient $D_{1,P}$ of Li^+ ions in transition metal oxides typically ranges from 10^{-16} to 10^{-10} m^2 s^{-1} [204]. Here, $D_{1,P}$ varied between 10^{-14} and 10^{-12} m^2 s^{-1} for different cases of the parametric study (10^{-14} m^2 s^{-1} for the baseline case). The thickness of the electrolyte domain was taken as $L = 100$ nm with bulk ion concentration $c_\infty = 1$ mol L^{-1} and valency $z = 1$. The electrolyte relative permittivity was set to that of PC with $\epsilon_r = 64.4$ [207]. The effective ion diameter and the ion diffusion coefficient of both Li^+ and ClO_4^- ions were set to those of solvated Li^+ ions in PC with $a = 0.67$ nm and $D = 2 \times 10^{-11}$ m^2 s^{-1}, respectively [208]. Finally, the temperature was set to $T = 293$ K, and the potential window ranged from $\psi_{s,min} = 0$ V to $\psi_{s,max} = 0.4$ V. This potential window covered both the Faradaic and the capacitive regimes for the simulated electrode [134]. Specifically, the Faradaic regime consisted of potentials below 0.2 V where the interfacial charge transfer kinetics was more favorable for Faradaic reactions to occur, and vice versa for the capacitive regime. In fact, as the potential approached 0.4 V, the area enclosed within the CV curves shrunk significantly indicating decreasing capacitance. Therefore, although simulating the potential window beyond 0.4 V was possible, it would not meaningfully change the main observations of the study, but it would further increase the computational cost and time of the simulations.

5.2.5 Method of solution and data processing

The governing equations along with the initial and boundary conditions were solved using finite element methods in the COMSOL Multiphysics solver. The time-dependent solver

proceeded at adaptive time steps controlled by an absolute tolerance of 0.01 for SPECS simulations and 0.001 for CV simulations.

The total current density $j_{T,n}(\mathbf{r}_{E/E}, t)$ at the electrode/electrolyte interface located at $\mathbf{r}_{E/E}$ was expressed as the sum of the EDL current density $j_{EDL,n}(\mathbf{r}_{E/E}, t)$ and the Faradaic current density $j_{F,n}(\mathbf{r}_{E/E}, t)$ so that $j_{T,n}(\mathbf{r}_{E/E}, t) = j_{EDL,n}(\mathbf{r}_{E/E}, t) + j_{F,n}(\mathbf{r}_{E/E}, t)$. The EDL current density $j_{EDL,n}(\mathbf{r}_{E/E}, t)$ was defined as [214],

$$j_{EDL,n}(\mathbf{r}_{E/E}, t) = -\epsilon_0 \epsilon_r \frac{\partial^2 \psi}{\partial n \partial t}(\mathbf{r}_{E/E}, t) \tag{5.17}$$

where $\epsilon_0 = 8.854 \times 10^{-12}$ F m^{-1} is the vacuum permittivity. On the other hand, the Faradaic current density $j_{F,n}(\mathbf{r}_{E/E}, t)$ was computed from the generalized Frumkin-Butler-Volmer model evaluated at the electrode/electrolyte interface according to [41],

$$j_{F,n}(\mathbf{r}_{E/E}, t) = j_{F,0}(\mathbf{r}_{E/E}, t)\left\{ \exp\left[\frac{(1-\alpha) z F \eta(\mathbf{r}_{E/E}, t)}{R_u T}\right] - \exp\left[\frac{-\alpha z F \eta(\mathbf{r}_{E/E}, t)}{R_u T}\right]\right\} \tag{5.18}$$

where $j_{F,0}(\mathbf{r}_{E/E}, t)$ is the local exchange current density expressed as [209, 210],

$$j_{F,0}(\mathbf{r}_{E/E}, t) = zFk_0[c_1(\mathbf{r}_{E/E}, t)]^{1-\alpha}[c_{1,P,max} - c_{1,P}(\mathbf{r}_{E/E}, t)]^{\alpha}[c_{1,P}(\mathbf{r}_{E/E}, t)]^{\alpha}. \tag{5.19}$$

In addition, the surface overpotential $\eta(\mathbf{r}_{E/E}, t)$ necessary to drive the redox reactions at the electrode/electrolyte interface [Equation (5.18)] was expressed as [41],

$$\eta(\mathbf{r}_{E/E}, t) = \Delta\psi_H(\mathbf{r}_{E/E}, t) - \Delta\psi_{eq}(t) \tag{5.20}$$

where $\Delta\psi_H(\mathbf{r}_{E/E}, t)$ is the local potential drop across the Stern layer at the electrode/electrolyte interface and $\Delta\psi_{eq}(t)$ is the equilibrium potential difference.

Finally, the current density $j(t)$ (in A/m^2) averaged over the footprint surface area A_{fp} of the current collector was defined as [215],

$$j(t) = \frac{\iint_{A_{BET}} j_n(\mathbf{r}_{E/E}, t) \mathrm{d}A_{BET}}{A_{fp}}. \tag{5.21}$$

From the numerically simulated cyclic voltammograms, the differential capacitances associated with EDL formation at the geometric surface $C_{diff,1}(\psi_s)$ and at the porous surface $C_{diff,2}(\psi_s)$, defined per unit surface area A_{fp} of the current collector, were determined

as [203],

$$C_{diff,i}(\psi_s) = \left| \frac{\iint_{A_{BET,i}} j_{EDL,n}(\mathbf{r}_{E/E}, \psi_s) \mathrm{d}A_{BET,i}}{A_{fp}\nu} \right| \quad \text{with} \quad i = 1 \text{ or } 2. \tag{5.22}$$

Moreover, the differential total EDL footprint capacitance $C_{diff,EDL}(\psi_s)$ was simply the sum of $C_{diff,1}(\psi_s)$ and $C_{diff,2}(\psi_s)$, i.e.,

$$C_{diff,EDL}(\psi_s) = C_{diff,1}(\psi_s) + C_{diff,2}(\psi_s). \tag{5.23}$$

5.2.6 SPECS fitting model

In the absence of residual current density (i.e., $j_r^S(t) = 0$) and combining Equations (5.2) and (5.10), the original fitting function of the SPECS method for the total footprint current density response to an imposed potential step $\Delta\psi_s$ in a porous pseudocapacitive electrode is such that [113–115],

$$j_T^S(t) = \frac{\Delta\psi_s}{R_1} \exp\left(-\frac{t}{R_1 C_1}\right) + \frac{\Delta\psi_s}{R_2} \exp\left(-\frac{t}{R_2 C_2}\right) + P_1 \exp(-P_2 t). \tag{5.24}$$

Here, superscript "S" refers to fitting functions of the different current densities in the original SPECS method in order to distinguish them from the numerical evaluations of $j_{EDL}(t)$, $j_F(t)$ and $j_T(t)$ obtained from simulations [Equations (5.17), (5.18), and (5.21)]. The fitting parameters $R_1(\psi_s)$, $R_2(\psi_s)$, $C_1(\psi_s)$, $C_2(\psi_s)$, $P_1(\psi_s)$, and $P_2(\psi_s)$ were determined by nonlinear least squares fitting of the footprint current densities at each potential step by minimizing the objective function δ defined as [216],

$$\delta = \sum_{i=1}^{N_s} \left\{ \left[j_T(t_i) - j_T^S(t_i) \right] \frac{\Delta t_i}{t_e} \right\}^2 \tag{5.25}$$

where $\Delta t_i = t_i - t_{i-1}$ is the adaptive time step. This definition of δ ensured that the results were unaffected by the exact size of the adaptive time steps taken by the time-dependent solver.

A genetic algorithm solver was used for this optimization problem [217]. For each fitting trial, the algorithm randomly generated an initial population of 200 fitting parameter values. During each generation, a portion of the existing population was selected, based

on the objective function δ, to generate a new population of 200 fitting parameter values. Convergence was reached if (i) the average relative change in the best objective function δ over 200 generations was less than 10^{-5}, or (ii) 10^5 generations had been produced [217].

5.3 Results and discussion

5.3.1 SPECS simulation and original SPECS fitting model

Figure 5.2(a) plots the temporal evolution of the imposed potential $\psi_s(0, y, z, t)$ given by Equation (5.14) during a charging/discharging cycle for numerical simulations of the SPECS method. It involved a series of small potential steps of $\Delta\psi_s = 0.04$ V with equilibration time $t_e = 0.4$ s. To avoid discontinuity in the potential $\psi(\mathbf{r}, t)$ and the associated numerical instabilities at the transition from one step to another, the potential step was smoothed using a polynomial function with a continuous second order derivative during a transition time $t_t = 0.5$ ms, as developed previously [186].

Figure 5.2(b) plots the numerically simulated total footprint current density $j_T(t)$ resulting from the imposed potential $\psi_s(0, y, z, t)$. Figure 5.2 also plots the simulated footprint current densities due to (c) EDL formation $j_{EDL}(t)$ [Equations (5.17) and (5.21)] and (d) Faradaic reactions $j_F(t)$ [Equations (5.18) and (5.21)] such that $j_T(t) = j_{EDL}(t) + j_F(t)$. Here, the current densities were recorded at intervals based on adaptive time steps, giving 129 data points per potential step for the fitting analysis of the SPECS method.

Figure 5.3 compares the numerically simulated Faradaic footprint current density $j_F(t)$ [Equations (5.18) and (5.21)] with the fitted current density $j_F^S(t)$ using the original SPECS fitting function [Equation (5.10)] (a) at $\psi_s = 0.4$ V during charging and (b) at $\psi_s = 0$ V during discharging, with potential steps $\Delta\psi_s = 0.04$ V. Here, the simulated current density $j_F(t)$ showed significant discrepancies with the fitted current density $j_F^S(t)$ at both potentials. At $\psi_s = 0$ V in particular, the fitted Faradaic current density $j_F^S(t)$ failed to capture the spike and the rapid decay of the simulated current density $j_F(t)$ within 0.02 s after the imposed potential step. Figure 5.3 then plots $\log|j_F(t)|$ as a function of time t (c) at $\psi_s = 0.4$ V during

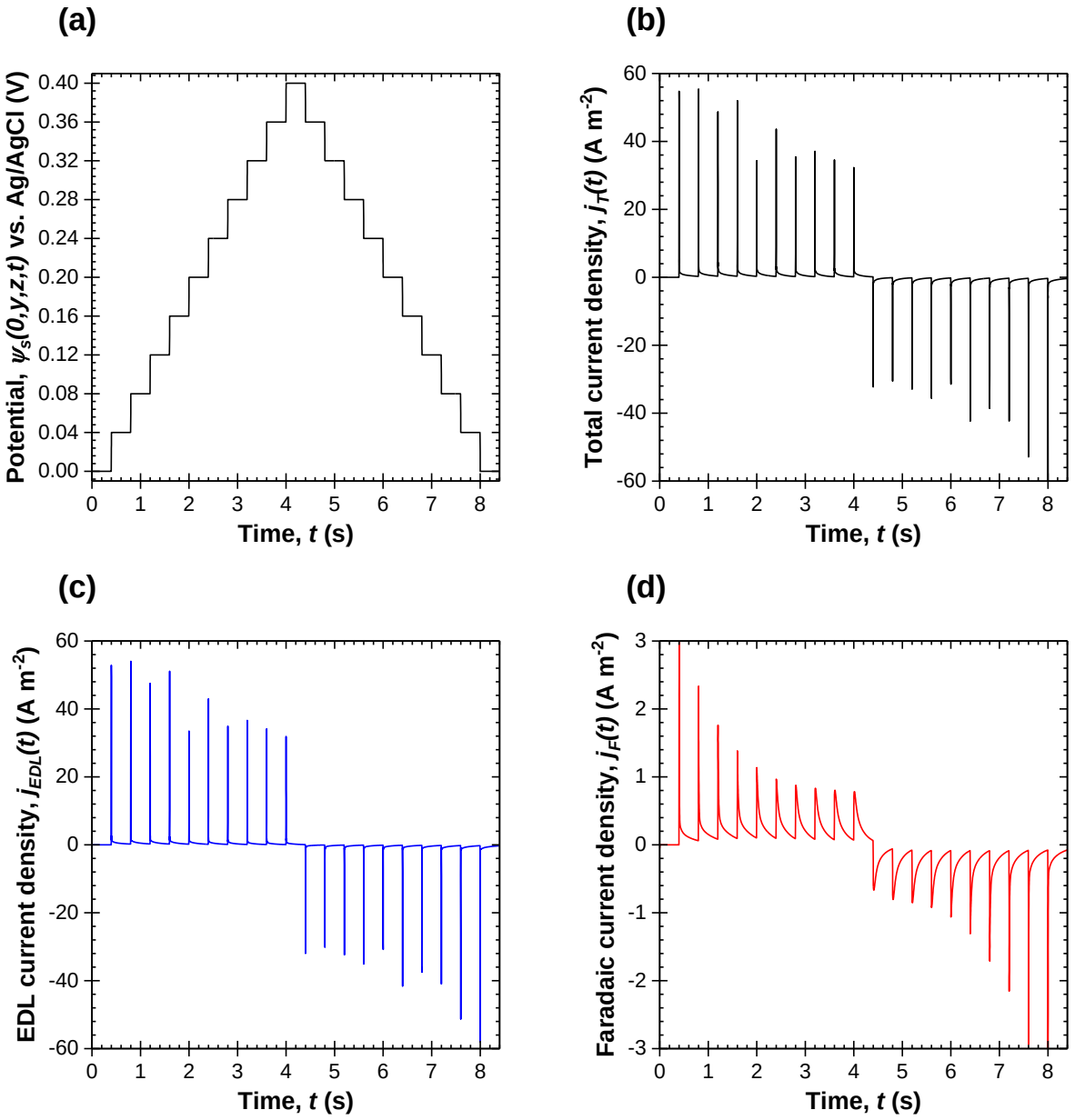

Figure 5.2: Temporal evolution of (a) the imposed potential $\psi_s(0, y, z, t)$ [Equation (5.14)] with step size $\Delta\psi_s = 0.04$ V and equilibration time $t_e = 0.4$ s and resulting (b) total $j_T(t)$, (c) EDL $j_{EDL}(t)$, and (d) Faradaic $j_F(t)$ footprint current densities [Equations (5.17), (5.18), and (5.21)] obtained with the SPECS method.

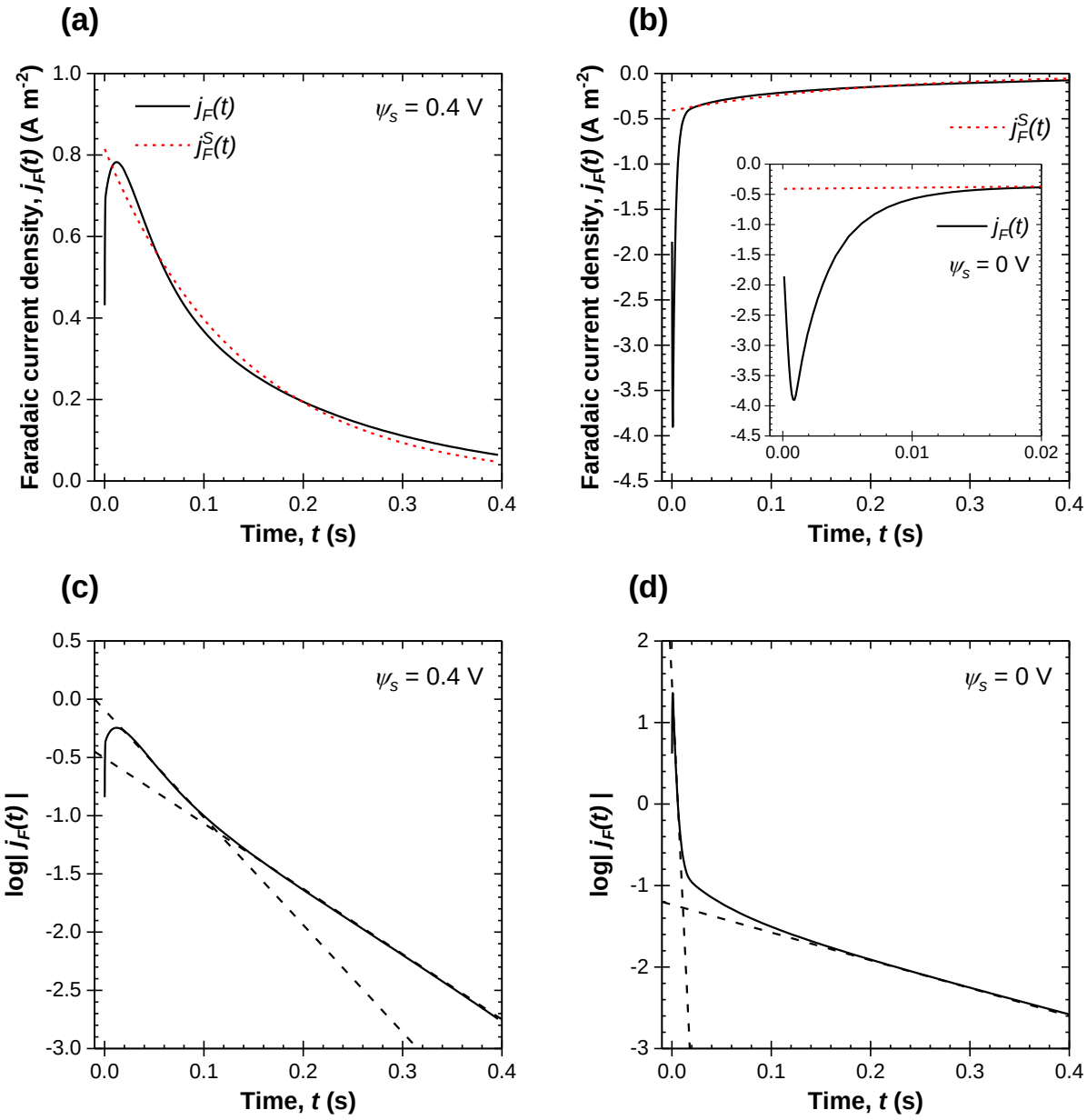

Figure 5.3: Numerically simulated Faradaic footprint current density $j_F(t)$ [Equations (5.18) and (5.21)] and fitted current density $j_F^S(t)$ using the original SPECS fitting function [Equation (5.24)] (a) at $\psi_s = 0.4$ V during charging and (b) at $\psi_s = 0$ V during discharging, with potential steps $\Delta\psi_s = 0.04$ V. (c, d) Data of (a, b) plotted as $\log|j_F(t)|$ vs. time t.

charging and (d) at $\psi_s = 0$ V during discharging. In both cases, $\log|j_F(t)|$ featured a clear change in slope during the potential step, and it approached separate asymptotes (dashed lines) on either side of this inflection point. This suggests that the Faradaic footprint current density $j_F(t)$ in a porous pseudocapacitive electrode featured two distinct relaxation time constants. Thus, the expression of Equation (5.10), validated for planar electrodes, should be modified.

5.3.2 Modified SPECS fitting model

In light of the previous observations, the original SPECS fitting function given by Equation (5.10) for the Faradaic footprint current density was revised to include two exponential decays, i.e.,

$$j_F^M(t) = j_{F1}^M(t) + j_{F2}^M(t) = P_1 \exp(-P_2 t) + P_3 \exp(-P_4 t) \tag{5.26}$$

where superscript "M" refers to the modified SPECS fitting model. Here, $j_{F1}^M(t)$ represents the surface-controlled Faradaic footprint current density due to reversible redox reactions occurring at or near the electrode/electrolyte interface and limited by interfacial charge transfer kinetics [49, 99]. Similarly, $j_{F2}^M(t)$ represents the diffusion-controlled Faradaic footprint current density due to ion intercalation/deintercalation in/out of the electrode spherical particles and limited by solid state ion diffusion [49, 99]. Thus, the fitting function of the SPECS method for the total footprint current density response to an imposed potential step $\Delta\psi_s$ in a porous pseudocapacitive electrode is now written as,

$$\begin{aligned} j_T^M(t) = {} & \frac{\Delta\psi_s}{R_1} \exp\left(-\frac{t}{R_1 C_1}\right) + \frac{\Delta\psi_s}{R_2} \exp\left(-\frac{t}{R_2 C_2}\right) \\ & + P_1 \exp(-P_2 t) + P_3 \exp(-P_4 t). \end{aligned} \tag{5.27}$$

The rest of the fitting procedure was the same as that previously described. Here, Equation (5.27) included four time constants namely (i) the EDL time constant $\tau_{EDL1}(\psi_s) = R_1(\psi_s)C_1(\psi_s)$ associated with fast EDL formation at the so-called geometric surface, (ii) the EDL time constant $\tau_{EDL2}(\psi_s) = R_2(\psi_s)C_2(\psi_s)$ associated with slower EDL formation at the electrode/electrolyte interface within the porous electrode, (iii) the Faradaic time

constant $\tau_{F1}(\psi_s) = 1/P_2(\psi_s)$ depending on the rate of interfacial charge transfer kinetics in surface-controlled Faradaic reactions, and (iv) the Faradaic time constant $\tau_{F2}(\psi_s) = 1/P_4(\psi_s)$ representing the diffusion time constant τ_d associated with diffusion-controlled Faradaic reactions [186]. As such, $\tau_{EDL1}(\psi_s)$ and $\tau_{F1}(\psi_s)$ were expected to be smaller than $\tau_{EDL2}(\psi_s)$ and $\tau_{F2}(\psi_s)$, respectively. The fitting parameters $R_1(\psi_s)$, $R_2(\psi_s)$, $C_1(\psi_s)$, $C_2(\psi_s)$, $P_2(\psi_s)$, and $P_4(\psi_s)$ were positive real numbers, while $P_1(\psi_s)$ and $P_3(\psi_s)$ were positive during charging and negative during discharging.

Figure 5.4 compares the numerically simulated (a, b) total $j_T(t)$, (c, d) EDL $j_{EDL}(t)$, and (e, f) Faradaic $j_F(t)$ footprint current densities (same as in Figure 5.2) with their respective fit (a, b) $j_T^M(t)$, (c, d) $j_{EDL}^M(t)$, and (e, f) $j_F^M(t)$ using the modified SPECS fitting function [Equation (5.27)] at $\psi_s = 0.4$ V during charging and $\psi_s = 0$ V during discharging, with potential steps $\Delta\psi_s = 0.04$ V. Here, the numerically simulated current densities $j_T(t)$, $j_{EDL}(t)$, and $j_F(t)$ were closely matched by the fitted current densities $j_T^M(t)$, $j_{EDL}^M(t)$, and $j_F^M(t)$ retrieved from the modified SPECS fitting function at both potentials within the entire time range, unlike from the original SPECS fitting function (Figure 5.3).

Figure 5.5 plots the EDL footprint current densities at the geometric surface $j_{EDL1}^M(t)$ and at the porous surface $j_{EDL2}^M(t)$ as well as the surface-controlled $j_{F1}^M(t)$ and diffusion-controlled $j_{F2}^M(t)$ Faradaic footprint current densities [Equation (5.27)] predicted by the modified SPECS fitting function at $\psi_s = 0.4$ V during charging and $\psi_s = 0$ V during discharging, with potential steps $\Delta\psi_s = 0.04$ V. Note that the fitted EDL $j_{EDL}^M(t)$ and Faradaic $j_F^M(t)$ footprint current densities are such that $j_{EDL}^M(t) = j_{EDL1}^M(t) + j_{EDL2}^M(t)$ and $j_F^M(t) = j_{F1}^M(t) + j_{F2}^M(t)$. Immediately after imposing a potential step, the footprint current densities featured a spike due to EDL formation, redox reactions, and ion intercalation/deintercalation in/out of the electrode spherical particles [186]. This spike was not captured by the fitting function due to the truncation performed to obtain Equation (5.10) from Equation (5.7). Afterwards, $j_{EDL1}(t)$ decayed faster than $j_{EDL2}(t)$ with respect to time t as EDL was forming or dissolving faster at the geometric surface than at surfaces within the porous electrode. Therefore, as expected, the time constants were such that $\tau_{EDL1}(\psi_s) < \tau_{EDL2}(\psi_s)$ [113–115]. In addition, $j_{F1}(t)$ decayed rapidly at low potentials due to fast interfacial charge transfer kinetics in

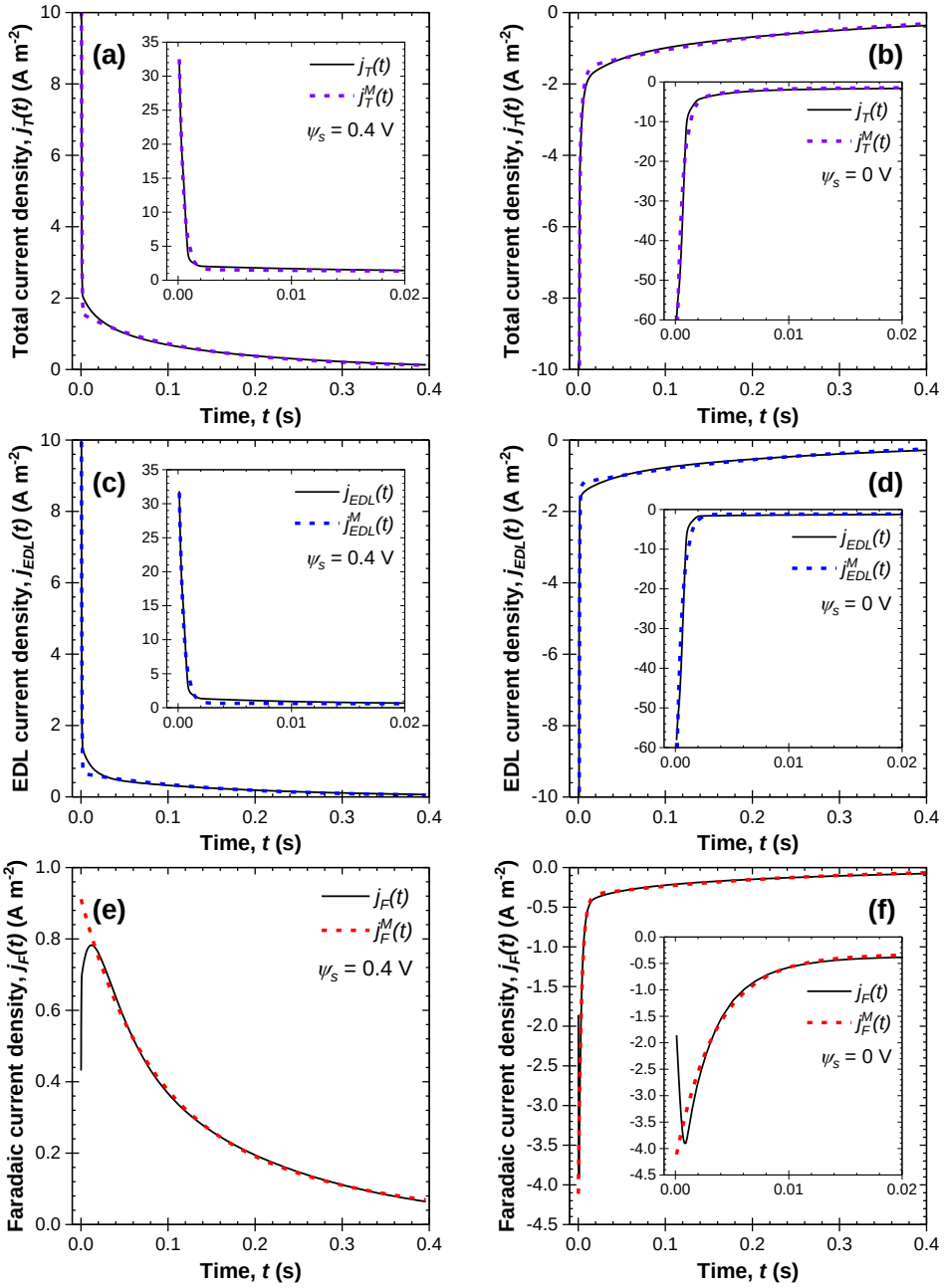

Figure 5.4: Numerically simulated (a, b) total $j_T(t)$, (c, d) EDL $j_{EDL}(t)$, and (e, f) Faradaic $j_F(t)$ footprint current densities [Equations (5.17), (5.18), and (5.21)] along with their respective fit (a, b) $j_T^M(t)$, (c, d) $j_{EDL}^M(t)$, and (e, f) $j_F^M(t)$ using the modified SPECS fitting function [Equation (5.27)] at $\psi_s = 0.4$ V during charging and at $\psi_s = 0$ V during discharging, with potential steps $\Delta\psi_s = 0.04$ V. Insets show the rapid changes between 0 and 0.02 s.

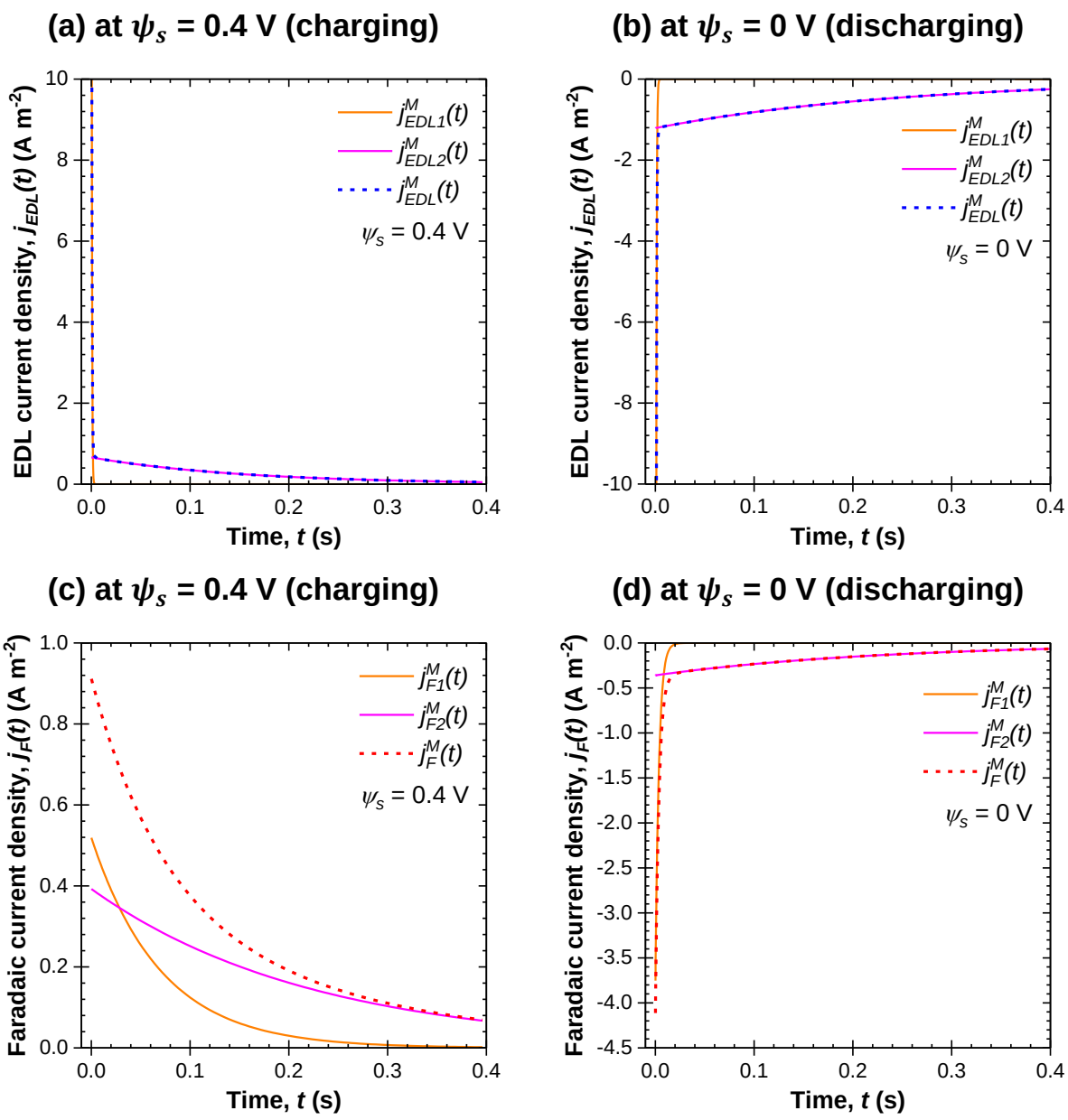

Figure 5.5: EDL footprint current densities at the geometric surface $j^M_{EDL1}(t)$ and at the porous surface $j^M_{EDL2}(t)$ as well as surface-controlled $j^M_{F1}(t)$ and diffusion-controlled $j^M_{F2}(t)$ Faradaic footprint current densities [Equation (5.27)] predicted by the modified SPECS fitting function (a, c) at $\psi_s = 0.4$ V during charging and (b, d) at $\psi_s = 0$ V during discharging, with potential steps $\Delta\psi_s = 0.04$ V. Note that the fitted EDL $j^M_{EDL}(t)$ and Faradaic $j^M_F(t)$ footprint current densities are such that $j^M_{EDL}(t) = j^M_{EDL1}(t) + j^M_{EDL2}(t)$ and $j^M_F(t) = j^M_{F1}(t) + j^M_{F2}(t)$.

the Faradaic regime but slowly at high potentials due to slow kinetics in the capacitive regime [134]. By contrast, $j_{F2}(t)$ decayed slowly at all potentials due to consistently slow ion intercalation/deintercalation in/out of the electrode spherical particles and the relatively large time constant $\tau_{F2}(\psi_s)$.

5.3.3 SPECS fitting parameters interpretation

Figure 5.6 plots the fitting parameters $R_1(\psi_s)$, $C_1(\psi_s)$, $R_2(\psi_s)$, and $C_2(\psi_s)$ associated with EDL formation while Figure 5.7 plots $|P_1(\psi_s)|$, $P_2(\psi_s)$, $|P_3(\psi_s)|$, and $P_4(\psi_s)$ associated with Faradaic reactions of the modified SPECS model as functions of potential ψ_s during a charging/discharging cycle between $\psi_{s,min} = 0$ V and $\psi_{s,max} = 0.4$ V with potential steps $\Delta\psi_s = 0.04$ V. First, all eight fitting parameters retrieved independently at each step formed continuous functions of ψ_s and their values obtained for the charging phase were similar to those of the discharging phase across the potential window. They were also approximately continuous functions of ψ_s, consistent with the results reported in our previous study [186].

Figures 5.6(a) and 5.6(c) indicate that the footprint resistance $R_2(\psi_s)$ associated with the porous surface EDL was two orders of magnitude larger than $R_1(\psi_s)$ associated with the geometric surface EDL. Indeed, ions from the bulk electrolyte had to transport along tortuous paths through the porous electrode structure before reaching the surface of the particles, while they could reach the geometric surface from the bulk electrolyte without much resistance [113–115]. Similarly, Figures 5.6(b) and 5.6(d) indicate that the porous surface EDL footprint capacitance $C_2(\psi_s)$ was one order of magnitude larger than the geometric surface EDL footprint capacitance $C_1(\psi_s)$. In fact, compared to the geometric surface, the porous surface accounted for the vast majority of the total electrode/electrolyte interfacial area [113–115]. These results were consistent with the observations by Dupont and Donne [113–115]. Finally, Figures 5.6(e) and 5.6(f) plot the geometric EDL time constant $\tau_{EDL1}(\psi_s) = R_1(\psi_s)C_1(\psi_s)$ and the porous EDL time constant $\tau_{EDL2}(\psi_s) = R_2(\psi_s)C_2(\psi_s)$. Here also, the values of each time constant were not only similar between charging and discharging but also relatively consistent across the entire potential window. This suggests that

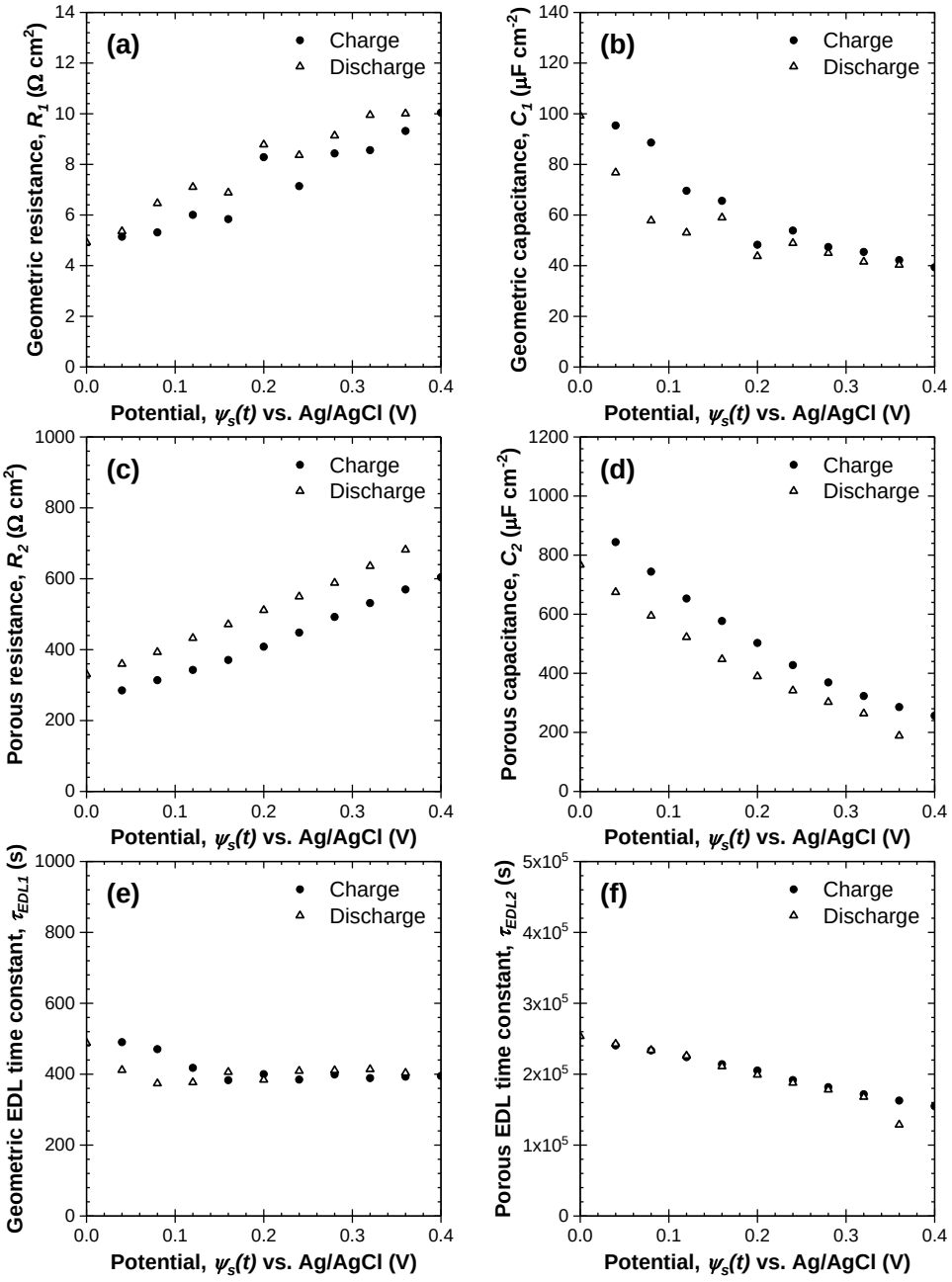

Figure 5.6: Fitting parameters of the modified SPECS model associated with EDL formation (a) $R_1(\psi_s)$, (b) $C_1(\psi_s)$, (c) $R_2(\psi_s)$, and (d) $C_2(\psi_s)$ along with EDL time constants (e) $\tau_{EDL1}(\psi_s) = R_1(\psi_s)C_1(\psi_s)$ and (f) $\tau_{EDL2}(\psi_s) = R_2(\psi_s)C_2(\psi_s)$ as functions of potential ψ_s during a charging/discharging cycle between $\psi_{s,min} = 0$ V and $\psi_{s,max} = 0.4$ V with potential steps $\Delta\psi_s = 0.04$ V.

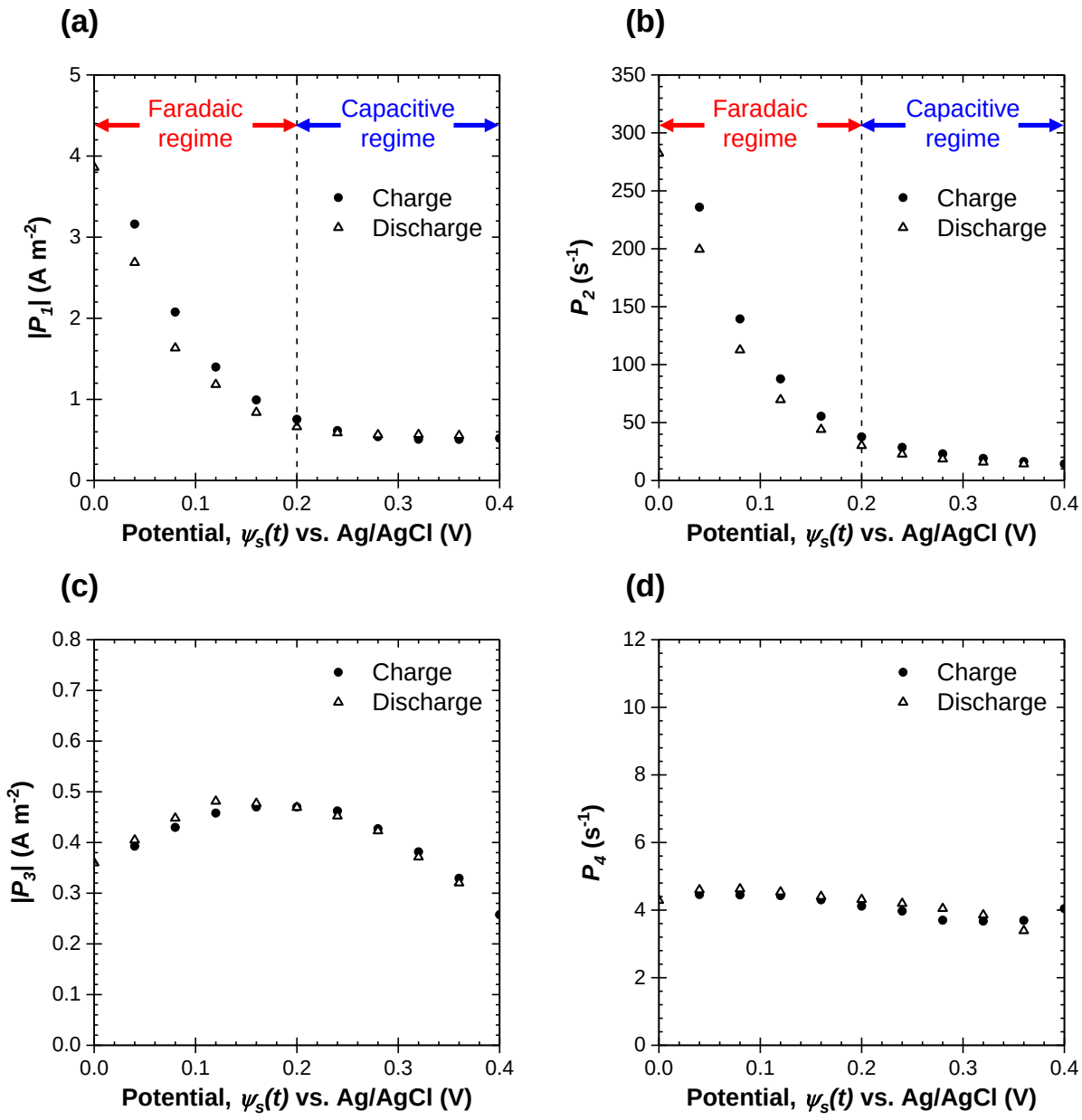

Figure 5.7: Fitting parameters of the modified SPECS model associated with Faradaic reactions (a) $|P_1(\psi_s)|$, (b) $P_2(\psi_s)$, (c) $|P_3(\psi_s)|$, and (d) $P_4(\psi_s)$ as functions of potential ψ_s during a charging/discharging cycle between $\psi_{s,min} = 0$ V and $\psi_{s,max} = 0.4$ V with potential steps $\Delta\psi_s = 0.04$ V.

the kinetics of EDL formation, either at the interface of the electrode with the bulk electrolyte (geometric surface) or at the interfacial surface of micropores and mesopores within the porous electrode (porous surface), did not vary significantly with changing potential. Moreover, as expected, the geometric surface was more accessible than the porous surface such that at any potential $\tau_{EDL1}(\psi_s) < \tau_{EDL2}(\psi_s)$.

In order to investigate the influence of electrode particle layer number N on the fitting parameters, three cases were compared with $N = 2.5$, 3.5, and 4.5, respectively. Figure B.5 in Appendix B plots the four fitting parameters associated with EDL formation at the electrode/electrolyte interface: (a) $R_1(\psi_s)$, (b) $C_1(\psi_s)$, (c) $R_2(\psi_s)$, and (d) $C_2(\psi_s)$. Here, the porous surface area $A_{BET,2}$ increased with larger particle layer number [Figure 5.1(c)]. For example, the three cases provided $A_{BET,2}$ of 176.7, 265.1, and 353.4 nm^2, respectively. As the porous surface area available for EDL formation increased, the porous surface EDL footprint capacitance $C_2(\psi_s)$ increased correspondingly [Figure B.5(d)]. By contrast, the geometric surface area $A_{BET,1}$ remained the same at 44.2 nm^2 regardless of particle layer number [Figure 5.1(b)]. Therefore, all three cases had similar geometric surface EDL footprint capacitances $C_1(\psi_s)$ [Figure B.5(b)]. The same applied for the footprint resistances associated with the geometric surface $R_1(\psi_s)$ and the porous surface $R_2(\psi_s)$ EDL [Figures B.5(a) and B.5(c)], chiefly because the main factors contributing to the resistance of EDL formation, such as ion transport properties in the electrolyte, or the tortuosity of the porous pseudocapacitive electrode, remained the same regardless of particle layer number.

Figures 5.7(a) and 5.7(b) indicate that $|P_1(\psi_s)|$ and $P_2(\psi_s)$ were strongly dependent on the rate of interfacial charge transfer kinetics but were the same at any given potential ψ_s during charging and discharging. Indeed, the diminishing kinetics rate with increasing potential and the transition from the Faradaic to the capacitive regime led to a sharp decrease in both $|P_1(\psi_s)|$ and $P_2(\psi_s)$. In fact, according to our previous study [186] validating the original SPECS fitting function [Equation (5.24)] for 1D planar pseudocapacitive electrodes, $|P_1(\psi_s)|$ was a function of both Λ and b_1, while $P_2(\psi_s)$ was a function of b_1 only. Specifically, with increasing potential, the interfacial charge transfer resistance R_{ct} increased but the diffusion resistance R_d was relatively constant, such that Λ decreased according to Equation

(5.9). This meant that b_1, as the first root of Equation (5.8), decreased as well. As a result, both $|P_1(\psi_s)|$ and $P_2(\psi_s)$ decreased sharply with increasing potential, according to Equation (5.11). Finally, a parametric study was performed where the reaction rate constant k_0 varied between 10^{-10} and 10^{-8} $\mathrm{m}^{2.5}$ $\mathrm{mol}^{-0.5}$ s^{-1} for different cases. Here, increasing k_0 increased the rate of interfacial charge transfer kinetics and resulted in faster surface redox reactions. Consequently, both $|P_1(\psi_s)|$ and $P_2(\psi_s)$ increased. These results are described in detail in Appendix B (see Section B.3.1).

Figures 5.7(c) and 5.7(d) indicate that $|P_3(\psi_s)|$ and $P_4(\psi_s)$ did not vary significantly with changing potential. This suggests that the transport rate of ion intercalation/deintercalation in/out of the electrode spherical particles and the associated time constants were relatively constant across the entire potential window [134]. Indeed, the local concentration of Li^+ ions in the electrode $c_{1,P}(\mathbf{r}, t)$ was governed by the 3D transient mass diffusion equation (see Appendix B) and the ion diffusion coefficient was assumed to be constant with $D_{1,P} = 10^{-14}$ m^2 s^{-1} for the baseline case. Finally, a parametric study was performed where the ion diffusion coefficient $D_{1,P}$ varied between 10^{-14} and 10^{-12} m^2 s^{-1} for different cases. Here, increasing $D_{1,P}$ increased the rate of solid state ion diffusion. Consequently, both $|P_3(\psi_s)|$ and $P_4(\psi_s)$ increased. These results are described in detail in Appendix B (see Section B.3.2).

Figure 5.8(a) plots the numerically simulated cyclic voltammograms after imposing the potential $\psi_s(0, y, z, t)$ given by Equation (5.15) in the same porous pseudocapacitive electrode as that simulated in Figures 5.6 and 5.7. The potential window ranged from $\psi_{s,min} = 0$ V to $\psi_{s,max} = 0.4$ V, and the scan rate was chosen as $\nu = \Delta\psi_s/t_e = 0.1$ V s^{-1}, both consistent with the conditions in the SPECS simulations. The overall shapes of the simulated cyclic voltammograms were similar to those typically measured experimentally [218]. Figures 5.8(b) and 5.8(c) compare the EDL footprint capacitances for the geometric surface $C_1(\psi_s)$ and the porous surface $C_2(\psi_s)$ obtained from SPECS using the modified fitting function with the differential capacitances $C_{diff,1}(\psi_s)$ and $C_{diff,2}(\psi_s)$ calculated from cyclic voltammograms [Equation (5.22)]. Good agreement was obtained between the two independent methods during both charging and discharging. Moreover, Figure 5.8(d) compares the total EDL footprint capacitance $C_{EDL}(\psi_s)$ calculated as the sum of $C_1(\psi_s)$ and $C_2(\psi_s)$ [Equation

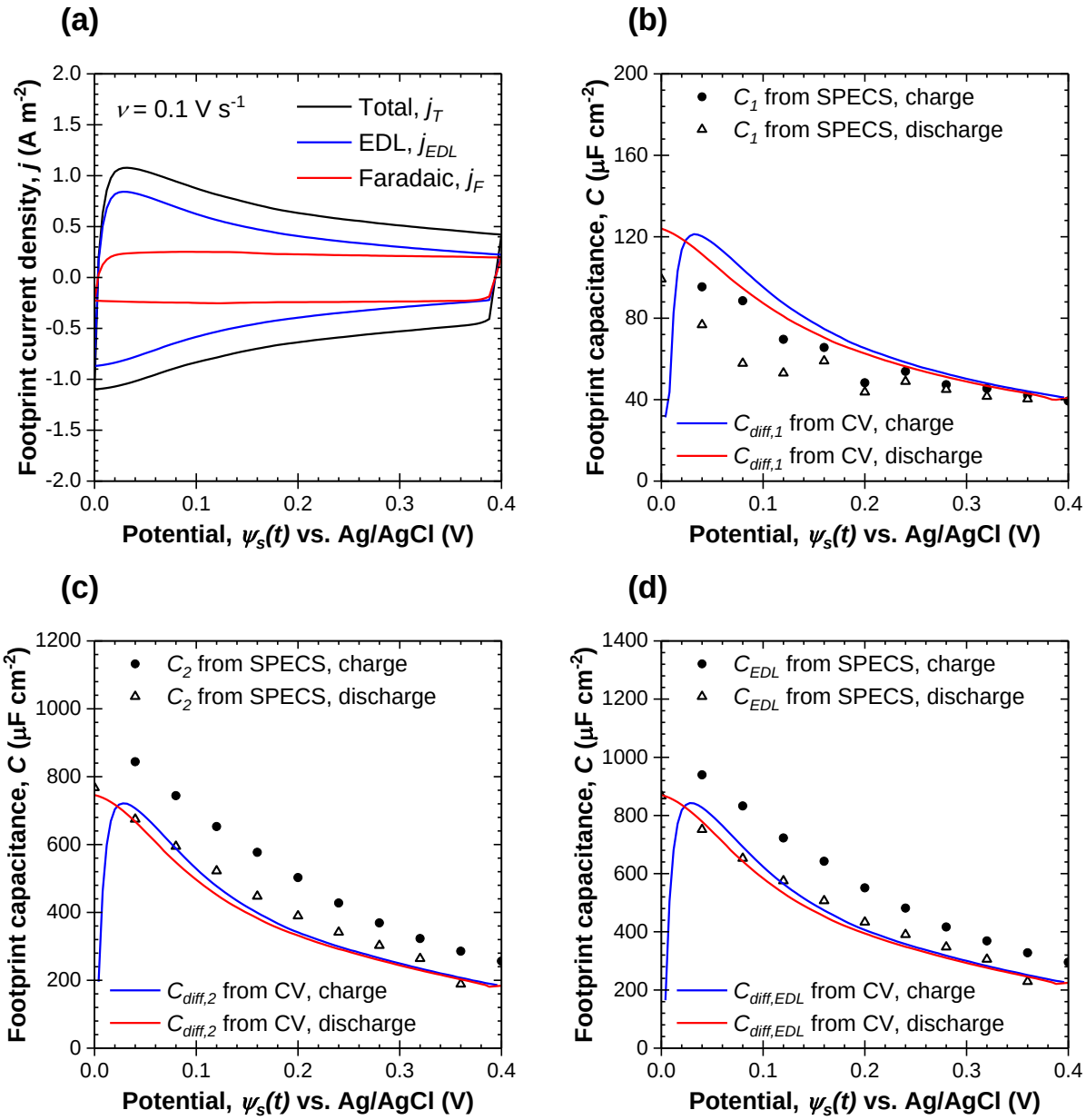

Figure 5.8: (a) Numerically simulated cyclic voltammograms after imposing the potential $\psi_s(0, y, z, t)$ given by Equation (5.15) in the porous pseudocapacitive electrode within a potential window from $\psi_{s,min} = 0$ V to $\psi_{s,max} = 0.4$ V at scan rate $\nu = 0.1$ V s^{-1}. Comparison of capacitances (b) $C_1(\psi_s)$, (c) $C_2(\psi_s)$, and (d) $C_{EDL}(\psi_s)$ obtained from SPECS using the modified fitting function with differential capacitances (b) $C_{diff,1}(\psi_s)$, (c) $C_{diff,2}(\psi_s)$, and (d) $C_{diff,EDL}(\psi_s)$ calculated from cyclic voltammograms [Equations (5.22) and (5.23)].

(5.3)] with the differential total EDL footprint capacitance $C_{diff,EDL}(\psi_s)$ calculated from cyclic voltammograms [Equation (5.23)]. Here also, $C_{EDL}(\psi_s)$ was in good agreement with $C_{diff,EDL}(\psi_s)$ during both charging and discharging. These results demonstrate that the modified SPECS method [Equation (5.27)] can accurately predict the contributions from EDL formation both at the geometric surface and at the porous surface to the differential EDL capacitance.

5.3.4 MUSCA method

The MUSCA method was applied to the various fitted footprint current densities $j_i^M(t)$ at a given scan rate ν to obtain the mean footprint current densities $j_i^A(\psi_s)$ at potential ψ_s expressed as,

$$j_i^A(\psi_s) = \frac{1}{t_\nu}\int_0^{t_\nu} j_i^M(t)\mathrm{d}t \tag{5.28}$$

with subscript $i = T$, EDL, $EDL1$, $EDL2$, F, $F1$, or $F2$. Then, cyclic voltammograms were reconstructed by plotting $j_i^A(\psi_s)$ vs. ψ_s. Finally, the integral footprint capacitance $C_{int,i}^A(\nu)$ associated with each charge storage mechanism at scan rate ν was determined as [203],

$$C_{int,i}^A(\nu) = \oint \frac{j_i^A(\psi_s)}{2\nu(\psi_{s,max} - \psi_{s,min})}\mathrm{d}\psi_s. \tag{5.29}$$

Figure 5.9(a) indicates that the total $j_T^A(\psi_s)$, EDL $j_{EDL}^A(\psi_s)$, and Faradaic $j_F^A(\psi_s)$ mean footprint current densities obtained from the MUSCA method within the potential window from $\psi_{s,min} = 0$ V to $\psi_{s,max} = 0.4$ V at scan rate $\nu = 0.1$ V s^{-1} were comparable with the numerically simulated cyclic voltammograms during both charging and discharging. Figures 5.9(b) and 5.9(c) proceed to plot the reconstructed cyclic voltammograms associated with each charge storage mechanism at scan rates $\nu = 0.1$ V s^{-1} and $\nu = 10$ V s^{-1}. Finally, Figure 5.9(d) plots the corresponding integral footprint capacitance $C_{int,i}^A(\nu)$ for scan rates ν from 0.1 to 10 V s^{-1} [Equation (5.29)]. Note that the chosen scan rates were higher than those typically imposed in experimental measurements. This was attributed to the fact that the simulated electrode was thin and the influence of resistive losses and ion diffusion limitations only became apparent at such high scan rates. In fact, similar behavior was also

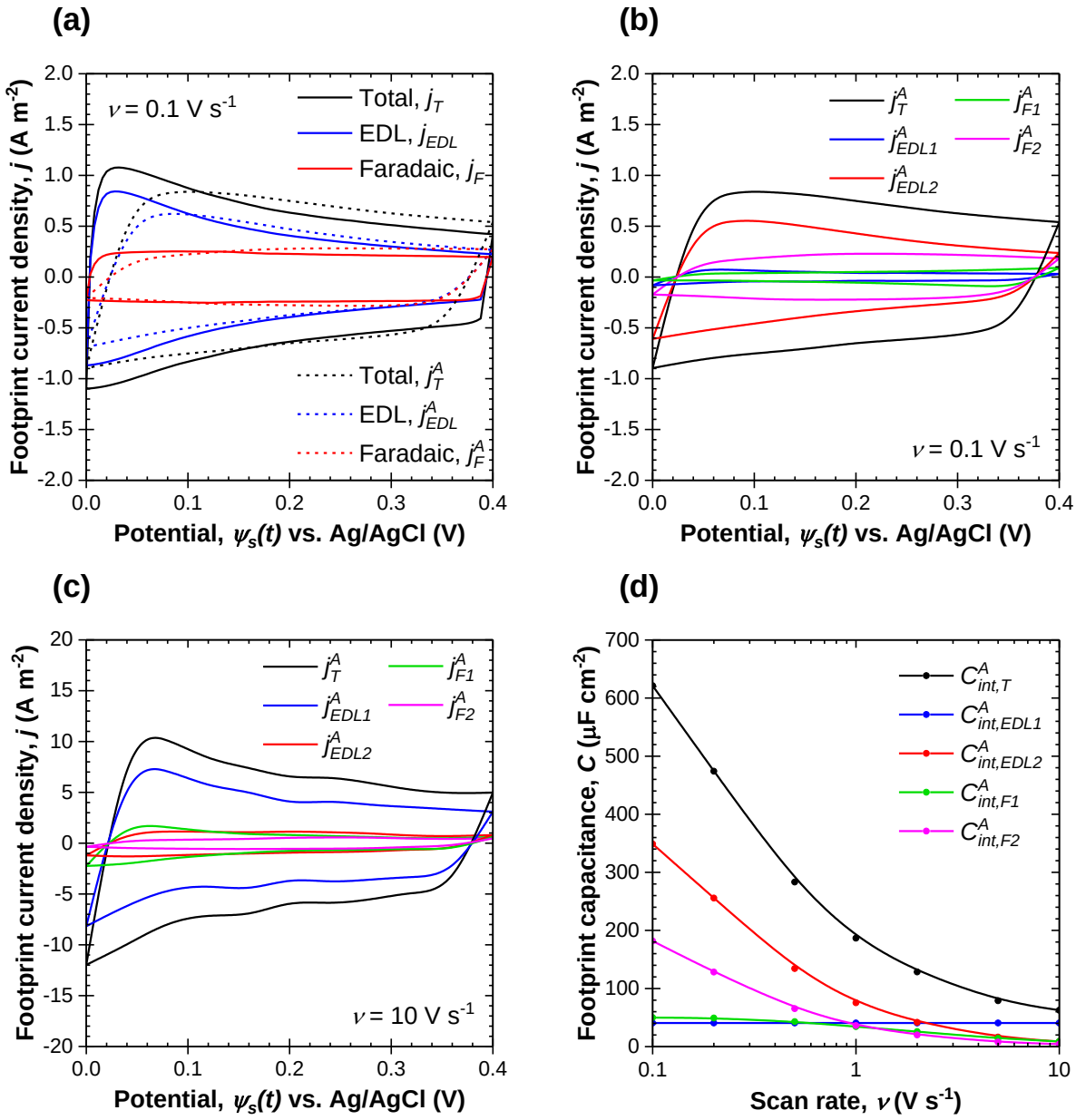

Figure 5.9: (a) Comparison of total $j_T^A(\psi_s)$, EDL $j_{EDL}^A(\psi_s)$, and Faradaic $j_F^A(\psi_s)$ mean footprint current densities obtained from the MUSCA method [Equations (5.13) and (5.28)] with the numerically simulated cyclic voltammograms at scan rate $\nu = 0.1$ V s^{-1}. Reconstructed cyclic voltammograms associated with each charge storage mechanism at scan rates (b) $\nu = 0.1$ V s^{-1} and (c) $\nu = 10$ V s^{-1}. (d) Corresponding integral footprint capacitance $C_{int,i}^A(\nu)$ for scan rates ν from 0.1 to 10 V s^{-1} [Equation (5.29)].

observed in our previous studies simulating CV measurements in planar pseudocapacitive electrodes [135] and in ordered carbon spheres EDLC electrodes [215]. Figure 5.9(d) suggests that the integral total footprint capacitance $C^{A}_{int,T}(\nu)$ decreased with increasing scan rate. The integral geometric surface EDL footprint capacitance $C^{A}_{int,EDL1}(\nu)$ remained nearly constant across the range of scan rates considered. This was due to the fast transport and adsorption of ions at the geometric surface [219]. By contrast, the integral porous surface EDL footprint capacitance $C^{A}_{int,EDL2}(\nu)$ decreased monotonously with increasing scan rate due to slower ion transport through the tortuous porous electrode. On the other hand, the integral surface-controlled Faradaic footprint capacitance $C^{A}_{int,F1}(\nu)$ first remained constant, then decreased as the scan rate increased above 0.2 V s^{-1} when the rate of interfacial charge transfer kinetics became limiting. Finally, the integral diffusion-controlled Faradaic footprint capacitance $C^{A}_{int,F2}(\nu)$ decreased monotonously with increasing scan rate due to rate-limited transport associated with solid state ion diffusion in the particle [219]. At low scan rates, EDL formation and diffusion-controlled Faradaic reactions within the porous electrode contributed to the majority of the total charge storage. However, as the scan rate increased, EDL formation and Faradaic reactions at the geometric surface became the dominant charge storage mechanism.

5.4 Chapter summary

In a previous study, we numerically validated the SPECS method proposed by Dupont and Donne [113–115] against numerical simulations for 1D planar pseudocapacitive electrodes. However, in this follow-up study, numerical simulations showed that the original SPECS fitting function could not adequately describe the current response in 3D porous pseudocapacitive electrodes. Therefore, the SPECS method was modified with a new fitting function to account for contributions from EDL formation at the electrode surface or at the electrode/electrolyte interface within the porous electrode, and from surface-controlled or diffusion-controlled Faradaic reactions. The modified SPECS method was successfully validated against numerical simulations for 3D porous pseudocapacitive electrodes, based on the

modified Poisson-Nernst-Planck (MPNP) model coupled with the Frumkin-Butler-Volmer theory to reproduce experimental data obtained from the SPECS method. Specifically, the numerically simulated total $j_T(t)$, EDL $j_{EDL}(t)$, and Faradaic $j_F(t)$ current densities were properly fitted by the current densities $j_T^M(t)$, $j_{EDL}^M(t)$, and $j_F^M(t)$ retrieved from the modified SPECS fitting function. Furthermore, the capacitances associated with EDL formation obtained from SPECS were in good agreement with those obtained from CV simulations. Finally, cyclic voltammograms were reconstructed from the MUSCA method. The integral capacitances associated with various charge storage mechanisms illustrated the faster kinetics of EDL formation at the geometric surface vs. at the porous surface, and the faster kinetics of surface-controlled vs. diffusion-controlled Faradaic reactions. Overall, this modified fitting function makes the SPECS method more accurate in distinguishing the different charge storage mechanisms in actual porous pseudocapacitive electrodes.

CHAPTER 6

Conclusions and Future Work

6.1 Conclusions

The objectives of this dissertation were (i) to investigate the effect of particle size on thermodynamics and energy dissipation in electrodes made of $Ti_2Nb_2O_9$ microparticles or nanoparticles, (ii) to demonstrate the superior electrochemical performance and reduced heat generation in 3D printed vs. 2D tape-casted NMC622 electrodes, (iii) to develop a novel microcalorimetry electrothermal impedance spectroscopy (ETIS) measurement method to rapidly determine the open-circuit voltage U_{OCV}, the entropic potential $\partial U_{OCV}/\partial T$, and the partial entropy changes at each electrode of a battery cell, and (iv) to numerically adapt and validate the step potential electrochemical spectroscopy (SPECS) method for three-dimensional porous pseudocapacitive electrodes.

First, this dissertation investigated the tunnel-structured $Ti_2Nb_2O_9$ with fast charging capabilities at potentials above 1.0 V vs. Li/Li^+ to limit SEI and dendrite formation. A novel sol-gel method was proposed to synthesize $Ti_2Nb_2O_9$ nanoparticles (around 50 nm) for use in lithium-ion battery electrodes. These electrodes were compared with those made of $Ti_2Nb_2O_9$ microparticles (around 1 μm) synthesized by the traditional solid-state method using unique characterization techniques including potentiometric entropy measurements and *operando* isothermal calorimetry. Cyclic voltammetry and galvanostatic cycling demonstrated the superior specific capacity, greater cycling reversibility, and smaller capacity drop with increasing current for electrodes made of $Ti_2Nb_2O_9$ nanoparticles compared to those made of $Ti_2Nb_2O_9$ microparticles. Furthermore, *in situ* XRD measurements revealed only minor and reversible distortions to the crystallographic structures of both types of $Ti_2Nb_2O_9$. In ad-

dition, potentiometric entropy measurements indicated that both types of electrodes underwent lithium ion intercalation/deintercalation in a homogeneous solid solution of $Ti_2Nb_2O_9$ during cycling. In fact, overlapping entropic potential profiles suggested that the particle size had no influence on the thermodynamics behavior of $Ti_2Nb_2O_9$. However, according to *operando* isothermal calorimetry, electrodes made of $Ti_2Nb_2O_9$ nanoparticles exhibited less energy dissipation and heat generation at any given C-rate than those made of $Ti_2Nb_2O_9$ microparticles, thanks to their smaller particle size and larger specific surface area which facilitate lithium ion transport.

Then, this dissertation compared the thermodynamics behavior, ion transport, and energy dissipation in NMC622 electrodes made by a novel 3D printing technology with those made by the conventional 2D tape casting procedure. Here also, potentiometric entropy measurements indicated that both types of electrodes had similar thermodynamics behavior. They both underwent lithium deintercalation in a homogeneous solid solution of NMC622 followed by a transition from a hexagonal (H1) phase to another hexagonal (H2) phase through a monoclinic (M) phase, as identified in previous studies. *Operando* isothermal calorimetry revealed that, at high C-rates, the 3D printed electrodes exhibited larger specific capacity and better rate performance than the 2D tape-casted electrodes. This could be attributed to the larger electrode/electrolyte interfacial surface area and electrical conductivity, and to the faster lithium ion transport in the 3D printed electrodes. These features also contributed to the smaller instantaneous heat generation rates and the reduced overall specific electrical energy and thermal energy dissipation per unit charge stored at the 3D printed electrodes than at the 2D tape-casted electrodes when tested under the same conditions. The superior electrochemical performance and the reduced heat generation of 3D printed NMC622 electrodes highlights the prospects of employing additive manufacturing techniques to create electrodes for fast charging batteries.

Furthermore, this dissertation presented a novel and fast microcalorimetry ETIS measurement method using an *operando* isothermal calorimeter to determine the open-circuit voltage U_{OCV}, the entropic potential $\partial U_{OCV}/\partial T$, and the partial entropy changes at each electrode as functions of the state of charge of a battery cell, all within only a few hours while

other state-of-the-art methods would take at least a few days. The apparatus was designed for cells with material mass loadings on the order of milligrams and measured heat generation rates on the order of microwatts. The method consists of imposing a sinusoidal current and measuring the potential response as well as the heat generation rates at each electrode separately. The open-circuit voltage U_{OCV} of the cell was acquired by time-averaging the measured potential response. Furthermore, FFT analysis of the measured total heat generation rate was used to retrieve the entropic potential $\partial U_{OCV}/\partial T$ of the entire cell without having to measure the cell potential at several different temperatures. The procedure was first validated numerically and then demonstrated experimentally with battery cells consisting of PNb_9O_{25} or $TiNb_2O_7$ working electrodes and metallic lithium counter electrodes. The open-circuit voltage and the normalized entropic potential retrieved from the novel microcalorimetry ETIS measurements agreed well with those previously determined by potentiometric entropy measurements based on GITT at three different temperatures [1, 59]. Finally, the partial entropy changes at each electrode were calculated from the individually measured heat generation rates. Compared to other state-of-the-art methods, this is the first method capable of retrieving the partial entropy changes of LIB materials at each electrode.

Finally, this dissertation focused on numerical simulations of another novel characterization method, namely the SPECS method in three-dimensional porous pseudocapacitive electrodes. In a previous study, we numerically validated the SPECS method proposed by Dupont and Donne [113–115] against numerical simulations for 1D planar pseudocapacitive electrodes. However, this follow-up study showed that the original SPECS fitting function could not adequately describe the current response in 3D porous pseudocapacitive electrodes. Therefore, the SPECS method was modified with a new fitting function to account for contributions from EDL formation at the electrode surface or at the electrode/electrolyte interface within the porous electrode, and from surface-controlled or diffusion-controlled Faradaic reactions. The modified SPECS method was successfully validated against numerical simulations for 3D porous pseudocapacitive electrodes, based on the modified Poisson-Nernst-Planck model coupled with the Frumkin-Butler-Volmer theory to reproduce experimental data obtained from the SPECS method. Furthermore, the capacitances associated with

EDL formation obtained from SPECS were in good agreement with those obtained from CV simulations. Finally, cyclic voltammograms were reconstructed from the multiple potential step chronoamperometry (MUSCA) method. The integral capacitances associated with various charge storage mechanisms illustrated the faster kinetics of EDL formation at the geometric surface vs. at the porous surface, and the faster kinetics of surface-controlled vs. diffusion-controlled Faradaic reactions. Overall, this modified fitting function makes the SPECS method more accurate in distinguishing the different charge storage mechanisms in actual porous pseudocapacitive electrodes.

6.2 Future work

6.2.1 Effect of temperature on electrochemical performance, transport phenomena, and thermodynamics of γ-phase MnO_2

Chapter 2 showed that electrodes made of $Ti_2Nb_2O_9$ microparticles or nanoparticles had similar thermodynamics behavior due to their identical chemical composition. However, electrodes made of $Ti_2Nb_2O_9$ nanoparticles exhibited not only superior electrochemical performance but also reduced heat generation compared to those made of microparticles. This difference was attributed to the enhanced reaction kinetics and ion transport within $Ti_2Nb_2O_9$ nanoparticles compared to microparticles. Similarly, Chapter 3 showed that 3D printed or 2D tape-casted NMC622 electrodes had similar thermodynamics behavior. However, at high C-rates, the 3D printed electrodes exhibited larger specific capacity, better rate performance, and reduced heat generation than the 2D tape-casted electrodes. This difference came as a result of the larger electrode/electrolyte interfacial surface area and electrical conductivity, and the faster lithium ion transport in the 3D printed electrodes. Both studies demonstrated that the intrinsic microstructure of the electrodes have a significant effect on their performance.

The external conditions that the electrodes operate in, specifically the temperature, is also a major factor when evaluating their thermodynamics behavior, captured by the open-circuit

voltage $U_{OCV}(x,T)$ and the entropic potential $\partial U_{OCV}(x,T)/\partial T$. In light of the growing focus on employing electrochemical energy storage systems in extreme environments, future work should consider performing electrochemical tests, potentiometric entropy measurements, and *operando* isothermal calorimetry of battery or pseudocapacitive devices at varying temperatures. In particular, low temperatures generally slow down the ion transport within the electrodes, and may also shift the surface kinetics for the redox reactions [152].

Here we use γ-phase MnO_2 as a reference pseudocapacitive electrode material for its excellent specific capacity and rate performance [106]. A batch of CR2032 coin cells were fabricated consisting of (i) γ-phase MnO_2 working electrode (mass ratio of MnO_2:conductive carbon:PVDF = 80:10:10, mass loading around 2 mg/cm^2, 0.5 inch diameter), (ii) lithium metal counter electrode (250 μm thickness, 16 mm diameter), (iii) Celgard 2325 separator, and (iv) 1.2 M $LiPF_6$ in EC:EMC 3:7 w/w electrolyte. Figure 6.1 plots the potential profiles during galvanostatic cycling of γ-phase MnO_2/lithium metal coin cells cycled between 2.0 and 4.0 V vs. Li/Li$^+$ at C-rate of C/10 at temperature of (a) 45 °C, (b) 20 °C, and (c) -5 °C, as well as the comparison of the third cycle at each temperature. Here, the coin cells showed consistently increasing specific capacity with increasing temperature, including both the first formation cycle and the two subsequent cycles. Figure 6.2 plots the cyclic voltammogram of γ-phase MnO_2/lithium metal coin cells cycled between 2.0 and 3.5 V vs. Li/Li$^+$ at scan rates ν ranging between 0.1 and 10 mV/s at temperature of (a) 45 °C, (b) 20 °C, and (c) -5 °C, as well as the comparison of the specific integral capacitance $C_{int,m}$ at each temperature. Here also, the coin cells showed consistently smaller polarization and better performance with increasing temperature, particularly at high scan rates. Both tests suggest that the rates of transport phenomena within the electrodes is enhanced at elevated temperatures and diminished under freezing conditions.

Finally, Figure 6.3 plots the cell potential $V(x,T)$, the open-circuit voltage $U_{OCV}(x,T)$, and the entropic potential $\partial U_{OCV}(x,T)/\partial T$ of γ-phase MnO_2/lithium metal coin cells as functions of lithium composition x during lithiation at C-rate of C/10 at temperature of (a) 45 °C, (b) 20 °C, and (c) -5 °C, as well as the comparison between the profiles of entropic potential $\partial U_{OCV}(x,T)/\partial T$ as a function of open-circuit voltage $U_{OCV}(x,T)$ at each temper-

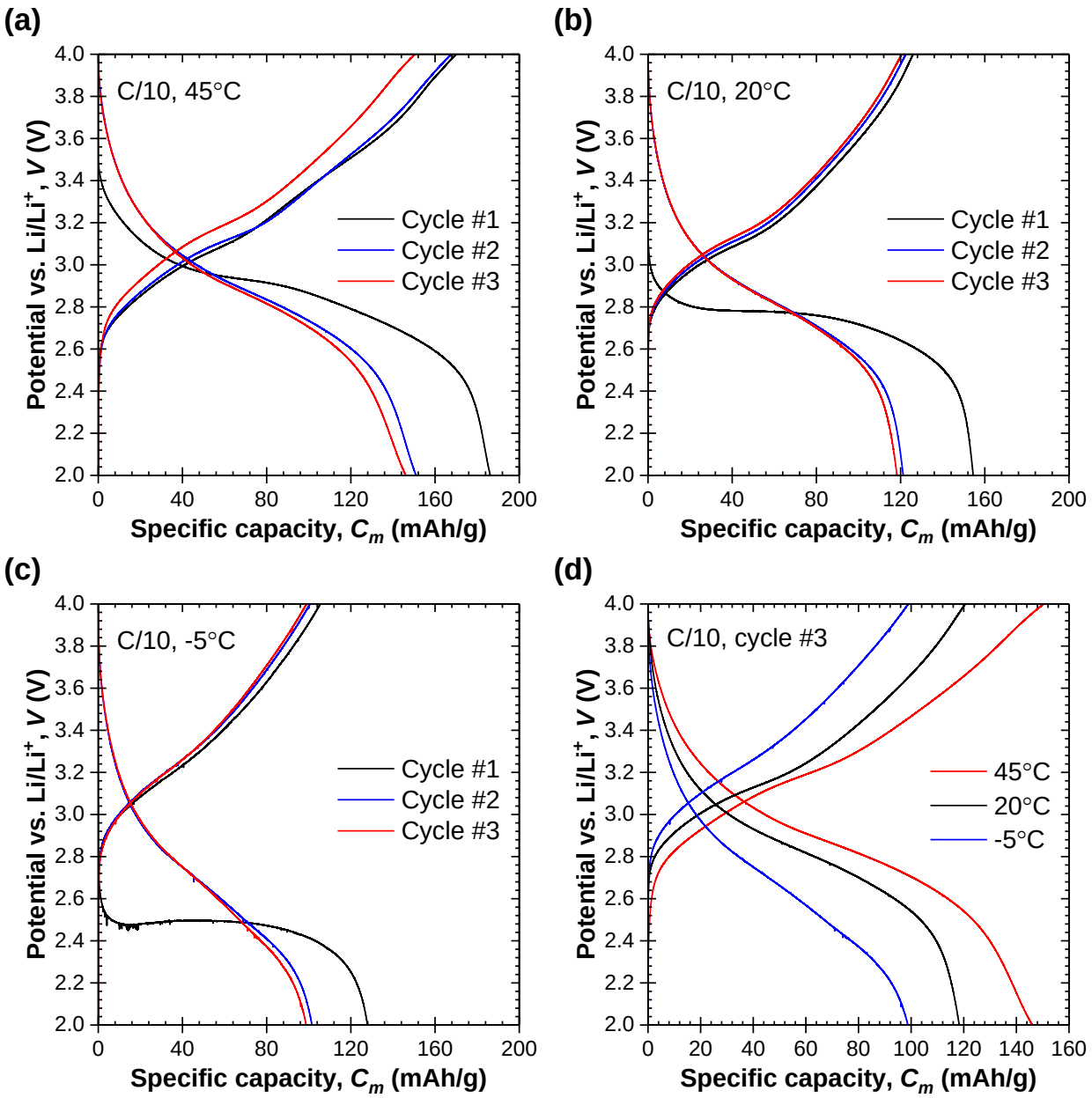

Figure 6.1: Potential profiles during galvanostatic cycling of γ-phase MnO_2/lithium metal coin cells cycled between 2.0 and 4.0 V vs. Li/Li^+ at C-rate of C/10 at temperature of (a) 45 °C, (b) 20 °C, and (c) -5 °C, as well as (d) comparison of the third cycle at each temperature.

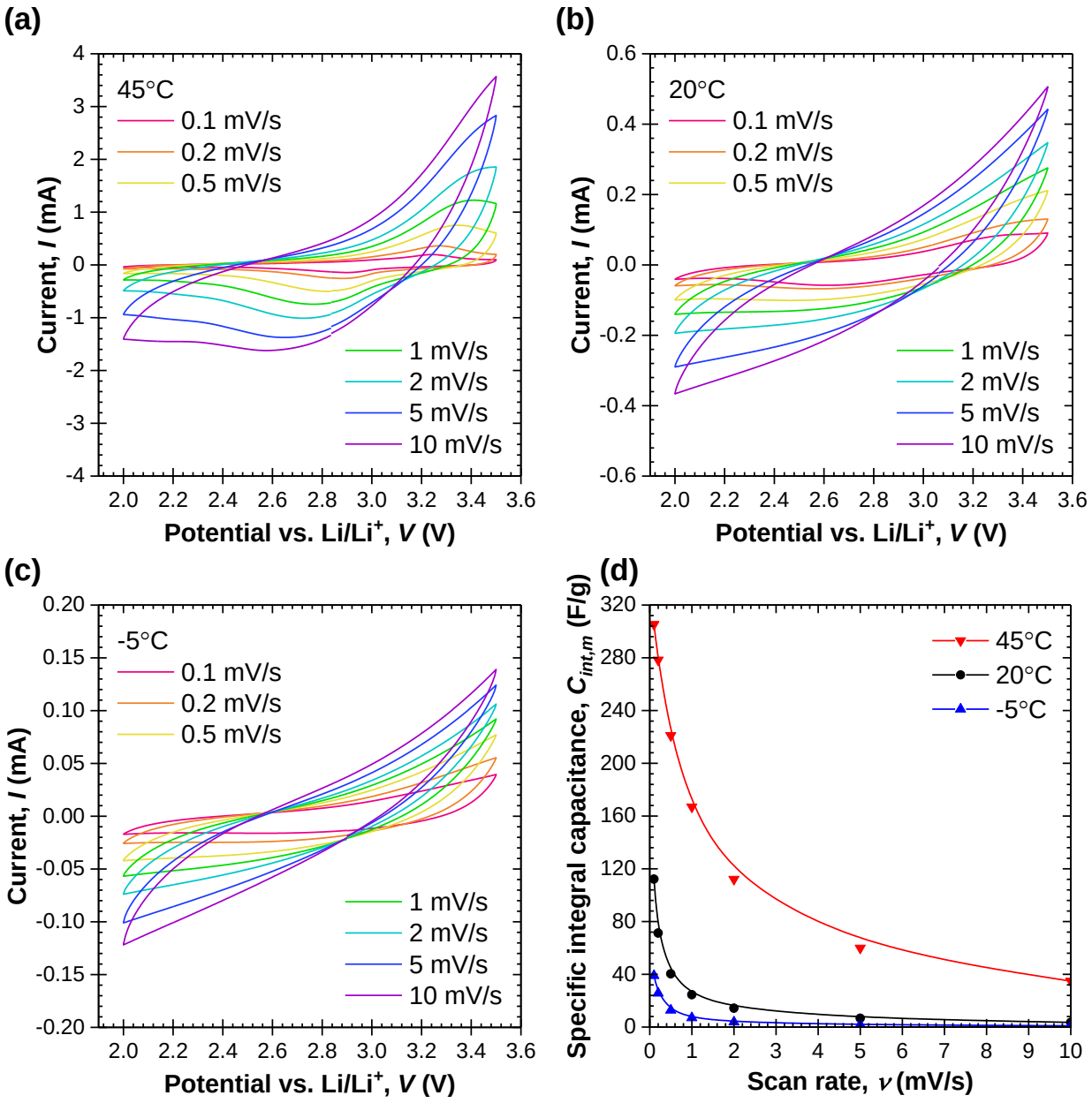

Figure 6.2: Cyclic voltammogram of γ-phase MnO_2/lithium metal coin cells cycled between 2.0 and 3.5 V vs. Li/Li^+ at scan rates ν ranging between 0.1 and 10 mV/s at temperature of (a) 45 °C, (b) 20 °C, and (c) -5 °C, as well as (d) comparison of the specific integral capacitance $C_{int,m}$ at each temperature.

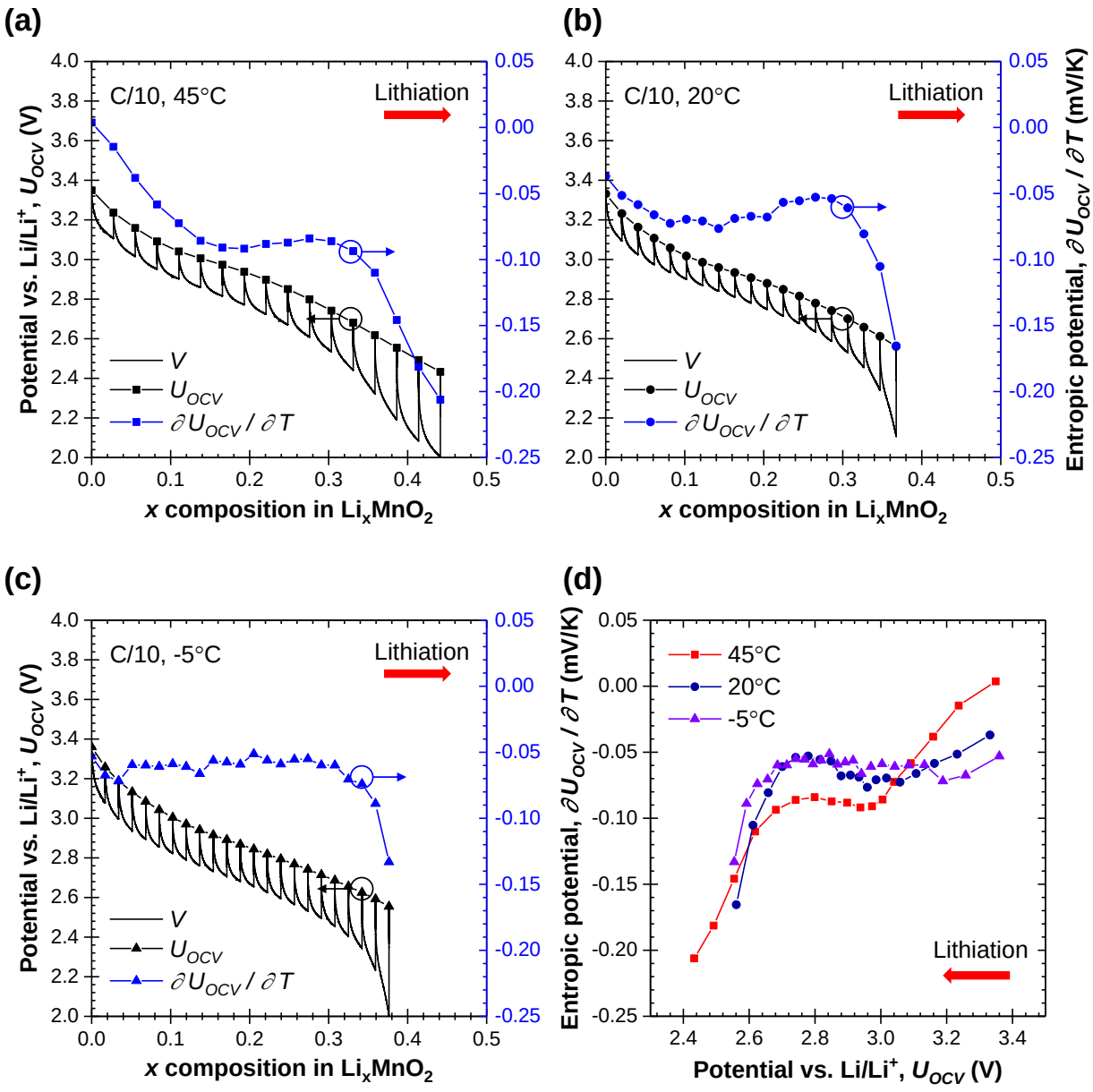

Figure 6.3: Cell potential $V(x,T)$, open-circuit voltage $U_{OCV}(x,T)$, and entropic potential $\partial U_{OCV}(x,T)/\partial T$ of γ-phase MnO_2/lithium metal coin cells as functions of lithium composition x during lithiation at C-rate of C/10 at temperature of (a) 45 °C, (b) 20 °C, and (c) -5 °C. (d) Comparison between the profiles of entropic potential $\partial U_{OCV}(x,T)/\partial T$ as a function of open-circuit voltage $U_{OCV}(x,T)$ at each temperature.

ature. Interestingly, these results from potentiometric entropy measurements indicate that the temperature variations also impacted the thermodynamics of the γ-phase MnO_2. The open-circuit voltage $U_{OCV}(x,T)$ exhibited an inflection point for $0.1 < x < 0.2$ at 45 °C, which almost disappeared at -5 °C. The entropic potential $\partial U_{OCV}(x,T)/\partial T$ visibly decreased alongside a tilde-shaped fluctuation for $0.1 < x < 0.3$ at 45 °C, but at -5 °C it became relatively flat and only dropped towards the end of lithiation. This suggests that both the ion intercalation and the ion ordering phenomena were inhibited at low temperatures, possibly due to reduced ion mobility and thermal agitation under those conditions. Further investigations could be conducted to explain the mechanisms behind such observations. This study would give additional insight into the behavior of electrode materials at various temperatures, from the perspectives of transport phenomena and thermodynamics. Overall, it would provide guidelines for the synthesis, fabrication, and design of battery or pseudocapacitive electrodes with improved performance for extreme temperature applications.

6.2.2 Developing strategies to retrieve material and electrochemical properties from various characterization methods of redox-active intercalation electrodes

Chapter 5 presented numerical simulations of a three-dimensional porous pseudocapacitive electrode model. In constitutive relationships (Section 5.2.4), we described that the values of various properties required for the physical model (Table 5.1) were generally retrieved from the literature based on past experimental measurements. The completeness and accuracy of these values were important for the validity of the physical model. Therefore, it would be useful to summarize and refine strategies of using different characterization methods to retrieve the key material and electrochemical properties of battery or pseudocapacitive electrodes or devices.

Figure 6.4 presents a proposed flowchart for this entire procedure considering a redox-active intercalation electrode in a three-electrode configuration. The electrode is tested under three different electrochemical characterization methods: cyclic voltammetry (CV), step

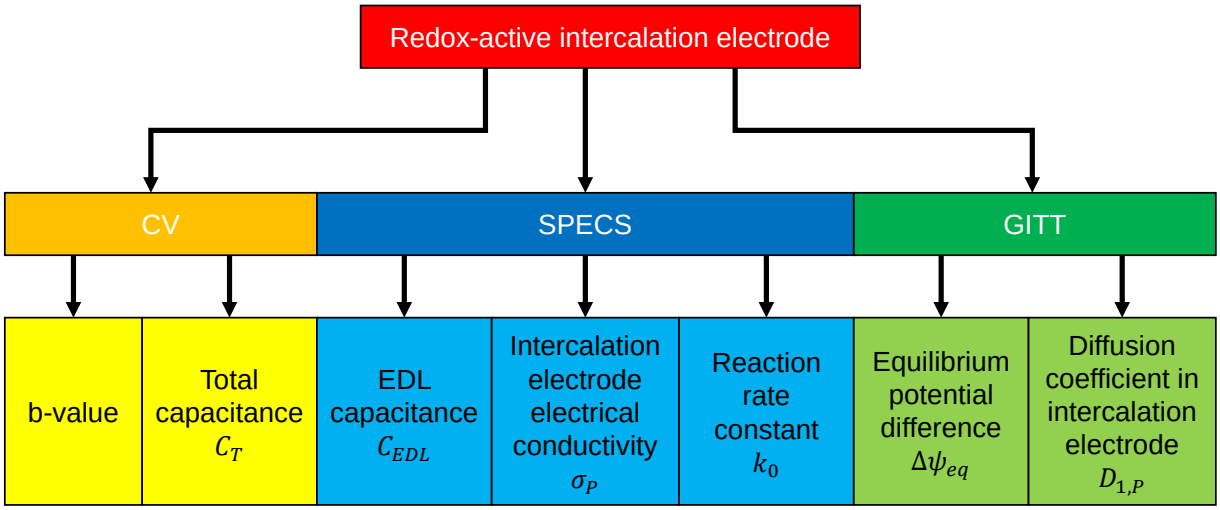

Figure 6.4: Procedure using different characterization methods to retrieve the key material and electrochemical properties imposed in the physical model.

potential electrochemical spectroscopy (SPECS), and galvanostatic intermittent titration technique (GITT). The CV method performs a potential sweep within a potential window at different scan rates and records the associated currents. From the cyclic voltammograms, the total capacitance of the electrode, both in integral $C_{int,T}$ and differential $C_{diff,T}$ form, can be calculated along with the b-value across this potential window. The SPECS method consists of numerically fitting the total current response to a series of imposed potential steps. Consequently, the respective contributions of EDL formation and Faradaic reactions can be distinguished. Moreover, as presented in Chapter 5, for a porous electrode, eight physical parameters can be determined from the fitting process. On the one hand, the resistances R_1 and R_2 as well as the capacitances C_1 and C_2 are associated with EDL formation. The total EDL resistance R_{EDL} and the total EDL capacitance C_{EDL} can be determined according to Equation 5.3, with R_{EDL} related to the electrical conductivity σ_P of the intercalation electrode. On the other hand, the fitting parameters P_1, P_2, P_3, and P_4 are associated with Faradaic reactions. As suggested in Appendix B, P_1 and P_2 are qualitatively dependent on the reaction rate constant k_0. Further investigations could be

conducted to establish the exact quantitative relationships between these fitting parameters and the properties of interest. The GITT method imposes a series of current pulses and records the potential response. Here, the ion diffusion coefficient in the electrode $D_{1,P}$ can be retrieved from the potential decay during each relaxation period. In addition, the equilibrium potential difference $\Delta\psi_{eq}$ can be identified from the open-circuit voltage U_{OCV} at the end of each relaxation period. Overall, this entire procedure could be first established numerically and then demonstrated experimentally with known pseudocapacitive electrodes such as MnO_2 and Nb_2O_5. In fact, the end goal would be to apply the developed strategies in actual experiments for systematic retrieval of the required properties for any battery or pseudocapacitive electrodes or devices.

APPENDIX A

Supplementary Materials for Chapter 2

A.1 Structural characterization

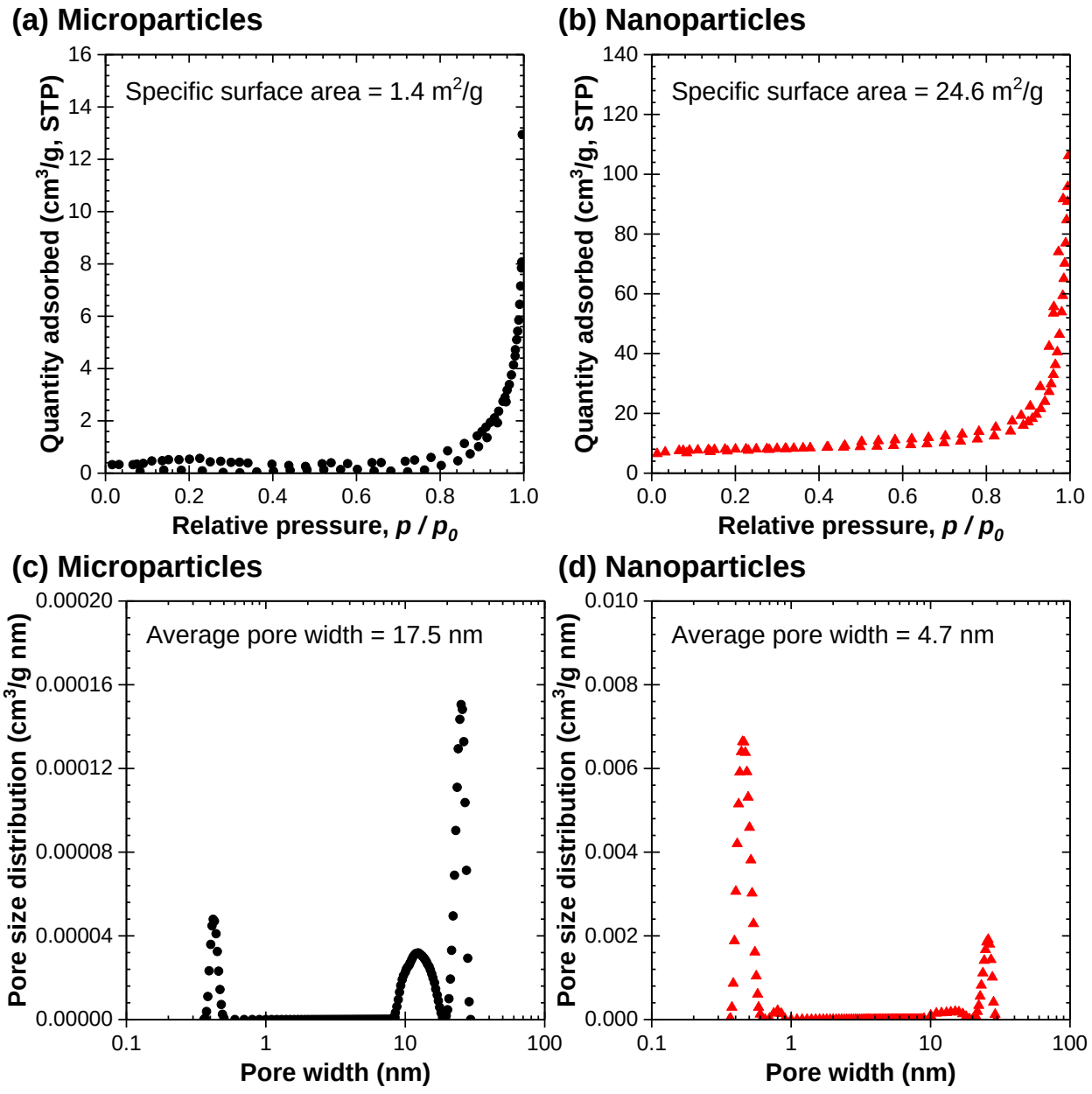

Figure A.1: Quantity adsorbed as a function of relative pressure p/p_0 in low-temperature nitrogen adsorption porosimetry of $Ti_2Nb_2O_9$ (a) microparticles or (b) nanoparticles. Pore size distribution as a function of pore width in low-temperature nitrogen adsorption porosimetry of $Ti_2Nb_2O_9$ (c) microparticles or (d) nanoparticles.

A.2 *Operando* isothermal calorimetry

A.2.1 Cell potential

Figure A.2 plots the temporal evolution of the potential $V(t)$ of the calorimetric cells with slurry-cast working electrodes made of $Ti_2Nb_2O_9$ (a) microparticles or (b) nanoparticles and lithium metal counter electrodes for six consecutive galvanostatic cycles with potential window between 1.0 and 3.0 V vs. Li/Li^+ for each current I ranging from 2 to 8 mA. Here, the five colored regions corresponded to the different current I from 2 to 4 to 6 to 8 and back to 2 mA. The $Ti_2Nb_2O_9$ active material mass loading of both cells was identical at 5.5 mg, such that identical currents I would result in identical C-rates. The current $I = 2$, 4, 6, and 8 mA amounted to C-rate of 1.5C, 3C, 4.5C, and 6C, respectively. Furthermore, the potential $V(t)$ of both cells was nonlinear and asymmetric between charging and discharging. This followed the typical potential profiles under galvanostatic cycling. In addition, the potential $V(t)$ was repeatable between every cycle for any given current I.

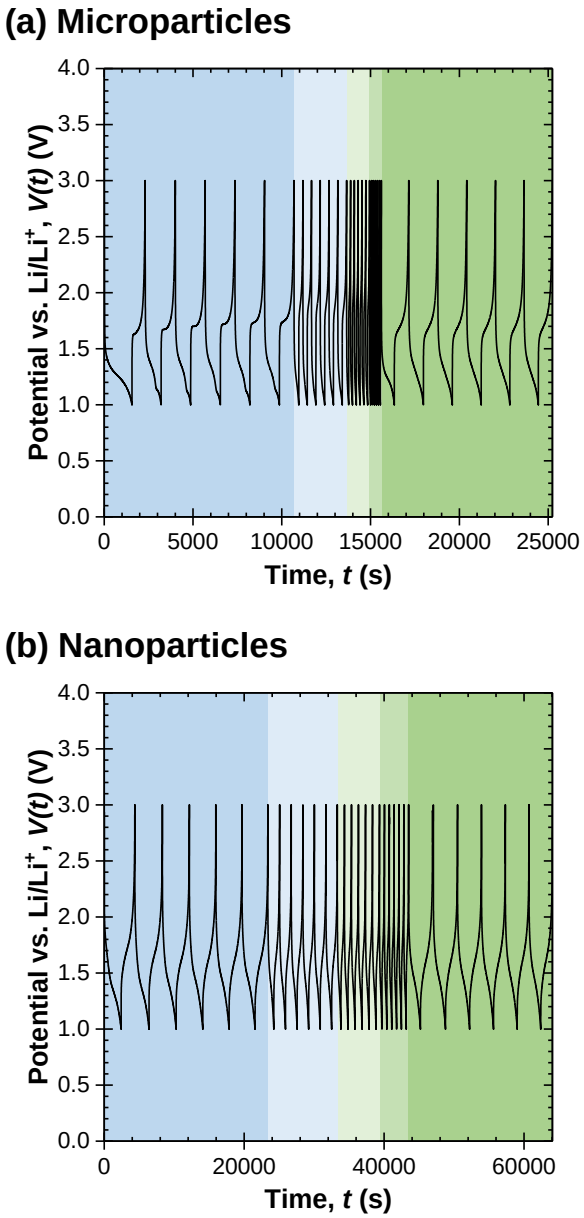

Figure A.2: Temporal evolution of potential $V(t)$ of calorimetric cells for six consecutive galvanostatic cycles with potential window between 1.0 and 3.0 V vs. Li/Li^+ for each current I ranging from 2 to 8 mA with slurry-cast working electrodes made of $Ti_2Nb_2O_9$ (a) microparticles or (b) nanoparticles and lithium metal counter electrodes.

A.2.2 Instantaneous heat generation rates

Figures A.3 and A.4 plot the instantaneous heat generation rates $\dot{Q}_{TNO}(t)$ measured at the working electrodes made of $Ti_2Nb_2O_9$ microparticles or nanoparticles and $\dot{Q}_{Li}(t)$ measured at the lithium metal counter electrodes as functions of dimensionless time t/t_{cd} during the last three consecutive cycles at current (a) $I = 2$ mA, (b) $I = 4$ mA, (c) $I = 6$ mA, and (d) $I = 8$ mA. Here, $\dot{Q}_{TNO}(t)$ and $\dot{Q}_{Li}(t)$ in both cells showed negligible differences at any given current I. This indicates that heat generation had reached oscillatory steady-state after the first three consecutive cycles.

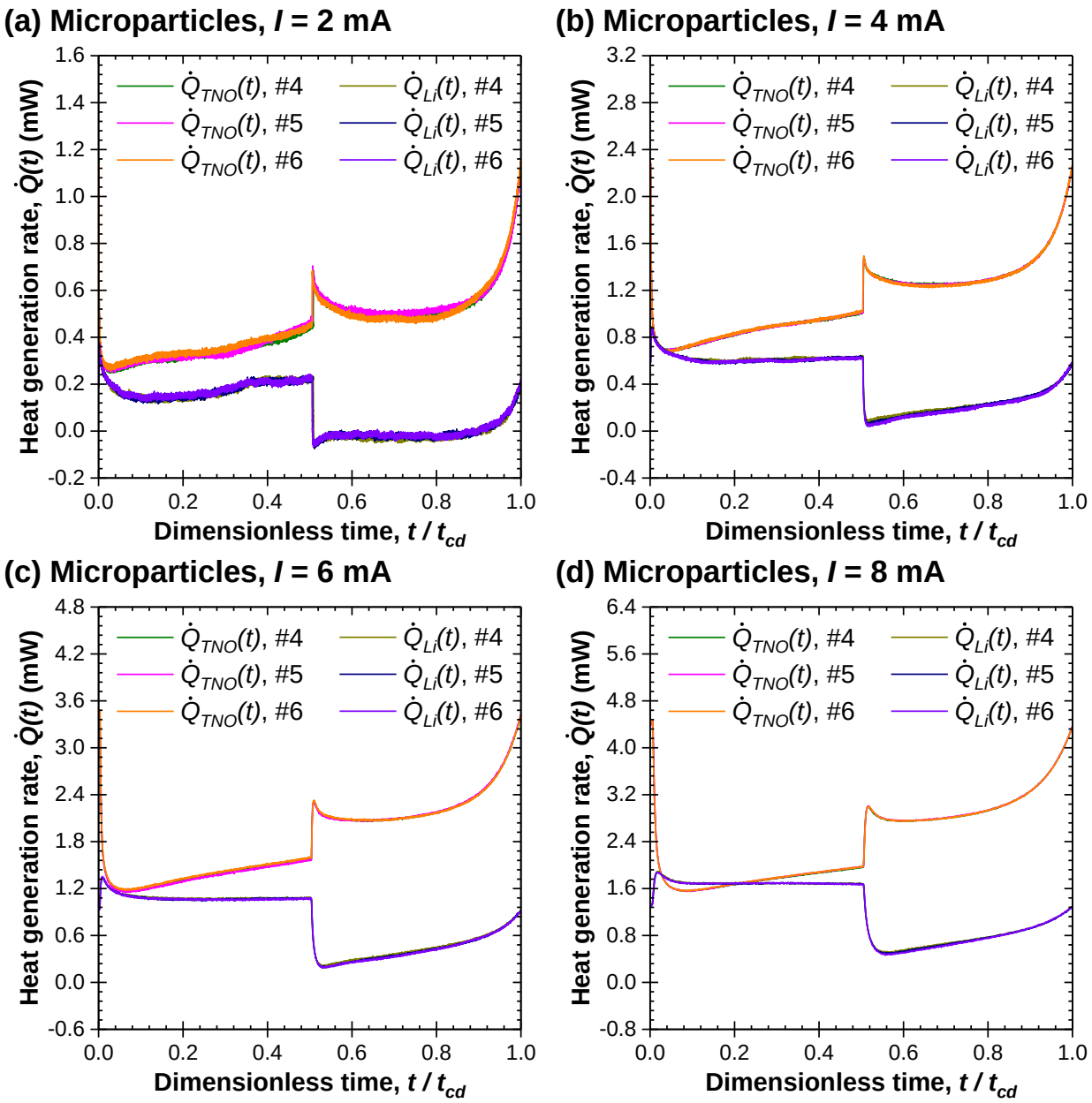

Figure A.3: Instantaneous heat generation rates $\dot{Q}_{TNO}(t)$ measured at the working electrode made of $Ti_2Nb_2O_9$ microparticles and $\dot{Q}_{Li}(t)$ measured at the lithium metal counter electrode as functions of dimensionless time t/t_{cd} during the last three consecutive cycles at current (a) $I = 2$ mA, (b) $I = 4$ mA, (c) $I = 6$ mA, and (d) $I = 8$ mA.

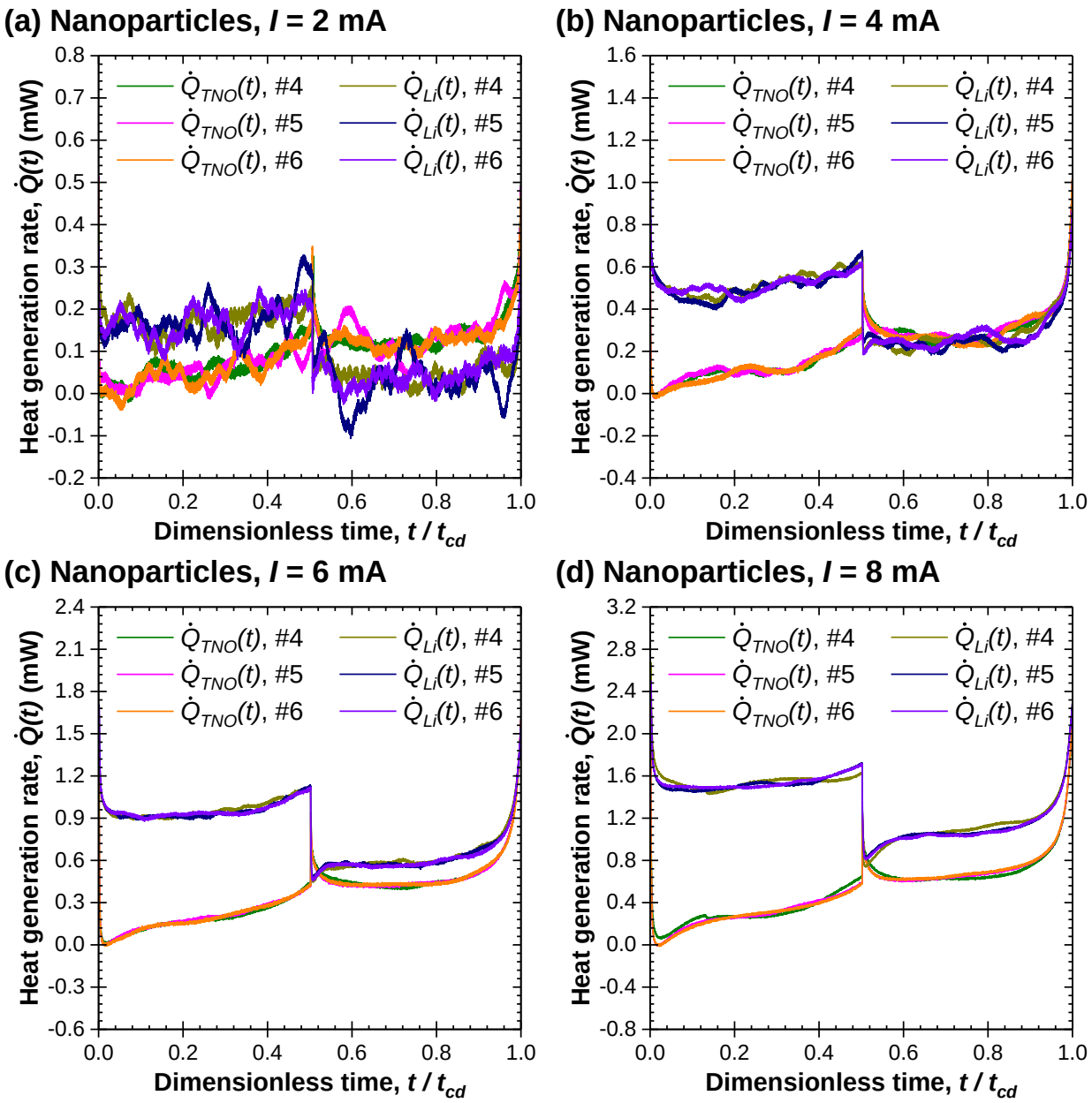

Figure A.4: Instantaneous heat generation rates $\dot{Q}_{TNO}(t)$ measured at the working electrode made of $Ti_2Nb_2O_9$ nanoparticles and $\dot{Q}_{Li}(t)$ measured at the lithium metal counter electrode as functions of dimensionless time t/t_{cd} during the last three consecutive cycles at current (a) $I = 2$ mA, (b) $I = 4$ mA, (c) $I = 6$ mA, and (d) $I = 8$ mA.

A.2.3 Total heat generation rate of the cell

Figure A.5 plots the open-circuit voltage $U_{OCV}(C_m, T)$ and entropic potential $\partial U_{OCV}(C_m, T)/\partial T$ of the coin cells with slurry-cast working electrodes made of $Ti_2Nb_2O_9$ microparticles or nanoparticles as functions of specific capacity C_m during lithiation and delithiation of the first cycle at C-rates of 1.5C and 6C. Here, the values of $U_{OCV}(C_m, T)$ and $\partial U_{OCV}(C_m, T)/\partial T$ measured at 1.5C were used as the values of $U^{avg}(x, T)$ and $\partial U^{avg}(x, T)/\partial T$ in Equations (1.6) and (1.7) for both $I = 2$ and 4 mA, while those measured at 6C were used for both $I = 6$ and 8 mA. Note that the conversion between specific capacity C_m and lithium composition x was performed such that the theoretical specific capacity of 252 mAh/g corresponded to 4 units of lithium ion insertion per unit of $Ti_2Nb_2O_9$. Thus, Figures A.6 to A.9 plot the measured total heat generation rate $\dot{Q}_T(x, T)$ in the calorimetric cells with slurry-cast working electrodes made of $Ti_2Nb_2O_9$ microparticles or nanoparticles and lithium metal counter electrodes as a function of lithium composition x during lithiation or delithiation for current I ranging from 2 to 8 mA. The figures also show the heat generation rates $\dot{Q}_J(x, T)$ and $\dot{Q}_J(x, T) + \dot{Q}_{rev}(x, T)$ calculated according to Equations (1.6) and (1.7). Previously in cells with $TiNb_2O_7$ [59] or PNb_9O_{25} [1] working electrodes and lithium metal counter electrodes in 1 M $LiPF_6$ in EC:DMC 1:1 v/v electrolyte, the measured heat generation rate $\dot{Q}_T(x, T)$ agreed relatively well with that calculated as $\dot{Q}_J(x, T) + \dot{Q}_{rev}(x, T)$, with the difference attributed to heat of mixing $\dot{Q}_{mix}(x, T)$ [1]. Here however, major discrepancies were observed between the measurements of $\dot{Q}_T(x, T)$ and the calculations of $\dot{Q}_J(x, T) + \dot{Q}_{rev}(x, T)$ for nearly every current I in both cells. Moreover, for significant portions of the lithiation or delithiation steps, the calculated Joule heating $\dot{Q}_J(x, T)$ was negative.

Here, we hypothesize that the problem arose from limitations in the analysis. Specifically, the analysis is formulated upon the following assumption: the $U^{avg}(x, T)$ and $\partial U^{avg}(x, T)/\partial T$ in Equations (1.6) and (1.7) are equivalent to the $U_{OCV}(x, T)$ and $\partial U_{OCV}(x, T)/\partial T$ obtained from potentiometric entropy measurements but for current pulses corresponding to the same C-rate as that imposed during galvanostatic cycling in the *operando* isothermal calorimetry

measurements of $\dot{Q}_T(x,T)$ [1]. However, this assumption could be invalid in some circumstances. For example, for the cell with $Ti_2Nb_2O_9$ microparticles, a specific capacity of C_m = 203 mAh/g was extracted during lithiation under potentiometric entropy measurements with current pulses at 6C [Figure A.5(a)]. By contrast, during lithiation under galvanostatic cycling at I = 8 mA (∼6C), the lithium composition varied from x = 1.8 to x = 2.2 corresponding to a specific capacity of C_m = 25 mAh/g only [Figure A.7(c)]. Meanwhile, a specific capacity of C_m = 254 mAh/g with current pulses at 1.5C [Figure A.5(a)] did not agree either with a specific capacity of C_m = 82 mAh/g from x = 1.6 to x = 2.9 obtained at I = 2 mA (∼1.5C) [Figure A.6(a)]. Similar behavior was observed for the cell with $Ti_2Nb_2O_9$ nanoparticles: C_m = 270 mAh/g at 6C [Figure A.5(c)] against C_m = 139 mAh/g from x = 1.5 to x = 3.7 at I = 8 mA (∼6C) [Figure A.9(c)], or C_m = 314 mAh/g at 1.5C [Figure A.5(c)] against C_m = 189 mAh/g from x = 1.2 to x = 4.2 at I = 2 mA (∼1.5C) [Figure A.8(a)]. These comparisons suggest that the actual $U^{avg}(x,T)$ and $\partial U^{avg}(x,T)/\partial T$ reached under galvanostatic cycling did not equate to the $U_{OCV}(x,T)$ and $\partial U_{OCV}(x,T)/\partial T$ determined by potentiometric entropy measurements, otherwise the specific capacity C_m from the two measurements at the same C-rate should be much closer. In fact, the discrepancy was more significant at higher C-rates when the capacity retention was the worst. Most likely, the long relaxation periods required in potentiometric entropy measurements mitigated some dynamic processes occurring in the cell. For instance, the ion concentration gradients had time to decay, the lattice displacements had time to recover, the intercalated lithium ions had time to migrate towards more energetically favorable sites. It is interesting to note that, while previous studies did achieve good agreement between the measured $\dot{Q}_T(x,T)$ and the calculated $\dot{Q}_J(x,T) + \dot{Q}_{rev}(x,T)$ heat generation rates in cells with $TiNb_2O_7$ [59] or PNb_9O_{25} [1] working electrodes, the cells were only cycled at C-rates with good capacity retention. Therefore, the specific capacity C_m from potentiometric entropy measurements and galvanostatic cycling at the same C-rates were relatively close. As a result, in such cases the $U^{avg}(x,T)$ and $\partial U^{avg}(x,T)/\partial T$ in Equations (1.6) and (1.7) could be substituted with the measured $U_{OCV}(x,T)$ and $\partial U_{OCV}(x,T)/\partial T$.

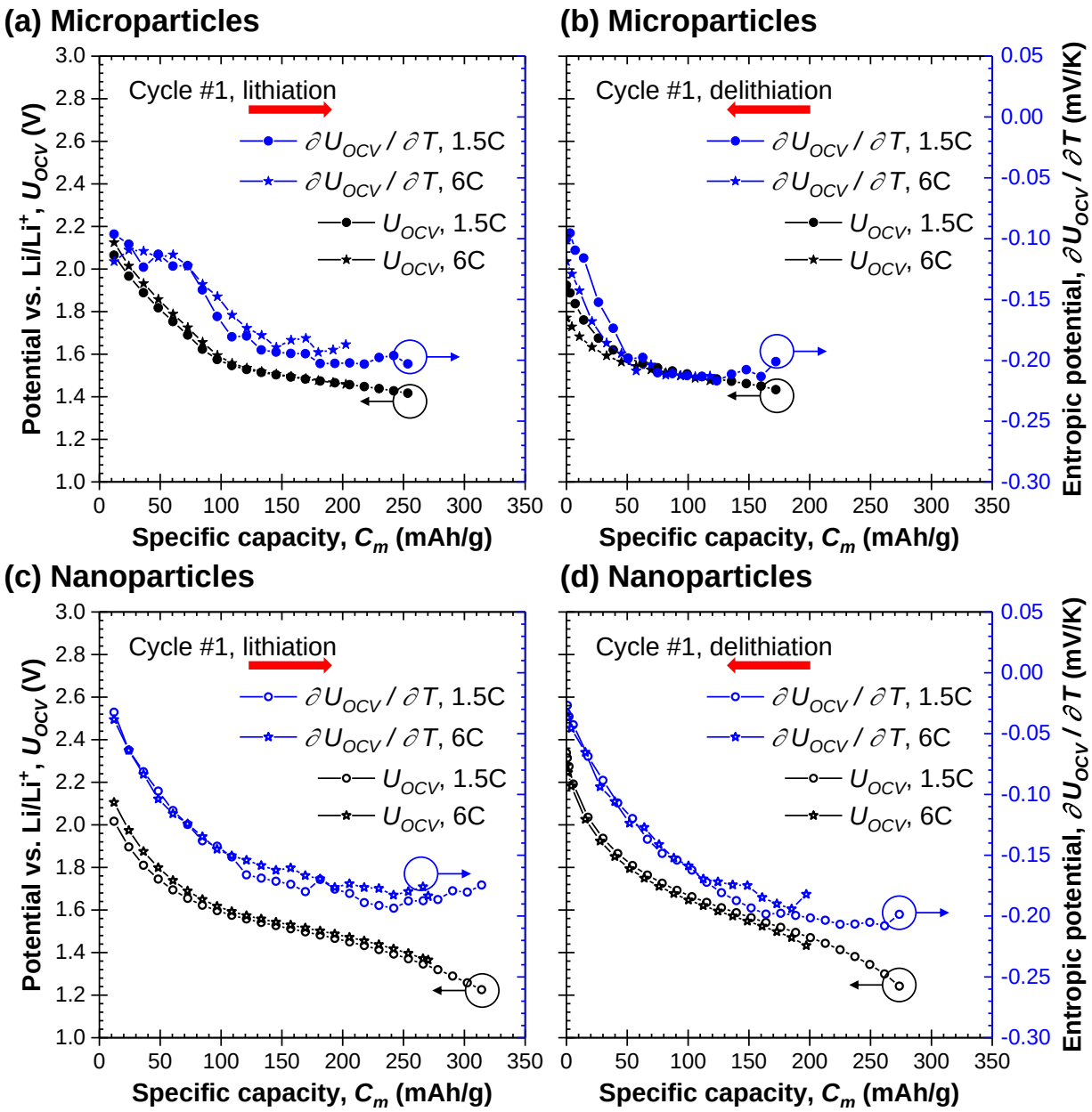

Figure A.5: Open-circuit voltage $U_{OCV}(C_m, T)$ and entropic potential $\partial U_{OCV}(C_m, T)/\partial T$ of coin cells with working electrodes made of $Ti_2Nb_2O_9$ microparticles or nanoparticles as functions of specific capacity C_m during lithiation and delithiation of the first cycle at C-rates of 1.5C and 6C.

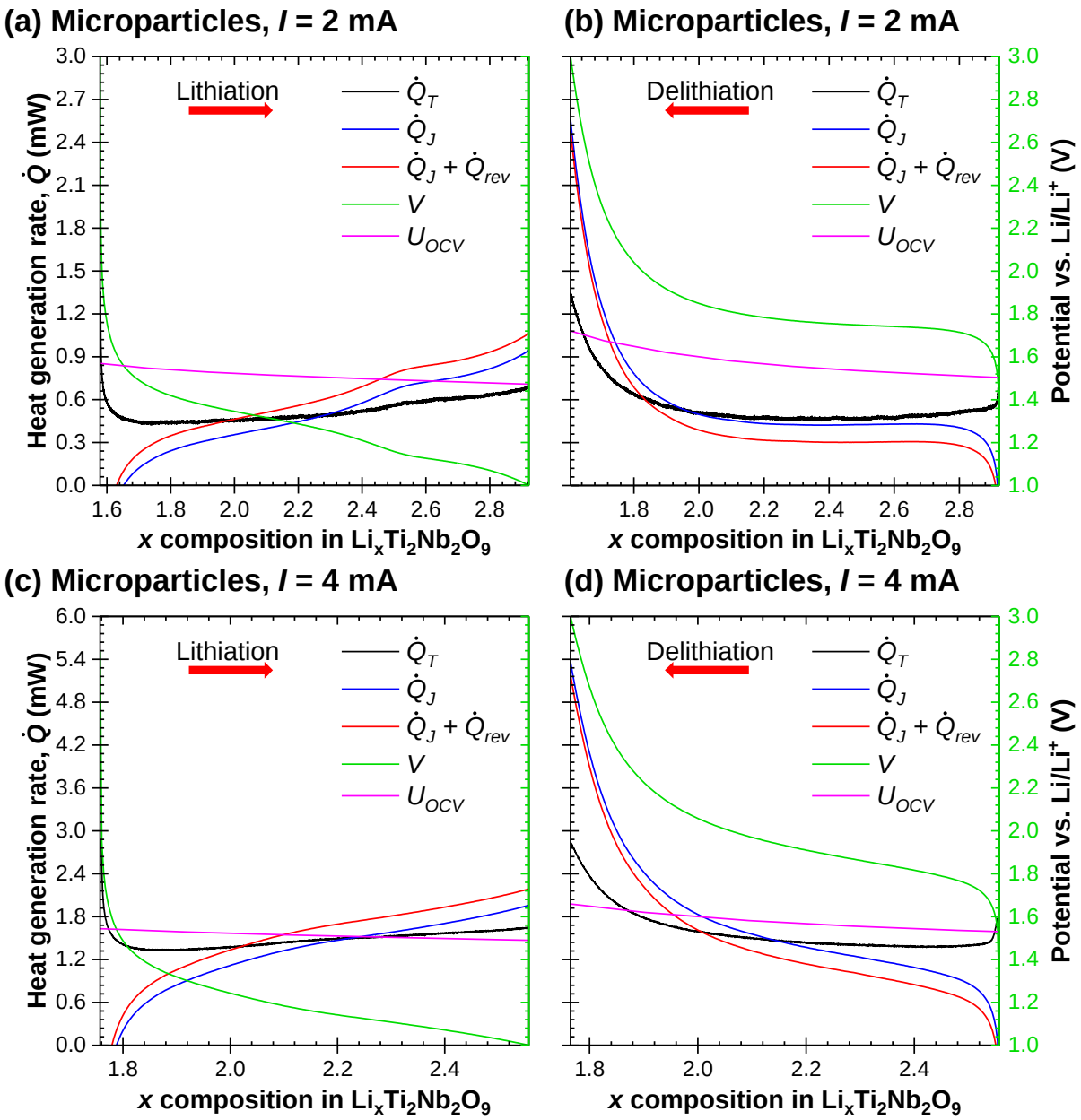

Figure A.6: Measured total heat generation rate $\dot{Q}_T(x,T)$, along with heat generation rates $\dot{Q}_J(x,T)$ and $\dot{Q}_J(x,T) + \dot{Q}_{rev}(x,T)$ calculated according to Equations (1.6) and (1.7), as well as measured cell potential $V(x,T)$ and open-circuit voltage $U_{OCV}(x,T)$ as functions of lithium composition x during (a) lithiation, (b) delithiation at current $I = 2$ mA, (c) lithiation, (d) delithiation at current $I = 4$ mA in calorimetric cell with working electrode made of $Ti_2Nb_2O_9$ microparticles and lithium metal counter electrode.

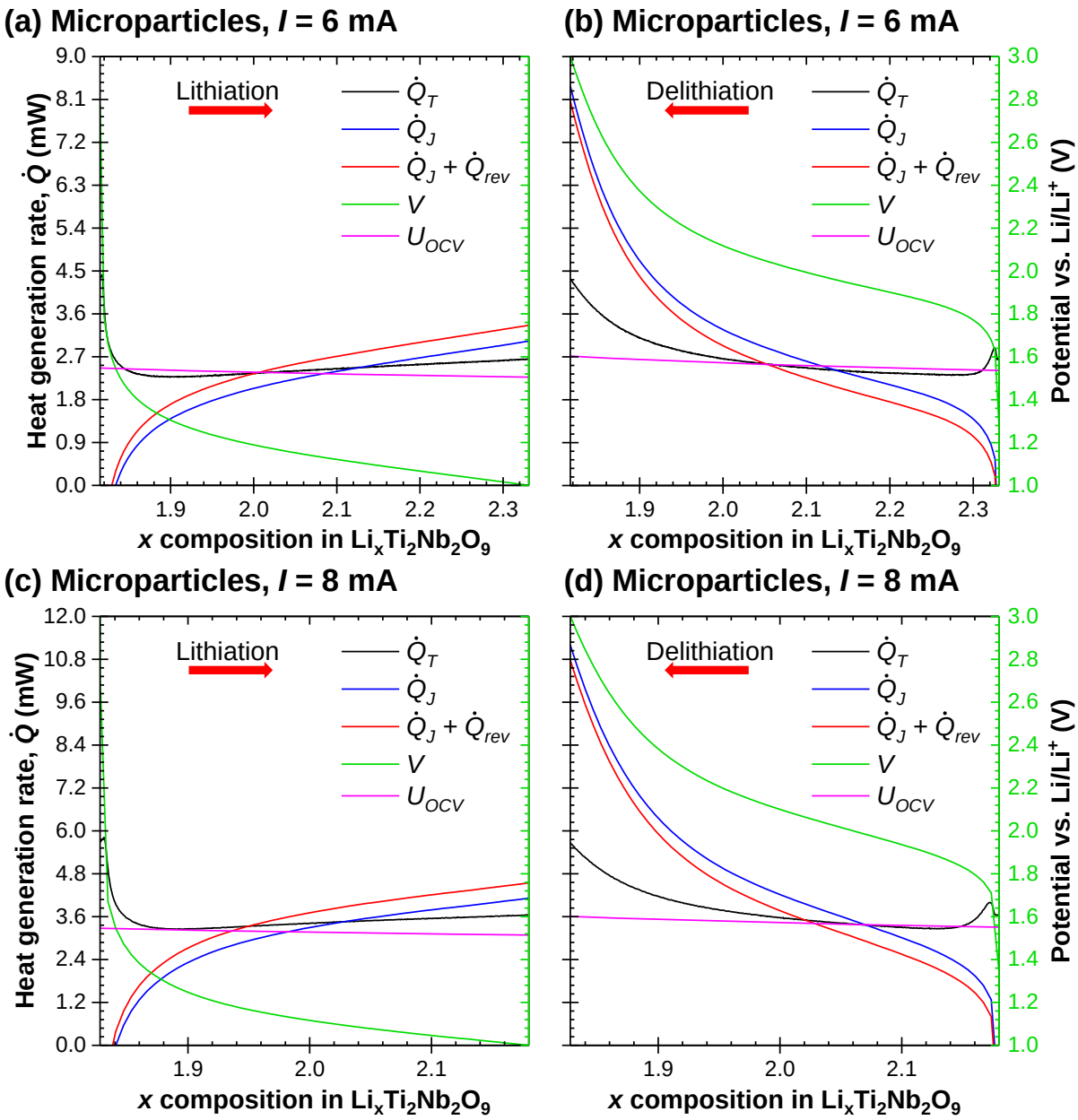

Figure A.7: Measured total heat generation rate $\dot{Q}_T(x,T)$, along with heat generation rates $\dot{Q}_J(x,T)$ and $\dot{Q}_J(x,T) + \dot{Q}_{rev}(x,T)$ calculated according to Equations (1.6) and (1.7), as well as measured cell potential $V(x,T)$ and open-circuit voltage $U_{OCV}(x,T)$ as functions of lithium composition x during (a) lithiation, (b) delithiation at current $I = 6$ mA, (c) lithiation, (d) delithiation at current $I = 8$ mA in calorimetric cell with working electrode made of $Ti_2Nb_2O_9$ microparticles and lithium metal counter electrode.

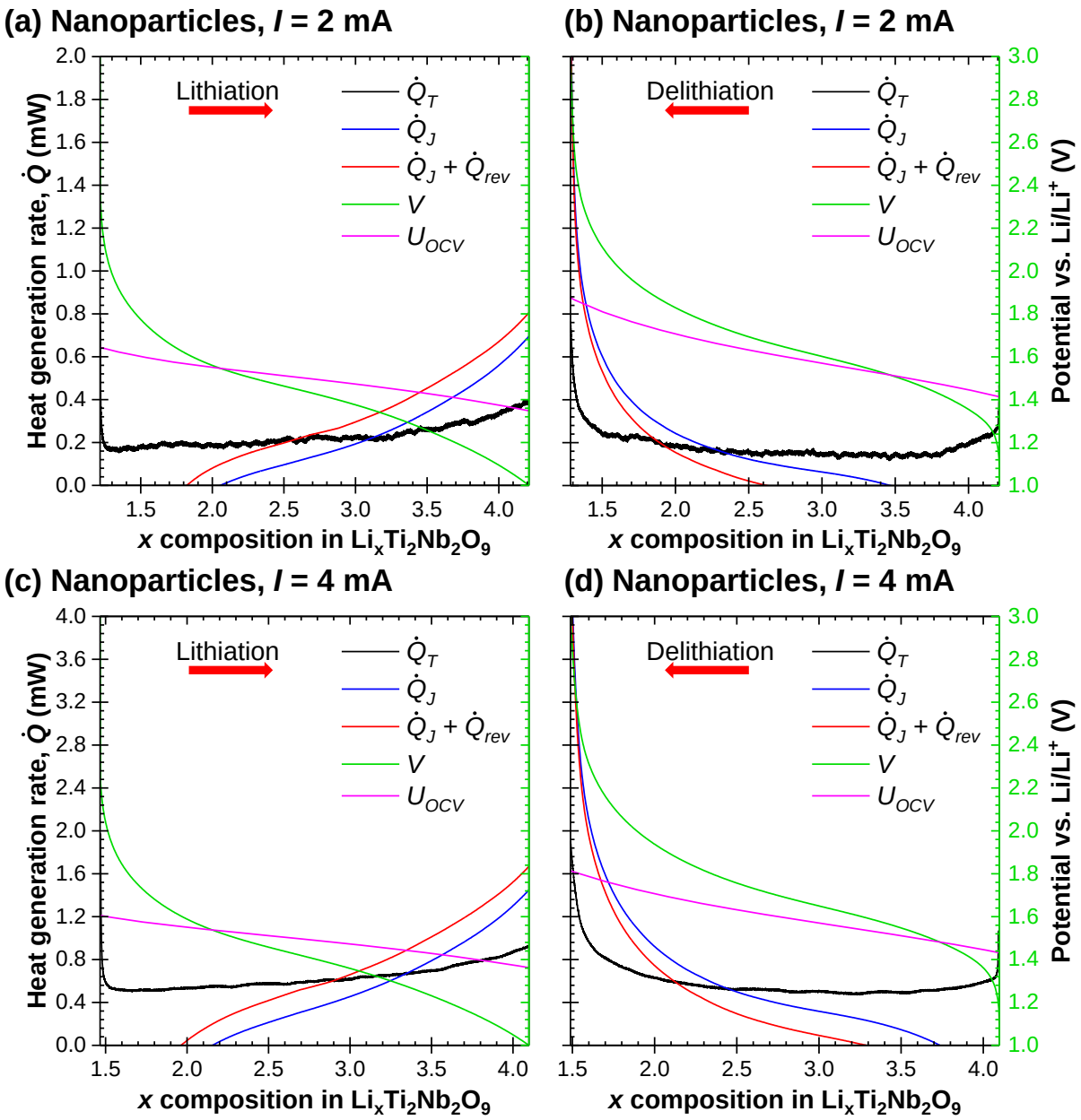

Figure A.8: Measured total heat generation rate $\dot{Q}_T(x,T)$, along with heat generation rates $\dot{Q}_J(x,T)$ and $\dot{Q}_J(x,T) + \dot{Q}_{rev}(x,T)$ calculated according to Equations (1.6) and (1.7), as well as measured cell potential $V(x,T)$ and open-circuit voltage $U_{OCV}(x,T)$ as functions of lithium composition x during (a) lithiation, (b) delithiation at current $I = 2$ mA, (c) lithiation, (d) delithiation at current $I = 4$ mA in calorimetric cell with working electrode made of $Ti_2Nb_2O_9$ nanoparticles and lithium metal counter electrode.

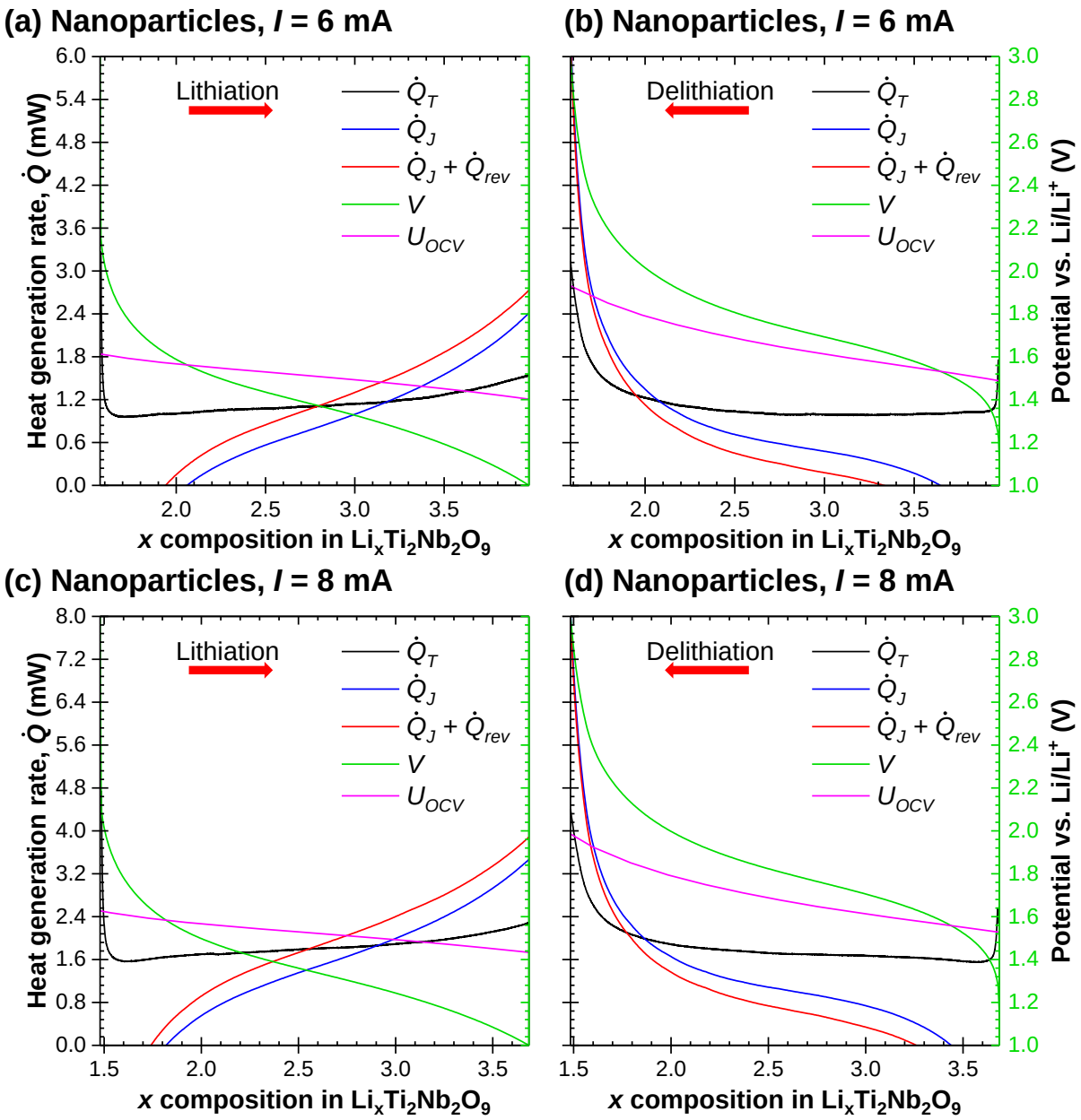

Figure A.9: Measured total heat generation rate $\dot{Q}_T(x,T)$, along with heat generation rates $\dot{Q}_J(x,T)$ and $\dot{Q}_J(x,T) + \dot{Q}_{rev}(x,T)$ calculated according to Equations (1.6) and (1.7), as well as measured cell potential $V(x,T)$ and open-circuit voltage $U_{OCV}(x,T)$ as functions of lithium composition x during (a) lithiation, (b) delithiation at current $I = 6$ mA, (c) lithiation, (d) delithiation at current $I = 8$ mA in calorimetric cell with working electrode made of $Ti_2Nb_2O_9$ nanoparticles and lithium metal counter electrode.

APPENDIX B

Supplementary Materials for Chapter 5

B.1 Governing equations

The local electric potential $\psi(\mathbf{r}, t)$ in the current collector and the electrode was governed by the continuity equation combined with Ohm's law to yield [210],

$$\nabla \cdot (\sigma_C \nabla \psi) = 0 \quad \text{and} \quad \nabla \cdot (\sigma_P \nabla \psi) = 0 \tag{B.1}$$

where σ_C and σ_P are the electrical conductivity of the current collector and the electrode, respectively.

The generalized modified Poisson-Nernst-Planck (GMPNP) model predicted the time-dependent local electric potential $\psi(\mathbf{r}, t)$ and ion concentrations $c_i(\mathbf{r}, t)$ in binary and symmetric electrolytes accounting for finite ion size. The local electric potential $\psi(\mathbf{r}, t)$ was governed by the Poisson equation expressed as [220],

$$\nabla \cdot (\epsilon_0 \epsilon_r \nabla \psi) = \begin{cases} 0 & \text{in the Stern layer} \\ -F \sum_{i=1}^{N} z_i c_i & \text{in the diffuse layer} \end{cases} \tag{B.2}$$

where ϵ_0 is the vacuum permittivity, ϵ_r is the relative permittivity of the electrolyte, F is the Faraday constant, and z_i is the valency of ion species i. The local concentration $c_i(\mathbf{r}, t)$ of ion species i in the diffuse layer was governed by the generalized modified Nernst-Planck equation [221],

$$\frac{\partial c_i}{\partial t} = -\nabla \cdot \mathbf{N}_i \quad \text{in the diffuse layer} \tag{B.3}$$

where $\mathbf{N}_i(\mathbf{r},t)$ is the local molar flux vector of species i expressed as [221],

$$\mathbf{N}_i = -D_i\nabla c_i - \frac{z_i F D_i c_i}{R_u T}\nabla\psi - \frac{D_i N_A c_i}{1 - N_A\sum_{i=1}^{N} a_i^3 c_i}\sum_{i=1}^{N} a_i^3\nabla c_i \tag{B.4}$$

where D_i is the diffusion coefficient of ion species i in the electrolyte, R_u is the universal gas constant, T is the temperature, N_A is the Avogadro number, and a_i is the effective ion diameter of species i. Here, the first, second, and third terms on the right hand side of Equation (B.4) represent diffusion, electromigration, and steric repulsion, respectively [196, 222]. This model accounts for finite ion size and is applicable to cases with large electric potential and/or high electrolyte concentrations.

The local concentration of Li^+ ions in the electrode, denoted by $c_{1,P}(\mathbf{r},t)$, was governed by the 3D transient mass diffusion equation given by [210, 223],

$$\frac{\partial c_{1,P}}{\partial t} = \nabla\cdot(D_{1,P}\nabla c_{1,P}) \quad \text{in the electrode} \tag{B.5}$$

where $D_{1,P}$ is the diffusion coefficient of Li^+ ions in the electrode.

B.2 Initial and boundary conditions

To solve the governing Equations (B.2) to (B.4) for the spatiotemporal evolution of potential $\psi(\mathbf{r},t)$ and ion concentrations $c_i(\mathbf{r},t)$, one initial condition and two boundary conditions were needed for each variable. Zero electric potential and uniform ion concentrations equal to the bulk concentrations c_∞ were used as initial conditions for solving the GMPNP model, i.e.,

$$\psi(\mathbf{r},0) = 0 \quad \text{and} \quad c_i(\mathbf{r},0) = c_\infty. \tag{B.6}$$

The boundary condition at the reference electrode, located at the device centerline $\mathbf{r}_{cl} = (x = L_C + L_P + L, y, z)$, was given by,

$$\psi(\mathbf{r}_{cl},t) = 0 \quad \text{and} \quad c_i(\mathbf{r}_{cl},t) = c_\infty. \tag{B.7}$$

The boundary conditions at the current collector/electrode interface varied for different simulations. Moreover, the electric potential and current density were both continuous across

the spherical electrode/electrolyte interface located at $\mathbf{r}_{E/E}$ and the planar current collector/electrolyte interface located at $\mathbf{r}_{C/E}$ so that,

$$\begin{aligned} \psi(\mathbf{r}_k^-, t) &= \psi(\mathbf{r}_k^+, t), \\ -\sigma_P \frac{\partial \psi}{\partial n}(\mathbf{r}_k^-, t) &= -\epsilon_0 \epsilon_r \frac{\partial^2 \psi}{\partial n \partial t}(\mathbf{r}_k^+, t) \quad \text{with} \quad k = E/E \text{ or } C/E. \end{aligned} \tag{B.8}$$

The electric potential varied linearly across the Stern layer so that the normal electric field at the planar and spherical Stern/diffuse layer interfaces located at $\mathbf{r}_H$ satisfied [198, 200],

$$\frac{\partial \psi}{\partial n}(\mathbf{r}_H, t) = \frac{\psi(\mathbf{r}_{C/E}) - \psi(\mathbf{r}_H)}{H} \quad \text{for planar current collector surfaces,} \tag{B.9}$$

$$\begin{aligned} -\epsilon_0 \epsilon_r \frac{\partial \psi}{\partial n}(\mathbf{r}_H, t) &= C_s^{St} \left(\frac{d}{d + 2H} \right)^2 [\psi(\mathbf{r}_{E/E}, t) - \psi(\mathbf{r}_H, t)] \\ &\text{for spherical electrode surfaces.} \end{aligned} \tag{B.10}$$

Here, the Stern layer capacitance for a sphere of diameter d is given by the Helmholtz model expressed as,

$$C_s^{St} = \frac{\epsilon_0 \epsilon_r}{H} \left(1 + \frac{2H}{d} \right). \tag{B.11}$$

These boundary conditions accounted for the presence of the Stern layer without explicitly simulating it in the computational domain, thus significantly reducing the number of mesh elements [198, 200].

The normal molar flux vector of Li^+ ions through the electrode/electrolyte interface was related to the normal faradaic current density vector $\mathbf{j}_{F,n}(\mathbf{r}_{E/E}, t)$ based on stoichiometry as,

$$\mathbf{N}_{1,n}(\mathbf{r}_{E/E}, t) = -D_{1,P} \frac{\partial c_{1,P}}{\partial n}(\mathbf{r}_{E/E}, t) = \frac{\mathbf{j}_{F,n}(\mathbf{r}_{E/E}, t)}{z_1 F}. \tag{B.12}$$

Finally, the electrode was impermeable to ClO_4^- ions so that,

$$\mathbf{N}_{2,n}(\mathbf{r}_{E/E}, t) = 0. \tag{B.13}$$

B.3 Parametric studies

B.3.1 Influence of reaction rate constant k_0

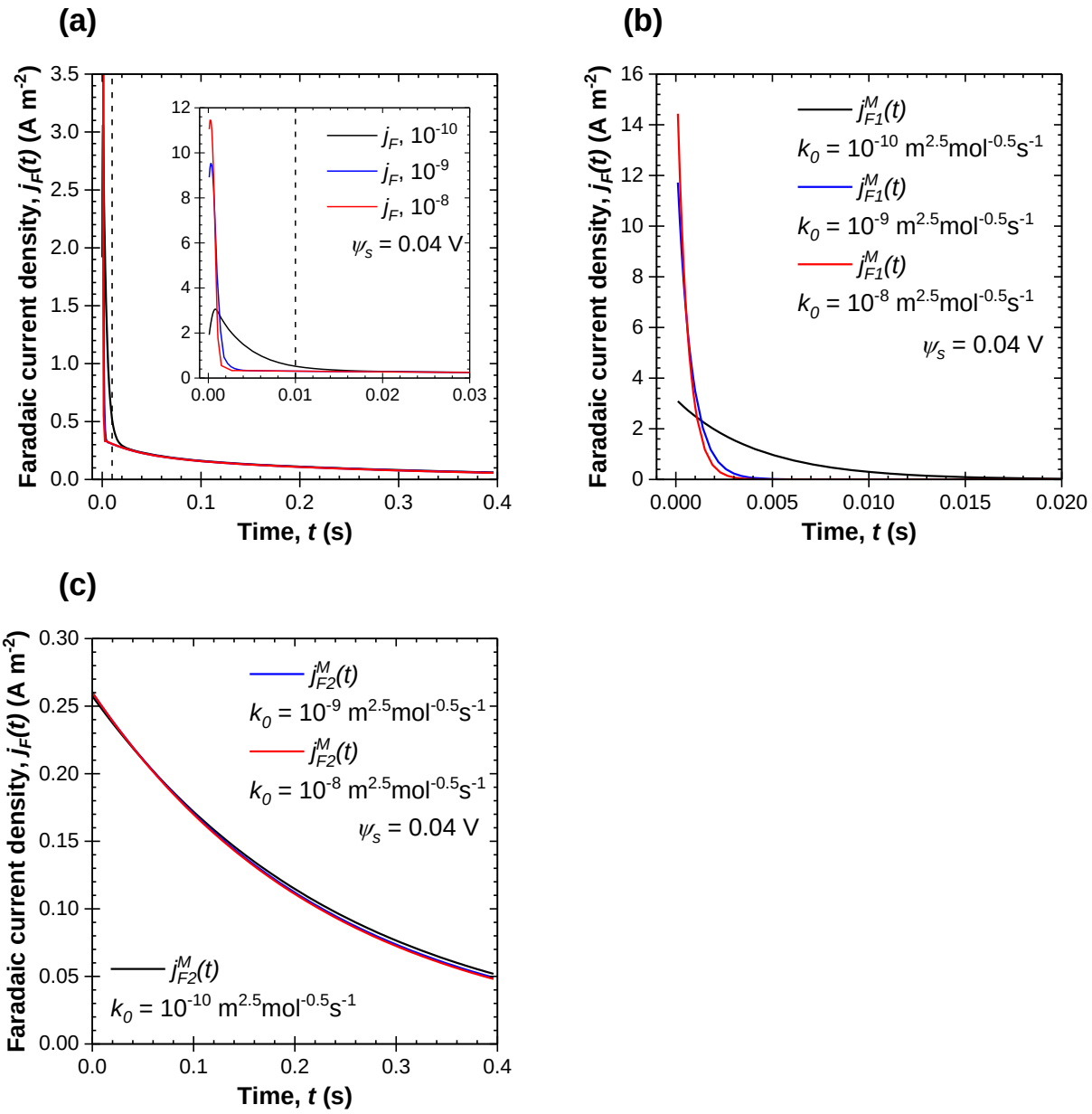

Figure B.1: (a) Numerically simulated Faradaic footprint current density response $j_F(t)$ [Equations (5.18) and (5.21)] to a potential step of $\Delta\psi_s = 0.04$ V at $\psi_s = 0.04$ V during charging for reaction rate constant $k_0 = 10^{-10}$, 10^{-9}, and 10^{-8} m$^{2.5}$ mol$^{-0.5}$ s^{-1}, along with (b) surface-controlled $j_{F1}^M(t)$ and (c) diffusion-controlled $j_{F2}^M(t)$ Faradaic footprint current densities [Equation (5.26)] predicted by the modified fitting function.

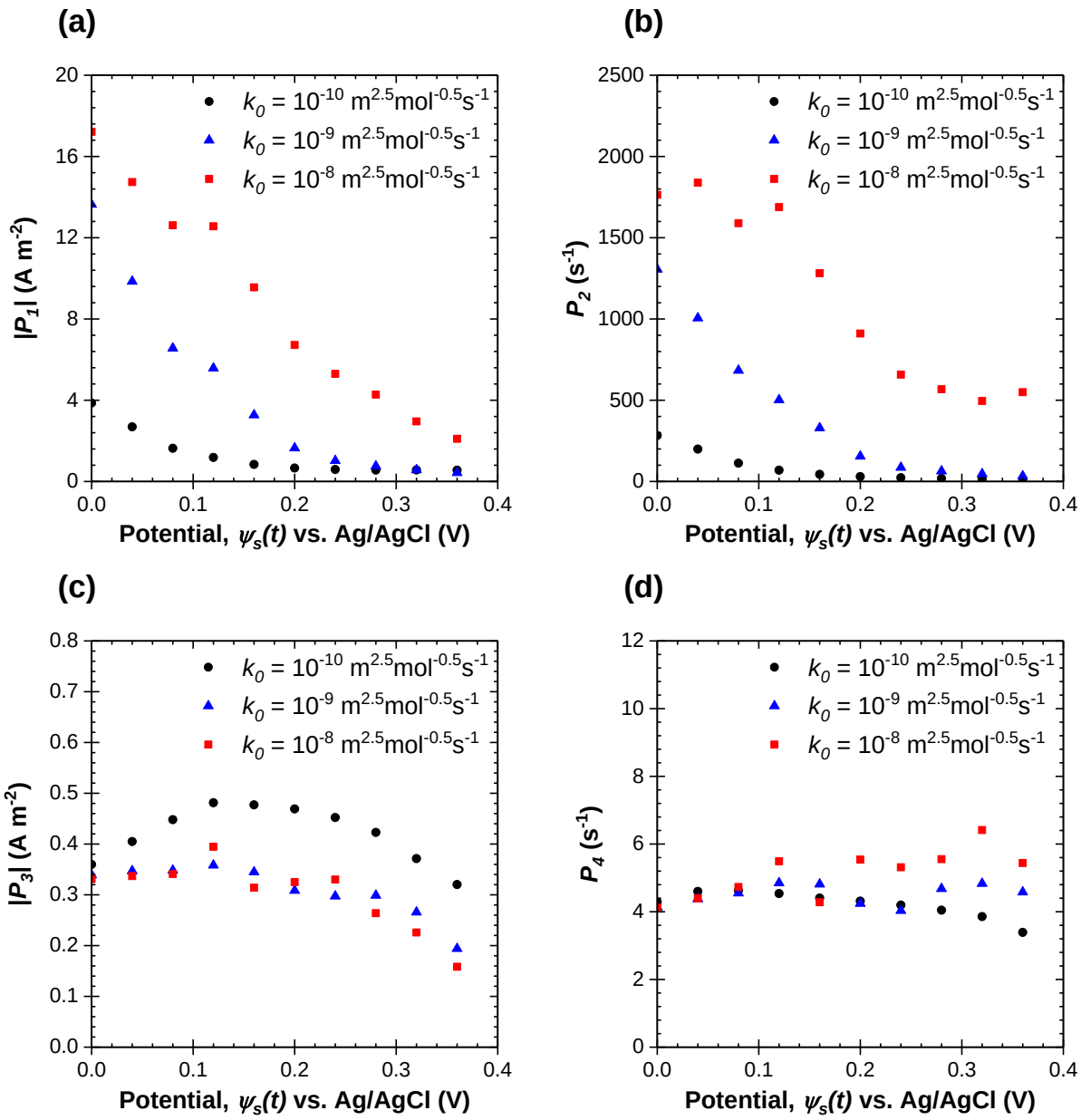

Figure B.2: Fitting parameters of the modified SPECS model (a) $|P_1(\psi_s)|$, (b) $P_2(\psi_s)$, (c) $|P_3(\psi_s)|$, and (d) $P_4(\psi_s)$ as functions of potential ψ_s during charging between $\psi_{s,min} = 0$ V and $\psi_{s,max} = 0.4$ V with potential steps $\Delta\psi_s = 0.04$ V for reaction rate constant $k_0 = 10^{-10}$, 10^{-9}, and 10^{-8} m$^{2.5}$ mol$^{-0.5}$ s^{-1}.

In order to investigate the influence of reaction rate constant k_0 on the fitting parameters, three cases were compared with $k_0 = 10^{-10}$, 10^{-9}, and 10^{-8} m$^{2.5}$ mol$^{-0.5}$ s^{-1}, respectively.

First, Figure B.1(a) plots the numerically simulated Faradaic footprint current density response $j_F(t)$ [Equations (5.18) and (5.21)] to a potential step of $\Delta\psi_s = 0.04$ V at $\psi_s = 0.04$ V during charging for all three cases. For $t < 0.01$ s, $j_F(t)$ was dominated by contributions from kinetics-controlled surface redox reactions. Therefore, as k_0 increased, so did the rate of interfacial charge transfer kinetics, resulting in faster surface redox reactions and a larger $j_F(t)$. For $t > 0.01$ s, $j_F(t)$ was dominated by contributions from diffusion-controlled ion intercalation/deintercalation in/out of the electrode spherical particles. Therefore, k_0 had no influence on $j_F(t)$, and the response curves of $j_F(t)$ for all three cases overlapped. In addition, Figures B.1(b) and B.1(c) plot the surface-controlled $j_{F1}^M(t)$ and diffusion-controlled $j_{F2}^M(t)$ Faradaic footprint current densities [Equation (5.26)] predicted by the modified fitting function. Here, $j_{F1}^M(t)$ increased in both peak value and decaying rate with higher k_0, while $j_{F2}^M(t)$ was independent of k_0. Finally, Figure B.2 plots the four fitting parameters associated with Faradaic reactions: (a) $|P_1(\psi_s)|$, (b) $P_2(\psi_s)$, (c) $|P_3(\psi_s)|$, and (d) $P_4(\psi_s)$. On the one hand, $|P_1(\psi_s)|$ and $P_2(\psi_s)$, which modeled the surface-controlled Faradaic footprint current density $j_{F1}^M(t)$, increased with higher k_0. On the other hand, $|P_3(\psi_s)|$ and $P_4(\psi_s)$, which modeled the diffusion-controlled Faradaic footprint current density $j_{F2}^M(t)$, were relatively independent of k_0.

B.3.2 Influence of ion diffusion coefficient in the electrode $D_{1,P}$

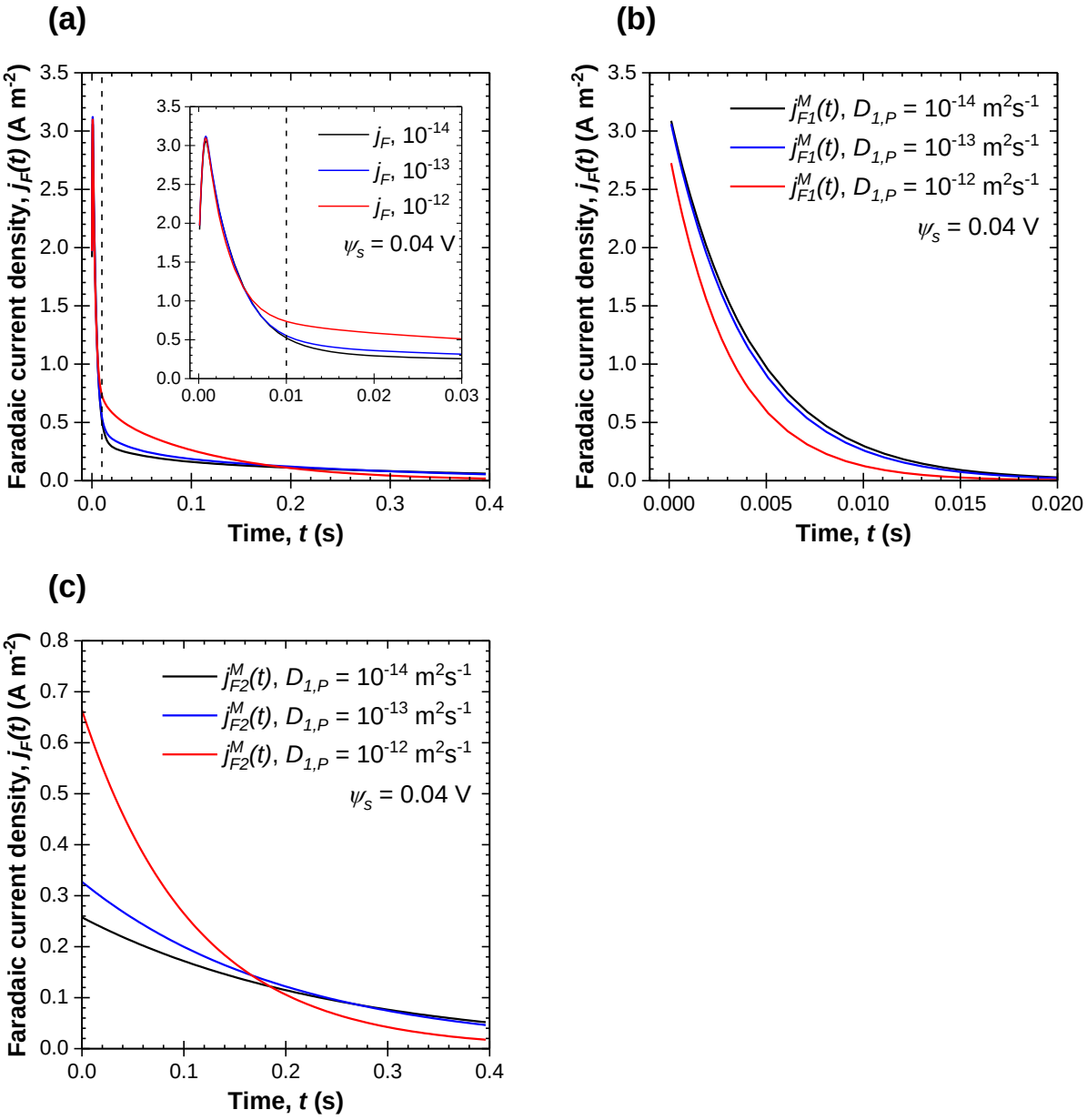

Figure B.3: (a) Numerically simulated Faradaic footprint current density response $j_F(t)$ [Equations (5.18) and (5.21)] to a potential step of $\Delta\psi_s = 0.04$ V at $\psi_s = 0.04$ V during charging for ion diffusion coefficient in the electrode $D_{1,P} = 10^{-14}$, 10^{-13}, and 10^{-12} m^2 s^{-1}, along with (b) surface-controlled $j_{F1}^M(t)$ and (c) diffusion-controlled $j_{F2}^M(t)$ Faradaic footprint current densities [Equation (5.26)] predicted by the modified fitting function.

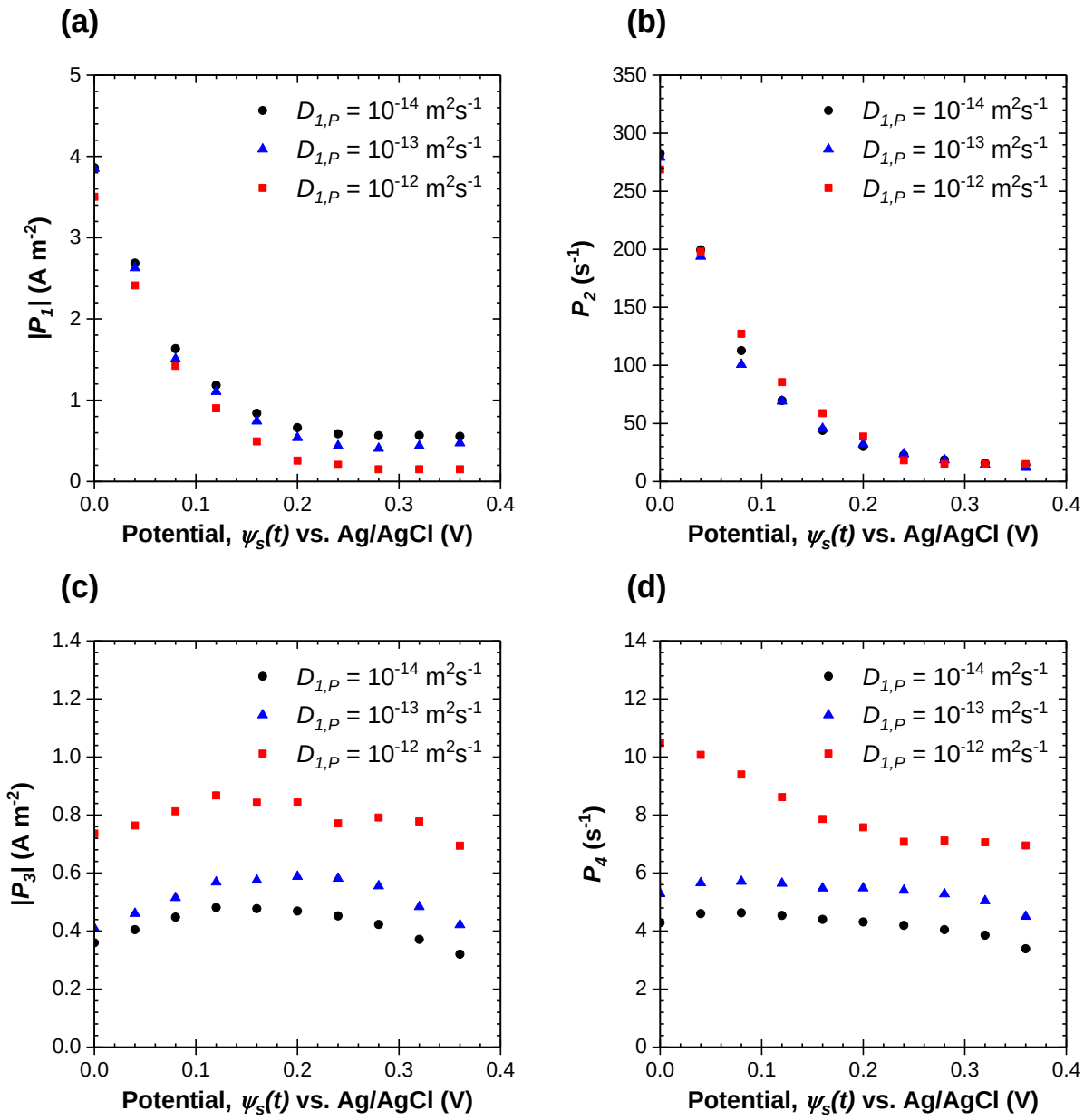

Figure B.4: Fitting parameters of the modified SPECS model (a) $|P_1(\psi_s)|$, (b) $P_2(\psi_s)$, (c) $|P_3(\psi_s)|$, and (d) $P_4(\psi_s)$ as functions of potential ψ_s during charging between $\psi_{s,min} = 0$ V and $\psi_{s,max} = 0.4$ V with potential steps $\Delta\psi_s = 0.04$ V for ion diffusion coefficient in the electrode $D_{1,P} = 10^{-14}$, 10^{-13}, and 10^{-12} m^2 s^{-1}.

In order to investigate the influence of ion diffusion coefficient in the electrode $D_{1,P}$ on the fitting parameters, three cases were compared with $D_{1,P} = 10^{-14}$, 10^{-13}, and 10^{-12} m^2 s^{-1},

respectively. First, Figure B.3(a) plots the numerically simulated Faradaic footprint current density response $j_F(t)$ [Equations (5.18) and (5.21)] to a potential step of $\Delta\psi_s = 0.04$ V at $\psi_s = 0.04$ V during charging for all three cases. For $t < 0.01$ s, $j_F(t)$ was dominated by contributions from kinetics-controlled surface redox reactions. Therefore, $D_{1,P}$ had no influence on $j_F(t)$, and the response curves of $j_F(t)$ for all three cases overlapped. For $t > 0.01$ s, $j_F(t)$ was dominated by contributions from diffusion-controlled ion intercalation/deintercalation in/out of the electrode spherical particles. Therefore, as $D_{1,P}$ increased, so did the rate of solid state ion diffusion, resulting in a larger $j_F(t)$. In addition, Figures B.3(b) and B.3(c) plot the surface-controlled $j_{F1}^M(t)$ and diffusion-controlled $j_{F2}^M(t)$ Faradaic footprint current densities [Equation (5.26)] predicted by the modified fitting function. Here, $j_{F1}^M(t)$ was independent of $D_{1,P}$, while $j_{F2}^M(t)$ increased in both peak value and decaying rate with larger $D_{1,P}$. Finally, Figure B.4 plots the four fitting parameters associated with Faradaic reactions: (a) $|P_1(\psi_s)|$, (b) $P_2(\psi_s)$, (c) $|P_3(\psi_s)|$, and (d) $P_4(\psi_s)$. On the one hand, $|P_1(\psi_s)|$ and $P_2(\psi_s)$, which modeled the surface-controlled Faradaic footprint current density $j_{F1}^M(t)$, were relatively independent of $D_{1,P}$. On the other hand, $|P_3(\psi_s)|$ and $P_4(\psi_s)$, which modeled the diffusion-controlled Faradaic footprint current density $j_{F2}^M(t)$, increased with larger $D_{1,P}$.

B.3.3 Influence of electrode particle layer number N

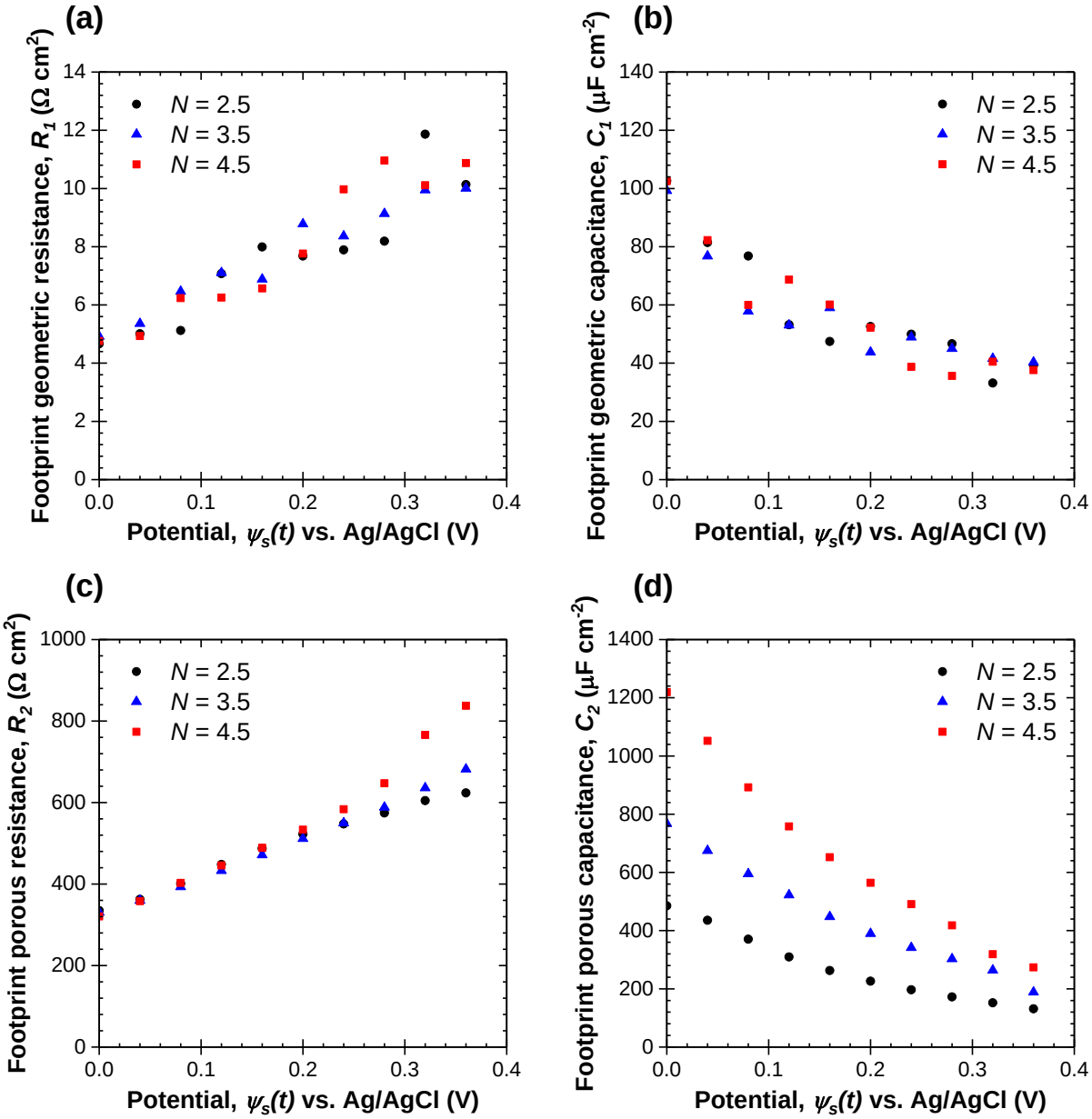

Figure B.5: Fitting parameters of the modified SPECS model (a) $R_1(\psi_s)$, (b) $C_1(\psi_s)$, (c) $R_2(\psi_s)$, and (d) $C_2(\psi_s)$ as functions of potential ψ_s during charging between $\psi_{s,min} = 0$ V and $\psi_{s,max} = 0.4$ V with potential steps $\Delta\psi_s = 0.04$ V for electrode particle layer number $N = 2.5$, 3.5, and 4.5.

References

[1] S. W. Baek, M. B. Preefer, M. Saber, K. Zhai, M. Frajnkovič, Y. Zhou, B. S. Dunn, A. Van der Ven, R. Seshadri, and L. Pilon, "Potentiometric entropy and *operando* calorimetric measurements reveal fast charging mechanisms in PNb_9O_{25}", *Journal of Power Sources*, vol. 520, pp. 230776, 2022.

[2] B. E. Conway, *Electrochemical Supercapacitors: Scientific Fundamentals and Technological Applications*, Springer, New York, NY, 1999.

[3] B. E. Conway, V. Birss, and J. Wojtowicz, "The role and utilization of pseudocapacitance for energy storage by supercapacitors", *Journal of Power Sources*, vol. 66, no. 1-2, pp. 1–14, 1997.

[4] M. R. Lukatskaya, B. Dunn, and Y. Gogotsi, "Multidimensional materials and device architectures for future hybrid energy storage", *Nature Communications*, vol. 7, no. 1, pp. 1–13, 2016.

[5] Z. Zhao, S. Hao, P. Hao, Y. Sang, A. Manivannan, N. Wu, and H. Liu, "Lignosulphonate-cellulose derived porous activated carbon for supercapacitor electrode", *Journal of Materials Chemistry A*, vol. 3, no. 29, pp. 15049–15056, 2015.

[6] H.-J. Liu, W.-J. Cui, L.-H. Jin, C.-X. Wang, and Y.-Y. Xia, "Preparation of three-dimensional ordered mesoporous carbon sphere arrays by a two-step templating route and their application for supercapacitors", *Journal of Materials Chemistry*, vol. 19, no. 22, pp. 3661–3667, 2009.

[7] B. Zhang, J. Liang, C. L. Xu, B. Q. Wei, D. B. Ruan, and D. H. Wu, "Electric double-layer capacitors using carbon nanotube electrodes and organic electrolyte", *Materials Letters*, vol. 51, no. 6, pp. 539–542, 2001.

[8] K. L. Van Aken, C. R. Perez, Y. Oh, M. Beidaghi, Y. J. Jeong, M. F. Islam, and Y. Gogotsi, "High rate capacitive performance of single-walled carbon nanotube aerogels", *Nano Energy*, vol. 15, pp. 662–669, 2015.

[9] B. E. Conway, "Transition from "supercapacitor" to "battery" behavior in electrochemical energy storage", *Journal of The Electrochemical Society*, vol. 138, no. 6, pp. 1539–1548, 1991.

[10] M. S. Halper and J. C. Ellenbogen, "Supercapacitors: A brief overview", Tech. Rep. No. MP 05W0000272, The MITRE Corporation, McLean, VA, 2006.

[11] X. Wang, G. Li, Z. Chen, V. Augustyn, X. Ma, G. Wang, B. Dunn, and Y. Lu, "High-performance supercapacitors based on nanocomposites of Nb_2O_5 nanocrystals and carbon nanotubes", *Advanced Energy Materials*, vol. 1, no. 6, pp. 1089–1093, 2011.

[12] J. Chang, M. Jin, F. Yao, T. H. Kim, V. T. Le, H. Yue, F. Gunes, B. Li, A. Ghosh, S. Xie, and Y. H. Lee, "Asymmetric supercapacitors based on graphene/MnO_2 nanospheres and graphene/MoO_3 nanosheets with high energy density", *Advanced Functional Materials*, vol. 23, no. 40, pp. 5074–5083, 2013.

[13] Y. Wang, J. Guo, T. Wang, J. Shao, D. Wang, and Y.-W. Yang, "Mesoporous transition metal oxides for supercapacitors", *Nanomaterials*, vol. 5, no. 4, pp. 1667–1689, 2015.

[14] G. Zhang, X. Xiao, B. Li, P. Gu, H. Xue, and H. Pang, "Transition metal oxides with one-dimensional/one-dimensional-analogue nanostructures for advanced supercapacitors", *Journal of Materials Chemistry A*, vol. 5, no. 18, pp. 8155–8186, 2017.

[15] G. A. Snook, P. Kao, and A. S. Best, "Conducting-polymer-based supercapacitor devices and electrodes", *Journal of Power Sources*, vol. 196, no. 1, pp. 1–12, 2011.

[16] D. Belanger, T. Brousse, and J. W. Long, "Manganese oxides: Battery materials make the leap to electrochemical capacitors", *The Electrochemical Society Interface*, vol. 17, no. 1, pp. 49–52, 2008.

[17] S. W. Lee, J. Kim, S. Chen, P. T. Hammond, and Y. Shao-Horn, "Carbon nanotube/manganese oxide ultrathin film electrodes for electrochemical capacitors", *ACS Nano*, vol. 4, no. 7, pp. 3889–3896, 2010.

[18] Z. Lei, F. Shi, and L. Lu, "Incorporation of MnO_2-coated carbon nanotubes between graphene sheets as supercapacitor electrode", *ACS Applied Materials & Interfaces*, vol. 4, no. 2, pp. 1058–1064, 2012.

[19] Q. Li, X.-F. Lu, H. Xu, Y.-X. Tong, and G.-R. Li, "Carbon/MnO_2 double-walled nanotube arrays with fast ion and electron transmission for high-performance supercapacitors", *ACS Applied Materials & Interfaces*, vol. 6, no. 4, pp. 2726–2733, 2014.

[20] P. Yang, Y. Ding, Z. Lin, Z. Chen, Y. Li, P. Qiang, M. Ebrahimi, W. Mai, C. P. Wong, and Z. L. Wang, "Low-cost high-performance solid-state asymmetric supercapacitors based on MnO_2 nanowires and Fe_2O_3 nanotubes", *Nano Letters*, vol. 14, no. 2, pp. 731–736, 2014.

[21] US Department of Energy, Basic Research Needs for Electrical Energy Storage: Report of the Basic Energy Sciences Workshop on Electrical Energy Storage, www.osti.gov/accomplishments/documents/fullText/ACC0330.pdf.

[22] L. L. Zhang and X. S. Zhao, "Carbon-based materials as supercapacitor electrodes", *Chemical Society Reviews*, vol. 38, no. 9, pp. 2520–2531, 2009.

[23] M. Salanne, "Ionic liquids for supercapacitor applications", *Topics in Current Chemistry*, vol. 375, no. 63, 2017.

[24] E. Frackowiak, "Carbon materials for supercapacitor application", *Physical Chemistry Chemical Physics*, vol. 9, no. 15, pp. 1774–1785, 2007.

[25] R.-S. Kuhnel and A. Balducci, "Lithium ion transport and solvation in N-butyl-N-methylpyrrolidinium bis(trifluoromethanesulfonyl)imide–propylene carbonate mixtures", *The Journal of Physical Chemistry C*, vol. 118, no. 11, pp. 5742–5748, 2014.

[26] H. Nishide and K. Oyaizu, "Toward flexible batteries", *Science*, vol. 319, no. 5864, pp. 737–738, 2008.

[27] J. A. Rogers, "Electronics for the human body", *Journal of American Medical Association*, vol. 313, no. 6, pp. 561–562, 2015.

[28] H. Guo, M.-H. Yeh, Y. Zi, Z. Wen, J. Chen, G. Liu, C. Hu, and Z. L. Wang, "Ultralight cut-paper-based self-charging power unit for self-powered portable electronic and medical systems", *ACS Nano*, vol. 11, no. 5, pp. 4475–4482, 2017.

[29] A. Meintz, J. Zhang, R. Vijayagopal, C. Kreutzer, S. Ahmed, I. Bloom, A. Burnham, R. B. Carlson, F. Dias, E. J. Dufek, J. Francfort, K. Hardy, A. N. Jansen, M. Keyser, A. Markel, C. Michelbacher, M. Mohanpurkar, A. Pesaran, D. Scoffield, M. Shirk, T. Stephens, and T. Tanim, "Enabling fast charging - Vehicle considerations", *Journal of Power Sources*, vol. 367, pp. 216–227, 2017.

[30] M. Walter, M. V. Kovalenko, and K. V. Kravchyk, "Challenges and benefits of post-lithium-ion batteries", *New Journal of Chemistry*, vol. 44, no. 5, pp. 1677–1683, 2020.

[31] D. Linden and T. B. Reddy, "Handbook of batteries", 2002.

[32] A. C. Marschilok, Y. J. Kim, K. J. Takeuchi, and E. S. Takeuchi, "Silver vanadium phosphorous oxide, $Ag_{0.48}VOPO_4$: exploration as a cathode material in primary and secondary battery applications", *Journal of The Electrochemical Society*, vol. 159, no. 10, pp. A1690–A1695, 2012.

[33] X. Hu, W. Zhang, X. Liu, Y. Mei, and Y. Huang, "Nanostructured Mo-based electrode materials for electrochemical energy storage", *Chemical Society Reviews*, vol. 44, no. 8, pp. 2376–2404, 2015.

[34] T. Sakai, H. Ishikawa, K. Oguro, C. Iwakura, and H. Yoneyama, "Effects of microencapsulation of hydrogen storage alloy on the performances of sealed nickel/metal hydride batteries", *Journal of The Electrochemical Society*, vol. 134, no. 3, pp. 558–562, 1987.

[35] S. R. Ovshinsky, M. A. Fetcenko, and J. Ross, "A nickel metal hydride battery for electric vehicles", *Science*, vol. 260, no. 5105, pp. 176–181, 1993.

[36] E.-J. Yoo, J. Kim, E. Hosono, H.-S. Zhou, T. Kudo, and I. Honma, "Large reversible Li storage of graphene nanosheet families for use in rechargeable lithium ion batteries", *Nano Letters*, vol. 8, no. 8, pp. 2277–2282, 2008.

[37] J.-M. Tarascon, N. Recham, M. Armand, J.-N. Chotard, P. Barpanda, W. Walker, and L. Dupont, "Hunting for better Li-based electrode materials via low temperature inorganic synthesis", *Chemistry of Materials*, vol. 22, no. 3, pp. 724–739, 2010.

[38] M. D. Slater, D. Kim, E. Lee, and C. S. Johnson, "Sodium-ion batteries", *Advanced Functional Materials*, vol. 23, no. 8, pp. 947–958, 2013.

[39] Y. Wang and G. Cao, "Developments in nanostructured cathode materials for high-performance lithium-ion batteries", *Advanced Materials*, vol. 20, no. 12, pp. 2251–2269, 2008.

[40] L.-X. Yuan, Z.-H. Wang, W.-X. Zhang, X.-L. Hu, J.-T. Chen, Y.-H. Huang, and J. B. Goodenough, "Development and challenges of $LiFePO_4$ cathode material for lithium-ion batteries", *Energy & Environmental Science*, vol. 4, no. 2, pp. 269–284, 2011.

[41] A. J. Bard and L. R. Faulkner, *Electrochemical Methods: Fundamentals and Applications*, John Wiley & Sons, New York, NY, 2000.

[42] H. Panda, "Handbook on electroplating with manufacture of electrochemicals", 2017.

[43] M. S. Whittingham, "Electrical energy storage and intercalation chemistry", *Science*, vol. 192, no. 4244, pp. 1126–1127, 1976.

[44] K. Mizushima, P. C. Jones, P. J. Wiseman, and J. B. Goodenough, "Li_xCoO_2 (0<x<-1): A new cathode material for batteries of high energy density", *Materials Research Bulletin*, vol. 15, no. 6, pp. 783–789, 1980.

[45] Z. Liu, A. Yu, and J. Y. Lee, "Synthesis and characterization of $LiNi_{1-x-y}Co_xMn_yO_2$ as the cathode materials of secondary lithium batteries", *Journal of Power Sources*, vol. 81-82, pp. 416–419, 1999.

[46] M. Noel and R. Santhanam, "Electrochemistry of graphite intercalation compounds", *Journal of Power Sources*, vol. 72, no. 1, pp. 53–65, 1998.

[47] K. Song, D.-H. Seo, M. R. Jo, Y.-I. Kim, K. Kang, and Y.-M. Kang, "Tailored oxygen framework of $Li_4Ti_5O_{12}$ nanorods for high-power Li ion battery", *The Journal of Physical Chemistry Letters*, vol. 5, no. 8, pp. 1368–1373, 2014.

[48] M. M. Thackeray and K. Amine, "$Li_4Ti_5O_{12}$ spinel anodes", *Nature Energy*, vol. 6, no. 6, pp. 683, 2021.

[49] V. Augustyn, J. Come, M. A. Lowe, J. W. Kim, P.-L. Taberna, S. H. Tolbert, H. D. Abruna, P. Simon, and B. Dunn, "High-rate electrochemical energy storage through Li^+ intercalation pseudocapacitance", *Nature Materials*, vol. 12, no. 6, pp. 518–522, 2013.

[50] J. Come, V. Augustyn, J. W. Kim, P. Rozier, P.-L. Taberna, P. Gogotsi, J. W. Long, B. Dunn, and P. Simon, "Electrochemical kinetics of nanostructured Nb_2O_5 electrodes", *Journal of The Electrochemical Society*, vol. 161, no. 5, pp. A718–A725, 2014.

[51] K. J. Griffith, Y. Harada, S. Egusa, R. M. Ribas, R. S. Monteiro, R. B. Von Dreele, K. A. Cheetham, R. J. Cava, C. P. Grey, and J. B. Goodenough, "Titanium niobium oxide: From discovery to application in fast-charging lithium-ion batteries", *Chemistry of Materials*, vol. 33, no. 1, pp. 4–18, 2021.

[52] E. P. Roth and C. J. Orendorff, "How electrolytes influence battery safety", *The Electrochemical Society Interface*, vol. 21, no. 2, pp. 45, 2012.

[53] S. W. Baek, M. Saber, A. Van der Ven, and L. Pilon, "Thermodynamic analysis and interpretative guide to entropic potential measurements of lithium-ion battery electrodes", *The Journal of Physical Chemistry C*, vol. 126, no. 14, pp. 6096–6110, 2022.

[54] A. Van der Ven, J. Bhattacharya, and A. A. Belak, "Understanding Li diffusion in Li-intercalation compounds", *Accounts of Chemical Research*, vol. 46, no. 5, pp. 1216–1225, 2013.

[55] M. J. Moran, H. N. Shapiro, D. D. Boettner, and M. B. Bailey, *Fundamentals of Engineering Thermodynamics*, John Wiley & Sons, New York, NY, 2018.

[56] A. Van der Ven and M. Wagemaker, "Effect of surface energies and nano-particle size distribution on open circuit voltage of Li-electrodes", *Electrochemistry Communications*, vol. 11, no. 4, pp. 881–884, 2009.

[57] M. W. Chase, *NIST-JANAF Thermochemical Tables*, American Chemical Society, Washington DC, 1998.

[58] W. Weppner and R. A. Huggins, "Determination of the kinetic parameters of mixed-conducting electrodes and application to the system Li_3Sb", *Journal of The Electrochemical Society*, vol. 124, no. 10, pp. 1569–1578, 1977.

[59] S. W. Baek, K. E. Wyckoff, D. M. Butts, J. Bienz, A. Likitchatchawankun, M. B. Preefer, M. Frajnkovič, B. S. Dunn, R. Seshadri, and L. Pilon, "*Operando* calorimetry informs the origin of rapid rate performance in microwave-prepared $TiNb_2O_7$ electrodes", *Journal of Power Sources*, vol. 490, pp. 229537, 2021.

[60] Y. Zhou, E. Le Calvez, S. W. Baek, M. Frajnkovič, C. Douard, E. Gautron, O. Crosnier, T. Brousse, and L. Pilon, "Effect of particle size on thermodynamics and lithium ion transport in electrodes made of $Ti_2Nb_2O_9$ microparticles or nanoparticles", *Energy Storage Materials*, vol. 52, pp. 371–385, 2022.

[61] K. E. Wyckoff, J. L. Kaufman, S. W. Baek, C. Dolle, J. J. Zak, J. Bienz, L. Kautzsch, R. C. Vincent, A. Zohar, K. A. See, Y. M. Eggeler, L. Pilon, A. Van der Ven, and R. Seshadri, "Metal-metal bonding as an electrode design principle in the low-strain cluster compound $LiScMo_3O_8$", *Journal of the American Chemical Society*, vol. 144, no. 13, pp. 5841–5854, 2022.

[62] R. C. Vincent, Y. Luo, J. L. Andrews, A. Zohar, Y. Zhou, Q. Yan, E. M. Mozur, M. B. Preefer, J. N. Weker, A. K. Cheetham, J. Luo, L. Pilon, B. C. Melot, B. Dunn, and R. Seshadri, "High-rate lithium cycling and structure evolution in Mo_4O_{11}", *Chemistry of Materials*, vol. 34, no. 9, pp. 4122–4133, 2022.

[63] G. Assat, S. L. Glazier, C. Delacourt, and J.-M. Tarascon, "Probing the thermal effects of voltage hysteresis in anionic redox-based lithium-rich cathodes using isothermal calorimetry", *Nature Energy*, vol. 4, no. 8, pp. 647–656, 2019.

[64] X. Feng, M. Fang, X. He, M. Ouyang, L. Lu, H. Wang, and M. Zhang, "Thermal runaway features of large format prismatic lithium ion battery using extended volume accelerating rate calorimetry", *Journal of Power Sources*, vol. 255, pp. 294–301, 2014.

[65] Y. Wang, K. Zaghib, A. Guerfi, F. F. C. Bazito, R. M. Torresi, and J. R. Dahn, "Accelerating rate calorimetry studies of the reactions between ionic liquids and charged lithium ion battery electrode materials", *Electrochimica Acta*, vol. 52, no. 22, pp. 6346–6352, 2007.

[66] A. Du Pasquier, F. Disma, T. Bowmer, A. S. Gozdz, G. Amatucci, and J.-M. Tarascon, "Differential scanning calorimetry study of the reactivity of carbon anodes in plastic Li-ion batteries", *Journal of The Electrochemical Society*, vol. 145, no. 2, pp. 472–477, 1998.

[67] H. Giel, D. Henriques, G. Bourne, and T. Markus, "Investigation of the heat generation of a commercial 2032 ($LiCoO_2$) coin cell with a novel differential scanning battery calorimeter", *Journal of Power Sources*, vol. 390, pp. 116–126, 2018.

[68] Y. Saito, K. Kanari, and K. Takano, "Thermal studies of a lithium-ion battery", *Journal of Power Sources*, vol. 68, no. 2, pp. 451–454, 1997.

[69] O. Munteshari, J. Lau, A. Krishnan, B. Dunn, and L. Pilon, "Isothermal calorimeter for measurements of time-dependent heat generation rate in individual supercapacitor electrodes", *Journal of Power Sources*, vol. 374, pp. 257–268, 2018.

[70] O. Munteshari, J. Lau, D. S. Ashby, B. Dunn, and L. Pilon, "Effects of constituent materials on heat generation in individual EDLC electrodes", *Journal of The Electrochemical Society*, vol. 165, no. 7, pp. A1547–A1557, 2018.

[71] A. Likitchatchawankun, A. Kundu, O. Munteshari, T. S. Fisher, and L. Pilon, "Heat generation in all-solid-state supercapacitors with graphene electrodes and gel electrolytes", *Electrochimica Acta*, vol. 303, pp. 341–353, 2019.

[72] A. Likitchatchawankun, G. Whang, J. Lau, O. Munteshari, B. Dunn, and L. Pilon, "Effect of temperature on irreversible and reversible heat generation rates in ionic liquid-based electric double layer capacitors", *Electrochimica Acta*, vol. 338, pp. 135802, 2020.

[73] O. Munteshari, A. Borenstein, R. H. DeBlock, J. Lau, G. Whang, Y. Zhou, A. Likitchatchawankun, R. B. Kaner, B. Dunn, and L. Pilon, "*In operando* calorimetric measurements for activated carbon electrodes in ionic liquid electrolytes under large potential windows", *ChemSusChem*, vol. 13, no. 5, pp. 1013–1026, 2020.

[74] A. Likitchatchawankun, R. H. DeBlock, G. Whang, O. Munteshari, M. Frajnkovič, B. S. Dunn, and L. Pilon, "Heat generation in electric double layer capacitors with neat and diluted ionic liquid electrolytes under large potential window between 5 and 80 °C", *Journal of Power Sources*, vol. 488, pp. 229368, 2021.

[75] O. Munteshari, J. Lau, A. Likitchatchawankun, B.-A. Mei, C. S. Choi, D. Butts, B. S. Dunn, and L. Pilon, "Thermal signature of ion intercalation and surface redox reactions mechanisms in model pseudocapacitive electrodes", *Electrochimica Acta*, vol. 307, pp. 512–524, 2019.

[76] M. Frajnkovič, A. Likitchatchawankun, C. Douard, Y. Zhou, S. W. Baek, I. Catton, O. Crosnier, T. Brousse, and L. Pilon, "Calorimetry can detect the early onset of hydrolysis in hybrid supercapacitors with aqueous electrolytes", *Journal of Power Sources*, vol. 548, pp. 232069, 2022.

[77] J. Newman, K. E. Thomas, H. Hafezi, and D. R. Wheeler, "Modeling of lithium-ion batteries", *Journal of Power Sources*, vol. 119, pp. 838–843, 2003.

[78] G. Liu, M. Ouyang, L. Lu, J. Li, and X. Han, "Analysis of the heat generation of lithium-ion battery during charging and discharging considering different influencing factors", *Journal of Thermal Analysis and Calorimetry*, vol. 116, no. 2, pp. 1001–1010, 2014.

[79] K. E. Thomas and J. Newman, "Thermal modeling of porous insertion electrodes", *Journal of The Electrochemical Society*, vol. 150, no. 2, pp. A176–A192, 2003.

[80] S. Ma, M. Jiang, P. Tao, C. Song, J. Wu, J. Wang, T. Deng, and W. Shang, "Temperature effect and thermal impact in lithium-ion batteries: A review", *Progress in Natural Science: Materials International*, vol. 28, no. 6, pp. 653–666, 2018.

[81] D. Andre, M. Meiler, K. Steiner, C. Wimmer, T. Soczka-Guth, and D. U. Sauer, "Characterization of high-power lithium-ion batteries by electrochemical impedance spectroscopy. I. Experimental investigation", *Journal of Power Sources*, vol. 196, no. 12, pp. 5334–5341, 2011.

[82] M. Ecker, J. B. Gerschler, J. Vogel, S. Kabitz, F. Hust, P. Dechent, and D. U. Sauer, "Development of a lifetime prediction model for lithium-ion batteries based on extended accelerated aging test data", *Journal of Power Sources*, vol. 215, pp. 248–257, 2012.

[83] Y. Bai, L. Li, Y. Li, G. Chen, H. Zhao, Z. Wang, C. Wu, H. Ma, X. Wang, H. Cui, and J. Zhou, "Reversible and irreversible heat generation of NCA/Si–C pouch cell during electrochemical energy-storage process", *Journal of Energy Chemistry*, vol. 29, pp. 95–102, 2019.

[84] D. M. Seo, S. Reininger, M. Kutcher, K. Redmond, W. B. Euler, and B. L. Lucht, "Role of mixed solvation and ion pairing in the solution structure of lithium ion battery electrolytes", *The Journal of Physical Chemistry C*, vol. 119, no. 25, pp. 14038–14046, 2015.

[85] O. Borodin, M. Olguin, P. Ganesh, P. R. C. Kent, J. L. Allen, and W. A. Henderson, "Competitive lithium solvation of linear and cyclic carbonates from quantum chemistry", *Physical Chemistry Chemical Physics*, vol. 18, no. 1, pp. 164–175, 2016.

[86] W. Cui, Y. Lansac, H. Lee, S.-T. Hong, and Y. H. Jang, "Lithium ion solvation by ethylene carbonates in lithium-ion battery electrolytes, revisited by density functional theory with the hybrid solvation model and free energy correction in solution", *Physical Chemistry Chemical Physics*, vol. 18, no. 34, pp. 23607–23612, 2016.

[87] M. Shakourian-Fard, G. Kamath, and S. K. R. S. Subramanian, "Evaluating the free energies of solvation and electronic structures of lithium-ion battery electrolytes", *ChemPhysChem*, vol. 17, no. 18, pp. 2916–2930, 2016.

[88] C. L. Berhaut, D. Lemordant, P. Porion, L. Timperman, G. Schmidt, and M. Anouti, "Ionic association analysis of LiTDI, LiFSI and $LiPF_6$ in EC/DMC for better Li-ion battery performances", *RSC advances*, vol. 9, no. 8, pp. 4599–4608, 2019.

[89] W. Lu and J. Prakash, "*In situ* measurements of heat generation in a Li/mesocarbon microbead half-cell", *Journal of The Electrochemical Society*, vol. 150, no. 3, pp. A262–A266, 2003.

[90] K. E. Thomas and J. Newman, "Heats of mixing and of entropy in porous insertion electrodes", *Journal of Power Sources*, vol. 119, pp. 844–849, 2003.

[91] K. Smith and C.-Y. Wang, "Power and thermal characterization of a lithium-ion battery pack for hybrid-electric vehicles", *Journal of Power Sources*, vol. 160, no. 1, pp. 662–673, 2006.

[92] A. Van der Ven, K. A. See, and L. Pilon, "Hysteresis in electrochemical systems", *Battery Energy*, vol. 1, no. 2, pp. 20210017, 2022.

[93] A. K. Shukla and T. P. Kumar, "Materials for next-generation lithium batteries", *Current Science*, vol. 94, no. 3, pp. 314–331, 2008.

[94] J. Cao and A. Emadi, "A new battery/ultracapacitor hybrid energy storage system for electric, hybrid, and plug-in hybrid electric vehicles", *IEEE Transactions on Power Electronics*, vol. 27, no. 1, pp. 122–132, 2011.

[95] H. Kim, G. Jeong, Y.-U. Kim, J.-H. Kim, C.-M. Park, and H.-J. Sohn, "Metallic anodes for next generation secondary batteries", *Chemical Society Reviews*, vol. 42, no. 23, pp. 9011–9034, 2013.

[96] L. Lu, X. Han, J. Li, J. Hua, and M. Ouyang, "A review on the key issues for lithium-ion battery management in electric vehicles", *Journal of Power Sources*, vol. 226, pp. 272–288, 2013.

[97] J. Zhang, L. Zhang, F. Sun, and Z. Wang, "An overview on thermal safety issues of lithium-ion batteries for electric vehicle application", *IEEE Access*, vol. 6, pp. 23848–23863, 2018.

[98] M. Toupin, T. Brousse, and D. Belanger, "Charge storage mechanism of MnO_2 electrode used in aqueous electrochemical capacitor", *Chemistry of Materials*, vol. 16, no. 16, pp. 3184–3190, 2004.

[99] V. Augustyn, P. Simon, and B. Dunn, "Pseudocapacitive oxide materials for high-rate electrochemical energy storage", *Energy & Environmental Science*, vol. 7, no. 5, pp. 1597–1614, 2014.

[100] J. B. Cook, H.-S. Kim, T. C. Lin, C.-H. Lai, B. Dunn, and S. H. Tolbert, "Pseudocapacitive charge storage in thick composite MoS_2 nanocrystal-based electrodes", *Advanced Energy Materials*, vol. 7, no. 2, pp. 1601283, 2017.

[101] N. Mahmood and Y. Hou, "Electrode nanostructures in lithium-based batteries", *Advanced Science*, vol. 1, no. 1, pp. 1400012, 2014.

[102] Y. Sun, N. Liu, and Y. Cui, "Promises and challenges of nanomaterials for lithium-based rechargeable batteries", *Nature Energy*, vol. 1, no. 7, pp. 16071, 2016.

[103] E. Pomerantseva, F. Bonaccorso, X. Feng, Y. Cui, and Y. Gogotsi, "Energy storage: The future enabled by nanomaterials", *Science*, vol. 366, no. 6468, pp. eaan8285, 2019.

[104] K. Fu, Y. Wang, C. Yan, Y. Yao, Y. Chen, J. Dai, S. Lacey, Y. Wang, J. Wan, T. Li, Z. Wang, Y. Xu, and L. Hu, "Graphene oxide-based electrode inks for 3D-printed lithium-ion batteries", *Advanced Materials*, vol. 28, no. 13, pp. 2587–2594, 2016.

[105] C. Zhu, T. Liu, F. Qian, T. Y.-J. Han, E. B. Duoss, J. D. Kuntz, C. M. Spadaccini, M. A. Worsley, and Y. Li, "Supercapacitors based on three-dimensional hierarchical graphene aerogels with periodic macropores", *Nano Letters*, vol. 16, no. 6, pp. 3448–3456, 2016.

[106] B. Yao, S. Chandrasekaran, J. Zhang, W. Xiao, F. Qian, C. Zhu, E. B. Duoss, C. M. Spadaccini, M. A. Worsley, and Y. Li, "Efficient 3D printed pseudocapacitive electrodes with ultrahigh MnO_2 loading", *Joule*, vol. 3, no. 2, pp. 459–470, 2019.

[107] S. Chandrasekaran, D. Lin, Y. Li, and M. A. Worsley, "Aerogels, additive manufacturing, and energy storage", *Joule*, vol. 7, no. 5, pp. 866–883, 2023.

[108] J. P. Schmidt, D. Manka, D. Klotz, and E. Ivers-Tiffee, "Investigation of the thermal properties of a Li-ion pouch-cell by electrothermal impedance spectroscopy", *Journal of Power Sources*, vol. 196, no. 19, pp. 8140–8146, 2011.

[109] J. P. Schmidt, A. Weber, and E. Ivers-Tiffee, "A novel and precise measuring method for the entropy of lithium-ion cells: ΔS via electrothermal impedance spectroscopy", *Electrochimica Acta*, vol. 137, pp. 311–319, 2014.

[110] M. F. Dupont and S. W. Donne, "Separating the faradaic and non-faradaic contributions to the total capacitance for different manganese dioxide phases", *Journal of The Electrochemical Society*, vol. 162, no. 5, pp. A5096–A5105, 2015.

[111] M. F. Dupont and S. W. Donne, "Separating faradaic and non-faradaic charge storage contributions in activated carbon electrochemical capacitors using electrochemical methods: I. Step potential electrochemical spectroscopy", *Journal of The Electrochemical Society*, vol. 162, no. 7, pp. A1246–A1254, 2015.

[112] M. F. Dupont and S. W. Donne, "A step potential electrochemical spectroscopy analysis of electrochemical capacitor electrode performance", *Electrochimica Acta*, vol. 167, pp. 268–277, 2015.

[113] M. F. Dupont and S. W. Donne, "Electrolytic manganese dioxide structural and morphological effects on capacitive performance", *Electrochimica Acta*, vol. 191, pp. 479–490, 2016.

[114] M. F. Dupont and S. W. Donne, "Faradaic and non-faradaic contributions to the power and energy characteristics of electrolytic manganese dioxide for electrochemical capacitors", *Journal of The Electrochemical Society*, vol. 163, no. 6, pp. A888–A897, 2016.

[115] M. F. Dupont and S. W. Donne, "Charge storage mechanisms in electrochemical capacitors: Effects of electrode properties on performance", *Journal of Power Sources*, vol. 326, pp. 613–623, 2016.

[116] J. Livage, M. Henry, and C. Sanchez, "Sol-gel chemistry of transition metal oxides", *Progress in Solid State Chemistry*, vol. 18, no. 4, pp. 259–341, 1988.

[117] J.-F. Colin, V. Pralong, M. Hervieu, V. Caignaert, and B. Raveau, "Lithium insertion in an oriented nanoporous oxide with a tunnel structure: $Ti_2Nb_2O_9$", *Chemistry of Materials*, vol. 20, no. 4, pp. 1534–1540, 2008.

[118] A. D. Wadsley, "Alkali titanoniobates: The crystal structures of $KTiNbO_5$ and KTi_3NbO_9", *Acta Crystallographica*, vol. 17, no. 6, pp. 623–628, 1964.

[119] M. Fang, C. H. Kim, and T. E. Mallouk, "Dielectric properties of the lamellar niobates and titanoniobates $AM_2Nb_3O_{10}$ and $ATiNbO_5$ (A = H, K, M = Ca, Pb), and their condensation products $Ca_4Nb_6O_{19}$ and $Ti_2Nb_2O_9$", *Chemistry of Materials*, vol. 11, no. 6, pp. 1519–1525, 1999.

[120] Y. Gogotsi and P. Simon, "True performance metrics in electrochemical energy storage", *Science*, vol. 334, no. 6058, pp. 917–918, 2011.

[121] J. B. Leriche, S. Hamelet, J. Shu, M. Morcrette, C. Masquelier, G. Ouvrard, M. Zerrouki, P. Soudan, S. Belin, E. Elkaim, and F. Baudelet, "An electrochemical cell for *operando* study of lithium batteries using synchrotron radiation", *Journal of The Electrochemical Society*, vol. 157, no. 5, pp. A606–A610, 2010.

[122] H. Wang and L. Pilon, "Reply to comments on "Intrinsic limitations of impedance measurements in determining electric double layer capacitances" by H. Wang, L. Pilon [Electrochimica Acta 63 (2012) 55]", *Electrochimica Acta*, vol. 76, pp. 529–531, 2012.

[123] A. Burke and M. Miller, "Testing of electrochemical capacitors: Capacitance, resistance, energy density, and power capability", *Electrochimica Acta*, vol. 55, no. 25, pp. 7538–7548, 2010.

[124] M. D. Stoller and R. S. Ruoff, "Best practice methods for determining an electrode material's performance for ultracapacitors", *Energy & Environmental Science*, vol. 3, no. 9, pp. 1294–1301, 2010.

[125] S. Zhao, F. Wu, L. Yang, L. Gao, and A. F. Burke, "A measurement method for determination of dc internal resistance of batteries and supercapacitors", *Electrochemistry Communications*, vol. 12, no. 2, pp. 242–245, 2010.

[126] B.-A. Mei, O. Munteshari, J. Lau, B. Dunn, and L. Pilon, "Physical interpretations of Nyquist plots for EDLC electrodes and devices", *The Journal of Physical Chemistry C*, vol. 122, no. 1, pp. 194–206, 2018.

[127] M. Thommes, K. Kaneko, A. V. Neimark, J. P. Olivier, F. Rodriguez-Reinoso, J. Rouquerol, and K. S. W. Sing, "Physisorption of gases, with special reference to the evaluation of surface area and pore size distribution (IUPAC Technical Report)", *Pure and Applied Chemistry*, vol. 87, no. 9-10, pp. 1051–1069, 2015.

[128] H. Rebbah, G. Desgardin, and B. Raveau, "Les oxydes $ATiMO_5$: Echangeurs cationiques", *Materials Research Bulletin*, vol. 14, no. 9, pp. 1125–1131, 1979.

[129] J. Huang, Z. Wang, M. Hou, X. Dong, Y. Liu, Y. Wang, and Y. Xia, "Polyaniline-intercalated manganese dioxide nanolayers as a high-performance cathode material for an aqueous zinc-ion battery", *Nature Communications*, vol. 9, no. 1, pp. 2906, 2018.

[130] O. A. Drozhzhin, V. V. Grigoryev, A. M. Alekseeva, R. R. Samigullin, D. A. Aksyonov, O. V. Boytsova, D. Chernyshov, V. V. Shapovalov, A. A. Guda, A. V. Soldatov, K. J. Stevenson, A. M. Abakumov, and E. V. Antipov, "Revisited $Ti_2Nb_2O_9$ as an anode material for advanced Li-ion batteries", *ACS Applied Materials & Interfaces*, vol. 13, no. 47, pp. 56366–56374, 2021.

[131] R. J. Cava, D. W. Murphy, and S. M. Zahurak, "Lithium insertion in Wadsley-Roth phases based on niobium oxide", *Journal of The Electrochemical Society*, vol. 130, no. 12, pp. 2345–2351, 1983.

[132] S. Patoux, M. Dolle, G. Rousse, and C. Masquelier, "A reversible lithium intercalation process in an ReO_3 type structure PNb_9O_{25}", *Journal of The Electrochemical Society*, vol. 149, no. 4, pp. A391–A400, 2002.

[133] J. Wang, J. Polleux, J. Lim, and B. Dunn, "Pseudocapacitive contributions to electrochemical energy storage in TiO_2 (anatase) nanoparticles", *The Journal of Physical Chemistry C*, vol. 111, no. 40, pp. 14925–14931, 2007.

[134] H.-L. Girard, H. Wang, A. d'Entremont, and L. Pilon, "Physical interpretation of cyclic voltammetry for hybrid pseudocapacitors", *The Journal of Physical Chemistry C*, vol. 119, no. 21, pp. 11349–11361, 2015.

[135] H.-L. Girard, B. Dunn, and L. Pilon, "Simulations and interpretation of three-electrode cyclic voltammograms of pseudocapacitive electrodes", *Electrochimica Acta*, vol. 211, pp. 420–429, 2016.

[136] A. Tornheim and D. C. O'Hanlon, "What do coulombic efficiency and capacity retention truly measure? A deep dive into cyclable lithium inventory, limitation type, and redox side reactions", *Journal of The Electrochemical Society*, vol. 167, no. 11, pp. 110520, 2020.

[137] J. Shim and K. A. Striebel, "Effect of electrode density on cycle performance and irreversible capacity loss for natural graphite anode in lithium-ion batteries", *Journal of Power Sources*, vol. 119-121, pp. 934–937, 2003.

[138] H. Buqa, D. Goers, M. Holzapfel, M. E. Spahr, and P. Novak, "High rate capability of graphite negative electrodes for lithium-ion batteries", *Journal of The Electrochemical Society*, vol. 152, no. 2, pp. A474–A481, 2005.

[139] X. Li, P. Yan, X. Xiao, J. H. Woo, C. Wang, J. Liu, and J.-G. Zhang, "Design of porous Si/C–graphite electrodes with long cycle stability and controlled swelling", *Energy & Environmental Science*, vol. 10, no. 6, pp. 1427–1434, 2017.

[140] D. Rehnlund, Z. Wang, and L. Nyholm, "Lithium-diffusion induced capacity losses in lithium-based batteries", *Advanced Materials*, vol. 34, no. 19, pp. 2108827, 2022.

[141] N. S. Hudak, L. E. Davis, and G. Nagasubramanian, "Cycling-induced changes in the entropy profiles of lithium cobalt oxide electrodes", *Journal of The Electrochemical Society*, vol. 162, no. 3, pp. A315–A321, 2015.

[142] H. Liu, M. Wolfman, K. Karki, Y.-S. Yu, E. A. Stach, J. Cabana, K. W. Chapman, and P. J. Chupas, "Intergranular cracking as a major cause of long-term capacity fading of layered cathodes", *Nano Letters*, vol. 17, no. 6, pp. 3452–3457, 2017.

[143] P. Yan, J. Zheng, M. Gu, J. Xiao, J.-G. Zhang, and C.-M. Wang, "Intragranular cracking as a critical barrier for high-voltage usage of layer-structured cathode for lithium-ion batteries", *Nature Communications*, vol. 8, no. 1, pp. 14101, 2017.

[144] A. J. Merryweather, Q. Jacquet, S. P. Emge, C. Schnedermann, A. Rao, and C. P. Grey, "*Operando* monitoring of single-particle kinetic state-of-charge heterogeneities and cracking in high-rate Li-ion anodes", *arXiv*, 2021.

[145] F. Hao, A. Verma, and P. P. Mukherjee, "Mechanistic insight into dendrite–SEI interactions for lithium metal electrodes", *Journal of Materials Chemistry A*, vol. 6, no. 40, pp. 19664–19671, 2018.

[146] U. Janakiraman, T. R. Garrick, and M. E. Fortier, "Review—lithium plating detection methods in Li-ion batteries", *Journal of The Electrochemical Society*, vol. 167, no. 16, pp. 160552, 2020.

[147] K. R. Tallman, G. P. Wheeler, C. J. Kern, E. Stavitski, X. Tong, K. J. Takeuchi, A. C. Marschilok, D. C. Bock, and E. S. Takeuchi, "Nickel-rich nickel manganese cobalt (NMC622) cathode lithiation mechanism and extended cycling effects using *operando* X-ray absorption spectroscopy", *The Journal of Physical Chemistry C*, vol. 125, no. 1, pp. 58–73, 2021.

[148] X. Wang, H. Zhou, Z. Chen, and X. Meng, "Synchrotron-based X-ray diffraction and absorption spectroscopy studies on layered $LiNi_xMn_yCo_zO_2$ cathode materials: A review", *Energy Storage Materials*, vol. 49, pp. 181–208, 2022.

[149] M. Drews, S. Tepner, P. Haberzettl, H. Gentischer, W. Beichel, M. Breitwieser, S. Vierrath, and D. Biro, "Towards 3D-lithium ion microbatteries based on silicon/graphite blend anodes using a dispenser printing technique", *RSC Advances*, vol. 10, no. 38, pp. 22440–22448, 2020.

[150] J. Zhao, Y. Zhang, X. Zhao, R. Wang, J. Xie, C. Yang, J. Wang, Q. Zhang, L. Li, C. Lu, and Y. Yao, "Direct ink writing of adjustable electrochemical energy storage device with high gravimetric energy densities", *Advanced Functional Materials*, vol. 29, no. 26, pp. 1900809, 2019.

[151] C. Zhu, N. B. Schorr, Z. Qi, B. R. Wygant, D. E. Turney, G. G. Yadav, M. A. Worsley, E. B. Duoss, S. Banerjee, E. D. Spoerke, A. van Buuren, and T. N. Lambert, "Direct ink writing of 3D Zn structures as high-capacity anodes for rechargeable alkaline batteries", *Small Structures*, vol. 4, no. 4, pp. 2200323, 2023.

[152] B. Yao, H. Peng, H. Zhang, J. Kang, C. Zhu, G. Delgado, D. Byrne, S. Faulkner, M. Freyman, X. Lu, M. A. Worsley, J. Q. Lu, and Y. Li, "Printing porous carbon aerogels for low temperature supercapacitors", *Nano Letters*, vol. 21, no. 9, pp. 3731–3737, 2021.

[153] M. Idrees, S. Batool, J. Cao, M. S. Javed, S. Xiong, C. Liu, and Z. Chen, "3D printed PC/SiOC@Zn hybrid composite as dendrite-free anode for Zn-ion battery", *Nano Energy*, vol. 100, pp. 107505, 2022.

[154] E. Brown, P. Yan, H. Tekik, A. Elangovan, J. Wang, D. Lin, and J. Li, "3D printing of hybrid MoS_2-graphene aerogels as highly porous electrode materials for sodium ion battery anodes", *Materials & Design*, vol. 170, pp. 107689, 2019.

[155] B. Yao, S. Chandrasekaran, H. Zhang, A. Ma, J. Kang, L. Zhang, X. Lu, F. Qian, C. Zhu, E. B. Duoss, C. M. Spadaccini, M. A. Worsley, and Y. Li, "3D-printed structure boosts the kinetics and intrinsic capacitance of pseudocapacitive graphene aerogels", *Advanced Materials*, vol. 32, no. 8, pp. 1906652, 2020.

[156] D. Lin, S. Chandrasekaran, J.-B. Forien, X. Xue, A. Pinongcos, E. Coester, M. A. Worsley, and Y. Li, "3D-printed graded electrode with ultrahigh MnO_2 loading for non-aqueous electrochemical energy storage", *Advanced Energy Materials*, vol. 13, no. 20, pp. 2300408, 2023.

[157] C. Chen, J. Jiang, W. He, W. Lei, Q. Hao, and X. Zhang, "3D printed high-loading lithium-sulfur battery toward wearable energy storage", *Advanced Functional Materials*, vol. 30, no. 10, pp. 1909469, 2020.

[158] K. Shen, B. Li, and S. Yang, "3D printing dendrite-free lithium anodes based on the nucleated MXene arrays", *Energy Storage Materials*, vol. 24, pp. 670–675, 2020.

[159] H. Yang, H. Wang, W. Li, B. Tian, T. Xu, D. Kong, S. Huang, K. Liu, X. Li, H. Y. Yang, and Y. Wang, "A simple and effective host for sodium metal anode: a 3D-printed high pyrrolic-N doped graphene microlattice aerogel", *Journal of Materials Chemistry A*, vol. 10, no. 32, pp. 16842–16852, 2022.

[160] L. Zeng, H. He, H. Chen, D. Luo, J. He, and C. Zhang, "3D printing architecting reservoir-integrated anode for dendrite-free, safe, and durable Zn batteries", *Advanced Energy Materials*, vol. 12, no. 12, pp. 2103708, 2022.

[161] A. C. Martinez, A. Maurel, A. P. Aranzola, S. Grugeon, S. Panier, L. Dupont, J. A. Hernandez-Viezcas, B. Mummareddy, B. L. Armstrong, P. Cortes, S. T. Sreenivasan, and E. MacDonald, "Additive manufacturing of $LiNi_{1/3}Mn_{1/3}Co_{1/3}O_2$ battery electrode material via vat photopolymerization precursor approach", *Scientific Reports*, vol. 12, no. 1, pp. 19010, 2022.

[162] R. Tao, Y. Gu, J. Sharma, K. Hong, and J. Li, "A conformal heat-drying direct ink writing 3D printing for high-performance lithium-ion batteries", *Materials Today Chemistry*, vol. 32, pp. 101672, 2023.

[163] T. Roy, M. A. Salazar de Troya, M. A. Worsley, and V. A. Beck, "Topology optimization for the design of porous electrodes", *Structural and Multidisciplinary Optimization*, vol. 65, no. 6, pp. 171, 2022.

[164] X. Xue, D. Lin, and Y. Li, "Low tortuosity 3D-printed structures enhance reaction kinetics in electrochemical energy storage and electrocatalysis", *Small Structures*, vol. 3, no. 12, pp. 2200159, 2022.

[165] M. D. Reale Batista, S. Chandrasekaran, B. D. Moran, M. Salazar de Troya, A. Pinongcos, Z. Wang, R. Hensleigh, A. Carleton, M. Zeng, T. Roy, D. Lin, X. Xue, V. A. Beck, D. A. Tortorelli, M. Stadermann, R. Zheng, Y. Li, and M. A. Worsley, "Design and additive manufacturing of optimized electrodes for energy storage applications", *Carbon*, vol. 205, pp. 262–269, 2023.

[166] S. W. Baek, K. E. Wyckoff, D. D. Robertson, M. Frajnkovič, Y. Zhou, S. H. Tolbert, R. Seshadri, and L. Pilon, "*Operando* calorimetry investigation of particle size effects on heat generation in Wadsley-Roth $(W_{0.2}V_{0.8})_3O_7$-based electrodes", *ACS Applied Energy Materials*, vol. 6, no. 3, pp. 1355–1367, 2023.

[167] H. Y. Alolaywi, K. Uzun, and Y.-T. Cheng, ""Zero" porosity high loading NMC622 positive electrodes for Li-ion batteries", *Journal of The Electrochemical Society*, vol. 171, no. 1, pp. 010514, 2024.

[168] M. Frigo and S. G. Johnson, "FFTW: an adaptive software architecture for the FFT", in *Proceedings of the 1998 IEEE International Conference on Acoustics, Speech and Signal Processing, ICASSP '98 (Cat. No.98CH36181)*, 1998, vol. 3, pp. 1381–1384.

[169] L. H. Hess, A. Bothe, and A. Balducci, "Design and use of a novel in situ simultaneous thermal analysis cell for an accurate "real time" monitoring of the heat and weight changes occurring in electrochemical capacitors", *Energy Technology*, vol. 9, no. 9, pp. 2100329, 2021.

[170] A. Bothe and A. Balducci, "Thermal analysis of electrical double layer capacitors: Present status and remaining challenges", *Journal of Power Sources*, vol. 548, pp. 232090, 2022.

[171] A. Bothe, S. E. M. Pourhosseini, P. Ratajczak, F. Beguin, and A. Balducci, "Analysis of thermal and electrochemical properties of electrical double-layer capacitors by using an in-situ simultaneous thermal analysis cell", *Electrochimica Acta*, vol. 444, pp. 141974, 2023.

[172] Z. Li and B.-A. Mei, "Complex thermal analysis of supercapacitor by thermal impedance spectroscopy", *Thermochimica Acta*, vol. 710, pp. 179175, 2022.

[173] Y. Hu and S.-Y. Choe, "Simultaneous and continuous characterization of reversible and irreversible heat of lithium-ion battery using wavelet transform technique", *Electrochimica Acta*, vol. 375, pp. 137973, 2021.

[174] Y. Hu, S.-Y. Choe, and T. R. Garrick, "Measurement of heat generation rate and heat sources of pouch type Li-ion cells", *Applied Thermal Engineering*, vol. 189, pp. 116709, 2021.

[175] B.-A. Mei, J. Lau, T. Lin, S. H. Tolbert, B. S. Dunn, and L. Pilon, "Physical interpretations of electrochemical impedance spectroscopy of redox active electrodes for electrical energy storage", *The Journal of Physical Chemistry C*, vol. 122, no. 43, pp. 24499–24511, 2018.

[176] M. B. Preefer, M. Saber, Q. Wei, N. H. Bashian, J. D. Bocarsly, W. Zhang, G. Lee, J. Milam-Guerrero, E. S. Howard, R. C. Vincent, B. C. Melot, A. Van der Ven, R. Seshadri, and B. S. Dunn, "Multielectron redox and insulator-to-metal transition upon lithium insertion in the fast-charging, Wadsley-Roth phase PNb_9O_{25}", *Chemistry of Materials*, vol. 32, no. 11, pp. 4553–4563, 2020.

[177] M. Saber, M. B. Preefer, S. K. Kolli, W. Zhang, G. Laurita, B. Dunn, R. Seshadri, and A. Van der Ven, "Role of electronic structure in Li ordering and chemical strain in the fast charging Wadsley-Roth phase PNb_9O_{25}", *Chemistry of Materials*, vol. 33, no. 19, pp. 7755–7766, 2021.

[178] K. J. Griffith, I. D. Seymour, M. A. Hope, M. M. Butala, L. K. Lamontagne, M. B. Preefer, C. P. Kocer, G. Henkelman, A. J. Morris, M. J. Cliffe, S. E. Dutton, and C. P. Grey, "Ionic and electronic conduction in $TiNb_2O_7$", *Journal of the American Chemical Society*, vol. 141, no. 42, pp. 16706–16725, 2019.

[179] P. Zhai, L. Liu, X. Gu, T. Wang, and Y. Gong, "Interface engineering for lithium metal anodes in liquid electrolyte", *Advanced Energy Materials*, vol. 10, no. 34, pp. 2001257, 2020.

[180] Y. Han, B. Liu, Z. Xiao, W. Zhang, X. Wang, G. Pan, Y. Xia, X. Xia, and J. Tu, "Interface issues of lithium metal anode for high-energy batteries: Challenges, strategies, and perspectives", *InfoMat*, vol. 3, no. 2, pp. 155–174, 2021.

[181] E. Deiss, "Spurious potential dependence of diffusion coefficients in Li^+ insertion electrodes measured with PITT", *Electrochimica Acta*, vol. 47, no. 25, pp. 4027–4034, 2002.

[182] C. Montella, "Apparent diffusion coefficient of intercalated species measured with PITT: A simple formulation", *Electrochimica Acta*, vol. 51, no. 15, pp. 3102–3111, 2006.

[183] C. Montella, "Discussion of the potential step method for the determination of the diffusion coefficients of guest species in host materials", *Journal of Electroanalytical Chemistry*, vol. 518, no. 2, pp. 61–83, 2002.

[184] J. Li, F. Yang, X. Xiao, M. W. Verbrugge, and Y.-T. Cheng, "Potentiostatic intermittent titration technique (PITT) for spherical particles with finite interfacial kinetics", *Electrochimica Acta*, vol. 75, pp. 56–61, 2012.

[185] H. Shao, Z. Lin, K. Xu, P.-L. Taberna, and P. Simon, "Electrochemical study of pseudocapacitive behavior of $Ti_3C_2T_x$ MXene material in aqueous electrolytes", *Energy Storage Materials*, vol. 18, pp. 456–461, 2019.

[186] O. Munteshari, Y. Zhou, B.-A. Mei, and L. Pilon, "Theoretical validation of the step potential electrochemical spectroscopy (SPECS) and multiple potential step chronoamperometry (MUSCA) methods for pseudocapacitive electrodes", *Electrochimica Acta*, vol. 321, pp. 134648, 2019.

[187] M. Forghani, H. Mavroudis, J. McCarthy, and S. W. Donne, "Electroanalytical characterization of electrochemical capacitor systems using step potential electrochemical spectroscopy", *Electrochimica Acta*, vol. 332, pp. 135508, 2020.

[188] M. Forghani and A. J. Roberts, "Application of step potential electrochemical spectroscopy in pouch cell prototype capacitors", *Electrochimica Acta*, vol. 390, pp. 138845, 2021.

[189] M. A. Hughes, J. A. Allen, and S. W. Donne, "Optimized electrolytic carbon and electrolyte systems for electrochemical capacitors", *ChemElectroChem*, vol. 7, no. 1, pp. 266–282, 2020.

[190] A. P. Cameron, S. B. Davey, K. G. Latham, and S. W. Donne, "Capacitive charge storage at the glassy carbon electrode: Comparison between aqueous and non-aqueous electrolytes", *Journal of The Electrochemical Society*, vol. 168, no. 10, pp. 100508, 2021.

[191] M. Forghani, A. P. Cameron, and S. W. Donne, "Redox mechanism contributions to the behaviour of electrochemical capacitor materials", *Journal of The Electrochemical Society*, vol. 168, no. 5, pp. 050503, 2021.

[192] M. Forghani, J. McCarthy, A. P. Cameron, S. B. Davey, and S. W. Donne, "Semiconductor properties of electrodeposited manganese dioxide for electrochemical capacitors: Mott-Schottky analysis", *Journal of The Electrochemical Society*, vol. 168, no. 2, pp. 020508, 2021.

[193] S. A. Abbas, M. Forghani, S. Anh, S. W. Donne, and K.-D. Jung, "Carbon hollow spheres as electrochemical capacitors: Mechanistic insights", *Energy Storage Materials*, vol. 24, pp. 550–556, 2020.

[194] T. Wang, R. L. Sacci, J. Liang, C.-L. Do-Thanh, J. Fan, H. Chen, Y. Sun, B. P. Thapaliya, S. M. Mahurin, M. Zhou, J. Wu, S. W. Donne, and S. Dai, "Mechanistic insights of pore contributions in carbon supercapacitors by modified step potential electrochemical spectroscopy", *Journal of The Electrochemical Society*, vol. 168, no. 6, pp. 060530, 2021.

[195] R. Qiao and N. R. Aluru, "Ion concentrations and velocity profiles in nanochannel electroosmotic flows", *The Journal of Chemical Physics*, vol. 118, no. 10, pp. 4692–4701, 2003.

[196] M. Z. Bazant, M. S. Kilic, B. D. Storey, and A. Ajdari, "Towards an understanding of induced-charge electrokinetics at large applied voltages in concentrated solutions", *Advances in Colloid and Interface Science*, vol. 152, no. 1-2, pp. 48–88, 2009.

[197] J. H. Masliyah and S. Bhattacharjee, *Electrokinetic and Colloid Transport Phenomena*, John Wiley & Sons, New York, NY, 2006.

[198] H. Wang and L. Pilon, "Mesoscale modeling of electric double layer capacitors with three-dimensional ordered structures", *Journal of Power Sources*, vol. 221, pp. 252–260, 2013.

[199] M. Z. Bazant, K. Thornton, and A. Ajdari, "Diffuse-charge dynamics in electrochemical systems", *Physical Review E*, vol. 70, no. 2, pp. 021506, 2004.

[200] H. Wang, A. Thiele, and L. Pilon, "Simulations of cyclic voltammetry for electric double layers in asymmetric electrolytes: A generalized modified Poisson-Nernst-Planck model", *The Journal of Physical Chemistry C*, vol. 117, no. 36, pp. 18286–18297, 2013.

[201] H.-L. Girard, H. Wang, A. L. d'Entremont, and L. Pilon, "Enhancing faradaic charge storage contribution in hybrid pseudocapacitors", *Electrochimica Acta*, vol. 182, pp. 639–651, 2015.

[202] B.-A. Mei, B. Li, J. Lin, and L. Pilon, "Multidimensional cyclic voltammetry simulations of pseudocapacitive electrodes with a conducting nanorod scaffold", *Journal of The Electrochemical Society*, vol. 164, no. 13, pp. A3237–A3252, 2017.

[203] H. Wang and L. Pilon, "Physical interpretation of cyclic voltammetry for measuring electric double layer capacitances", *Electrochimica Acta*, vol. 64, pp. 130–139, 2012.

[204] A. M. Colclasure and R. J. Kee, "Thermodynamically consistent modeling of elementary electrochemistry in lithium-ion batteries", *Electrochimica Acta*, vol. 55, no. 28, pp. 8960–8973, 2010.

[205] P. Guillemet, T. Brousse, O. Crosnier, Y. Dandeville, L. Athouel, and Y. Scudeller, "Modeling pseudocapacitance of manganese dioxide", *Electrochimica Acta*, vol. 67, pp. 41–49, 2012.

[206] Q. Zhong, B. Huang, J. Ma, and H. Li, "Experimental study on relationship between SOC and OCV of lithium-ion batteries", *International Journal of Smart Grid and Clean Energy*, vol. 3, no. 2, pp. 149–153, 2014.

[207] G. J. Janz and R. P. T. Tomkins, *Nonaqueous Electrolytes Handbook*, Academic Press, New York, NY, 1972.

[208] K. Nishikawa, Y. Fukunaka, T. Sakka, Y. H. Ogata, and J. R. Selman, "Measurement of $LiClO_4$ diffusion coefficient in propylene carbonate by Moire pattern", *Journal of The Electrochemical Society*, vol. 153, no. 5, pp. A830–A834, 2006.

[209] V. R. Subramanian, V. Boovaragavan, V. Ramadesigan, and M. Arabandi, "Mathematical model reformulation for lithium-ion battery simulations: Galvanostatic boundary conditions", *Journal of The Electrochemical Society*, vol. 156, no. 4, pp. A260–A271, 2009.

[210] G. M. Goldin, A. M. Colclasure, A. H. Wiedemann, and R. J. Kee, "Three-dimensional particle-resolved models of Li-ion batteries to assist the evaluation of empirical parameters in one-dimensional models", *Electrochimica Acta*, vol. 64, pp. 118–129, 2012.

[211] T. R. Jow and J. P. Zheng, "Electrochemical capacitors using hydrous ruthenium oxide and hydrogen inserted ruthenium oxide", *Journal of The Electrochemical Society*, vol. 145, no. 1, pp. 49–52, 1998.

[212] H. Kim and B. N. Popov, "A mathematical model of oxide/carbon composite electrode for supercapacitors", *Journal of The Electrochemical Society*, vol. 150, no. 9, pp. 1153–1160, 2003.

[213] G. Sikha, R. E. White, and B. N. Popov, "A mathematical model for a lithium-ion battery/electrochemical capacitor hybrid system", *Journal of The Electrochemical Society*, vol. 152, no. 8, pp. 1682–1693, 2005.

[214] H. Cohen and J. W. Cooley, "The numerical solution of the time-dependent Nernst-Planck equations", *Biophysical Journal*, vol. 5, no. 2, pp. 145–162, 1965.

[215] B.-A. Mei and L. Pilon, "Three-dimensional cyclic voltammetry simulations of EDLC electrodes made of ordered carbon spheres", *Electrochimica Acta*, vol. 255, pp. 168–178, 2017.

[216] C. T. Kelley, *Iterative Methods for Optimization*, Society for Industrial and Applied Mathematics, Philadelphia, PA, 1999.

[217] D. E. Goldberg, *Genetic Algorithms in Search, Optimization, and Machine Learning*, Addison-Wesley Publishing Company, Boston, MA, 1989.

[218] Y. Gogotsi and R. M. Penner, "Energy storage in nanomaterials - capacitive, pseudocapacitive, or battery-like?", *ACS Nano*, vol. 12, no. 3, pp. 2081–2083, 2018.

[219] M. Forghani and S. W. Donne, "Method comparison for deconvoluting capacitive and pseudo-capacitive contributions to electrochemical capacitor electrode behavior", *Journal of The Electrochemical Society*, vol. 165, no. 3, pp. A664–A673, 2018.

[220] V. S. Bagotsky, *Fundamentals of Electrochemistry*, John Wiley & Sons, New York, NY, 2005.

[221] M. S. Kilic, M. Z. Bazant, and A. Ajdari, "Steric effects in the dynamics of electrolytes at large applied voltages. II. Modified Poisson-Nernst-Planck equations", *Physical Review E*, vol. 75, no. 2, pp. 021503, 2007.

[222] M. S. Kilic, M. Z. Bazant, and A. Ajdari, "Steric effects in the dynamics of electrolytes at large applied voltages. I. Double-layer charging", *Physical Review E*, vol. 75, no. 2, pp. 021502, 2007.

[223] C.-W. Wang and A. M. Sastry, "Mesoscale modeling of a Li-ion polymer cell", *Journal of The Electrochemical Society*, vol. 154, no. 11, pp. A1035–A1047, 2007.